UNIVERSITY OF PAVIA

Faculty of Engineering

Department of Electrical, Computer and Biomedical Engineering

DOCTORAL THESIS

Optimal Control and Reinforcement-Learning Strategies for Advanced Management of Lithium-Ion Battery Packs

---

Author:
Andrea POZZI

Supervisor:
Prof. Davide M. RAIMONDO

March 16, 2021

UNIVERSITY OF PAVIA

Abstract

Faculty of Engineering

Department of Electrical, Computer and Biomedical Engineering

Doctor of Philosophy

Optimal Control and Reinforcement-Learning Strategies for Advanced Management of Lithium-Ion Battery Packs

by Andrea POZZI

The use of mathematical models and predictive control in advanced battery management is fundamental in order to achieve high performance, especially in the case of large battery packs in which several cells are arranged both in series and parallel connections. A basic requirement for the development of predictive control is the exploitation of an accurate model. Within this context, as a first contribution, this Thesis provides a thorough investigation of optimal design of experiments methodologies which are able to enhance the identifiability of electrochemical battery models, relying both on the concept of Fisher information, which exhibits a local nature, and global sensitivity analysis. A further contribution is provided in the battery control field, where dissipation and ageing-aware fast-charging strategies are developed for a single lithium-ion cell. Subsequently, model-predictive control is exploited for both the state-of-charge balancing of series-connected cells and the optimal charge of a whole battery pack. In the latter case cells connected in series and parallel arrangements are considered and a sensitivity-based linearization of the overall model is proposed in order to maintain the computational burden at a reasonable level.

Finally, the use of model-free reinforcement learning is considered with application to battery fast charging and optimal velocity planning for autonomous hybrid electric vehicles in an urban context.

Acknowledgements

First, I thank my parents Bruno and Antonella for their love and support throughout my life. You have always been there, always ready to help me solve the problems that this life is facing us, but also able to enjoy every peaceful moment that we spent together. Thank you both for giving me strength to reach this goal. My grandmother Rosangela deserves my wholehearted thanks as well.

I thank my supervisor, Prof. Davide M. Raimondo, for being a guide and supporting me during the Ph.D. program and for his confidence in me.

I also thank Prof. Scott Moura for letting me join for six months the eCAL Laboratory at the UC Berkeley.

I thank Prof. Lalo Magni, Prof. Antonella Ferrara, Prof. Giuseppe De Nicolao, Prof. Chiara Toffanin, Dr. Marcello Torchio, Prof. Gabriele Ciaramella, Prof. Richard D. Braatz, Prof. Paolo Di Barba and Prof. Evelenina Mognaschi for all the valuable discussions.

To all my colleagues, I would like to say thanks for all the breaks at work that we enjoyed together. In particular I would like to thank Giulia, Bianca, Alessandro, Giacomo, Diego, Alessio, Teng, Saehong, Sangjae and Dimitris.

I thank my friends Matteo, Pippo and Marco. Also, I would like to thank the friends from Martinasca (Fede, Ari, Isa e Marco) and the friends from Berkeley (Vittorio, Mauricio, Federico and Alice).

I thank Gianni and Melina, my neighbours, with whom I have always loved to chat in the courtyard during the restful summer hours.

I thank Gianluca, Massimo and Behrouz for being my "bros" during this journey.

Finally, my thanks go to all those who, staying at home or working in hospitals, have fought the pandemic. Andrà tutto bene.

Contents

List of Figures

List of Tables

To my Family...

Chapter 1

Introduction

In the modern world, the importance of high-performance energy accumulators is twofold. On one hand the use of storage systems in power networks has become necessary due to the widespread exploitation of unpredictable renewable resources for energy production. On the other hand, the ever-increasing demand for consumer electronics and (hybrid) electric vehicles has determined growth in the request for portable energy sources (Whittingham, 2012). While the main accumulators in electrical grids are based on pumped hydroelectric systems, electric vehicles usually rely on electrochemical batteries due to their unique characteristics (Perrin et al., 2005; Dunn, Kamath, and Tarascon, 2011; Omar et al., 2014). Within this context, due to the commitment of governments to encourage sustainable mobility to reduce polluting emissions, significant increase in the electric vehicles market is expected in the upcoming years (Pollet, Staffell, and Shang, 2012). For all these reasons, the presented work focuses on electrochemical accumulators and, in particular, on lithium-ion batteries, which exhibit the most promising features among all the different chemistries. In particular, a lithium-ion battery is composed of elementary units, i.e. the electrochemical cells, which are arranged in series and parallel connections and rely on the lithium-ion technology. Such cells are characterized by high energy density, low self-discharge and negligible memory effect. However, safety hazards may occur in case of damages or improper management of the battery, due to the presence of a flammable electrolyte which can lead to explosions and fires (Lisbona and Snee, 2011). Moreover, degradation mechanisms of the performance are experienced over the battery life-time, which are dramatically affected by the different operating conditions (Gao et al., 2017). In particular, the applied current, the cell temperature and the terminal voltage have to be suitably limited to avoid safety risks and premature ageing of the accumulator (Bandhauer, Garimella, and Fuller, 2011; Jain et al., 2015). Therefore, an appropriate Battery Management System (BMS) is required for guaranteeing the proper functioning of such complex devices (Bergveld, Kruijt, and Notten, 2002; Tarascon and Armand, 2011; Lu et al., 2013).

FIGURE 1.1: As of March 2020, the Tesla Model 3 is the world's best-selling electric car in history, with more than 500,000 units delivered. *Photo by Martin Katler on Unsplash*

The performance can be further improved if advanced BMS solutions are employed. These latter rely on mathematical models of the accumulator (Chaturvedi et al., 2010). In fact, mathematical models can be used inside an optimization framework both in the design phase of new cells and during the ordinary management of the battery pack. Among the different tasks of an advanced BMS, the ones mainly considered in the literature are states estimation, fault diagnosis, safety management and fast charging (Lu et al., 2013; Waag, Fleischer, and Sauer, 2014). Moreover, detailed models can be exploited for simulating battery cycles under specific initial and environment conditions, thus allowing the researchers to understand the plant behaviour while avoiding a large amount of time-consuming experiments. Several detailed battery simulator software packages are available and open-source examples include: DUALFOIL (Albertus and Newman, 2007), Scott Moura's fastDFN, LIONSIMBA (Torchio et al., 2016b), M-PET (Smith and Bazant, 2017) and PyBaMM (Sulzer et al., 2020). Within this context, the two main categories of models employed in advanced BMSs are Equivalent Circuit Models (ECMs) (He, Xiong, and Fan, 2011;

Nejad, Gladwin, and Stone, 2016), and Electrochemical Models (EMs) (Gomadam et al., 2002; Santhanagopalan et al., 2006; Ramadesigan et al., 2012). While the former are simple and intuitive, the latter provide a detailed description of the electrochemical phenomena which occur inside a cell. Among the EMs, the Pseudo-Two-Dimensional (P2D) model (Doyle, Fuller, and Newman, 1993) – also known as Doyle-Fuller-Newman (DFN) – is the most widely used. This model consists of coupled and nonlinear Partial Differential Algebraic Equations (PDAEs). Due to its high computational cost, the P2D is more suited for simulation purposes rather than for on-board control applications. Moreover, the use of the P2D model within a control framework is limited by identifiability and observability issues (Moura, 2015). For all these reasons, the research community has been interested in the development of simplified electrochemical models, which are faster to simulate, are identifiable and observable, and still provide a reasonable description of the internal cell phenomena (Zou, Manzie, and Anwar, 2014; Zou, Manzie, and Nešić, 2015). Among them, the Single-Particle Model (SPM) (Santhanagopalan et al., 2006), which is derived from the P2D by modelling the electrodes as single particles, has received a lot of attention.

In the following, some open issues related to parameters estimation, optimal charging and model-free control of lithium-ion batteries are discussed in 1.1, 1.2 and 1.3, respectively.

1.1 Identification and Design of Experiments for Lithium-Ion Batteries

It is known in the literature that the foundations of an adequate model-based control methodology lie in the accuracy of the prediction of the real process behaviours (Nafsun and Yusoff, 2011). In order to enhance such accuracy, a parameter identification process can be exploited based on experimentally collected input and output data. Identifiability and parameters identification for lithium-ion battery models have been investigated by several authors. Although many of them addressed the estimation of the parameters for ECMs, e.g. in (He, Xiong, and Fan, 2011; Sharma and Fathy, 2014), the focus is here dedicated to the ones which consider EMs, since their parameters exhibit a clear physical meaning. In particular, the work in (Bizeray et al., 2018) discusses the identifiability of the SPM parameters, by operating a model linearization and grouping them in hyper-parameters that can be experimentally identified. In (Lopez et al., 2016) structural identifiability and a deep analysis of ill-conditioned sources of the P2D model is considered, based on the Fisher Information Matrix (FIM) (Akaike, 1998). The latter gives a measure of how informative a certain input signal is in terms of parameters sensitivity, relying on the fact that the inverse of the FIM provides an approximation of the covariance parameter matrix. In particular, the authors show that repeating a discharging experiment with several discharging currents may improve the parameter identification process, reducing their variances. However, some parameters of such a model still result unidentifiable if one considers only voltage measurements during simple experiments. In (Forman et al., 2012) the FIM is used to evaluate the accuracy of the P2D parameters estimated using a genetic algorithm. Also in this case some parameters result unidentifiable for that particular experimental setting. As can be noticed from the results of the previously discussed works, the choice of a suitable data-set is extremely important since the amount of information about the real plant behaviours contained in the different sets may not be the same. For this reason, Optimal Experimental Design (OED) approaches can be employed (Whittle, 1973; Pronzato, 2008), thus leading to a data-set which allows for a sufficiently low uncertainty on the estimated parameters of the considered cell. Within the context of lithium-ion batteries,

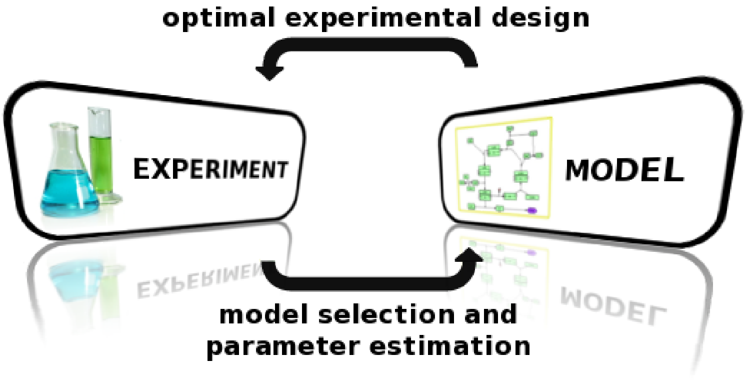

FIGURE 1.2: Conceptual scheme of an optimal experimental design approach. Credit to *ETH Zurich, D-INFK Institute for Machine Learning*.

the OED concept has been exploited by (Mendoza et al., 2017) to maximize the FIM for the case of an equivalent circuit model, while the importance of OED for the accurate estimation of the battery parameters has been underlined in (Liu et al., 2016). Moreover, the authors in (Hametner and Jakubek, 2013) have proposed an optimal design of experiment for a fuzzy model of a lithium-ion cell, while the parameter identification of a battery ageing model has been enhanced by the experiments designed in (Mathieu et al., 2017). Finally, an interesting analysis has been conducted in (Park et al., 2018), where the optimal design of experiments for the P2D model has been considered. In such work, the parameters are grouped into different sets, accordingly to their characteristics, and an optimal input profile has been iteratively selected from a library in order to maximize the resulting FIM. However, even in this case, some parameters have not been identified with high accuracy, thus confirming the need for a simpler model for control purposes. Also, one of the main drawbacks of FIM-based optimal design of experiments relies on the fact that the FIM provides only a local index of how informative a measured signal is in terms of parameter sensitivity. As a consequence, inaccuracy in the information appears when the FIM is evaluated in correspondence of biased reference parameters (Manesso, Sridharan, and Gunawan, 2017). The possibility of biased parameters guess is likely to happen due to the fact that the actual parameters are unknown in a realistic scenario and are the object of the identification process. A possible solution to this issue can be achieved by exploiting Global Sensitivity Analysis (GSA) in order to compute the amount of information provided by a given experiment without depending on the parameters guess. In particular, GSA considers model parameters as random variables and is able to represent nonlinear and multivariate parameters dependencies adequately (Chen, Jin, and Sudjianto, 2005; Schenkendorf et al., 2018). For all the reasons discussed above, one of the goals of the presented Thesis is to assess the effectiveness of both FIM-based and GSA-based optimal design of experiment for control-oriented reduced electrochemical battery models.

1.2 Charging Control of Lithium-Ion Batteries

Nowadays, the standard method used in the industry for the charging of lithium-ion cells is the well known Constant-Current Constant-Voltage (CC-CV) protocol. Such algorithm, however, is rule-based and usually relies on excessively conservative constraints which reduce the probability of safety hazards at the expense of a higher charging time. Moreover, CC-CV is not able to adapt to the variation of the cell parameters due to the ageing and therefore its performance may deteriorate during the cell lifetime (Notten, Veld, and Van Beek, 2005; Keil and Jossen, 2016). Beyond the numerous CC-CV variants proposed over the years, two other rule-based charging methods need to be recalled: the multi-stage current charging algorithm and the pulse charging protocol (Shen, Vo, and Kapoor, 2012). In particular, the former applies a sequence of constant current values which are computed a priori in order to minimize the charging time while the latter relies on a train of current impulses whose frequency is chosen to minimize the battery impedance. In contrast to these rule-based methodologies, there the class of charging algorithms that use a mathematical model within the BMS to optimize the battery performance. Specifically, Model-Predictive Control (MPC) (Camacho and Alba, 2013) appears to be the most used strategy in the literature for solving the optimal charging control problem, due to its the ability to optimize an objective function while dealing with multivariable nonlinear systems subject to constraints on both inputs and states. In the context of lithium-ion cells, a possible objective function to be minimized can be for instance related to the charging time while satisfying temperature and voltage constraints. These latter are fundamental to guarantee safe battery operations, as it is shown in Figure 1.3, where the main issues related to constraints violations are reported.

Most of the literature focuses on the control of a single cell. The works in (Yan et al., 2011a; Xavier and Trimboli, 2015) have proposed MPC strategies based on ECMs, while (Klein et al., 2011; Lucia et al., 2017; Zou, Manzie, and Nešić, 2018) have suggested the use of more accurate electrochemical models. To alleviate the complexity of physics-based models, input-output descriptions have been used in combination with MPC in (Torchio et al., 2015) and (Torchio et al., 2016c). Finally, a reasonable tradeoff between computational time and accuracy in the prediction is

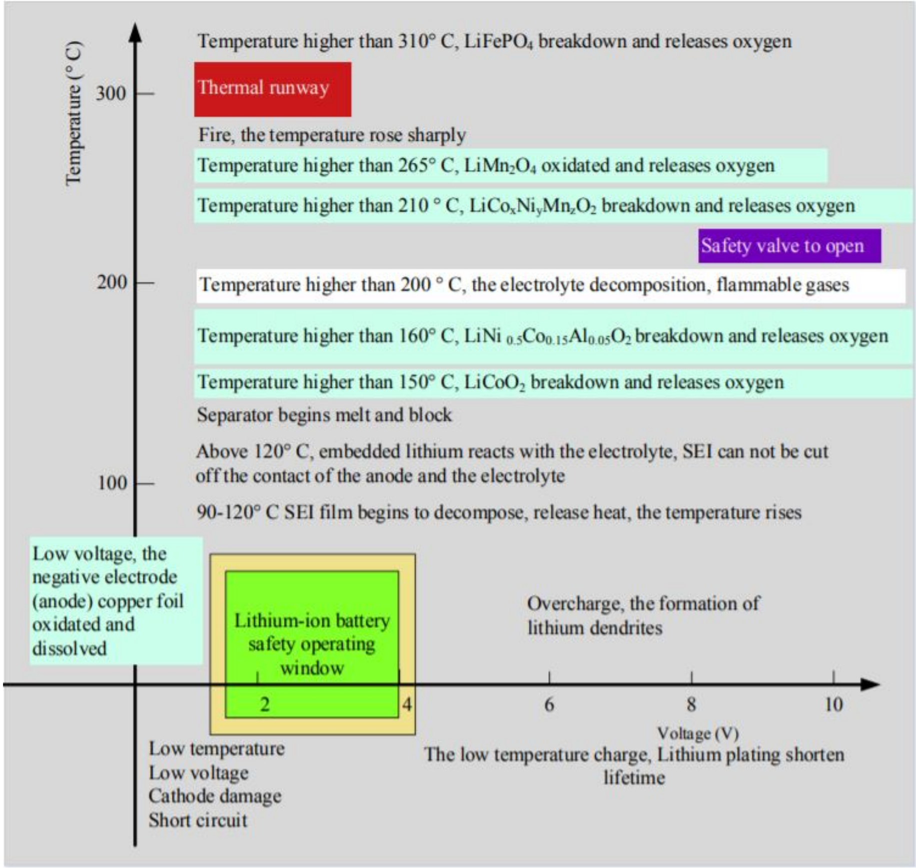

FIGURE 1.3: Safe operating window for a lithium-ion battery (Lu et al., 2013).

achieved through the exploitation of Linear-Time-Varying (LTV) models for MPC in (Torchio et al., 2017; Zou et al., 2017). Also, it has been pointed out in the literature the necessity of accounting for battery changes with ageing degradation and developing charging protocols able to mitigate ageing effects such as Solid-Electrolyte-Interphase (SEI) resistance growth and lithium plating deposition. Despite some predictive control strategies focused on ageing mitigation have been proposed over the years (Klein et al., 2011; Torchio et al., 2016a; Torchio et al., 2016c; Torchio et al., 2017; Lucia et al., 2017), all of them have obtained an ageing reduction to the detriment of the charging duration. Indeed, with a less aggressive charging strategy, it is straightforward to obtain lower degradation effects. In this Dissertation a more interesting perspective based on a fixed charging time is proposed, that allows addressing such trade-off without falling back into trivial solutions.

Although many different portable appliances, such as mobile phones and wearable devices, are powered by a single lithium-ion cell, battery packs used in Electric Vehicles (EVs) are usually constituted by hundreds of cells which are arranged in series and parallel connections to meet power and capacity requirements (Larminie and Lowry, 2012). In such complex scenario further problems relating to efficient and safe management of the accumulator emerge. However, the optimal charging of battery packs has been little investigated. In particular, most of the available literature relies, as control models, on very simple lumped ECMs, see e.g. (Liu and Peng, 2008; Moura et al., 2010b), while only a few works tackle the optimal control of lithium-ion batteries by directly modelling each cell individually.

A cell-scale level of detail is necessary for tasks such as model-based State of Charge (SOC) balancing of series-connected cells (Moore and Schneider, 2001a). It is important to know that, because of unavoidable inconsistencies in the manufacturing process and non-homogeneities in the operating conditions, which may produce diverse ageing effects, the cells composing a battery pack normally have slightly different characteristics (e.g. in terms of internal impedance, self-discharge rate and physical volume) (Bentley, 1997; Dubarry, Vuillaume, and Liaw, 2010). As a consequence, if conventional charging methods are employed, a noticeable unbalancing in the stored charge may appear already after a few charge/discharge cycles (Cao, Schofield, and Emadi, 2008). This is due to the fact that standard charging methods

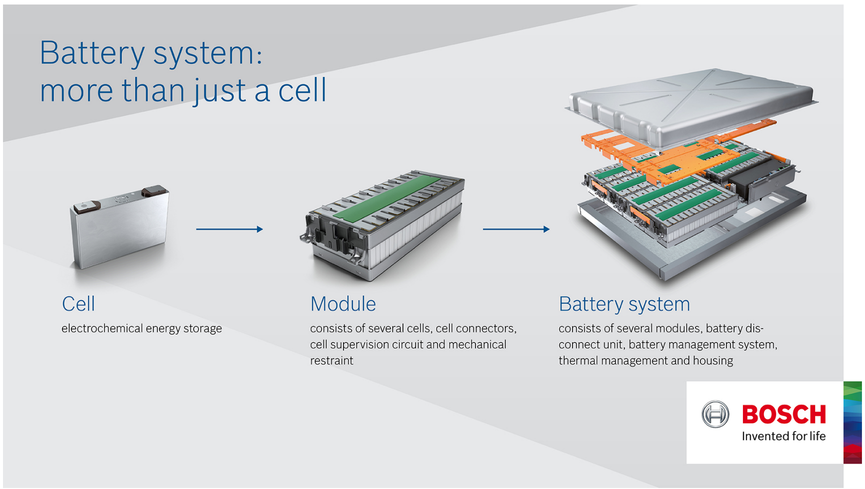

FIGURE 1.4: A battery pack is constituted by multiple connected modules each of which consists of several connected cells.

rely on fixed voltage limits that assure reasonable performance for each cell composing the pack over its lifetime, thus leading to suboptimal exploitation of the battery, in which some cells are undercharged and some are overcharged. As a consequence, some cells may experience fast degradation, thermal runaway, and, in certain cases, even explosions. For all these reasons cell balancing represents an extremely important procedure in order to guarantee safety, full exploitation of the battery charge and preservation of its state of health. However, the majority of the equalization algorithms in the literature are designed to operate off-line, at time instants defined by specific policies, with the aim of mitigating the unbalancing effects of the different cells characteristics (Einhorn, Roessler, and Fleig, 2011; Danielson et al., 2012; Caspar and Hohmann, 2014; Altaf, Egardt, and Mårdh, 2016; McCurlie, Preindl, and Emadi, 2016). An off-line algorithm is hardly applicable in a real scenario since it requires a sort of idle time during which only the charge balancing is performed. Another drawback is that most of the research produced in this area relies on linear ECMs for each cell. Although the usage of such models in the battery optimal control context has the advantage of a low computational cost, simple linear models often fail to grasp the real behaviour of the battery pack. As a consequence, the resulting charging may be suboptimal and may not even satisfy the safety constraints on all the different cells. As a possible solution to all the listed issues related to the balancing of series-connected cells, in this Thesis an MPC-based strategy which relies on a reduced electrochemical model is considered for the development of a balancing-aware charging protocol.

Besides the ones that address the balancing of series-connected cells, no other works in the literature cope with the optimal charging of a battery pack while considering constraints on every single cell. Note that the only to achieve this is to model every cell separately. Also, no attention at all is given to the case of parallel connections whose presence increases significantly the computational burden of the optimization. In fact, even if simple models for the different cells are considered, such as linear ECMs consisting of Ordinary Differential Equations (ODEs), the whole battery pack with both series and parallel connected cells results to be described by Differential Algebraic Equations (DAEs). These latter are far more difficult than ODEs to be managed within an optimization framework (Petzold, 1982). It is important to notice that, as discussed above, the exploitation of an electrochemical model for the different cells would greatly enhance the accuracy in the prediction and the performance of the control strategy. However, the use of electrochemical models, even in the case of reduced-order ones, can be a possibility only if few series-connected cells are considered. In fact, for the whole battery pack of a hybrid electric vehicle, composed by hundreds of cells with both series and parallel connections, the computational cost would become prohibitive. Within this context, we explore in this Dissertation the possibility of employing linearized electrochemical models in order to achieve high performance in the charging of large battery packs with a reasonable computational load.

1.3 Reinforcement Learning Strategies for Batteries and Hybrid Electric Vehicles Management

From the previous discussion, it is clear how battery modelling plays a central role in the development of control algorithms. In fact, proper battery management can be achieved only if the considered model is accurate enough to grasp the main physical behaviours of the process to be controlled. To this end, it is required not only a suitable identification procedure but also an appropriate selection of the model structure. As a possible alternative to the use of first-principle models, some data-driven and learning-based approaches, mainly devoted to states estimation, have been developed in the literature (Nuhic et al., 2013; Hu, Li, and Yang, 2015; Chemali et al., 2018). Nevertheless, it can be argued that both first-principle models and data-driven ones are based on complex parameters identification procedures, and that data-driven approaches require an even larger data-set due to the fact that their structure is more general. Therefore, a totally different approach can be adopted, based on the concept that learning an optimal policy directly from the interaction with the real plant (a.k.a. the environment) is sometimes more straightforward than building an accurate model from experimental data and subsequently solve an optimization problem (Sutton, Barto, et al., 1998). This is particularly true in the case of very complex physical systems such as lithium-ion batteries. However, in the literature, only the authors in (Attia et al., 2020) rely on machine learning, and in particular on a Bayesian optimization, to develop a fast-charging algorithm, subject to voltage and current constraints, which is also oriented to maximize the battery life-time. As an alternative, we consider in the presented Thesis for the first time to the knowledge of the author the exploitation of Reinforcement Learning (RL) for achieving fast-charing in the presence of safety constraints.

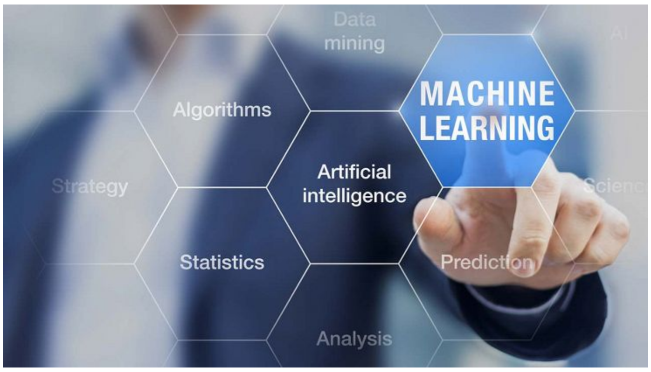

FIGURE 1.5: Reinforcement learning is a control methodology which belongs to the class of machine learning techniques. These latter build a mathematical model based on training data, to make predictions or take decisions without being explicitly programmed to do so.

In conclusion, we have highlighted several times that one of the most important applications for Lithium-ion batteries lies in the field of electric vehicles. While the issues in batteries control are apparent from the previous discussion, it is of interest to understand where the focus should be directed when the more general management of an electric vehicles is considered (Sciarretta and Guzzella, 2007). In particular, in this thesis we focus on Hybrid Electric Vehicles (HEVs) since the presence of both an electric motor and a combustion engine requires a more sophisticated control framework with respect to pure electric vehicles. Within this context, a huge research effort has been oriented during the last decades to the optimal power management of HEVs, which is now a well established and mature field (Liu and Peng, 2008; Moura et al., 2010b; Sun et al., 2014a; Sun et al., 2014b; Huang et al., 2017). On the other hand, the optimal planning of an ecological and efficient velocity trajectory for autonomous HEVs has received attention only in recent years (Dib et al., 2014; Sciarretta, De Nunzio, and Ojeda, 2015; Han et al., 2018) and it appears to be one of the most appealing research topics. In fact, wireless communication technologies in the context of autonomous vehicles have not only enhanced the driving safety in urban areas, but they have also enabled the possibility for an improved vehicle energy management (Guanetti, Kim, and Borrelli, 2018). In particular, in addition to advanced driving assistant systems such as adaptive cruise control and lane-tracking assistance, the idea of an ecological velocity planner which allows for smooth accelerations and braking has become increasingly popular in order to increase vehicle efficiency. Such approach is usually known as optimal eco-driving and its applicability becomes even more interesting within an urban context characterized by signalized intersections, where the Signal Phase and Timing (SPaT) information of

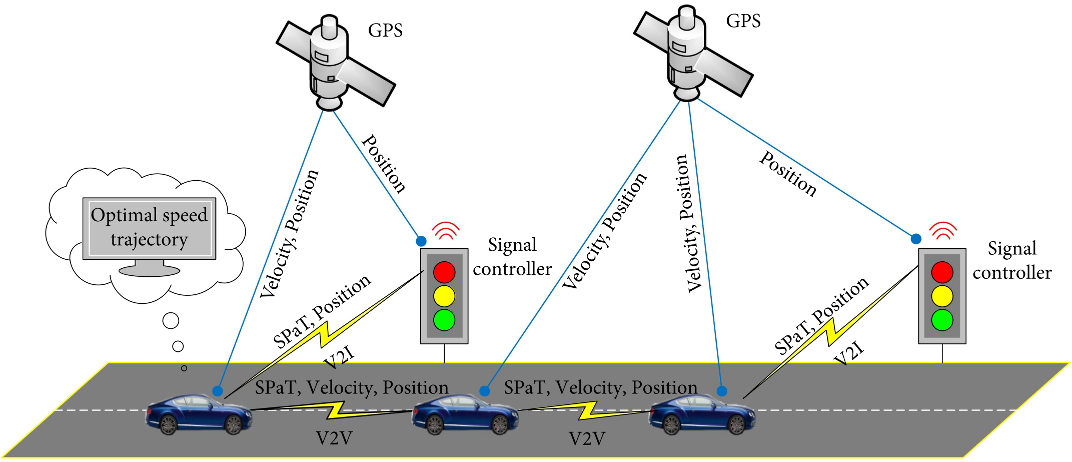

FIGURE 1.6: Conceptual scheme of an eco-driving approach for autonomous vehicles in an urban context (Zhao et al., 2020).

the traffic light is usually uncertain (see Figure 1.6). Several works have been proposed in this field with the aim of solving the eco-driving optimization problem and most of them rely on deterministic or stochastic model-based Dynamic Programming (DP) (Miyatake, Kuriyama, and Takeda, 2011; Bae et al., 2019a; Bae et al., 2019b; Sun et al., 2020). Specifically, the methodology proposed by the authors in (Bae et al., 2019a) consists of a two-stage mathematical framework for ecological velocity planning that has been proposed for a generic autonomous vehicle: the eco-driving controller computes a velocity profile which minimizes the wheel energy consumption given traffic signal information, while at a lower level a velocity controller tracks the reference velocity while avoiding collisions and complying with traffic lights. The procedure is then specialized in (Bae et al., 2019b) for the case of a plug-in HEV, where the powertrain dynamics is considered to more accurately predict the energy consumption. However, one of the main issues in developing model-based optimal eco-driving lies in the complexity of a model which has to describe both the vehicle and the battery dynamics, especially due to the high number of states. In fact, it is well known in the literature that the use of standard DP algorithms in this context is limited by the so-called "curse of dimensionality", which implies exponential growth of computational burden and memory as the state and action dimensions grow (Rust, 1997). A possible solution can be the exploitation even in this case of reinforcement learning strategies (Powell, 2007). While the use of these latter has been already proposed for the optimal power management of HEVs (Wu et al., 2018; Liu and Murphey, 2019), it may constitute, to the best of our knowledge, a novel approach in the field of optimal eco-driving.

1.4 Thesis Contribution

The control of lithium-ion batteries is an appealing topic and the related problems are addressed by researchers of different communities. The proposed Thesis has the aim of exploring and addressing some of the issues which have remained unsolved in the literature. Ideally, a route from the estimation of the cell parameters to the operation of a hybrid electric vehicle, passing through the battery pack management, is followed in the next chapters with both the aims of making the reader aware of the considered problems as well as proposing possible solutions.

1.4.1 Optimal Experimental Design for the Estimation of the Cell Parameters

Due to the fact that several control methodologies explored in this Dissertation are based on mathematical models, we firstly devote attention to the optimal design of experiments for the estimation of the battery parameters. Within this context, FIM-based methodologies are exploited and inserted into a novel sub-optimal recursive framework in order to design even longer experiments with reasonable computational load for reduced-order electrochemical models. In particular, a nonlinear optimization problem is solved in order to minimize the trace of the parameter covariance matrix, over multiple experiments, as proposed in (Körkel and Kostina, 2005). It is of interest that a validation process is presented which is based on measurements collected from the P2D model, considered as the real plant due to its high level of detail. Subsequently, with the aim of overcoming the issue that the FIM constitutes only a local index, a GSA-based approach is proposed for the first time to the knowledge of the authors in the fields of lithium-ion batteries. The considered GSA relies on the Point Estimate Method (PEM) as a highly efficient sampling technique to determine global parameter sensitivities. A comparison between techniques which rely on FIM and GSA is also provided, highlighting the advantages of the latter in terms of low variance on the estimated parameters. The material related to this contribution has appeared in:

- (Pozzi et al., 2018a) - Pozzi, A., Ciaramella, G., Gopalakrishnan, K., Volkwein, S., Raimondo, D. M. (2018, December). Optimal Design of Experiment for Parameter Estimation of a Single Particle Model for Lithium-ion Batteries. In 2018 IEEE Conference on Decision and Control (CDC) (pp. 6482-6487). IEEE.

- (Pozzi et al., 2018b) - Pozzi, A., Ciaramella, G., Volkwein, S., Raimondo, D. M. (2018). Optimal design of experiments for a lithium-ion cell: parameters identification of an isothermal single particle model with electrolyte dynamics. Industrial Engineering Chemistry Research, 58(3), 1286-1299.

- (Pozzi et al., 2020b) - Pozzi, A., Xie, X., Raimondo, D.M. , Schenkendorf, R. (2020). Global Sensitivity Methods for Design of Experiments in Lithium-ion Battery Context. In IFAC World Congress 2020, Germany.

1.4.2 Model-Based Control of a Single Cell

From the control perspective, the case of the model-based optimal charging of a single cell is firstly addressed. Methodologies are discussed with the objective of achieving fast charging while guaranteeing safety and minimizing a certain cost function. First, MPC is employed in order to reduce the energy dissipation during the charging phase. A theoretical analysis is also conducted in order to assess if the energy-saving capability of pulse-charging-current strategies, which has been experimentally demonstrated in the literature, can be reproduced on a linear inductive ECM. Then, the task of limiting the ageing processes is addressed relying on a very detailed electrochemical model along with an MPC framework. This goal is achieved by constraining the charging time of the proposed optimal methodology to be the same as the CC-CV protocol, thus allowing for a fair comparison and addressing the trade-off between charging time and ageing reduction. Furthermore, to guarantee safe operation, the possibility to use a constraint on the plating side reaction overpotential instead of the more conservative terminal voltage limit is considered. The results achieved within this field has been presented in:

- (Pozzi, Torchio, and Raimondo, 2018b) - Pozzi, A., Torchio, M., Raimondo, D. M. (2018, June). Film growth minimization in a Li-ion cell: a Pseudo Two Dimensional model-based optimal charging approach. In 2018 European Control Conference (ECC) (pp. 1753-1758). IEEE.

- (Pozzi, Torchio, and Raimondo, 2018a) - Pozzi, A., Torchio, M., Raimondo, D. M. (2018, August). Assessing the performance of model-based energy saving charging strategies in Li-ion cells. In 2018 IEEE Conference on Control Technology and Applications (CCTA) (pp. 806-811). IEEE.

1.4.3 Balancing of Series-Connected Cells and Battery Pack Management

The problem of state-of-charge balancing in series-connected cells is also tackled and a general nonlinear MPC approach is proposed as a possible solution, relying on a reduced electrochemical model which is sufficiently detailed but also suitable for control applications. The main novelty here introduced is to consider a charging procedure which is able to achieve the SOC equalization at the end of the charge, thus avoiding the idle times typical of standard balancing algorithms. Moreover, the procedure is applied to an easily implementable proposed supply scheme based on switching elements. Although the most immediate formulation of the optimal charging problem with the considered scheme is a mixed-integer program, a continuous approximation is proposed in order to reduce the computational burden. In addition, to consider a realistic scenario in which only voltage and temperature measurements are available, the development of a state observer based on the extended Kalman filter concept is addressed. Moving towards a whole battery pack with both series and parallel connections, a nonlinear MPC is presented for optimally designing the charging phase while taking voltage and temperature limits on each cell into account. Since the computational cost of nonlinear MPC grows significantly with the complexity of the underlying model, a sensitivity-based MPC (sMPC) is proposed, in which the model adopted is obtained by linearizing the dynamics along a nominal trajectory that is updated over time. The resulting sMPC optimizations are quadratic programs which can be solved in real-time even for large battery packs (e.g. fully electric motorbike with 156 cells) while achieving the same performance of the nonlinear MPC. The material related to these contributions has appeared in:

- (Pozzi et al., 2020a) - Pozzi, A., Zambelli, M., Ferrara, A., Raimondo, D. M. (2020). Balancing-aware charging strategy for series-connected lithium-ion cells: A nonlinear model predictive control approach. IEEE Transactions on Control Systems Technology, 28(5), 1862-1877.

- (Pozzi et al., 2020c) - Pozzi, A., Torchio, M., Braatz, R. D., Raimondo, D. M. (2020). Optimal charging of an electric vehicle battery pack: A real-time sensitivity-based model predictive control approach. Journal of Power Sources, 461, 228133.

1.4.4 Fast Charging Approach Based on Reinforcement Learning

We have repeatedly stated that model-based optimal control can achieve higher performance in the context of lithium-ion batteries management compared to rule-based approaches (e.g. the CC-CV). On the other hand, however, the development of a proper model requires a deep knowledge of electrochemistry as well as the exploitation of suitable parameter identification procedures. Furthermore, we highlight that, for large battery packs, the computational cost related to the optimization becomes intractable when nonlinear models are employed. For these reasons, a further contribution of the presented thesis lies in the effort that has been made in order to develop model-free charging protocols for lithium-ion cells which can achieve performance similar to the ones of model-based approaches. In particular, we propose a fast-charging strategy subject to safety constraints which relies on a model-free reinforcement-learning framework. We focus on the policy-gradient-based actor-critic algorithm, i.e., Deep-Deterministic Policy-Gradient (DDPG) (Lillicrap et al., 2015), in order to deal with continuous sets of actions and states. The validity of the proposal is assessed in simulations when a reduced electrochemical model is considered as the real plant. The methodology and the results here discussed have been proposed in:

- (Park et al., 2020) - Park, S., Pozzi, A., Whitmeyer, M., Perez, H., Joe, W. T., Raimondo, D. M., Moura, S. (2020, August). Reinforcement learning-based fast charging control strategy for li-ion batteries. In 2020 IEEE Conference on Control Technology and Applications (CCTA) (pp. 100-107). IEEE.

1.4.5 Eco-Driving for HEVs Based on Reinforcement Learning

Finally, we believe that a contribution is given also in the field of optimal eco-driving for autonomous plug-in HEVs within an urban context. In particular, it has been shown that most of the works in the literature rely on model-based DP approaches, which are often limited by the "curse of dimensionality" as well as by the accuracy of the employed models for the powertrain and vehicle dynamics. In order to overcome these issues, we propose the use of RL strategies which have proven effective in learning complex system dynamics and finding a solution that is statically optimal even in the presence of large states and actions spaces (Sutton, Barto, et al., 1998; Powell, 2007). That said, in the literature RL is utilized for non-safety critical problems, e.g. energy management for hybrid electric powertrains, due to the fact that it does not explicitly guarantee the satisfaction of safety constraints. Indeed, ensuring safety with RL is an essential yet open problem (Garcıa and Fernández, 2015), especially in applications like autonomous driving. For this reason, we propose for the first time to the authors knowledge and RL agent for the velocity planner which is combined with a safety controller (i.e. an adaptive cruise control) in a two-stage structure, to ensure successful crossing of the intersections while exploiting the ecological velocity profile. Although we assume that the communication with traffic lights is limited within a certain range, the RL agent has proven effective in learning an energy management strategy for the PHEV without prior knowledge and finding solutions in a timely manner. The article related to this contribution has been accepted for publication in the proceedings of the 2020 IEEE Conference on Decision and Control (CDC) :

- Pozzi, A., Bae, S., Choi, Y., Borrelli, F., Raimondo, D. M., Moura, S. (2020, December). Ecological Velocity Planning through Signalized Intersections: A Deep Reinforcement Learning Approach. In 2020 59th IEEE Conference on Decision and Control (CDC) (pp. 245-252). IEEE.

1.5 Structure of the Thesis

The rest of the Thesis is structured as follows:

- Chapter 2: this chapter introduces the main features of lithium-ion batteries along with their fields of application. In particular, focus is devoted to the historical development of such technology and to the main issues which need to be faced by an advanced BMS. In addition, the equations of the most common battery models are recalled.

- Chapter 3: this chapter describes the concept of optimal design of experiments and its applicability to the field of lithium-ion batteries in order to improve the accuracy in the estimation of the parameters and significantly reduce the experimental time. Firstly, a FIM-based methodology is applied within an iterative framework, by considering a sub-optimal strategy which allows for computational burden reduction. The proposed algorithm is also validated on the P2D model, which is assumed to be the real battery, thus demonstrating the effectiveness of the methodology in a realistic scenario. Also, to overcome to the limits due to the local nature of the FIM, the use of global sensitivity is also considered.

- Chapter 4: this chapter is devoted to the optimal control of lithium-ion batteries. First, model-predictive control is introduced as one of the more suited methodologies in this field and its main theoretical concepts are presented. Subsequently, the use of MPC is considered for the optimization of the charging procedure for a single cell, to minimize both energy dissipation and degradation mechanisms while satisfying safety constraints. Then, the case of a battery composed of multiple cells is considered. Within this context, an MPC-based charging protocols which aims to reduce the state-of-charge unbalancing for series-connected cells is presented. In conclusion, a whole battery pack with both series and parallel connections is considered and an optimal charging procedure is developed, where the computational burden of the MPC is reduced through a novel sensitivity-based linearization.

- Chapter 5: this chapter proposes the exploitation of reinforcement-learning algorithm in the context of battery and hybrid electric vehicles management. The main features of RL are firstly described in detail, with attention paid to its advantages compared to dynamic programming: the model-free nature of RL is highlighted as well as the fact that the use of approximate dynamic programming can address the so-called "curse of dimensionality". In particular, we focus on the deep-deterministic policy-gradient approach which is able to deal with a continuous set of actions and states. The DDPG is then applied to both the fast charging of a single cell while taking into account safety constraints and to the design of ecological velocity profiles for autonomous HEVs.

- Chapter 6: this chapter concludes the Thesis with a brief overview of the possible future work.

Chapter 2

Lithium-Ion Batteries

In this chapter the main features of the lithium-ion technology are recalled. Starting from the historical evolution of the electrochemical accumulators in Section 2.1, a description of the working principle of modern lithium-ion batteries is provided in Section 2.2. Specifically, we focus on the concept of the electrochemical cell, which constitutes the elementary unit of a battery pack. The latter in fact is usually constituted of several cells which are arranged in series and parallel connections in order to meet power and capacity requirements. The discussion then continues in Section 2.3 with attention to the basic tasks of a battery management system and the possible improvements that can be obtained by exploiting optimization-based techniques which rely on a battery model. Finally, the main equations of the best known lithium-ion cell models are summarized in Section 2.4.

2.1 History of Batteries

Modern Lithium-ion batteries are the result of a technology that has evolved over the centuries. According to the definition, a battery is a device which converts into electricity the energy that is generated by a chemical reaction. Although there exist the belief that a vessel from 250 BC found during archeological excavation in an area near Baghdad (and therefore called the "Baghdad Battery") may constitute a primitive example of a galvanic cell (Rolison and Nazar, 2011), traditionally, the invention of the first electrochemical accumulator is attributed to Alessandro Volta (1745-1827), an Italian scientist that demonstrated how an electric current can flow, through an external circuit, between two metals immersed in an electrolyte solution

(Scrosati, 2011). The "voltaic pile" (see Figure 2.1) consisted of alternated disks of zinc and silver separated by a cloth soaked in a sodium chloride solution.

FIGURE 2.1: Example of "voltaic pile" from (Scrosati, 2011).

Volta's work was the starting point for subsequent discoveries and further developments in the field of electrochemical accumulators. In fact, in 1866 the French Georges-Lionel Leclanché gave birth to the concept at the basis of the modern carbon–zinc cells. It has to say that both Volta's and Leclanché's prototypes were examples of primary batteries, i.e. cells which are not normally rechargeable. Rechargeable batteries, also known as secondary cells, appeared for the first time in 1859, thanks to French scientist Gaston Plantè who proposed the lead–acid chemistry. Another example of rechargeable battery was designed by the Swedish engineer Waldmar Jungner in 1901, exploiting nickel–cadmium chemistry. After that, no further improvement took place in the context of batteries for almost half a century, due to the fact that the available cells were able to satisfy the requirements of the time.

It has been only in the late 1960s that the sudden growth of the consumer electronics market and the need of long-lasting portable energy sources for implantable medical devices has stimulated the resumption of scientific research in the battery field. Attention has been paid to the improvement of the energy density (i.e. the amount of energy stored per weight or per volume), which was found to be the main limitation of the existing technology. For instance, the power supply of the first cardiac pacemaker models was constituted by two mercuric oxide battery which were extremely large and heavy and with only two years of operational life (Scrosati, 2011). The turning point was the choice of exploiting lithium as electrode material, thanks to the fact that it enables theoretical specific capacity almost five times higher than zinc. Lithium is a soft and silver-white metal which occupies the third place in the periodic table and it is the lightest and least dense solid element on the planet (Hanusa, 2015). Lithium is a highly reactive element which easily loses its most external electron. For this reason, it does not occur as a pure element in nature but is contained within minerals in a range of hard rock types or in brine solutions in salt lakes (Kesler et al., 2012). Due to lithium high reactivity, its exploitation together with water-based electrolytes is not possible and therefore the employment of more electrochemically stable organic electrolytes is required. Generally, these latter are formed by a solution of lithium salt in a carbonate organic solvent (e.g. propylene carbonate, ethylene carbonate) or in a mixture of them (Scrosati, 2011). The first prototype of lithium-based technology in battery applications consisted of a cell with a lithium-metal anode and an iodine-based cathode, the so called lithium–iodine battery. Such lithium-iodine cell led to a revolution in the context of cardiac pacemaker, enabling the extension of the operation life of such devices up to seven years. On the other hand, the spread of consumer electronics during the 1970s led to the invention of a lithium battery which relies on a manganese-dioxide cathode and that was fabricated in a coin-type cell version thus fitting into the different device cases. Due to their high energy densities, lithium-ion batteries are nowadays employed in several popular portable appliances such as cellular phones, notebooks, and camcorders. In addition, lithium-ion batteries exhibit rapid charge capability, no memory effects, broad temperature range of operation, relatively long cycle life and low self-discharge rate.

If on the one hand the success of lithium technology for primary batteries was rapid and evident, the process that led to the invention of secondary lithium batteries was more articulated and complex. The outbreak happened in 1978 when the

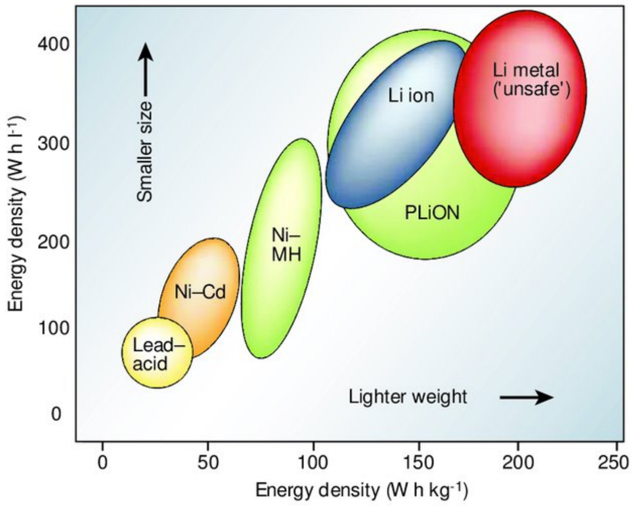

FIGURE 2.2: Comparison of the different battery technologies in terms of volumetric and gravimetric energy density (Tarascon and Armand, 2011).

concept of "intercalation" electrodes was developed, which rely on the idea that the electrodes should reversibly accept and release lithium ions in and out their open structure. Within this context the choice of proper electrode materials became fundamental in order to guarantee reversibility both from the electronic and structural point of view. In the early 1980s rechargeable batteries based on a titanium-sulfide cathode were firstly produced, but they were immediately defined as dangerous due to some breakdowns and accidents that occurred. Due to the fact that such faults were mainly related to the interaction between lithium ions and the electrolyte, the exploitation of a solvent-free polymer electrolyte, formed by a complex between a lithium salt and a coordinating polymer, was proposed and its effectiveness successfully demonstrated. However, due to the risks associated with the exploitation of a lithium-metal electrode, the lithium-polymer battery never achieved a large-scale commercial production. The winning idea came with the so-called *rocking-chair battery*, which relies on two insertion electrodes, one capable of accepting lithium ions, operating as the anode, and the other, capable of releasing lithium ions, operating as the cathode, immersed in a liquid electrolyte. However, a practical application of such concept appeared only ten years later with the battery introduced by the Japanese Sony manufacturer in 1991. Such a battery, that is usually named as the *lithium-ion battery*, was based on a graphite anode and on a lithium-cobalt-oxide cathode ($LiCoO_2$), indicated with the acronym LCO. Although other cathode materials have been developed, most of the commercial production of lithium rocking-chair batteries in fact still relies on lithium cobalt oxide as cathode, due to its ability of releasing and accepting ions during the cycles with a relative low degradation of the performance (Scrosati, 2011).

2.2 Modern Lithium-Ion Batteries Technology

In this section, we describe the working principle of the LCO technology, which is the most used in portable applications, with particular attention to the cell components, the intercalation phenomenon, as well as the most important degradation mechanisms. Moreover, we recall some cathode materials that are largely used nowadays as alternatives to cobalt, due to the fact that this latter constitutes the most expensive element in standard LCO batteries.

2.2.1 LCO Working Principle

As previously stated, the principal components of a lithium-ion cell are a graphite anode (e.g. mesocarbon microbeads) which exhibits a layered structure, a cathode which is constituted by lithium cobalt oxide ($LiCoO_2$) and an electrolyte which consists of a lithium salt solution (e.g. $LiPF_6$) in an organic solvent (e.g. ethylene carbonate–dimethyl carbonate) (Scrosati and Garche, 2010). A separator is immersed in the electrolyte in order to electronically isolate the two electrodes, thus preventing short circuits. A schematic representation of a Li-ion cell is given in Figure 2.3, where also the current collectors are depicted (usually, the negative one is in copper while the positive one is in aluminium). The working principle of such a cell involves the reversible extraction and insertion of lithium ions between the two electrodes with a simultaneous removal and addition of electrons. In particular, during the charging phase (i.e. when a power supply is applied to the cell terminals) a flow of ions is established from the cathode to the anode through the electrolyte, while electrons flows through the external circuit. In fact, one of the fundamental characteristics of both the electrolyte and the separator is their ability of allowing only the flux of ions and blocking the one of electrons. Thanks to the intercalation process, the ions are then stored within the layers of the anode structure. During the discharge phase (i.e. when a load is connected to the battery terminals) the opposite phenomenon happens: the ions move from the anode to the cathode through the electrolyte, while energy is released to the external circuit thanks to an electronic current flow (see Figure 2.3). The ions then intercalate in the cathode by establishing chemical links with the lithium cobalt oxide.

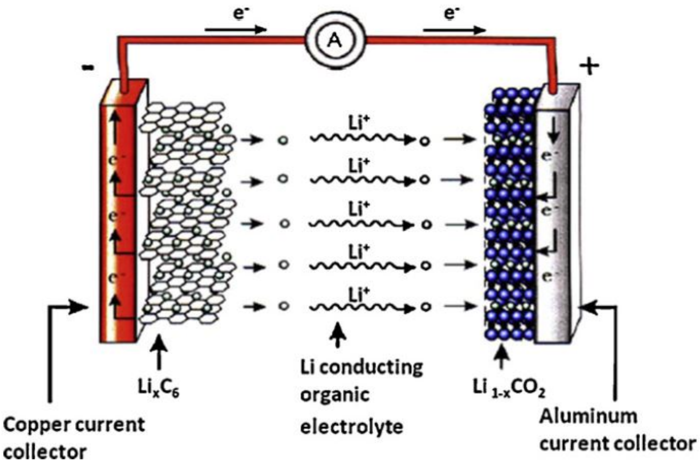

FIGURE 2.3: Schematic representation of the LCO working principle during the discharge phase (Scrosati, 2011).

It is also interesting to notice that a newly produced LCO cell exhibits a thermodynamic instability with these electrolytes. Nevertheless, in practice, the battery operates under a kinetic stability. In fact, during the first few cycles, the electrolyte reacts with the anode and forms a protective film on the anode surface, thus providing the condition to assure the continuation of its charge and discharge processes. Such protective film is known as Solid Electrolyte Interphase (SEI) (Balbuena and Wang, 2004).

2.2.1.1 Degradation Mechanisms

Like any other device, the lifespan of lithium-ion batteries is also limited. In particular, a high impact on the cell lifetime is determined by the presence of ageing and degradation mechanisms which mainly result in capacity fade and resistance growth (Yoshida et al., 2006). Such phenomena are not the consequence of a single process, but they come from a number of various causes and their interactions. Furthermore, most of these processes are not independent and occur at similar timescales (Vetter et al., 2005).

Anode Ageing Mechanisms Among the anode degradation phenomena (Agubra and Fergus, 2013), an important role is played by the SEI formation and growth which leads to a cell resistance rise. While SEI formation occurring at the beginning of cycling can be considered as a beneficial effect for the functioning of the cell as it improves the stability between electrolyte and anode, the SEI growth which proceeds during cycling and storage is a serious ageing phenomenon favoured by elevated temperatures and currents. The rise in the cell resistance is directly related to power fade, which is one of the main limiting factors in the exploitation of aged cells. Simultaneously to the SEI growth, lithium corrosion in the active carbon occurs, leading to capacity fade due to loss of mobile lithium. Finally, the deposition of lithium metal on the surface of anode particles might occur at low temperatures, at high current rates and for inhomogeneous current and potential distributions. Such phenomenon, due to the reaction between lithium ions and the electrolyte, is known as lithium plating and it is particularly dangerous since it can lead to dendrites formation on the anode particles. In this case safety is at risk, due to the fact that excessive growth of dendrites could puncture the separator putting the two electrodes in electronic contact and cause short circuits.

Cathode Ageing Mechanisms For what concerns the cathode, the main degradation mechanisms regard the oxidation of electrolyte components, which leads to surface film formation, and the interaction of ageing products with the negative electrode. In general, the cathodic degradation has a lower impact on the cell life-span, and therefore in the models that we consider later attention will be paid mainly on anodic ageing phenomena.

2.2.2 Alternatives Cathodic Chemistries

As previously discussed, the commercial success of lithium-ion batteries during the 1990s is related to the use of a lithium-cobalt-oxide cathode which became the popular choice for electronic devices such as laptops, mobile phones and digital cameras.

LCO cells, which exhibit high capacity at around $155\frac{Ah}{kg}$ and high nominal voltage of $3.9V$, have been employed in the EVs context by the Tesla Roadster. However, over the years some important drawbacks of this technology have emerged such as short life span, low thermal stability and limited specific power. Moreover, the availability of cobalt is limited thus making it highly expensive. For this reason, several alternatives to $LiCoO_2$-based cathode have been proposed (see (Chen et al., 2012b) for a review on this field), while the graphite remains the predominant material for the anode.

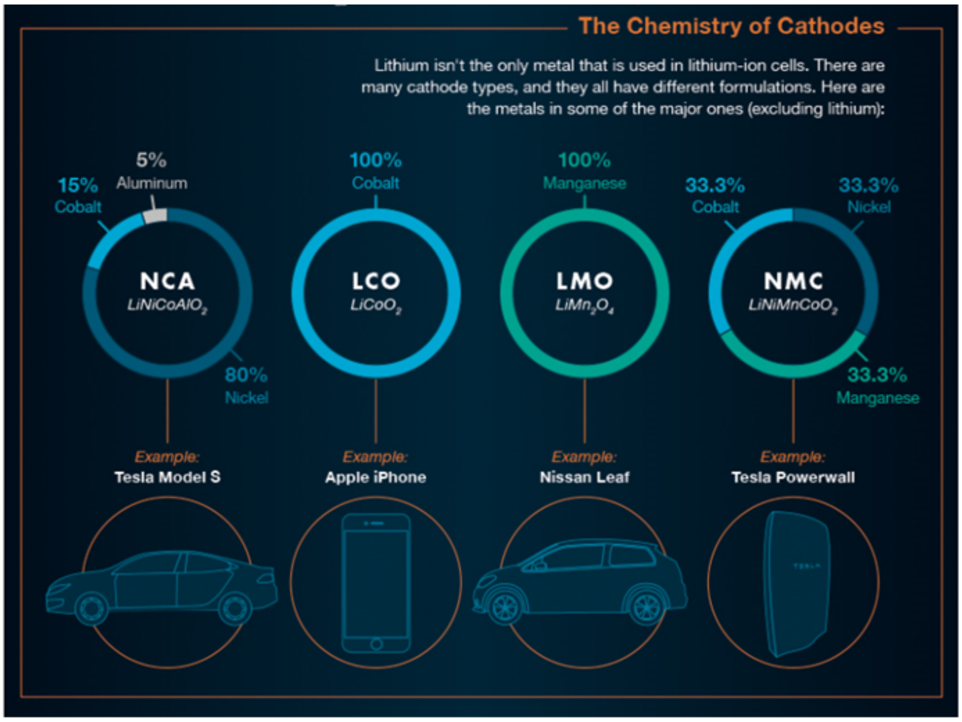

The Chemistry of Cathodes

Lithium isn't the only metal that is used in lithium-ion cells. There are many cathode types, and they all have different formulations. Here are the metals in some of the major ones (excluding lithium):

FIGURE 2.4: Cathodic chemistries and their applications. Credit to *Nevada Energy Metals, eCobalt Solutions Inc., and Great Lakes Graphite.*

2.2.2.1 Lithium Manganese Oxide

A first attempt to substitute the cobalt has been made with batteries based on a lithium-manganese-oxide cathode ($LiMn_2O_4$), usually known as LMO (or also as spinel). The main advantages of the LMO are the low cost of manganese due to its abundance in nature and low toxicity to environment. In the field of EVs the LMO technology has been exploited in the Nissan Leaf. With respect to LCO, the use of manganese allows for higher power density and safety, while as drawbacks, LMO cells exhibit lower capacity, around at $120\frac{Ah}{kg}$, and higher capacity loss while cycling at elevated temperature.

2.2.2.2 Lithium Iron Phosphate

The safest type of lithium-ion battery employs a lithium-iron-phosphate cathode ($LiFePO_4$), indicated with the acronym LFP. This is due to the fact that phosphates are extremely stable in overcharge or short-circuit conditions and have the ability to withstand high temperatures without decomposing. Such technology is considered to be one of the most promising due to the fact that it is non-toxic and relatively cheap. Moreover, LFP also allows for a relatively high specific capacity of about $160\frac{Ah}{kg}$ and an average voltage of $3.40V$. LFP batteries are employed in the Mitsubishi-iMiEV. The main drawback of the LFP cells is related to their high self-discharge rate.

2.2.2.3 Lithium Nickel Manganese Cobalt Oxide

In recent years, batteries based on a lithium-nickel-manganese-cobalt-oxide cathode ($LiNiMnCoO_2$) also known as NMC, have demonstrated to be one of the most promising candidates for the EVs markets, due to their high capacity density (around $200\frac{Ah}{kg}$) and their lower raw material costs (see (Berckmans et al., 2017)) and improved thermal stability during abuse. In fact, several automotive companies are exploiting NMC for their EV segment (Kia, Hyundai, BMW and Mercedes-Benz).

2.2.2.4 Lithium Nickel Cobalt Aluminium Oxide

Finally, we recall the cells based on lithium-nickel-cobalt-aluminium-oxide cathode ($LiNiCoAlO_2$), defined with the acronym NCA, which appeared on the commercial market in 1999 for special applications. Such technology shares analogies with the NMC one since it guarantees high specific energy, reasonably high specific power and a long life span. Nowadays, NCA cells constitute Tesla's main battery technology.

2.2.3 Cells Packaging

A comprehensive analysis of the packaging technology for electrochemical accumulators is given in (Kiehne, 2003). The aim of this section is to summarize the main packaging concepts for single lithium-ion cells (see Figure 2.5), which are usually employed in consumer electronics (Maiser, 2014).

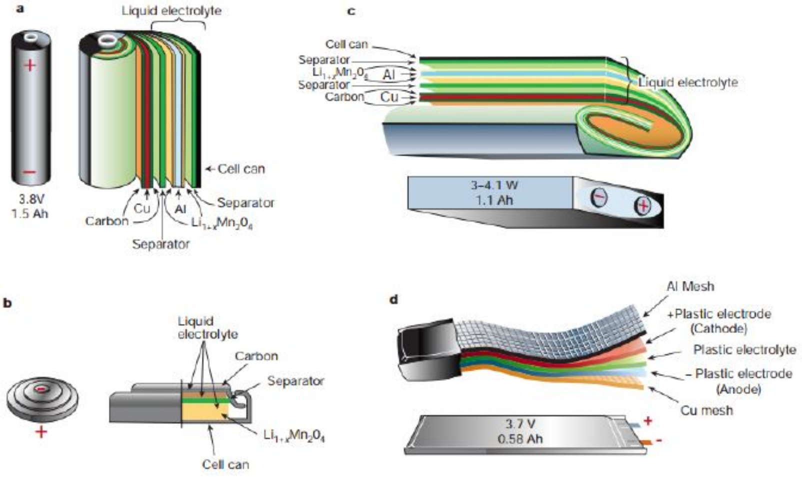

FIGURE 2.5: Different packaging types for lithium-ion cells (Mekonnen, Sundararajan, and Sarwat, 2016): a) cylindrical, b) coin, c) prismatic, d) pouch.

2.2.3.1 Cylindrical Cells

Among the different types of cell packaging, the cylindrical one exhibits the advantage of a high mechanical stability, which naturally withstands internal pressures without deformation. The standard cylindrical cell sizes (also known with the abbreviation AAAA) has appeared in the mid 1990s, with the production of the well known 18650 cell, where $18mm$ and $65mm$ refer to the diameter and the length, respectively. Such cell exhibits a mass of $45g$ and a capacity which ranges from $1.2Ah$ to $3Ah$. For what concerns the electrochemical structure, it consists of cathode, anode and separator cut in stripes and rolled into a metal can. The 18650 format has been widely exploited in the consumer electronics market as well as in the EVs one (Tesla is mainly employing cylindrical cells). It is important to notice that, although the energy density in battery packs constituted by cylindrical cell may be low due to their round shape, the resulting empty spaces enhance the development of efficient cooling systems.

2.2.3.2 Prismatic Cells

The changes in the shape of some electronic devices and the introduction on the market of new ones (e.g. mobile phones, digital cameras and tablet computers) led to the need for a new cell shape, able to adapt to the different requirements. In particular, the batteries for the aforementioned applications mostly exhibit a box-like shape, which is called prismatic. Prismatic cells have found employment also in EVs market (for instance Toyota adopts such cells for its hybrid electric segment) and no standard exists with respect to ratio or size. In particular, they consist of cathode, anode and separator manufactured in long stripes, which are wound up and then pressed to fit into the prismatic container. In this way it is possible to increase the energy efficiency of battery packs with respect to the case in which cylindrical cells are exploited, at the expense however of higher mechanical stress and more complex cooling systems.

2.2.3.3 Pouch Cells

The more interesting characteristic of pouch cells relies in the fact that they do not exhibit a rigid container. In fact pouch cells are sealed by a flexible foil and the components are stacked instead of wrapped. These cells are employed only for the lithium-ion chemistry and their particular package allows to increase the energy density while reducing the weight. A polymer electrolyte is exploited instead of a liquid one in order to increase the safety. This latter is the major concern when pouch cell are employed due to the fact that an increase in the internal pressure usually occurs when high currents are applied. Moreover, a serious swelling may happen in case of overheating. For this reason, pouch cells need a careful temperature management and a support structure when placed into a module.

2.2.3.4 Coin Cells

The coin cells were crucial in enabling compact design for the portable electronic devices of the 1980s, such as cordless telephones and medical devices. These kind of cells have been appreciated for their small size and their low cost. However, the main drawback relies in the possibility of swelling in case of excessively high current. Nowadays, they appear mainly as primary cell and are employed in medical implants, watches, hearing aids, car keys and memory backup.

2.3 Battery Management System

As previously discussed, in recent years we have seen an ever-increasing exploitation of lithium-ion batteries both for smart grids and electric vehicles applications. Although the discovery of new chemistry technologies has significantly improved battery performance in these fields, it is evident that higher results can be achieved if proper management systems are employed (Rahimi-Eichi et al., 2013; Lu et al., 2013). The BMS is an electronic device which manages a rechargeable electrochemical accumulator in order to accomplish some requirements, such as guaranteeing safety, monitoring battery states, and providing optimal charging profiles as well as a suitable thermal management. Moreover, the role of BMSs becomes fundamental in EVs and energy storage systems where batteries composed of several cells are employed, with respect to the case of consumer electronics in which a single-cell battery is usually exploited. Such battery packs can be composed up to hundreds of cells arranged in series and parallel connections. In particular, the series connections enable an higher terminal voltage while the parallel ones allow for an higher capacity, thus meeting the load requirements.

In the following the main tasks of a BMS are summarized together with some important definitions of cell and battery variables.

2.3.1 Cell Monitoring and Variables Estimation

Cell monitoring is one of the most important functions of a BMS. It is important to notice that the only accessible measurements related to a lithium-ion cell are the current, the surface temperature and the terminal voltage, while all the other variables need to be estimated. In particular, retrieving the amount of charge stored in the cell, namely the state of charge, constitutes the focus of most of the estimation algorithms, together with the observation of the battery State of Health (SOH) and Remaining Useful Life (RUL).

2.3.1.1 SOC Estimation

The knowledge of the state of charge is a fundamental prerequisite for a proper exploitation of the battery (Pop et al., 2008): there exists a conceptual analogy between the state of charge of the battery in an electric vehicle and the fuel level in the tank of a vehicle which relies on an internal combustion engine. One of the first methodologies that was adopted in the BMS for the SOC estimation is the so-called *Coulomb counting*, which is based on the time integral of the current in order to find the charge which is released and stored in the battery. However, such an algorithm is limited by both the presence of unavoidable measurement errors on the current sensor and the unknown initial value of the SOC. As an alternative, the static relationship between the Open-Circuit Potential (OCP) and the state of charge can be exploited. Nevertheless, due to the fact that the OCP corresponds to the terminal voltage which is measured in a rest condition, such methodology can not be applied for computing the SOC while the battery is being used and therefore it is not suitable for EVs.

In order to overcome the aforementioned issues, model-based SOC estimation approaches, such as Kalman filters (Welch, Bishop, et al., 1995) and sliding-mode observers (Yan and Edwards, 2007), have recently become popular. However, these methods usually rely of an off-line identification of the battery parameters, which instead exhibit a dependence on temperature, SOC and applied current values. Therefore, nowadays the research is focused on the simultaneous estimation of battery parameters and SOC.

2.3.1.2 SOH and RUL Estimation

Although it is clear that the state of health of a battery is related to its level of ageing, a common and standard definition for this index has not been adopted yet. Most of the works in the literature define the SOH as the ratio between the nominal capacity of the battery (C^n) and the actual one that is reduced due to the degradation mechanisms (C^{act}), i.e. through the following equation

$$SOH = \frac{C^{act}}{C^n} \tag{2.1}$$

However, a limit of this definition is that it does not take into account the context in which the battery is applied. Other works instead consider a combination of internal resistance and capacity loss for the definition of the SOH. In any case, the knowledge of the current state of health of a battery is extremely important due to the fact that it is used for predicting the remaining useful life. Note that it is common to consider the battery end of life when its capacity is reduced of the 20% with respect to its nominal value (although batteries which are considered exhausted for EVs applications may still be employed in the context of energy storage for smart grids). In general, the prediction of the RUL of a battery involves the following two steps

- estimating the current value of the SOH
- based on an accurate ageing model and on a statistical analysis of the user behaviours and environmental conditions, predicting the evolution of the SOH in the future.

2.3.2 Fault Diagnosis and Safety Protection

Ensuring safety and protection is a basic function of the BMS, especially in EVs operation where it is intended to prevent damage to both passengers and the battery. In particular, dangerous situations may occur in case of

- over-current
- over-voltage and under-voltage
- over-charge and under-charge
- over-temperature and under-temperature
- short-circuit conditions

In order to detect potentially hazardous conditions in timely manner various fault diagnostic methods are employed within the BMS. Once a fault is detected, the BMS may intervene by electrically disconnecting the battery if this latter is outside its safe operating area. Moreover, the BMS can request the devices to which the battery is connected to reduce or even terminate its operation in order to guarantee safety. Finally, an active control of the surrounding environment is also possible, such as through heaters, fans, air conditioning or liquid cooling. Note that, in the case of EVs, the compliance with the international ISO 26262 functional safety standard is required, in order to meet the automotive safety integrity level. It is important to notice that also sensor faults may occur during everyday battery operations, including temperature, voltage and current sensor faults as well as the ones related to cell connections and to the cooling system. In conclusion, fault diagnosis ans safety protection are essential features of BMSs since they allow to handle failures safely by going into failure mode, providing a safer environment for the users of lithium-ion batteries (Tran and Fowler, 2020).

2.3.3 Cell Balancing

As previously discussed, in order to increase the terminal voltage, certain applications require a battery pack constituted by several series-connected cells. However, a mismatch in the SOC or in the capacity of the different cells may lead to an unbalanced condition which degrades the overall battery performance. In fact, the discharge ends when the first cell reaches the cutoff voltage threshold, thus implying, in case of SOC unbalancing, that the remaining charge stored in the other cells cannot be utilized (see Figure 2.6). The BMS provides SOC balancing techniques which can be based on different approaches that will be discussed in detail in 4.3.2.

2.3.4 Charging Control

The discharging rate of the battery is usually determined by the applied load and depends on the specific application. On the other hand, from the point of view of the battery user the charging time should be the shortest possible. However, a lower

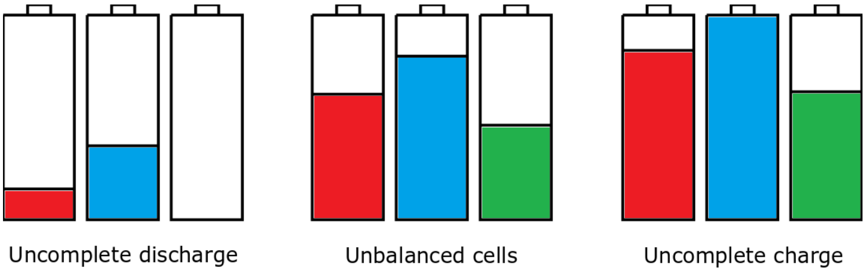

FIGURE 2.6: State of charge unbalancing for series connected lithium-ion cells inside a battery pack.

limit on the charging time is imposed by safety concerns and by the fact that an excessively aggressive charging protocol may lead to premature battery ageing. For this reason, the BMS has the task of providing the optimal charging profile for the considered battery in a specific environmental and states condition, in order to guarantee safety and find a reasonable trade-off between fast charging and ageing. Note that, in the case of large battery packs, the charging current applied to the whole battery needs to satisfy safety constraints on every cell thus preventing harmful conditions.

2.4 Lithium-Ion Cell Models

The development of a battery model is important from several points of view. For instance, an accurate model can be exploited for simulating battery behaviours as a consequence of specific applied current profiles and environmental conditions, so as to avoid the waiting times associated with long-lasting experiments. In this way it is possible to reproduce on a real battery only those experiments which have appeared to be meaningful during the simulation phase. Moreover, the use of a proper mathematical model of the considered lithium-ion cell is required in some of the previously discussed BMS tasks in order to improve control, diagnosis and estimation performance. Specifically, two main model groups exist, namely equivalent-circuit models and electrochemical ones, which are described in the following, where focus is also devoted to reduced EMs, which seem to provide a reasonable trade-off between computational complexity and accuracy.

2.4.1 Equivalent-Circuit Models

An equivalent-circuit model relies on electrical components in order to describe electrochemical phenomena such as ion diffusion and double-layer charging/discharging effects. Impedance-based battery models, derived from a frequency-domain analysis of the current–voltage relationship, were developed at an early stage of research and, subsequently, substituted by Thévenin models (Rahimi-Eichi et al., 2013). Initially, these latter used to rely on a large linear capacitor whose voltage and stored charge accounted for the battery OCP and SOC, respectively. However, this configuration was not able to grasp the nonlinear relationship between SOC and OCP. Therefore, modern Thévenin models exploit a controlled voltage source in which such nonlinear mapping is made evident. In practice, experimentally derived look-up tables describe the SOC/OCP map with different curves for charging and discharging cycles with aim of accounting for the hysteresis effect (Eichi and Chow, 2012).

2.4.1.1 Thévenin Model

Besides the controlled voltage source, which depends nonlinearly on the SOC, a general Thévenin model presents an internal resistance R_{int}, which accounts for the ohmic losses inside the cell (due to the resistance in the ion diffusions within the electrolyte, the presence of a SEI layer and the losses in the electrodes and in the current collectors), and a variable number of parallel resistor-capacitor (RC) pairs. These latter represent the battery relaxation phenomena and, in the case in which only two RC pairs are considered, they usually model the ion diffusion and the double-layer charging/discharging effects. In the following, we provide the circuital scheme (see Figure 2.7) and the main equations of a Thévenin model with two RC blocks, which appears to be one of the most used in the literature (for other ECM configurations the interested reader is referred to (He, Xiong, and Fan, 2011)).

Electrical Dynamics Considering the independent time variable $t \in \mathbb{R}$, one has that the dynamics of the normalized state of charge $SOC(t) \in [0, 1]$ can be obtained as

$$\frac{dSOC(t)}{dt} = -\frac{I_{app}(t)}{3600C(t)} \tag{2.2}$$

where $I_{app}(t)$ is the applied current, with the convention that a negative current is charging the battery, and $C(t)$ is the cell capacity in Ah, thus explaining the presence of the the factor 3600. The open-circuit potential is then described as a nonlinear function of the SOC, i.e. $OCP(t) = OCP(SOC(t))$.

The terminal voltage $V(t)$ is given as

$$V(t) = OCP(t) - V_{rc1}(t) - V_{rc2}(t) - R_{int}(t)I_{app}(t) \tag{2.3}$$

where $V_{rc1}(t)$ and $V_{rc2}(t)$ are the voltages on the first and second RC block, respectively, and the term $R_{int}(t)I_{app}(t)$ accounts for the voltage drop on the internal resistance ($R_{int}(t)$). Note that in this model the internal resistance includes the SEI resistance term ($R_{sei}(t)$). The voltage dynamics of the two RC blocks is given by

$$\frac{dV_{rc1}(t)}{dt} = \frac{I_{app}(t)}{C_1} - \frac{V_{rc1}(t)}{C_1R_1} \tag{2.4}$$

$$\frac{dV_{rc2}(t)}{dt} = \frac{I_{app}(t)}{C_2} - \frac{V_{rc2}(t)}{C_2R_2} \tag{2.5}$$

where C_1, C_2, R_1, R_2 represent the capacitors and the resistances in the two different blocks.

Thermal Dynamics The thermal dynamics is accounted through a lumped model which assumes a uniform temperature $T(t)$ for the cell (see Figure 2.8)

$$C_{th}\dot{T}(t) = Q_g(t) - \frac{T(t) - T_{env}}{R_{th}} \tag{2.6}$$

where C_{th} is the thermal capacity of the cell, and R_{th} is the thermal resistance with respect to the external environment (which may represent a coolant system), whose temperature is here assumed to be constant and equal to T_{env}. Note that the thermal resistance is a lumped parameter which accounts mainly for convection phenomena, i.e. $R_{th} = \frac{1}{A_c h_c}$ where h_c and A_c are respectively the convective coefficient and the heat exchange area. The heat $Q_g(t)$ generated inside the cell is described by

$$Q_g(t) = |I_{app}(t)| \cdot |V(t) - OCP(t)|. \tag{2.7}$$

Ageing Dynamics The battery capacity and the SEI resistance are in general considered as time-varying due to the presence of ageing factors. Such degradation phenomena, however, can not be accurately described within an ECM representation, where the capacity and the SEI resistance are usually assumed to be constant and equal to their nominal values (i.e. $C(t) = C^n$ and $R_{sei}(t) = R^n_{sei}$). The ECM inability of representing internal phenomena such as the ones related to ageing has motivated the need for more sophisticated electrochemical models.

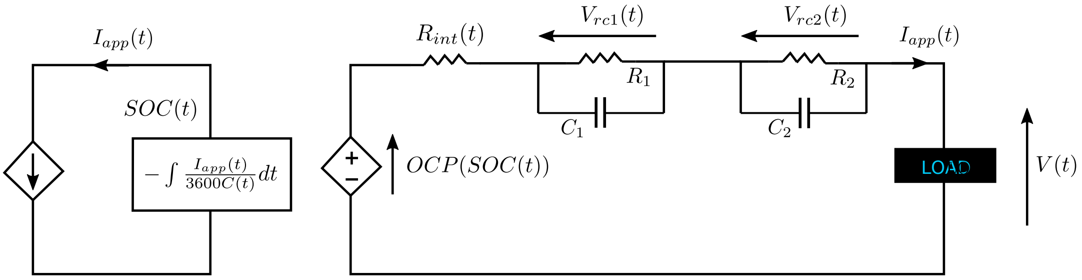

FIGURE 2.7: Circuital scheme of a Thévenin model with two RC blocks.

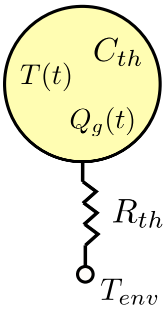

FIGURE 2.8: Schematic representation of the lumped thermal model used in 2.4.1.1 and 2.4.2.2.

2.4.2 Electrochemical Models

Electrochemical models are known to provide an accurate description of the internal cell phenomena at the expense of a huge amount of computational time and memory to be solved, due to the fact that the model is in general described by partial differential algebraic equations. EMs have proven to be useful for manufacturers to optimize the design of their batteries and for chemistry researchers to simulate specific experiments in order to predict the possible outcomes. Within this context the P2D model (Doyle, Fuller, and Newman, 1993) (also known with the acronym DFN) has been largely employed in the literature. However, its high computational burden, together with identifiability and observability issues (Moura, 2015), has led the interest of the research community to the development of reduced-order models which, although derived from the P2D, are able to overcome its aforementioned issues and still provide a reasonable description of the internal cell phenomena. Among this latter, the most popular is the SPM (Santhanagopalan et al., 2006), which has the peculiarity of describing the electrodes as single particles. While the SPM has much lower computational cost than the P2D, which is an advantage for control purposes, it neglects electrolyte, thermal, and ageing dynamics. Therefore, the model fidelity has been increased by extending the SPM to include electrolyte dynamics (SPMe) (Moura et al., 2016) and thermal dynamics (SPMeT) (Perez et al., 2017). In the following, the main equations of the P2D model are recalled in 2.4.2.1, while in 2.4.2.2 a reduced-order electrochemical model tailored for control purposes and based on the SPMeT concept augmented with ageing dynamics is proposed and constitutes one of the contributions of the presented Dissertation.

2.4.2.1 Pseudo-Two-Dimensional Model

The first-principles P2D model is here presented in order to provide a detailed description of the electrochemical behaviour of a lithium-ion cell. The model consists of nonlinear and tightly coupled PDAEs, which are used to represent the conservation of mass and charge within the main sections of the cell (Doyle, Fuller, and Newman, 1993). In particular, this latter is considered as the superposition of different layers: the cathode (p), the separator (sep), and the anode (n). The electrodes and the separator are immersed in an electrolytic solution, thus enabling ionic conduction. When carrying out a charging process, the ions *deintercalate* from the cathode and, flowing through the porous separator, *intercalate* into the anode. The opposite process occurs when a cell is discharged. A one-dimensional thermal model is considered with the aim of describing the temperature evolution in the different sections. Finally, in order to account for ageing dynamics, such as capacity loss and SEI resistance growth, the P2D equations are augmented as in (Torchio et al., 2016a), where the model presented in (Ramadass et al., 2004) is exploited.

In this Thesis, in the case in which the P2D model is employed as simulator we rely on the numerical implementation provided by the freely available Li-ION SIMulation BAttery Toolbox (LIONSIMBA) which is described in details in (Torchio et al., 2016b).

Electrochemical Dynamics In the following, the index $j \in \{p, sep, n\}$ refers to all the battery sections, while the index $i \in \{p, n\}$ is used in equations valid only for the electrodes. Consider the independent variable $x \in \mathbb{R}$ and $r \in \mathbb{R}$ for the axial and radial coordinate, respectively, and $t \in \mathbb{R}$ for the time. Note that, in the proposed model, some of the parameters exhibit a temperature dependency, which is modelled according to the Arrhenius law

$$\psi(T(x,t)) = \psi^0 e^{\frac{-E_{a,\psi}}{R}\left(\frac{1}{T(x,t)} - \frac{1}{T_{ref}}\right)} \tag{2.8}$$

where $T(x,t)$ is the temperature, $E_{a,\psi}$ is the activation energy associated with the generic parameter $\psi(T(x,t))$, R is the universal gas constant ($R = 8.314\frac{J}{K\,mol}$) and T_{ref} is the reference temperature. Note that the pre-exponential factor ψ^0 corresponds to the value of the parameter at the reference temperature. Such relationship will be explicitly highlighted for each of the temperature-dependent parameters.

In accordance to (Torchio et al., 2016b) and (Moura et al., 2016), the diffusion of the ions in the electrolyte within the electrodes is determined by

$$\epsilon_i \frac{\partial c_{e,i}(x,t)}{\partial t} = \frac{\partial}{\partial x}\left[D_{e,i}^{eff} \frac{\partial c_{e,i}(x,t)}{\partial x}\right] + a_i(t)(1 - t_+)j_i(x,t) \tag{2.9}$$

while in the separator it holds that

$$\epsilon_{sep} \frac{\partial c_{e,sep}(x,t)}{\partial t} = \frac{\partial}{\partial x}\left[D_{e,sep}^{eff} \frac{\partial c_{e,sep}(x,t)}{\partial x}\right] \tag{2.10}$$

where $c_{e,j}(x,t)$ is the electrolytic ions concentration and $j_i(x,t)$ is the ionic flux, which is assumed null in the separator. Moreover, t_+ defines the transference number, ϵ_j is the material porosity, $D_{e,j}^{eff} = \epsilon_j^{p_j} D_e(T(x,t))$ is the effective electrolyte diffusion, with $D_e(T(x,t))$ the temperature-dependent electrolyte diffusion coefficient which is assumed to be constant with respect to $c_{e,j}(x,t)$, and p_j is the Bruggeman coefficient. Note that, according to the Bruggeman's theory, the coefficient p_j is related to the tortuosity τ_j as follows

$$\tau_j = \epsilon_j^{1-p}. \tag{2.11}$$

The specific active surface area $a_i(t)$ is defined as

$$a_i(t) = \frac{3\epsilon_i^{act}(t)}{R_{p,i}} \tag{2.12}$$

where $R_{p,i}$ is the particle radius and $\epsilon_i^{act}(t)$ is the active material volume fraction, defined as

$$\epsilon_p^{act}(t) = -\frac{3600C(t)}{\Delta\theta_p A F L_p c_{s,p}^{max}} \tag{2.13a}$$

$$\epsilon_n^{act}(t) = \frac{3600C(t)}{\Delta\theta_n A F L_n c_{s,n}^{max}} \tag{2.13b}$$

where $C(t)$ is the battery capacity expressed in Ah, $\Delta\theta_i = \theta_i^c - \theta_i^d$ with θ_i^d and θ_i^c the battery stochiometries respectively when the cell is fully discharged and completely charged, L_j is the length of the j-th section, F is the Faraday constant ($F = 96485\frac{C}{mol}$), A is the current collector area and $c_{s,i}^{max}$ is the maximum concentration of ions in the solid phase. Notice that equations in (2.13) are in accordance with the fact that the SOC-OCP curve variations are small over the battery lifetime (Waag, Fleischer, and Sauer, 2014). Consider $\hat{x}_p$ as the position along the x-axis which corresponds to the interface between the positive current collector and the cathode, $\hat{x}_{p,sep} = \hat{x}_p + L_p$ to the one between the cathode and the separator, $\hat{x}_{sep,n} = \hat{x}_{p,sep} + L_{sep}$ to the one between the separator and the anode and, finally, $\hat{x}_n = \hat{x}_{sep,n} + L_n$ to the one between the anode and the negative current collector. The boundary conditions for the ions diffusion within the electrolyte are then given by

$$\begin{aligned}
\frac{\partial c_e(x,t)}{\partial x}|_{x=\hat{x}_p,\hat{x}_n} &= 0 && (2.14a)\\
-D_{e,p}^{eff}\frac{\partial c_e(x,t)}{\partial x}|_{x=\hat{x}_{p,sep}^-} &= -D_{e,sep}^{eff}\frac{\partial c_e(x,t)}{\partial x}|_{x=\hat{x}_{p,sep}^+} && (2.14b)\\
-D_{e,sep}^{eff}\frac{\partial c_e(x,t)}{\partial x}|_{x=\hat{x}_{sep,n}^-} &= -D_{e,n}^{eff}\frac{\partial c_e(x,t)}{\partial x}|_{x=\hat{x}_{sep,n}^+} && (2.14c)
\end{aligned}$$

where the superscripts in $\hat{x}_{p,sep}^-$, $\hat{x}_{sep,n}^-$ and $\hat{x}_{p,sep}^+$, $\hat{x}_{sep,n}^+$ represent the left and right limits, respectively.

The following equation, known as the Fick's law, describes the ion diffusion in the active material of the electrodes as

$$\frac{\partial c_s(x,r,t)}{\partial t} = \frac{D_{s,i}(T(x,t))}{r^2}\frac{\partial}{\partial r}\left[r^2\frac{\partial c_s(x,r,t)}{\partial r}\right] \tag{2.15}$$

with $c_s(x,r,t)$ the ion concentration in the solid phase and $D_{s,i}(T(x,t))$ the temperature-dependent solid diffusion coefficient. The boundary conditions for the ion diffusion in the solid phase are given by

$$\begin{aligned}
\frac{\partial c_s(x,r,t)}{\partial r}|_{r=0} &= 0 && (2.16a)\\
-D_{s,i}(T(x,t))\frac{\partial c_s(x,r,t)}{\partial r}|_{r=R_{p,i}} &= j_i^{int}(x,t) && (2.16b)
\end{aligned}$$

where $j_i^{int}(x,t)$ is the intercalation ionic flux, which is modelled by the following Butler-Volmer equation

$$j_i^{int}(x,t) = i_{0,i}(x,t)\sinh\left[\frac{0.5F}{\mathrm{R}T(x,t)}\eta_i(x,t)\right] \tag{2.17}$$

where $\eta_i(x,t)$ represents the electrode overpotential and $i_{0,j}(x,t)$ the intercalation exchange current density. The latter is computed as

$$i_{0,i}(x,t) = k_i(T(x,t))\sqrt{c_e(x,t)(c_{s,i}^{\max} - c_s^*(x,t))c_s^*(x,t)} \tag{2.18}$$

where $c_s^*(x,t)$ denotes the Li-ions surface concentration, and $k_{\mathrm{i}}(T(x,t))$ the temperature-dependent kinetic reaction rate. Notice that the overall ionic flux is given as

$$j_i(x,t) = j_i^{int}(x,t) + j_i^{side}(x,t) \tag{2.19}$$

where $j_i^{side}(x,t)$ refers to the side reactions which lead to ageing degradation (i.e. SEI resistance growth and capacity loss), which are considered to occur only at the electrolyte-anode interface, i.e. $j_p^{side}(x,t) = 0$.

The solid-phase potential $\Phi_s(x,t)$ inside the two electrodes is modelled according to the following Ohm's law

$$\frac{\partial}{\partial x}\left[\sigma_i^{eff}\frac{\partial}{\partial x}\Phi_s(x,t)\right] = a_i(t)Fj_i(x,t) \tag{2.20}$$

in which $\sigma_i^{eff} = \epsilon_i^{p_i}\sigma_i$, with σ_i the electrode conductivity. In this case, the boundary conditions are given by

$$\sigma_i\frac{\partial\Phi_s(x,t)}{\partial x}|_{x=\hat{x}_p,\hat{x}_n} = \frac{I_{app}(t)}{A} \tag{2.21a}$$

$$\frac{\partial\Phi_s(x,t)}{\partial x}|_{x=\hat{x}_{p,sep},\hat{x}_{sep,n}} = 0 \tag{2.21b}$$

where $I_{app}(t)$ is the current applied to the cell. Note that the convention adopted is such that the charging current is negative.

The Ohm's law for the electrolytic potential $\Phi_e(x,t)$ is given by the following equation for the electrodes

$$\frac{\partial}{\partial x}\left[\kappa_i^{eff}\frac{\partial\Phi_e(x,t)}{\partial x}\right] = \frac{2R}{F}(1-t_+)\frac{\partial}{\partial x}\left[\kappa_i^{eff}T(x,t)\frac{\partial \ln c_e(x,t)}{\partial x}\right] - a_i(t)Fj_i(x,t) \tag{2.22}$$

while in the separator it holds that

$$\frac{\partial}{\partial x}\left[\kappa_{sep}^{eff}\frac{\partial\Phi_e(x,t)}{\partial x}\right] = \frac{2R}{F}(1-t_+)\frac{\partial}{\partial x}\left[\kappa_{sep}^{eff}T(x,t)\frac{\partial \ln c_e(x,t)}{\partial x}\right] \tag{2.23}$$

where $\kappa_j^{eff} = \epsilon_j^{p_j}\kappa(c_e(x,t),T(x,t))$, in which $\kappa(c_e(x,t),T(x,t))$ is the temperature-dependent electrolyte conductivity coefficient, considered to be a nonlinear function of the electrolyte concentration. The boundary conditions for the Ohm's law related to the electrolytic potential are given by

$$\frac{\partial \Phi_e(x,t)}{\partial x}|_{x=\hat{x}_p} = 0 \tag{2.24a}$$

$$\Phi_e(x_n,t) = 0 \tag{2.24b}$$

$$-\kappa_p^{eff}\frac{\partial \Phi_e(x,t)}{\partial x}|_{x=\hat{x}_{p,sep}^-} = -\kappa_{sep}^{eff}\frac{\partial \Phi_e(x,t)}{\partial x}|_{x=\hat{x}_{p,sep}^+} \tag{2.24c}$$

$$-\kappa_{sep}^{eff}\frac{\partial \Phi_e(x,t)}{\partial x}|_{x=\hat{x}_{sep,n}^-} = -\kappa_n^{eff}\frac{\partial \Phi_e(x,t)}{\partial x}|_{x=\hat{x}_{sep,n}^+} \tag{2.24d}$$

The electrode overpotentials $\eta_p(x,t)$ and $\eta_n(x,t)$ are given by

$$\eta_p(x,t) = \Phi_s(x,t) - \Phi_e(x,t) - U_p(\theta_p^*(x,t)) \tag{2.25a}$$

$$\eta_n(x,t) = \Phi_s(x,t) - \Phi_e(x,t) - U_n(\theta_n^*(x,t)) - j_n(x,t)F\frac{R_{sei}(t)}{AL_n a_n(t)} \tag{2.25b}$$

where the open-circuit potential of each electrode $U_i(\theta_i^*(x,t))$ is a nonlinear function of the surface stoichiometry $\theta_i^*(x,t) = \frac{c_s^*(x,t)}{c_{s,i}^{max}}$, according to the chemistry of the considered cell, and $R_{sei}(t)$ represents the SEI resistance. Finally, the cell terminal voltage $V(t)$ is obtained as

$$V(t) = \Phi_s(\hat{x}_p,t) - \Phi_s(\hat{x}_n,t) \tag{2.26}$$

The normalized state of charge is defined as

$$SOC(t) = \frac{1}{L_n c_{s,n}^{max} \epsilon_n^{act}(t)} \int_{\hat{x}_{sep,n}}^{\hat{x}_n} c_s^{avg}(x,t)dx \tag{2.27}$$

where $c_s^{avg}(x,t) = \frac{3}{4\pi R_{p,n}^3}\int_0^{R_{p,n}} 4\pi r^2 c_{s,n}(x,r,t)dr$ is the volume average concentration within the solid particles in the anode. Note that in (2.27) the term $\epsilon_n^{act}(t)$ acts as a renormalization factor of the SOC while the cell ages, i.e. it is always possible for a cell to reach a unitary SOC value which corresponds to the full charge situation according to the particular ageing condition.

Thermal Dynamics The one-dimensional thermal dynamics is described by the following equation for the electrodes

$$\rho_i C_{p,i} \frac{\partial T(x,t)}{\partial t} = \frac{\partial}{\partial x}\left[\lambda_i \frac{\partial T(x,t)}{\partial x}\right] + Q_{ohm}(x,t) + Q_{rxn}(x,t) + Q_{rev}(x,t) \tag{2.28}$$

while for the separator it holds that

$$\rho_{sep} C_{p,sep} \frac{\partial T(x,t)}{\partial t} = \frac{\partial}{\partial x}\left[\lambda_{sep} \frac{\partial T(x,t)}{\partial x}\right] + Q_{ohm}(t) \tag{2.29}$$

where ρ_j is the material density, $C_{p,j}$ is the specific heat capacitance and λ_j is the thermal conductivity. The ohmic heat source is given by

$$\begin{aligned} Q_{ohm}(x,t) =& \sigma_i^{eff}\left(\frac{\partial \Phi_s(x,t)}{\partial x}\right)^2 + \kappa_i^{eff}\left(\frac{\partial \Phi_e(x,t)}{\partial x}\right)^2 + \\ &+ \frac{2R}{F}(1-t_+)\kappa_i^{eff} T(x,t) \frac{\partial \ln c_e(x,t)}{\partial x}\frac{\partial \Phi_e(x,t)}{\partial x} \end{aligned} \tag{2.30}$$

in the electrodes, and by

$$\begin{aligned} Q_{ohm}(x,t) =& \kappa_{sep}^{eff}\left(\frac{\partial \Phi_e(x,t)}{\partial x}\right)^2 + \\ &+ \frac{2R}{F}(1-t_+)\kappa_{sep}^{eff} T(x,t) \frac{\partial \ln c_e(x,t)}{\partial x}\frac{\partial \Phi_e(x,t)}{\partial x} \end{aligned} \tag{2.31}$$

in the separator. The reaction heat source $Q_{rxn}(x,t)$ is obtained as follows

$$Q_{rxn}(x,t) = F a_i(t) j_i(x,t) \eta_i(x,t) \tag{2.32}$$

while the reversible heat term $Q_{rev}(x,t)$ is present only if the open-circuit potentials of the electrodes exhibit an explicit dependence on the temperature, i.e. $U_i(\theta^*(x,t)) = U_i(\theta^*(x,t), T(x,t))$, and in that case one has

$$Q_{rev}(x,t) = F a_i(t) j_i(x,t) T(x,t) \frac{\partial U_i(\theta^*(x,t), T(x,t))}{\partial T(x,t)}|_{T_{ref}} \tag{2.33}$$

The boundary conditions for the temperature are given by

$$-\lambda_p \frac{\partial T(x,t)}{\partial x}|_{x=\hat{x}_p} = h_c(T_{env} - T(x,t)) \tag{2.34a}$$

$$-\lambda_n \frac{\partial T(x,t)}{\partial x}|_{x=\hat{x}_n} = h_c(T(x,t) - T_{env}) \tag{2.34b}$$

$$-\lambda_p \frac{\partial T(x,t)}{\partial x}|_{x=\hat{x}_{p,sep}^-} = -\lambda_{sep} \frac{\partial T(x,t)}{\partial x}|_{x=\hat{x}_{p,sep}^+} \tag{2.34c}$$

$$-\lambda_{sep} \frac{\partial T(x,t)}{\partial x}|_{x=\hat{x}_{sep,n}^-} = -\lambda_n \frac{\partial T(x,t)}{\partial x}|_{x=\hat{x}_{sep,n}^+} \tag{2.34d}$$

where h_c is the convective heat coefficient between the cell and the external environment (that may also consist of a coolant system), whose temperature is T_{env}. Note that the P2D model is employed in the literature also in the presence of a lumped thermal model such as the one described in 2.4.1.1 for the Thévenin model, see for instance the work in (Campbell et al., 2019).

Ageing Dynamics For the ageing model we are interested in the dynamics of the battery capacity and the SEI resistance, which are given as follows

$$\frac{dC(t)}{dt} = 3\frac{3600C(t)}{R_{p,n}A\Delta\theta_n c_{s,n}^{max} L_n} \int_{\hat{x}_{sep,n}}^{\hat{x}_n} j_n^{side}(x,t)dx \tag{2.35a}$$

$$\frac{dR_{sei}(t)}{dt} = -\frac{M_w}{\rho_n \nu L_n} \int_{\hat{x}_{sep,n}}^{\hat{x}_n} j_n^{side}(x,t)dx \tag{2.35b}$$

where M_w is the molar weight of the negative electrode and ν is the admittance of the film. The side-reaction flux is obtained through a Tafel equation as

$$j_n^{side}(x,t) = -\frac{i_0^{side}(t)}{F} exp\left(\frac{0.5F}{RT(x,t)}\eta_{n,sei}^{side}(x,t)\right) \tag{2.36}$$

where the side reaction exchange current $i_0^{side}(t)$ is described by

$$i_0^{side}(t) = \begin{cases} i_{0,base}\left(\frac{|I_{app}(t)|}{I_{1C}}\right)^w & \text{if} \quad I_{app}(t) < 0 \\ 0 & \text{otherwise} \end{cases} \tag{2.37}$$

where $i_{0,base}$ is the base side-reaction current, I_{1C} is the current corresponding to a 1C rate for the considered cell (i.e. the current able to completely discharge the cell in one hour) and w is an empirically obtained coefficient (usually $w = 2$). Note that, according to the presented model, no degradation occurs when the cell is discharged or at rest (i.e. for $I_{app}(t) \geq 0$). The modelling of calendar ageing for lithium-ion batteries is out of the scope of the present Dissertation and the interested reader can refer to (Liu et al., 2020) for further details. The side-reaction overpotential $\eta^{side}_{n,sei}(x,t)$, which is related to the SEI growth, is given by

$$\eta^{side}_{n,sei}(x,t) = \Phi_s(x,t) - \Phi_e(x,t) - U_{sei} - j_n(x,t)F\frac{R_{sei}(t)}{AL_n a_n(t)}, \quad x \in [\hat{x}_{sep,n}, \hat{x}_n] \tag{2.38}$$

where U_{sei} is the reference potential for the SEI side reaction. Note that the ageing model here described is valid under the assumption that no lithium plating deposition occurs, i.e. when the following condition holds (Arora, Doyle, and White, 1999)

$$\eta^{side}_{n,pl}(x,t) = \Phi_s(x,t) - \Phi_e(x,t) - U_{pl} - j_n(x,t)F\frac{R_{sei}(t)}{AL_n a_n(t)} > 0 \tag{2.39}$$

where U_{pl} is the reference potential for the lithium-deposition side reaction. Such constraint is in general satisfied if the voltage does not exceed a certain threshold ($V(t) \leq V_{max}$), although this latter corresponds to a conservative formulation. More details on ageing models can be found in (Arora, White, and Doyle, 1998; Ramadass et al., 2004; Torchio et al., 2016a).

2.4.2.2 SPMeT-Based Reduced-Order Model With Ageing Dynamics

In this section, we propose the main equations of a simplified electrochemical model oriented to control purposes which is obtained by extending the SPMeT with the ageing dynamics and consists of an approximation of the P2D model (see 2.4.2.1) which is suitable to be used within a real-time optimization-based controller. In particular, the model core is taken from the SPMe (Moura et al., 2016), with the exception that a spatial discretization according to the Finite Volume Method (Eymard, Gallouët, and Herbin, 2000) is here adopted for the Partial Differential Equation (PDE) which describes the diffusion of ions within the electrolyte. In addition, the Fick's laws are reduced into Ordinary Differential Equations (ODEs) by exploiting a polynomial approximation for the ions concentration along the radial axis of each electrode (Subramanian, Diwakar, and Tapriyal, 2005). Moreover, the equations described in (Perez et al., 2017) for the lumped thermal dynamics of the SPMeT are here adapted to the presented model. Finally, it is important to notice that ageing effects such as capacity fade and SEI resistance growth (Ramadass et al., 2004) are here considered. Similarly as in 2.4.2.1, two different indexes are considered for the equations used in all the sections ($j \in \{p, sep, n\}$) and the ones valid only in the electrodes ($i \in \{p, n\}$).

Electrochemical Dynamics The ion concentration along the radial axis r of each electrode is described by a fourth-order polynomial function of r, as we adopt the approximation in (Subramanian, Diwakar, and Tapriyal, 2005), where the coefficients are functions of $\bar{c}_{s,p}^{avg}(t) = \frac{1}{L_p}\int_{\hat{x}_p}^{\hat{x}_{p,sep}} c_s^{avg}(x,t)$ and $\bar{c}_{s,n}^{avg}(t) = \frac{1}{L_n}\int_{\hat{x}_{sep,n}}^{\hat{x}_n} c_s^{avg}(x,t)$, which are the mean values of the solid average concentration $c_s^{avg}(x,t)$ in the cathode and anode, respectively, and the mean concentration flux $\bar{q}_i(t)$. The variables considered in the following are all spatial mean values of the ones presented in 2.4.2.1 and therefore, with slightly abuse of notation, we will write $\phi(t)$ for describing the variable $\bar{\phi}(t) = \frac{1}{L_n}\int_{x\in[\hat{x}_a,\hat{x}_b]} \phi(x,t)dx$, where $[\hat{x}_a, \hat{x}_b]$ is the considered spatial domain for the variable $\phi(t)$. The variables $\phi^{avg}(t)$ and $\phi^*(t)$ represent, respectively, the average over the particle radial axis and the surface values.

In the following, the dynamics of the variables needed for reconstructing the ion concentration along the radial axis is recalled. In particular, we define the average stoichiometry in the electrodes as

$$\theta_i^{avg}(t) = \frac{c_{s,i}^{avg}(t)}{c_{s,i}^{max}} \tag{2.40}$$

Moreover, since we assume the preservation of the moles of lithium in the solid phase (Di Domenico, Stefanopoulou, and Fiengo, 2010), the following algebraic equation holds, which allows to express the anodic average stoichiometry in terms of the cathodic one

$$\theta_n^{avg}(t) = \theta_n^d + \frac{\theta_p^{avg}(t) - \theta_p^d}{\theta_p^c - \theta_p^d}(\theta_n^c - \theta_n^d) \tag{2.41}$$

The temporal evolution of the spatial mean of the cathodic average stoichiometry can be approximated by (Subramanian, Diwakar, and Tapriyal, 2005)

$$\frac{d\theta_p^{avg}(t)}{dt} = -\frac{\Delta\theta_p}{3600C(t)} I_{app}(t) \tag{2.42}$$

where the applied current is defined as being negative during charging by convention. The volume-averaged concentration fluxes can be expressed as

$$\frac{dq_p(t)}{dt} = -30\frac{D_{s,p}(T(t))}{R_{p,p}^2} q_p(t) + \frac{45}{2R_{p,p}^2 FAL_p a_p(t)} I_{app}(t) \tag{2.43a}$$

$$\frac{dq_n(t)}{dt} = -30\frac{D_{s,n}(T(t))}{R_{p,n}^2} q_n(t) - \frac{45}{2R_{p,n}^2 FAL_n a_n(t)} I_{app}(t) \tag{2.43b}$$

where $T(t)$ is the lumped cell temperature, which enters the Arrhenius law in the computation of the temperature-dependent solid diffusion coefficient $D_{s,i}(T(t))$ as follows

$$D_{s,i}(T(t)) = D_{s,i}^0 e^{\frac{-E_{a,D_{s,i}}}{RT(t)}} \tag{2.44}$$

The same is done for all the other parameters which depend on the temperature.

The spatial mean values of the surface stoichiometries in the electrodes are given by the following algebraic equations

$$\theta_p^*(t) = \theta_p^{avg}(t) + \frac{8R_{p,p}q_p(t)}{35c_{s,p}^{max}} + \frac{R_{p,p}I_{app}(t)}{35D_{s,p}(T(t))FAL_p a_p(t) c_{s,p}^{max}} \tag{2.45a}$$

$$\theta_n^*(t) = \theta_n^{avg}(t) + \frac{8R_{p,n}q_n(t)}{35c_{s,n}^{max}} - \frac{R_{p,n}I_{app}(t)}{35D_{s,n}(T(t))FAL_n a_n(t) c_{s,n}^{max}} \tag{2.45b}$$

while the normalized state of charge $SOC(t)$ is expressed by

$$SOC(t) = \frac{\theta_n^{avg}(t) - \theta_n^d}{\theta_n^c - \theta_n^d} \tag{2.46}$$

Remark 1 *The polynomial approximation used to describe the lithium solid concentration along the particle radial coordinate can be replaced by a more accurate one, if needed. For instance, a spatial discretization using Chebyshev orthogonal collocation can be employed*

(Bizeray et al., 2015).

In the P2D model and in the SPMe presented in (Moura et al., 2016) the diffusion mechanism of the ion concentration within the electrolyte $c_e(x,t)$ is described through PDEs (see (2.9) and (2.10)). In this section we propose a discretization of such PDEs according to the FV method, as previously done in this context by the authors in (Torchio et al., 2016b). In particular, the spatial domain is divided into P non-overlapping volumes for each section, and the k-th volume, with $k = 1, \cdots, P$, of the j-th section is centered at the spatial coordinate $x_{j,k}$ and spans the interval $\Omega_{j,k} = \left[x_{j,\bar{k}}, x_{j,\underline{k}} \right]$, whose width is $\Delta x_j = L_j / P$. If one defines the average electrolyte concentration over the k-th volume of j-th section as $c_{e,j}^{[k]}(t)$, it holds that

$$\epsilon_p \frac{dc_{e,p}^{[k]}(t)}{dt} = \left[\frac{\tilde{D}_e}{\Delta x_p} \frac{\partial c_{e,p}(x,t)}{\partial x} \right] \Bigg|_{x_{p,\underline{k}}}^{x_{p,\bar{k}}} - \frac{1-t_+}{FAL_p} I_{app}(t) \tag{2.47a}$$

$$\epsilon_{sep} \frac{dc_{e,sep}^{[k]}(t)}{dt} = \left[\frac{\tilde{D}_e}{\Delta x_{sep}} \frac{\partial c_{e,sep}(x,t)}{\partial x} \right] \Bigg|_{x_{sep,\underline{k}}}^{x_{sep,\bar{k}}} \tag{2.47b}$$

$$\epsilon_n \frac{dc_{e,n}^{[k]}(t)}{dt} = \left[\frac{\tilde{D}_e}{\Delta x_n} \frac{\partial c_{e,n}(x,t)}{\partial x} \right] \Bigg|_{x_{n,\underline{k}}}^{x_{n,\bar{k}}} + \frac{1-t_+}{FAL_n} I_{app}(t) \tag{2.47c}$$

where the terms are evaluated as explained in details in (Torchio et al., 2016b). In particular, defining the harmonic mean operator $\mathcal{H}$ as

$$\mathcal{H}\left(\rho_1, \rho_2, \lambda_1, \lambda_2\right) = \frac{\rho_1 \rho_2 (\lambda_1 + \lambda_2)}{\rho_1 \lambda_2 + \rho_2 \lambda_1} \tag{2.48}$$

then the electrolyte diffusion coefficients $\tilde{D}_e$ are computed from

$$\tilde{D}_e = \begin{cases} D_{e,1} & \text{if} \quad x \in \{x_{p,\underline{P}}, x_{sep,\bar{1}}\} \\ D_{e,2} & \text{if} \quad x \in \{x_{sep,\underline{P}}, x_{n,\bar{1}}\} \\ D_{e,j}^{eff} & \text{otherwise} \end{cases} \tag{2.49}$$

with

$$D_{e,1} = \mathcal{H}\left(D_{e,p}^{eff}, D_{e,sep}^{eff}, \Delta x_p, \Delta x_{sep}\right) \tag{2.50a}$$

$$D_{e,2} = \mathcal{H}\left(D_{e,sep}^{eff}, D_{e,n}^{eff}, \Delta x_{sep}, \Delta x_n\right) \tag{2.50b}$$

The terminal voltage is then given by

$$V(t) = U_p(\theta_p^*(t)) - U_n(\theta_n^*(t)) + \eta_p(t) - \eta_n(t) + \Delta\Phi_e(t) - I_{app}(t)R_{sei}(t) \tag{2.51}$$

where $\eta_p(t)$ and $\eta_n(t)$ are the mean overpotentials for the positive and negative electrodes given by

$$\eta_p(t) = \frac{2RT(t)}{F}\sinh^{-1}\left(\frac{-I_{app}(t)}{2AL_p a_p(t) i_{0,p}(t)}\right) \tag{2.52a}$$

$$\eta_n(t) = \frac{2RT(t)}{F}\sinh^{-1}\left(\frac{I_{app}(t)}{2AL_n a_n(t) i_{0,n}(t)}\right) \tag{2.52b}$$

with the following expression for the exchange current density

$$i_{0,i}(t) = Fk_i(T(t))c_{s,i}^{max}\sqrt{c_{e,i}(t)\theta_i(t)(1-\theta_i(t))} \tag{2.53}$$

where $c_{e,i}(t)$ is the mean electrolyte concentration in the i-th section, approximated by

$$c_{e,i}(t) = \frac{1}{P}\sum_{k=1}^{P} c_{e,i}^{[k]}(t). \tag{2.54}$$

Moreover, $\Delta\Phi_e(t)$ is computed as

$$\Delta\Phi_e(t) = \Phi_e^{drop}(t) + \frac{2R}{F}(1-t_+)T(t)\ln\left(\frac{c_{e,p}^{[1]}(t)}{c_{e,n}^{[P]}(t)}\right) \tag{2.55}$$

where, relying on the assumption of a trapezoidal shape for the ionic current $i_e(x,t)$ over the spatial domain (Moura et al., 2016), the electrolyte voltage drop $\Phi_e^{drop}(t)$ can be approximated by

$$\Phi_e^{drop}(t) \simeq -\frac{I_{app}(t)}{2A}\left(\phi_p(t) + 2\phi_{sep}(t) + \phi_n(t)\right) \tag{2.56}$$

in which

$$\phi_p(t) = \Delta x_p \sum_{k=1}^{P} \frac{2k-1}{\epsilon_p^{p_p} \kappa(c_{e,p}^{[k]}(t), T(t))} \tag{2.57a}$$

$$\phi_{sep}(t) = \Delta x_{sep} \sum_{k=1}^{P} \frac{1}{\epsilon_{sep}^{p_{sep}} \kappa(c_{e,sep}^{[k]}(t), T(t))} \tag{2.57b}$$

$$\phi_n(t) = \Delta x_n \sum_{k=1}^{P} \frac{2P-2k+1}{\epsilon_n^{p_n} \kappa(c_{e,n}^{[k]}(t), T(t))} \tag{2.57c}$$

where $\kappa(c_{e,j}^{[k]}(t), T(t))$ is the temperature-dependent electrolyte conductivity for the k-th volume of the j-th section. This latter is usually expressed through a nonlinear function of the electrolyte concentration in that volume which depends on the considered cell.

Thermal Dynamics Similarly to 2.4.1.1, the cell temperature is here considered as a lumped variable whose dynamics is given by

$$C_{th} \frac{dT(t)}{dt} = Q_g(t) - \frac{T(t) - T_{env}}{R_{th}} \tag{2.58}$$

where C_{th} is the thermal capacity of the cell and R_{th} the thermal resistance with respect to the external environment (e.g. the coolant), whose temperature is here assumed to be constant and equal to T_{env}. The heat generation term $Q_g(t)$ is due to the cell polarization and is described by

$$Q_g(t) = |I_{app}(t)| \cdot |V(t) - (U_p(\theta_p^*(t)) - U_n(\theta_n^*(t)))|. \tag{2.59}$$

Ageing Dynamics Finally, the model of the main degradation mechanisms is recalled. In particular, the capacity loss and the SEI resistance growth are expressed by the following equations (Ramadass et al., 2004)

$$\frac{dC(t)}{dt} = 3 \frac{3600C(t)}{R_{p,n} A \Delta\theta_n c_{s,n}^{max}} j_n^{side}(t) \tag{2.60a}$$

$$\frac{dR_{sei}(t)}{dt} = -\frac{M_w}{\rho_n \nu} j_n^{side}(t) \tag{2.60b}$$

where the mean side reaction flux is

$$j_n^{side}(t) = -\frac{i_0^{side}(t)}{F} exp\left(\frac{0.5F}{RT(t)}\eta_{n,sei}^{side}(t)\right) \tag{2.61}$$

Also in this case, we assume that no degradation occurs when the cell is discharged (see (2.37)). The mean side reaction overpotential $\eta_{n,sei}^{side}(t)$ is given by

$$\eta_{n,sei}^{side}(t) = \eta_n(t) + U_n(\theta_n^*(t)) - U_{sei} \tag{2.62}$$

under the assumption that no Lithium-ion deposition happens, i.e. (Arora, Doyle, and White, 1999)

$$\eta_{n,pl}^{side}(t) = \eta_n(t) + U_n(\theta_n^*(t)) - U_{pl} > 0 \tag{2.63}$$

2.4.3 Cell Models Employed in the Presented Thesis

In the rest of the Thesis, the mathematical models presented above are exploited for both control and simulative purposes, with slight adaptations in their formulation according to the specific task (e.g. neglecting electrolyte, ageing or temperature dynamics). In particular, in Chapter 3 the parameters of different versions of the reduced electrochemical model recalled in 2.4.2.2 are identified. Moreover, the possibility of collecting measurements from a simulator based on the P2D model, considered as the real cell, is assessed. In Chapter 4 the optimal control of a single lithium-ion cell is firstly addressed by exploiting the use of ECM and P2D as model for the control. Then, the control-oriented electrochemical model presented in 2.4.2.2 is employed for describing the different cells behaviour both in the context of SOC balancing of series-connected cells and optimal charging of a whole battery pack, with both series and parallel connections. Finally, in Chapter 5 the optimal charging based on reinforcement learning of a cell modelled through the SPMeT (Perez et al., 2017) is proposed.

2.5 Conclusions

In this chapter the main features of a lithium-ion battery have been discussed, with focus on both the electrochemical and the management aspects. Firstly we present a brief overview on the historical development of batteries and lithium-ion technology. Then, a description of the main tasks of the battery management system have been provided, by highlighting the issues on which the research community needs to devote attention in order to improve the performance of such electrochemical accumulators. Finally, the equations of the best known mathematical models for a lithium-ion cell have been provided.

Chapter 3

Optimal Experimental Design for Lithium-Ion Batteries

In the context of model-based state estimation and control, the model accuracy is fundamental in order to achieve high performance. Therefore, a lot of effort is devoted by the researcher in selecting a proper model structure and its parametrization. In particular, the value of the nominal parameters indicated in the data sheets may not be sufficiently accurate, thus requiring further estimation procedures based on the data collected from the actual controlled process. This is particularly true for the case of lithium-ion cells, where the use of invasive experiments, as in (Ecker et al., 2015a; Ecker et al., 2015b), allows to identify the physical parameters of a cell but at the price of making the cell unusable afterwards. For this reason, it is preferable to rely on non-invasive approaches that preserve the integrity of the cells. However, the use of standard identification current profiles (e.g. constant current, multistep discharging current) may not be sufficiently informative for this purpose. This has been shown in the context of lithium-ion batteries in e.g. (Lopez et al., 2016), where the authors investigate the structural identifiability of the P2D when constant discharging currents are applied. Within this context, the exploitation of the optimal design of experiments may be a possible solution in order to both improve the accuracy of the identification process and reduce the time required for the execution of the experiments.

In the following, we consider two different Optimal Experimental Design (OED) approaches that are suitable to improve the accuracy in the parameters estimation of reduced-order electrochemical models. In particular, the methodology presented in

Section 3.1 relies on the Fisher Information Matrix (FIM) which, exploiting local sensitivity analysis, allows to compute an approximation of the parameter covariance matrix. The trace of the latter is then minimized in order to optimally compute the experimental input profile. Although the results show the effectiveness of the proposed technique when compared to standard strategies, a not negligible drawback still exists: the approximation of the parameter covariance computed through the Fisher matrix exhibits a local nature with respect to the parameter guess in which the FIM is evaluated. Therefore, as a possible solution, in Section 3.2 we propose an optimal design of experiments approach based on Global Sensitivity Analysis (GSA), and a comparison with a Fisher-based technique is presented. Specifically, the use of GSA allows to approximate the covariance matrix of the parameters independently from their a-priori guessed values, thus enhancing the accuracy of the whole experimental design process. Finally, Section 3.3 concludes the chapter.

3.1 Fisher-Based Design of Experiments for the SPMe

In this section, an optimal design of experiments for lithium-ion batteries is proposed based on the Fisher information matrix. In particular, we pose a nonlinear minimization problem in which the trace of the approximated covariance matrix of the parameters, obtained through local sensitivity analysis, is considered as the cost function (Körkel and Kostina, 2005). A similar approach has been applied in this context by the authors in (Park et al., 2018), which select the optimal experiment among the ones available in an a-priori library. The present work differs from the latter by the fact that we fully design the input for each time instant. Moreover, in order to alleviate the computational complexity, we divide the design of the experiment into sub-problems, each involving only a fraction of the overall set of optimization variables.

The performance of the proposed scheme is firstly evaluated by considering the single-particle model with electrolyte dynamics as the real plant, with the output affected by a zero-mean Gaussian noise and the estimation accuracy evaluated in terms of mean and variance of the parameters (Pozzi et al., 2018a). Simulations highlight the effectiveness of the proposed approach when compared to standard profiles. In particular, the results show that the proposed approach can provide a significant improvement in terms of variance reduction and convergence to the true values of the parameters in minimum experimental time. Subsequently, a more realistic scenario is considered, where the isothermal P2D model is used to reproduce a real battery behaviour, while the SPMe is used as model for control (Pozzi et al., 2018b). In this case, the SPMe parameters need to be estimated based on data collected directly from the P2D model. Note that the use of a very detailed model, such as the P2D, together with a numerically stable simulation framework (LIONSIMBA) and a set of realistic parameters, provides important insights on the real battery behaviour and allows to estimate whether an approach (e.g. OED) will be worth in practice or not, saving a lot of time during the experimental phase. The results highlight that the SPMe, simulated using the parameters obtained from the OED, presents the best fitting in terms of prediction of the P2D output voltage when compared with benchmark approaches.

3.1.1 Fisher-Based OED Methodology

Consider a nonlinear model whose dynamics is represented by ordinary differential equations as follows

$$\dot{x}(t) = f(x(t), u(t), \phi) \tag{3.1a}$$

$$y(t) = g(x(t), u(t), \phi) \tag{3.1b}$$

$$x(t_0) = x_0, \tag{3.1c}$$

where $x(t) \in \mathbb{R}^{N_x}$ is the differential state vector, $u(t) \in \mathbb{R}^{N_u}$ is the control input, $y(t) \in \mathbb{R}^{N_y}$ is the model output and $\phi \in \mathbb{R}^{N_\phi}$ is the parameter vector to be estimated. Furthermore, $f : \mathbb{R}^{N_x} \times \mathbb{R}^{N_u} \times \mathbb{R}^{N_\phi} \rightarrow \mathbb{R}^{N_x}$ and $g : \mathbb{R}^{N_x} \times \mathbb{R}^{N_u} \times \mathbb{R}^{N_\phi} \rightarrow \mathbb{R}^{N_y}$ are the state and output functions respectively, while $t_0 \in \mathbb{R}^+$ and $x_0 \in \mathbb{R}^{N_x}$ are the initial time and the initial state vector. We consider ϕ^* as the true value of the parameter vector and ϕ_0 as the initial guess of the parameter estimation procedure. Without loss of generality, in the following we consider a single-input single-output model, i.e. $N_u = N_y = 1$. Also, we assume that both inputs and outputs are applied/measured at discrete instants with sample time t_s. Let $\mathbf{u}_\xi \in \mathbb{R}^N$ denote the input sequence for a given experiment ξ over a time interval $[t_0^\xi, t_N^\xi]$ and $\mathbf{y}_\xi(\phi) \in \mathbb{R}^N$ be the corresponding output sequence obtained by simulating the model equations in (3.1) with the parameter vector ϕ as follows

$$\mathbf{u}_\xi = \left[u(t_0^\xi)^\top, u(t_0^\xi + t_s)^\top, \cdots, u(t_N^\xi)^\top \right]^\top \tag{3.2a}$$

$$\mathbf{y}_\xi(\phi) = \left[y(t_0^\xi)^\top, y(t_0^\xi + t_s)^\top, \cdots, y(t_N^\xi)^\top \right]^\top \tag{3.2b}$$

where $N = \frac{t_N^\xi - t_0^\xi}{t_s}$ is the number of control inputs and acquired outputs. Note that the sequence $\mathbf{u}_\xi$ corresponds to a piecewise constant input. In the following, the measured output $\overline{y}(t)$ is assumed to be affected by a zero-mean Gaussian disturbance as follows

$$\overline{y}(t) = g(x(t), u(t), \phi^\star) + v(t), \tag{3.3}$$

where $v(t) \sim \mathcal{N}(0, \sigma_y^2)$. The vector of the noisy observed data $\overline{\mathbf{y}}_\xi \in \mathbb{R}^N$ is therefore defined as

$$\overline{\mathbf{y}}_\xi = \left[\overline{y}(t_0^\xi)^\top, \overline{y}(t_0^\xi + t_s)^\top, \cdots, \overline{y}(t_N^\xi)^\top \right]^\top \tag{3.4}$$

and it holds that $\overline{\mathbf{y}}_\xi \sim \mathcal{N}(\mathbf{y}_\xi(\phi^\star), C_y)$, where $C_y \in \mathbb{R}^{N \times N}$ is the measurement covariance matrix. In particular, C_y is a diagonal matrix with entries given by the measurement error variances σ_y^2, i.e.

$$C_y = \sigma_y^2 \mathbb{I}_N, \tag{3.5}$$

where $\mathbb{I}_N$ is the identity matrix of order N.

3.1.1.1 Sensitivity and Fisher Information Matrices

The local sensitivity matrix $S^\xi(\phi) \in \mathbb{R}^{N \times N_\phi}$ for an experiment ξ is given by the Jacobian matrix of the output vector $\mathbf{y}_\xi(\phi)$ with respect to the parameters that we aim to estimate, i.e.

$$S^\xi(\phi) = \nabla_\phi \, \mathbf{y}_\xi(\phi), \tag{3.6}$$

Note that the sensitivity matrix is not related to the noisy measurement data, but depends only on the model equations in (3.1), on the experiment ξ and on the parameter vector ϕ in which it is evaluated. Moreover, it is important to underline that the sensitivity matrix in (3.6) can be computed directly in simulation and exhibits a local nature with respect to the parameter vector ϕ.

The local sensitivity matrix is exploited in the computation of the so-called Fisher information matrix (Akaike, 1998), denoted by $F^{\xi}(\phi) \in \mathbb{R}^{N_\phi \times N_\phi}$, as follows

$$F^{\xi}(\phi) = S^{\xi}(\phi)^{\top} C_y^{-1} S^{\xi}(\phi), \tag{3.7}$$

that is a symmetric matrix that gives a measure of the amount of information that is carried by an experiment ξ. As for the sensitivity matrix, also the FIM is strictly dependent on the value of the parameter vector ϕ in which it is evaluated.

3.1.1.2 Covariance Matrix of the Parameters

Once the experiment ξ has been performed and the measurements sequence $\overline{\mathbf{y}}_{\xi}$ has been collected, the parameters are estimated by solving the following maximum-likelihood problem

$$\hat{\phi} = \underset{\phi \in [\phi^{lb}, \phi^{ub}]}{\arg\min} \, (\overline{\mathbf{y}}_{\xi} - \mathbf{y}_{\xi}(\phi))^{\top} (\overline{\mathbf{y}}_{\xi} - \mathbf{y}_{\xi}(\phi)), \tag{3.8}$$

where ϕ^{lb} and ϕ^{ub} are suitable lower and upper bound that restrict the feasible region of the optimization problem to a set that is physically meaningful. Due to the fact that $\overline{\mathbf{y}}_{\xi}$ is a random variable the estimated parameter vector $\hat{\phi}$ is also a random variable with covariance matrix $C_{\phi}^{\xi} \in \mathbb{R}^{N_\phi \times N_\phi}$. In the following we aim to minimize the variance of the parameters by suitably designing the experimental input sequence ξ. In particular, we rely on the fact that the generalized inverse of the FIM gives a lower bound for the parameter covariance matrix according to the Cramer-Rao bound (Scharf and McWhorter, 1993)

$$F^{\xi}(\phi)^{-1} \leq C_{\phi}^{\xi}. \tag{3.9}$$

3.1.1.3 Optimization Problem

In the following, we present an iterative design of experiments methodology which selects the input by optimizing a functional of the FIM inverse, thus enhancing a reduction in the covariance of the estimated parameters. Specifically, a sequence of experiments ξ_i, $i = 1, \dots, N_{exp}$ is designed in order to identify the parameter vector with high accuracy and maximal statistical reliability (Körkel and Kostina, 2005). At each iteration, the optimal input $\mathbf{u}^{\star}_{\xi_i}$ to be applied during the experiment ξ_i is obtained by solving the following constrained optimization problem

$$\mathbf{u}^{\star}_{\xi_i} = \arg\min_{\mathbf{u}_{\xi_i}} \mathrm{Tr}\left(F^{\xi_i}(\hat{\phi}_{i-1})^{-1}\right), \tag{3.10}$$

subject to

$$\begin{aligned}
&\text{model dynamics in (3.1)} && && (3.11a)\\
&x(t_0^{\xi_i}) = x_0^{\xi_i} && && (3.11b)\\
&u^{lb} \leq u(t) \leq u^{ub}, && t = t_0^{\xi_i}, t_0^{\xi_i} + t_s, \cdots, t_N^{\xi_i} && (3.11c)\\
&h(x(t), u(t), \hat{\phi}_{i-1}) \leq 0, && t = t_0^{\xi_i}, t_0^{\xi_i} + t_s, \cdots, t_N^{\xi_i} && (3.11d)
\end{aligned}$$

where $\hat{\phi}_{i-1}$ is the parameter vector estimated at the previous iteration, u^{lb} and u^{ub} are suitable bounds for the input and $x_0^{\xi_i}$ is the initial state for the experiment ξ_i. Nonlinear safety constraints are taken into account through (3.11d). Note that, since it is not possible to minimize directly the variance of the parameters, several optimization criteria can be used. Due to the the easiness of its implementation, in the formulation of problem (3.10) we rely on the A-criterion (Körkel et al., 2004), i.e. on the minimization of the trace of the inverse of the Fisher matrix.

The resulting optimal input $\mathbf{u}^{\star}_{\xi_i}$ is applied and the corresponding output measurements are collected. Subsequently, the estimated parameter vector is updated with $\hat{\phi}_i$, obtained as the solution of the maximum-likelihood estimation process in (3.8), using the output measurements collected during all the experiments $\xi_1, \dots, \xi_i$ performed so far. A schematic representation of the method is resumed in Figure 3.1.

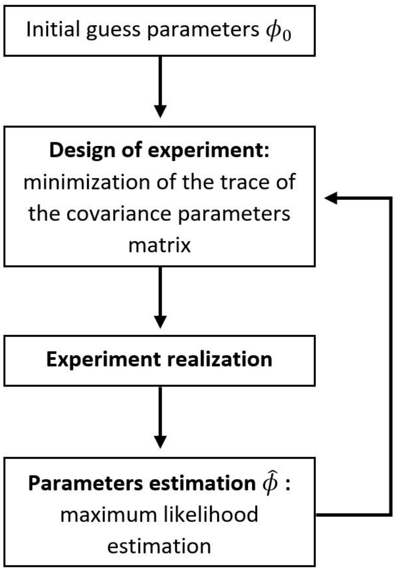

FIGURE 3.1: Schematic representation of the Fisher-based optimal experimental design and parameter estimation process.

3.1.1.4 Sub-Optimal Approach for Computational Cost Reduction

Since the objective of each experiment is to lead to a covariance parameter matrix low enough to guarantee a meaningful estimation, the input signal may need to be designed over a long experimental time. This, together with the nonlinearities of the model and the length of the parameter vector, could increase dramatically the computational burden of problem (3.10). For this reason, we divide the design of the i-th experiment ξ_i into M sub-problems, each involving only a fraction of the overall set of optimization variables, as shown in Figure 3.2. Each step aims

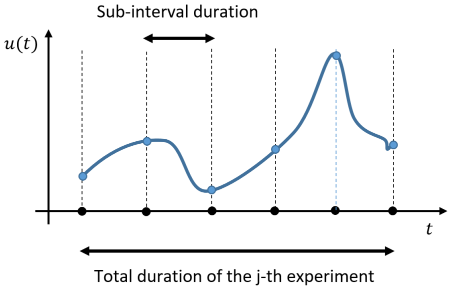

FIGURE 3.2: Schematic representation of the sub-optimal experimental design.

to design the input vector $\mathbf{u}_{\xi_{i,j}} \in \mathbb{R}^{\tilde{N}}$, $j = 1, \dots M$, over the time interval $[t_0^{\xi_{i,j}}, t_{\tilde{N}}^{\xi_{i,j}}]$, where $\tilde{N} = \frac{t_{\tilde{N}}^{\xi_{i,j}} - t_0^{\xi_{i,j}}}{t_s}$, i.e. $\tilde{N} = \frac{N}{M}$. Note that $t_0^{\xi_i} = t_0^{\xi_{i,1}}$ and that $t_N^{\xi_i} = t_{\tilde{N}}^{\xi_{i,M}}$. At the j-th step, the input $\mathbf{u}_{\xi_{i,j}}$ is designed by minimizing the trace of $F^{[\xi_{i,1} \dots \xi_{i,j}]}(\hat{\phi}_{i-1})^{-1}$, that is the generalized inverse of the Fisher matrix over the $1, \dots, j$ partial experiments performed so far in simulation. This latter can be computed as

$$F^{[\xi_{i,1} \cdots \xi_{i,j}]}(\hat{\phi}_{i-1}) = F^{[\xi_{i,1} \cdots \xi_{i,j-1}]}(\hat{\phi}_{i-1}) + F^{\xi_{i,j}}(\hat{\phi}_{i-1}) \tag{3.12}$$

where only the term $F^{\xi_{i,j}}(\hat{\phi}_{i-1})$ depends on the input profile $\mathbf{u}_{\xi_{i,j}}$. Note that (3.12) is obtained by considering that the sensitivity $S^{[\xi_{i,1} \cdots \xi_{i,j}]}(\hat{\phi}_{i-1})$ over the experiments $1, \dots, j$ can be expressed as follows

$$S^{[\xi_{i,1} \cdots \xi_{i,j}]}(\hat{\phi}_{i-1}) = \begin{bmatrix} S^{[\xi_{i,1} \cdots \xi_{i,j-1}]}(\hat{\phi}_{i-1}) \\ S^{\xi_{i,j}}(\hat{\phi}_{i-1}) \end{bmatrix} \tag{3.13}$$

where $S^{[\xi_{i,1} \cdots \xi_{i,j-1}]}(\hat{\phi}_{i-1})$ is the sensitivity over the $1, \dots, j-1$ partial experiments while $S^{\xi_{i,j}}(\hat{\phi}_{i-1})$ refers only to the partial experiment $\xi_{i,j}$. In particular, at each step the following constrained optimization problem is solved

$$\mathbf{u}^{\star}_{\xi_{i,j}} = \arg\min_{\mathbf{u}_{\xi_{i,j}}} \mathrm{Tr}\left(F^{[\xi_{i,1} \cdots \xi_{i,j}]}(\hat{\phi}_{i-1})^{-1}\right) \tag{3.14}$$

subject to

$$\text{model dynamics in (3.1)} \tag{3.15a}$$

$$x(t_0^{\xi_{i,j}}) = x_0^{\xi_{i,j}} \tag{3.15b}$$

$$u^{lb} \leq u(t) \leq u^{ub}, \qquad t = t_0^{\xi_{i,j}}, t_0^{\xi_{i,j}} + t_s, \cdots, t_{\tilde{N}}^{\xi_{i,j}} \tag{3.15c}$$

$$h(x(t), u(t), \hat{\phi}_{i-1}) \leq 0, \quad t = t_0^{\xi_{i,j}}, t_0^{\xi_{i,j}} + t_s, \cdots, t_{\tilde{N}}^{\xi_{i,j}} \tag{3.15d}$$

The different sub-problems are solved in sequence, $j = 1, \cdots, M$ and for each $j = 2, \cdots, M$, the initial condition is obtained by simulating the effect of the input designed so far on the model starting with initial condition x_0. Once all the M

steps have been performed, one obtains a sub-optimal input sequence $\tilde{\mathbf{u}}_{\xi_i}$, given by

$$\tilde{\mathbf{u}}_{\xi_i} = \left[{\mathbf{u}^{\star}_{\xi_{i,1}}}^{\top}, {\mathbf{u}^{\star}_{\xi_{i,2}}}^{\top}, \cdots, {\mathbf{u}^{\star}_{\xi_{i,M}}}^{\top} \right]^{\top} \tag{3.16}$$

Only at this point the sequence $\tilde{\mathbf{u}}_{\xi_i}$ is applied to the system and the result of the experiment ξ_i is then obtained. Finally, we solve (3.8) in order to estimate $\hat{\phi}_i$, which will be used as initial guess in the next experiment ξ_{i+1}. The sub-optimality comes from the division of the OED into M sub-problems, which was required for reducing the complexity of the optimization problem. Thanks to this scheme, it is possible to consider long experiments, useful for achieving low covariance of the parameters, without dramatically increasing the computational burden. The optimal input design process ends when one of the following conditions is satisfied:

- a variance threshold is achieved;
- a maximum numbers of experiments has been executed;
- no more significant covariance decrease is obtained.

This allows us to estimate the parameter vector $\hat{\phi}_i$ with high accuracy, while maintaining the computational burden at a reasonable level. In Algorithm 1 the main features of the sub-optimal approach are resumed. Each experiment ξ_i, $i = 1, \dots, N_{exp}$ is designed by iteratively applying the Algorithm 1.

3.1.2 Cell Modelling, Parameters and Optimization Solver

The battery models used in the following can be seen as slight variations of those described in 2.4.2. In particular, the SPMe is obtained from the model presented in 2.4.2.2 by neglecting the temperature and ageing dynamics, i.e. by considering $T(t) = T_{env}$, $C(t) = C^n$ and $R_{sei}(t) = R^n_{sei}$ constant over the time, with C^n and R^n_{sei} the nominal value for capacity and SEI resistance which can be retrieved from the battery data sheets. A similar argument can be made for the isothermal P2D whose equations are obtained from the ones in 2.4.2.1 with the assumption of constant temperature (over time and spacial domain) as well as constant capacity and SEI resistance.

Algorithm 1 Sub-optimal design of experiment ξ_i.

```
Initialize the time: $t_0^{\xi_{i,1}} \leftarrow t_0^{\xi_i}$
Initialize the state: $x_0^{\xi_{i,1}} \leftarrow x_0^{\xi_i}$
for $j = 1$ to $M$ do
    Compute the input $\mathbf{u}^\star_{\xi_{i,j}}$ by solving the optimization problem (3.14) with constraints in (3.15)
    Update the time: $t_0^{\xi_{i,j+1}} \leftarrow t_{\tilde{N}}^{\xi_{i,j}}$
    Apply the input sequence computed so far to the model in simulation and update the initial condition:
    $x_0^{\xi_{i,j+1}} \leftarrow x\left(t_{\tilde{N}}^{\xi_{i,j}}\right)$
end for
Concatenate the sub-problems solutions in order to obtain the input sequence $\tilde{\mathbf{u}}_{\xi_i}$ of the experiment $\xi_i$ as in (3.16)
Update the estimated parameter vector:
$\hat{\phi}_i = \arg\min_{\phi_i \in [\phi^{lb}, \phi^{ub}]} \left[ (\bar{\mathbf{y}}_{\xi_i} - \mathbf{y}_{\xi_i}(\phi_i))^\top (\bar{\mathbf{y}}_{\xi_i} - \mathbf{y}_{\xi_i}(\phi_i)) \right]$
Proceed with the next experiment $\xi_{i+1}$
```

We consider a cell based on the LMO chemistry with expressions for electrolyte conductivity and open-circuit potentials in the P2D model as follows

$$\begin{aligned} \kappa(c_e(x,t), T(x,t)) =& h_1 + h_2\gamma(x,t) + h_3\gamma(x,t)^2 + h_4\gamma(x,t)^3 + h_5\gamma(x,t)^4 \\ U_p(\theta_p^*(x,t)) =& f_1 + f_2 \tanh\left(f_3\theta_p^*(x,t) + f_4\right) + \frac{f_5}{(f_6 - \theta_p^*(x,t))^{f_7}} + f_5 f_8 + \\ & + f_9 e^{f_{10}\theta_p^*(x,t)^{f_{11}}} + f_{12} e^{f_{13}(\theta_p^*(x,t) + f_{14})} \end{aligned} \tag{3.17}$$

$$U_n(\theta_n^*(x,t)) = g_1 + g_2 e^{g_3\theta_n^*(x,t)} + g_4 e^{g_5\theta_n^*(x,t)} \tag{3.18}$$

with $\gamma(x,t) = 10^{-3}c_e(x,t)$ and $\tanh(\cdot)$ the hyperbolic tangent. Note that since we consider an isothermal setting all the temperature-dependent parameters according to the Arrhenius law can be considered as constants (i.e. $D_{s,i}(T(x,t)) = D_{s,i}$, $D_e(T(x,t)) = D_e$, $k_i(T(x,t)) = k_i$, $\kappa(c_e(x,t), T(x,t)) = \kappa(c_e(x,t))$). The constants, the model parameters and the coefficients of $U_p(\theta_p^*(x,t))$, $U_n(\theta_n^*(x,t))$ and $\kappa(c_e(x,t))$ are taken from (Lopez et al., 2016), except for the cathodic and electrolytic diffusion coefficients ($D_{s,p}$ and D_e) which are taken from (Ecker et al., 2015a; Ecker et al., 2015b), thus to better approximating the real lithium-ion cell behaviour.

Moreover, we consider the applied current $I_{app}(t)$ as the model input $u(t)$, the terminal voltage $V(t)$ as the model output $y(t)$ and the differential state vector $x(t)$

for the SPMe given by

$$x(t) = [\theta_p^{avg}(t), q_p(t), q_n(t), x_{c_e}(t)]^\top, \tag{3.19}$$

where

$$x_{c_e}(t) = \left[c_{e,p}^{[1]}(t), \cdots, c_{e,p}^{[P]}(t), c_{e,s}^{[1]}(t), \cdots, c_{e,s}^{[P]}(t), c_{e,n}^{[1]}(t), \cdots, c_{e,n}^{[P]}(t)\right]^\top \tag{3.20}$$

with $N_x = 3 + 3P$. Also, voltage and state-of-charge constraints are taken into account using the nonlinear constraint in (3.11d), that seeks to enhance safety during the experiments realization. In fact, (3.11d) can not guarantee a robust satisfaction of the constraints due to the fact that is only based on an estimate of the parameter vector.

Note that, in order to guarantee that each experiment ξ_i has the same initial state, i.e. $x_0^{\xi_i} = x_0$, a charging procedure, followed by a resting period which brings the system to a steady state, is applied to the cell before each new experiment.

3.1.2.1 Parameters to Be Identified

In this section we focus on the design of experiments to be conducted on a lithium-ion cell in order to estimate the same parameter vector as in (Lopez et al., 2016), where constant discharging currents are used to collect measurements, and in particular one has that

$$\phi = [p, t_+, D_e, D_{s,p}, k_p, k_n]^\top \tag{3.21}$$

with D_e, $D_{s,p}$, k_p, k_n assumed to be constant due to the fact that the thermal dynamics is neglected. It is important to notice that only a subset of the previous parameter vector results to be identifiable through the experiments conducted in (Lopez et al., 2016). In that work in fact, the cathodic diffusion coefficient ($D_{s,p}$) and the kinetic rate reactions (k_p, k_n) remain unidentifiable after multiple experiments.

The true value and the initial guess of the parameters are shown in Table 3.1, where the initial parameter values have been taken according to a range of parameters variability similar to the one adopted (Lopez et al., 2016). Note that in a realistic scenario the initial guess ϕ_0 should correspond to the value of the parameter vector given by the cell data sheets.

Parameter	Unit	Description	Initial guess ϕ_0	True value ϕ^*
p	-	Bruggeman coefficient	1.6613	1.5
t_+	-	Cationic transference number	0.4975	0.363
D_e	$\mathrm{m^2s^{-1}}$	Diffusion coefficient in the electrolyte	$1.3376 \cdot 10^{-10}$	$2.44 \cdot 10^{-10}$
$D_{s,p}$	$\mathrm{m^2s^{-1}}$	Diffusion coefficient in the cathode	$7.98 \cdot 10^{-13}$	$7.5 \cdot 10^{-13}$
$D_{s,n}$	$\mathrm{m^2s^{-1}}$	Diffusion coefficient in the anode	$1.17 \cdot 10^{-13}$	10^{-13}
k_p	$\mathrm{m^{2.5}mol^{-0.5}s^{-1}}$	Kinetic reaction rate constant in the cathode	$1.8266 \cdot 10^{-11}$	$2 \cdot 10^{-11}$
k_n	$\mathrm{m^{2.5}mol^{-0.5}s^{-1}}$	Kinetic reaction rate constant in the anode	$1.4769 \cdot 10^{-11}$	$2 \cdot 10^{-11}$

TABLE 3.1: Initial guess and true value of the parameters to be estimated.

3.1.2.2 Optimization Solver

The maximum-likelihood problem in (3.8) as well as the nonlinear optimization problem in (3.10) are here solved using the interior-point method (Nocedal and Wright, 2006) and *CasADi* (Andersson et al., 2019), an open-source tool which provides a symbolic framework for nonlinear numerical optimization algorithms.

3.1.3 Results on the SPMe

In this section, the OED approach described in 3.1.1 is applied to the SPMe, assuming this latter to be the real plant. The obtained results are then compared with the ones achieved using benchmark identification methods (CC and multistep discharging profiles). A zero-mean Gaussian measurement noise with standard deviation of $0.3mV$ is considered. Such noise is chosen to be consistent with the precision of the mostly used experimental instruments. In the following, the output is sampled with $t_s = 5s$. All the proposed approaches have the same initial condition x_0 , which is characterised by a positive stoichometry of 0.17 and the equilibrium values for the average concentration fluxes and for the electrolyte concentrations of zero and $2000\frac{mol}{m^3}$, respectively. The simulation settings for the proposed OED are given in 3.1.3.1, while the ones for the standard CC discharge and the multistep approach are given in 3.1.3.2 and 3.1.3.3, respectivley. The results of the different identification procedures are compared in 3.1.3.4 and, finally, in 3.1.3.5 the identified models are validated in terms of Root-Mean-Square (RMS) error on the predicted voltage.

3.1.3.1 OED Approach

The proposed method is based on a sequence of experiments $\xi_i,\ i = 1, \dots N_{exp}$, with $N_{exp} = 10$, each with duration $t_N^{\xi_i} - t_0^{\xi_i} = 1000s$ subdivided, for computational reasons, into $M = 4$ sub-optimal steps (Algorithm 1). In the following, the performance of the OED method is evaluated in terms of convergence of the estimated parameter vector to the true value and variances reduction. All the experiments present the same duration and initial condition. After each experiment, in order to bring the initial condition back to x_0 (i.e. $x_0^{\xi_i} = x_0,\ i = 1, \cdots N_{exp}$), the cell is charged with a constant current of $1C$-rate (i.e. a current value able to completely charge the cell in one hour) for a suitable time interval and then a resting period of $400s$ is considered. The input sequence of the OED approach is obtained as described in 3.1.1.4, with $u^{lb} = -I_{1C}$ and $u^{ub} = I_{1C}$, while the safety constraints on voltage and SOC in (3.11d) are as follows

$$V_{min} \leq V(t) \leq V_{max} \tag{3.22a}$$

$$SOC_{min} \leq SOC(t) \leq SOC_{max} \tag{3.22b}$$

where $V_{min} = 2.5V$, $V_{max} = 4.35V$, $SOC_{min} = 0.1$ and $SOC_{max} = 0.9$.

3.1.3.2 CC Discharging Protocol

The CC discharging approach is also based on a sequence of 10 experiments each of them consisting of a simple constant-current discharging protocol with a $1C$-rate current and time duration $1000s$. Also in this case, at the beginning of each experiment, the initial condition is brought back to x_0 by applying a CC charging current of $1C$, followed by a resting period of $400s$. Figure 3.3 reports the current and voltage profiles obtained with the OED and the CC discharging approaches. Note that the outcomes of the 10 CC discharges will be different among each other due to the presence of the output measurement noise.

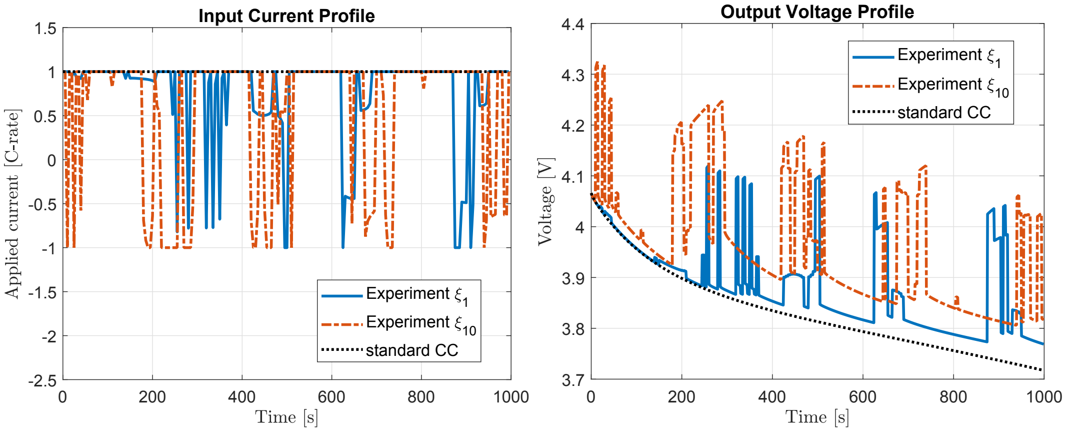

FIGURE 3.3: Current input profiles, applied during standard CC and OED methods, and the corresponding voltage responses.

3.1.3.3 Multistep Discharging Strategy

The multiple-step discharging current profile explores the whole battery state of charge range, as described in Figure 3.4. In particular, the battery is discharged from a unitary state-of-charge in 5 steps, each of which applies a current equal to I_{1C} for 600*s* followed by 1400*s* of rest. Differently from the previous approaches the multistep discharging protocol consists of a single experiment of time duration 10000*s*. As it can be noticed the overall duration of all the approaches is the same (10000*s*).

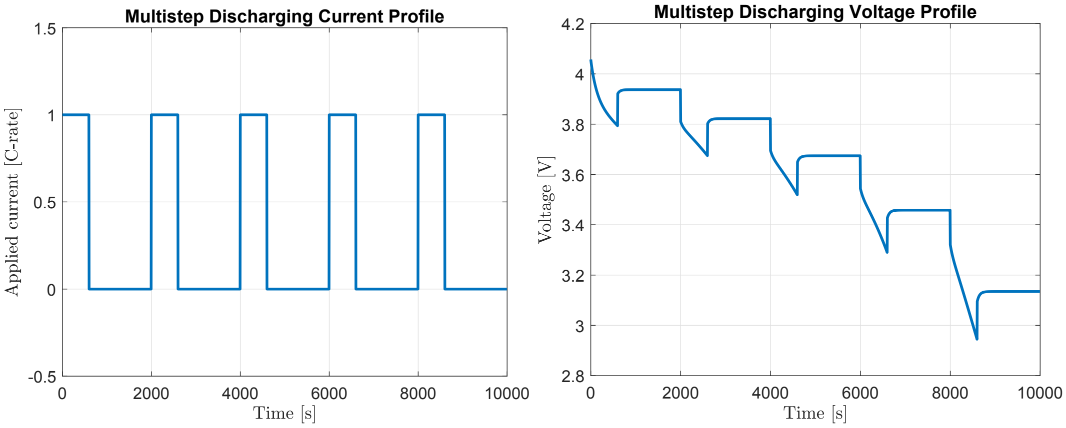

FIGURE 3.4: Current and voltage profiles for the multistep discharge identification.

3.1.3.4 Comparison of the Estimation Performance

In Figure 3.5, the experimental procedures are compared in terms of convergence of the estimated parameter vector $\hat{\phi}$ to the true values ϕ^*, i.e. in terms of the euclidean norm

$$\|\hat{\phi} - \phi^*\| = \sqrt{(\hat{\phi} - \phi^*)^\top (\hat{\phi} - \phi^*)}. \tag{3.23}$$

Note that, with the only aim of improving the readability of the results presented in this section, a normalization of the parameter vector is conducted a posteriori with respect to their true values, thus meaning that each parameter is perfectly identified when it assumes a unitary value. As can be noticed the parameter vector identified using the OED strategy presents a fast convergence to the real value and a very low error even after the first experiment (1000s). On the other side, standard approaches require a longer time to reduce the gap between the identified parameter vector and the true one. It is important to consider that the oscillations in the convergence of all the identification methods are motivated by the fact that the output of the identification process (i.e. the identified parameter vector) is a random variable due to the fact that the measurements are affected by Gaussian noise (Körkel and Kostina, 2005) and the inverse of the Fisher matrix (that we minimize) provides only a lower bound for the second moment of such random variables. Therefore, considering also the local nature of the Fisher matrix, it is not guaranteed that the Euclidean norm of successive solutions of the nonlinear least-square problem in (3.8) will decrease monotonically. Moreover, it has to be noticed that the observability for the CC method is much worse than the other methods: apparently, the exploration

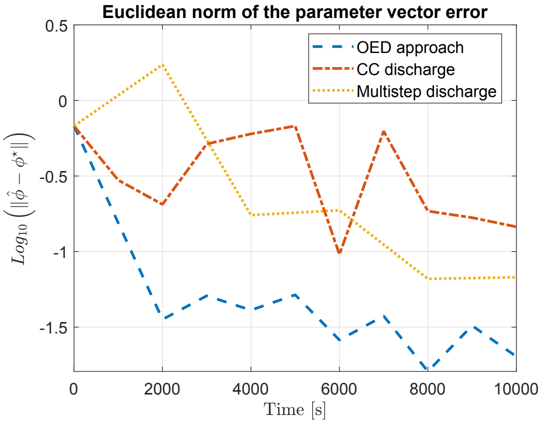

FIGURE 3.5: Comparison between the optimal experimental approach and the standard ones in terms of Euclidean distance of the scaled parameter vector to the true value.

of lower SOC values by applying consecutive discharging step (as in the multistep approach) leads to a more informative experiment. Figure 3.6 highlights how the different parameters converge to their true values using the OED approach. Table 3.2 shows the parameter vector estimated after the last experiment for all the approaches. In particular, the OED results in the most accurate method, although all the approaches show a small estimation error at the end of the experimental procedure. Finally, Table 3.3 shows the variance reduction during the experiments realization. In particular it emerges that the variance of all the parameters in the OED is very low already after the first experiment (1000s), while the multistep discharging approach requires 10000s to achieve high performance. In the CC discharging

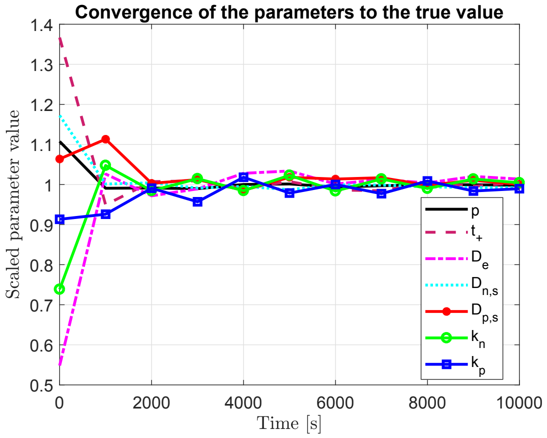

FIGURE 3.6: Convergence of the parameters to the true values. In order to improve the readability of the plot a normalization with respect to the true value of the parameters has been applied.

Parameter	ϕ_0	ϕ^*	$\hat{\phi}_{OED}$	$\hat{\phi}_{CC}$	$\hat{\phi}_{m-step}$
p	1.1075	1	0.9979	1.0105	0.9911
t_+	1.3668	1	1.0052	0.9944	0.9579
D_e	0.5482	1	1.0136	1.0975	0.9990
$D_{s,p}$	1.1724	1	0.9920	0.9707	1.0029
$D_{s,n}$	1.0638	1	1.0004	1.0192	1.0498
k_p	0.7385	1	1.0044	1.0866	0.9903
k_n	0.9133	1	0.9896	0.9460	0.9885

TABLE 3.2: Identified scaled parameters at the end of the experiment procedure using both optimal and standard approaches compared with the initial guess and the true value.

method the parameters variance still remains high at the last experiment. These results are promising since they underline that an optimal design of experiment can significantly improve parameter estimation accuracy (both in terms of converging parameter values and variances). Furthermore, the number of experiments required for the convergence of the parameters to the true values, i.e. the time duration of the experimental realization required for an accurate identification, is much shorter using the OED approach than the standard current profiles.

Parameter	Variance after ξ_1			Variance after ξ_{10}		
	OED	CC discharge	Multistep discharge	OED	CC discharge	Multistep discharge
p	$5 \cdot 10^{-5}$	1.21	0.0636	10^{-5}	0.24	10^{-4}
t_+	$8 \cdot 10^{-4}$	0.92	0.0225	$1.6 \cdot 10^{-4}$	0.19	$4 \cdot 10^{-4}$
D_e	$6 \cdot 10^{-3}$	6.97	0.5488	$1.2 \cdot 10^{-3}$	1.39	$6 \cdot 10^{-4}$
$D_{s,p}$	$6 \cdot 10^{-4}$	0.59	0.038	10^{-4}	0.12	10^{-5}
$D_{s,n}$	$9 \cdot 10^{-4}$	0.01	0.0166	$1.86 \cdot 10^{-4}$	$2.9 \cdot 10^{-3}$	$5 \cdot 10^{-4}$
k_p	$1.5 \cdot 10^{-3}$	14.88	0.8118	$3 \cdot 10^{-4}$	2.98	10^{-4}
k_n	$2.5 \cdot 10^{-3}$	1.10	0.1004	$4.9 \cdot 10^{-4}$	0.22	10^{-4}

TABLE 3.3: Comparison between scaled parameter variances during the identification process, both in case of optimal design of experiment and standard approach.

The average time needed to solve off-line the optimization problem described in 3.1.1.4 and to compute the current profile for a single experiment is 520.81 s, while the average time needed to solve the identification process in (3.8) is 13.59 s. The simulations are performed on a Windows 10 machine with 16Gbytes of RAM and Intel core I7-6700HK quad-core processor 3.5 GHz.

3.1.3.5 Validation of the SPMe With the Identified Parameters

A validation process of the models identified with the different strategies has been performed in order to highlights the benefits of the proposed optimal approach. In particular, the identification methods are compared in terms of RMS error of the predicted voltage with respect to the model simulated with the true parameter vector. The input current profile $u_{val}(t)$ used for the validation (Figure 3.7) consists of a biased multi-sinusoidal current with frequency $f_1 = 0.02Hz$ and $f_2 = 0.005Hz$, $I_{bias} = 0.75 I_{1C}$ as mean value and $I_{sin} = 0.25 I_{1C}$ as peak value of the sinusoidal components

$$u_{val}(t) = I_{sin}\left(\sin(2\pi f_1 t) + \sin(2\pi f_2 t)\right) + I_{bias}. \tag{3.24}$$

The input current has been chosen in the same range of the exciting input signal which has been applied during the parameter identification process. The results of the validation are shown in Figure 3.8. This latter reports the evolution of the voltage RMS error between the identified SPMe models and the real plant (assumed to be the SPMe model with true parameters ϕ^*), evaluated after each experiment on the validation profile. In particular, such evaluation is conducted for the different estimation methods (OED, CC, multistep) at each step in the iterative process (i.e. every 1000s of experiment for the OED and CC methods, and every 2000s for the multistep). We compute the RMS error between the identified models (with parameter vectors $\hat{\phi}_{OED}$, $\hat{\phi}_{CC}$, $\hat{\phi}_{m-step}$) and the real plant, in correspondence of a validation profile such as the one in Figure 3.7. The decrease of the errors in Figure 3.8 is therefore motivated by the fact that at each step the parameter vectors identified with the different approaches (OED, CC, multistep) become more accurate and closer to the true one ϕ^*. As it can be noticed, the RMS error using the OED approach is very low after the first experiment, while the benchmark methods present a slow convergence to an higher error.

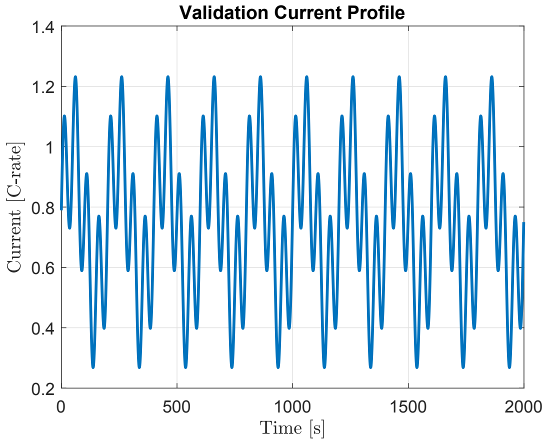

FIGURE 3.7: Input current profile used for validation.

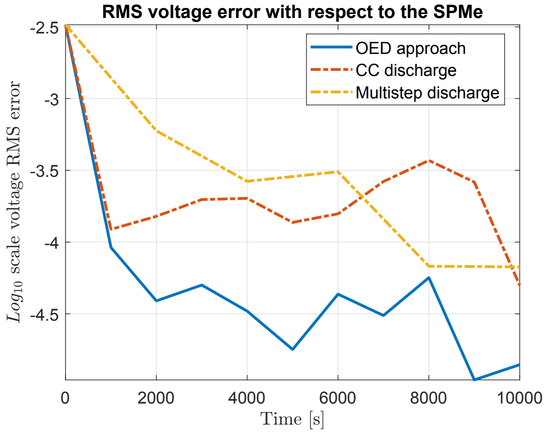

FIGURE 3.8: Comparison between the optimal experimental approach and the standard ones in terms of root-mean-square error of the predicted voltage.

3.1.4 Results on the P2D

In 3.1.3, the OED method has been conducted on the SPMe, assuming that the model used as the real plant and the one used for the parameters estimation were the same. For this reason, the measurement data has been collected by simulating the SPMe output affected by a zero-mean Gaussian error. However, while the SPMe is particularly suitable for control purposes, its use for accurately simulating a real lithium-ion cell may be inadequate. For this reason, LIONSIMBA (Torchio et al., 2016b), a battery simulator which implements the P2D model, is here assumed to be the real plant, with the output voltage affected by the same zero-mean Gaussian error as in 3.1.3. It is important to notice that the use of two models, one as the real plant simulator (very detailed) and the other for the control (simpler), is a well known procedure. In particular, this allows to assess, in a preliminary way, the practical effectiveness of a novel control approach thus reducing time and costs during the experimental phase.

In the following, we assign value ϕ^* (see Table 3.1) to the parameters of the P2D. Note that, in general, the parameter vector resulting from the optimization may be different from ϕ^*. In fact, although physically meaningful, the use of a simplified model with parameter values equal to the ones of the real plant (P2D) may not be the best choice in terms of output fitting. In particular, the voltage prediction of the SPMe with the parameter vector ϕ^* presents an RMS error which is around few mV with respect to the P2D during normal cycling. This lack of accuracy comes in the form of a bias, and, although this could seem negligible, such error may cause problems if the identified model has to be employed for states estimation. In the following, the parameters of the SPMe with the best fitting in terms of voltage are considered unknown, as in real experiments, and the parameter vector ϕ^* in Table 3.2 is used only to simulate for comparative purposes the SPMe with the P2D parameters. Also in this case, the optimal design of experiments technique is compared with benchmark experimental approaches, such as CC and multistep discharging protocols. The experimental setting adopted is the same of 3.1.3. Figure 3.9 shows the Euclidean distance between the estimated parameter vector $\hat{\phi}$ and ϕ^*. As discussed above, such distance is not expected to go to zero, since it is not guaranteed that the best fit will come with ϕ^*. However, a low value of this Euclidean norm ensures a physical meaning of the estimated parameters. Note that, in real experiments the true parameters are unknown but we can evaluate the model performance in terms of output fitting of validation data and in terms of closeness to the data-sheet parameters. As can be noticed from Figure 3.9, the parameter vector identified with the OED method is closer to the one of the P2D model than in the standard approaches. Table 3.4 shows the parameters estimated after the last experiment for all

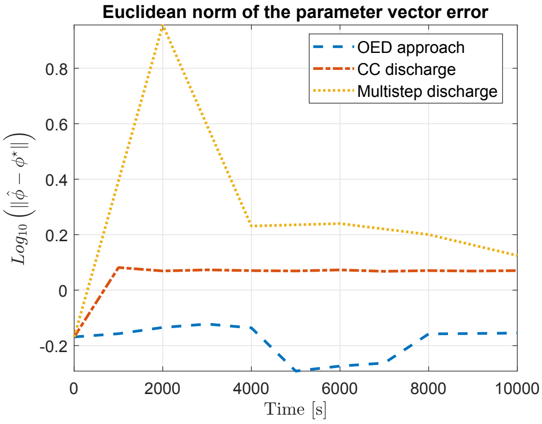

FIGURE 3.9: Comparison between the OED and the benchmark approaches, experimentally applied to LIONSIMBA.

the approaches. In this case, many parameters such as the Bruggeman coefficient (using the CC discharging approach) and the electrolyte diffusion coefficient (using the multistep discharging approach) seem to lose their physical meaning, while the OED strategy allows to identify parameters close to the nominal value.

Parameter	ϕ^*	$\hat{\phi}_{OED}$	$\hat{\phi}_{cc}$	$\hat{\phi}_{m-step}$
p	1	0.6150	0.1000	0.8776
t_+	1	0.9472	0.8537	0.8905
D_e	1	0.4478	0.4303	2.2264
$D_{s,p}$	1	1.1164	0.8236	0.8508
$D_{s,n}$	1	0.9065	0.7288	0.7400
k_p	1	1.0011	0.7331	1.3804
k_n	1	0.8897	0.7742	1.1032

TABLE 3.4: Identified scaled parameter of the SPMe after 10 experiments conducted on the P2D model.

3.1.4.1 Validation of the Identified SPMe on Data Collected From the P2D Model

In this section, the SPMe is validated, in terms of P2D voltage prediction, using the parameters identified in the section above with the OED and the standard approaches. Furthermore, the results are also compared with the SPMe using ϕ^*. In particular, the current input profile used for the validation $u_{val}(t)$ is the same adopted in 3.1.3.4 (see Figure 3.7). Also in this case, the results of the validation are shown in terms of RMS error of the voltage prediction. As can be noticed from Figure 3.10, the RMS error using the CC approach presents a fast convergence to a higher value with respect to the optimal method, while the error decrease with the multistep strategy is much slower than the OED one. Note that, all the estimation methods improve the accuracy in the P2D voltage prediction with respect to the one of the SPMe with ϕ^*. On the other side, the OED method is the one which provides physically meaningful parameters in the shortest time.

The validation performed so far shows promising results in the application of an OED technique when the P2D model is used as the real plant. In particular, it is demonstrated that the estimation of the SPMe parameters through the optimal design of experiments can increase the model performance in the P2D voltage prediction.

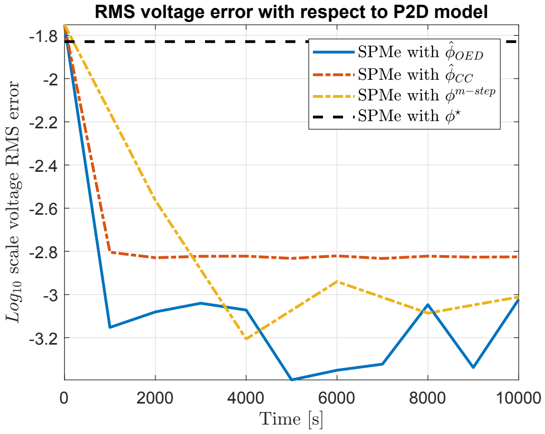

FIGURE 3.10: Comparison between the optimal experimental approach and the standard ones in terms of root mean square error of the predicted voltage.

3.2 Global Sensitivity Analysis Applied to OED for SPMeT

Most implementations of OED are based on the Fisher information matrix, which gives a local measurement of how informative an input signal is in terms of output sensitivity with respect to parameters variations. In particular, the FIM represents a perfect measure only for linear parameter identification problems (Kiefer, 1959; Walter and Pronzato, 1997), due to the fact that local sensitivities assume a linear relationship between model parameter variations and simulation results. In the nonlinear case, local sensitivities may lead to biased information measurements because of biased reference parameters (Manesso, Sridharan, and Gunawan, 2017). Moreover, the actual parameters for calculating the local sensitivities are unknown, and, in turn, the best estimate of the parameter vector has to be used.

In the last decade, the use of global sensitivities for the OED has been discussed in the literature (Schenkendorf et al., 2018) as a possible solution to the aforementioned issues. In particular, global sensitivities consider model parameters and simulation results as random variables and aim at quantifying in which measure the uncertainty on each model parameter contributes to the variation in the simulated outputs. While various studies in the context of lithium-ion batteries are based on Fisher information matrix, including ones for complex electrochemical models, the usefulness of GSA and its effective implementation for electrochemical processes in the context of OED have not been analysed thus far.

In this chapter, we propose a highly efficient OED framework that is based on GSA, and we implement, for the first time to the knowledge of the authors, this concept for a lithium-ion cell modelled as SPMeT (Pozzi et al., 2020b). To prevent a computation overload while replacing the local sensitivity matrix and solving the underlying dynamic optimization problem, we make use of the Point Estimate Method (PEM) as a highly efficient sampling technique to determine global parameter sensitivities. In contrast to previous work (Schenkendorf et al., 2018), the global parameter sensitivities are directly transferred to standard OED criteria.

3.2.1 Global Sensitivity Analysis for OED

In the following, the nonlinear model in (3.1) is considered together with the sequences of applied inputs ($\mathbf{u}_{\xi}$) and simulated outputs ($\mathbf{y}_{\xi}(\phi)$) defined in (3.2) for a given experiment ξ (which consists of N measurements). Note that the output sequence simulated through the model in (3.1) depends on both the applied input profile and the parameter vector.

3.2.1.1 Global Sensitivity Matrix

The global sensitivities approach treats both the model parameter vector ϕ and the output $y(t)$ as random variables, and it relies on the fact that the uncertainty of each entrance $\phi^i \in \mathbb{R}$ of the parameter vector, with $i \in \{1, 2, \cdots, N_\phi\}$, contributes to the total output variance, here indicated as $\mathbf{var}[y(t)]$. This latter is defined by

$$\mathbf{var}[y(t)] = \mathbb{E}\left[(y(t) - \mathbb{E}[y(t)])^2]\right] \tag{3.25}$$

where $\mathbb{E}[\cdot]$ is the operator of expectation. Without loss of generality, we assume here that the model in (3.1) is characterized by scalar inputs and outputs. Then, the global sensitivity matrix $S_G^{\xi} \in \mathbb{R}^{N \times N_\phi}$ for the experiment ξ over the time interval $[t_0^{\xi}, t_N^{\xi}]$ is given as follows

$$S_G^{\xi} = [S_G(t_0^{\xi}), S_G(t_0^{\xi} + t_s), \cdots, S_G(t_N^{\xi})]^\top \tag{3.26}$$

where the i-th entrance $S_G^i(t) \in \mathbb{R}$ of the vector $S_G(t) \in \mathbb{R}^{N_\phi}$ for $t = t_0^\xi, t_0^\xi + t_s, \cdots, t_N^\xi$ is given as

$$S_G^i(t) = \frac{\mathbf{var}_i[\mathbb{E}_{-i}[y(t)|\phi^i]]}{\mathbf{var}[y(t)]} \tag{3.27}$$

also known as first-order Sobol index (Sobol, 2001). Note that $\mathbb{E}_{-i}[y(t)|\phi^i]$ represents the conditional expectation of the variable $y(t)$ taken over the parameter space $\mathbf{\Phi}_{-i} \subset \mathbb{R}^{N_\phi - 1}$ consisting in all factors but ϕ^i, while $\mathbf{var}_i[\cdot]$ is the variance over all the possible values of ϕ_i. Finally, it is of interest to underline that the condition $\sum_{i=1}^{N_\phi} S_G^i(t) \leq 1$ holds $\forall t \in \{t_0^\xi, t_0^\xi + t_s, \ldots, t_N^\xi\}$ and $\forall i \in \{1, 2, \ldots, N_\phi\}$.

3.2.1.2 Point Estimate Method

The computation of the Sobol indices in (3.27) requires a proper and efficient uncertainty quantification (i.e. the estimation of the first- and the second-order moment of the output with respect to the parameters). Although Monte-Carlo simulations and polynomial chaos expansion (Crestaux, Le Maıtre, and Martinez, 2009) are frequently used methods for uncertainty quantification, their computational cost may be prohibitive and they may be inappropriate for correlated random variables. Therefore we consider here the exploitation of the point estimation method (Xie, Krewer, and Schenkendorf, 2018), which requires only a few deterministic evaluations of the analysed process model for estimating the statistical moments of the considered random variables. In particular the use of PEM has proven beneficial in various engineering problems (Lerner, 2002), including complex electrochemical processes (Laue et al., 2020).

Consider that the expected value and the variance of the output with respect to the uncertain parameter vector can be computed as follows

$$\mathbb{E}[y(t)] = \int_{\mathbb{I}_\phi} y(t) f(\phi) d\phi \tag{3.28a}$$

$$\mathbf{var}[y(t)] = \int_{\mathbb{I}_\phi} (y(t) - \mathbf{E}[y(t)])^2 f(\phi) d\phi \tag{3.28b}$$

where $f(\phi)$ is the joint distribution of the parameter vector and $\mathbb{I}_\phi$ is the corresponding support. We approximate the integral terms in (3.28) through a weighted sum as follows

$$\mathbb{E}[y(t)] \simeq \sum_{k=1}^{n_{PEM}} \omega_k y^{[k]}(t) \tag{3.29a}$$

$$\mathbf{var}[y(t)] \simeq \sum_{k=1}^{n_{PEM}} \omega_k (y^{[k]}(t) - \mathbb{E}[y(t)])^2 \tag{3.29b}$$

where $y^{[k]}(t) = y(t, \phi^{[k]})$ is the output corresponding to the parameter vector sample $\phi^{[k]}$, while ω_k is a weight factor and n_{PEM} is the number of sample points. The most challenging task is to retrieve a set of samples of the parameter vector and the corresponding weight factors which provide an accurate estimation of the first- and second-order moments of the random variable $y(t)$. According to (Lerner, 2002; Schenkendorf, 2014) we proceed by considering the normalized nominal parameter vector ϕ_0 and we extract the parameter samples $\phi^{[k]}$ from the set $\mathcal{O} := \{\phi_0, \mathcal{A}, \mathcal{B}\}$, where:

$$\mathcal{A} := \{[\phi_0^1, \cdots, \phi_0^i \pm \theta, \cdots, \phi_0^{N_\phi}]^\top, \ \forall i \in \{1, \ldots, N_\phi\}\} \tag{3.30a}$$

$$\mathcal{B} := \{[\phi_0^1, \cdots, \phi_0^i \pm \theta, \cdots, \phi_0^j \pm \theta, \cdots, \phi_0^{N_\phi}]^\top, \ \forall i, \underset{j>i}{\forall j} \in \{1, \ldots, N_\phi\}\} \tag{3.30b}$$

where the scalar parameter θ controls the spread of the sample points. With the considered set $\mathcal{O}$ the sample number scales quadratically with the dimension of the uncertain parameter vector, i.e. $n_{PEM} = 2N_\phi^2 + 1$. Assuming a Gaussian probability density function for the parameter vector, one has $\theta = \sqrt{3}$ and weight factors as follows

$$\omega_1 = 1 + \frac{N_\phi^2 - 7N_\phi}{18}, \quad \phi^{[1]} = \phi_0 \tag{3.31a}$$

$$\omega_k = \frac{4 - N_\phi}{18}, \quad \phi^{[k]} \in \mathcal{A}, \quad k = 2, \cdots, 2N_\phi + 1 \tag{3.31b}$$

$$\omega_k = \frac{1}{36}, \quad \phi^{[k]} \in \mathcal{B}, \quad k = 2N_\phi + 2, \cdots, n_{PEM} \tag{3.31c}$$

Note that the PEM assumes the knowledge of a prior for the parameter distribution and that any probability distribution of relevant model parameters can be considered via a (non)linear transformation step, including parameter correlations. For more details about the weight factors computation the interested reader is referred to (Xie, Krewer, and Schenkendorf, 2018). Finally, it is important to underline that due to a nested re-sampling strategy, the global sensitivity matrix can be determined highly efficiently with n_{PEM} model simulations, where appropriate subsets $\mathcal{P}_i \subset \mathcal{O}$ are evaluated to calculate S_G^i, $\forall i \in \{1, \ldots, N_\phi\}$.

3.2.1.3 Optimization Framework

In the following, we consider a similar problem formulation to the one presented in 3.1.1.3, except for the fact that here only a single experiment is designed (rather than a sequence of experiments) and a GSA-based objective function is taken into account. The optimization problem that we aim to solve in order to design the experiment ξ is the following

$$\mathbf{u}_\xi^\star = \arg\min_{\mathbf{u}_\xi} \mathrm{Tr}\left(({S_G^\xi}^\top C_y^{-1} S_G^\xi)^{-1} \right) \tag{3.32}$$

subject to

$$\text{model dynamics in (3.1)} \tag{3.33a}$$

$$x(t_0^\xi) = x_0^\xi \tag{3.33b}$$

$$u^{lb} \leq u(t) \leq u^{ub}, \qquad t = t_0^\xi,\, t_0^\xi + t_s,\, \cdots,\, t_N^\xi \tag{3.33c}$$

$$h(x(t), u(t), \hat{\phi}) \leq 0, \qquad t = t_0^\xi,\, t_0^\xi + t_s,\, \cdots,\, t_N^\xi \tag{3.33d}$$

where the cost function does not exhibit a dependency on the parameter vector, differently from the one in (3.10) which has a local nature due to the fact that it is based on the Fisher matrix and, therefore, on local sensitivities. Note that, as in 3.1.1.2, the parameter identification procedure is conducted through a maximum-likelihood estimation procedure, i.e. by solving (3.8).

In the following, the efficiency of the GSA method is compared to the one based on local sensitivity analysis, i.e. on the Fisher information, through the index η, defined as

$$\eta = \frac{\mathbf{var}_L[\hat{\phi}]}{\mathbf{var}_G[\hat{\phi}]} \tag{3.34}$$

where $\mathbf{var}_L[\cdot]$ and $\mathbf{var}_G[\cdot]$ denote the variance of the estimated parameter vector respectively in the case of local and global sensitivity analysis. Such variances are quantified exploiting empirical statistics based on Monte-Carlo simulations with artificial data assuming additive white measurement noise.

3.2.2 Cell Modelling and Parameters

In this section the lithium-ion cell has been modelled through the SPMeT, whose equations are obtained from the ones presented in 2.4.2.2 by neglecting the ageing dynamics. This constitutes a significant difference with respect to Section 3.1, where an isothermal model has been considered. The parameters are taken from (Ecker et al., 2015a; Ecker et al., 2015b) and the positive and negative open-circuit potentials $U_p(t)$ and $U_n(t)$ for the considered cell are given by the following nonlinear functions of the surface stoichiometries $\theta_i^*(t)$

$$\begin{aligned} U_p(t) =& 18.45\theta_p^*(t)^6 - 40.7\theta_p^*(t)^5 + 20.94\theta_p^*(t)^4 \\ & + 8.07\theta_p^*(t)^3 - 7.837\theta_p^*(t)^2 + 0.02414\theta_p^*(t) + 4.571 \end{aligned} \tag{3.35}$$

$$U_n(t) = \frac{0.1261\theta_n^*(t) + 0.00694}{\theta_n^*(t)^2 + 0.6995\theta_n^*(t) + 0.00405} \tag{3.36}$$

Since such functions must be referred to the particular type of cell under investigation, they are obtained by a fitting procedure on the experimental data collected in (Ecker et al., 2015a). Finally, the temperature-dependent electrolyte conductivity function is expressed as follows

$$\begin{aligned} k(c_{e,j}^{[k]}(t), T(t)) =& \Big(0.2667 \left(\gamma_j^{[k]}(t)\right)^3 - 1.2983 \left(\gamma_j^{[k]}(t)\right)^2 \\ & + 1.7919\gamma_j^{[k]}(t) + 0.1726\Big) e^{\frac{-E_{a,\kappa}}{RT(t)}} \end{aligned} \tag{3.37}$$

where $\gamma_j^{[k]}(t) = 10^{-3} c_{e,j}^{[k]}(t)$. The input is again the applied current, while we consider both voltage and temperature as the outputs $y(t) = [V(t), T(t)]^\top$. The states vector for the SPMeT is as follows

$$x(t) = [\theta_p^{avg}(t), q_p(t), q_n(t), x_{c_e}(t), T(t)]^\top, \tag{3.38}$$

with $N_x = 4 + 3P$.

3.2.2.1 Parameters to Be Estimated

For the sake of simplicity, nine normalized performance-relevant model parameters are studied, and the parameter vector reads as

$$\phi = [D_e^0,\ E_{a,D_{p,s}},\ k_p^0,\ k_n^0,\ E_{a,k_p},\ E_{a,k_n},\ \tau_s,\ \tau_n,\ h_c]^\top \tag{3.39}$$

where D_e^0, k_p^0 and k_n^0 are pre-exponential coefficients in the Arrhenius laws for the electrolyte diffusion and the kinetic rate reactions. Note that the value of all the nominal model parameters can be found in (Ecker et al., 2015a; Ecker et al., 2015b).

3.2.3 GSA-Based Optimal Experimental Design for the SPMeT

To demonstrate the effectiveness of global sensitivity analysis within the OED context, the optimization problem in (3.32) is solved and the results are compared to the ones obtained through the Fisher-based methodology which has been discussed in 3.1 and is here applied with the same settings as the GSA approach. In particular, we optimize an experiment with a fixed duration time, $t_N^\xi - t_0^\xi = 1000\text{s}$, with measurements collected every $t_s^{meas} = 5s$, while the optimal input sequence is assumed to be piece-wise constant over each $t_s^{ctr} = 100\text{s}$ resulting in a control variable vector of 10 elements. Note that a measurement sampling time which is independent from the number of control variables enables to adapt the OED to the time constants of different processes. Each element of the control vector is limited by $u^{lb} = -15I_{1\text{C}}$ and $u^{ub} = 15I_{1\text{C}}$. The initial condition x_0 is used for both the global and local approach. In particular, the positive stoichiometry is initialized as 0.83 (which corresponds to a SOC of 0.05), and the initial temperature is set equal to 298.15 K, while the initial electrolyte concentration and the average concentration flux are assumed to start at equilibrium values of 1000 mol/m^3 and zero, respectively. The experiments should not exceed temperature and voltage limits

$$T(t) \leq 320\,\text{K} \tag{3.40}$$

$$2.7\,\text{V} \leq V(t) \leq 4.2\,\text{V} \tag{3.41}$$

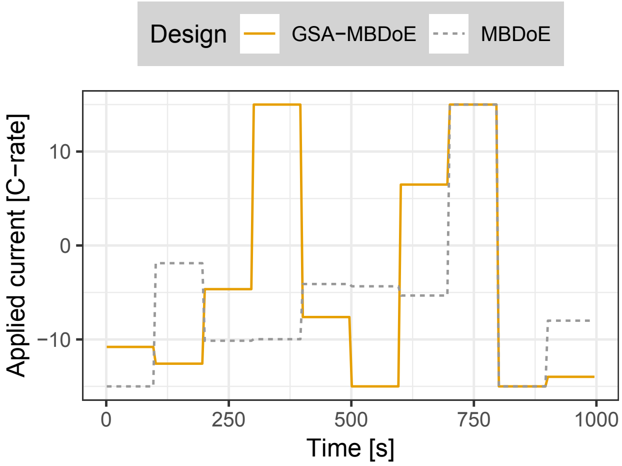

FIGURE 3.11: Current input profiles based on the MBDoE (local approach) and the GSA-MBDoE (global approach).

which are taken into account by the constraint in (3.33d). When considering nine model parameters (i.e. $N_\phi = 9$), the overall sample number required by the PEM method reads as $n_{PEM} = 163$. Note that, according to the assumption that a prior of the parameter distribution is known for the GSA approach, a standard deviation of 10% is considered for the parameters to be estimated.

Technically, the optimization problem (3.32) was solved by using the interior-point NLP solver IPOPT, where a multi-start strategy was used to avoid local minima. In Figure 3.11, we show the optimized current input profiles obtained with the Fisher-based method and the GSA approach, respectively. The profiles in the first interval, $t \leq 500\,\mathrm{s}$, show different trends. Both start with the high negative current input, but only the one based on GSA switches to the high positive current input afterwards. In the second interval, $t > 500\,\mathrm{s}$, both profiles show a *bang-bang* control behaviour, that is, switching from the high negative current input to the high positive one and back.

The Fisher-based method and the GSA approach are validated with Monte-Carlo simulations over 100 different scenarios in presence of additive white measurement noise with $\mathbf{var}(V(t)) = 10\mathrm{mV}$ and $\mathbf{var}(T(t)) = 0.3\mathrm{K}$. Based on the estimates, the resulting efficiency of the GSA-based approach (Eq. 3.34), is given in Table 3.5. The efficiency measure, η, clearly shows an improvement of the GSA-approach compared

TABLE 3.5: Efficiency of the GSA-based optimal desgin of experiments according to (3.34).

Parameter	D_e^0	$E_{a,D_{p,s}}$	k_p^0	k_n^0	E_{a,k_p}
Efficiency η	1.3970	2.2971	1.9015	17.6513	1.7172

Parameter	E_{a,k_n}	τ_s	τ_n	h_c
Efficiency η	3.2228	1.0050	1.8365	1.6938

to the one based on local sensitivities. For all the parameters, the GSA-method ensures more precise parameter estimates, that is, the optimized current input profile based on the global sensitivity analysis generates more informative data than the one which relies on local information. The model parameter uncertainties of k_n and E_{a,k_n} are reduced significantly, while the parameter τ_s is only marginally affected by the specific current input profile. In Figure 3.13, the resulting parameter uncertainties are depicted in details. In particular, we refer to MBDoE as the Model-Based Design of Experiment based on local sensitivity analysis, while GSA-MBDoE is used to refer to the global sensitivity approach. In the lower-left triangle, the scatter plots of all parameter combinations are given. The local approach results in higher parameter variations and outliers in comparison with the GSA-method (especially for k_n^0 and E_{a,k_n}). In the case of τ_s, two sample clusters can be detected, indicating two local minima of the parameter identification problem, which is insensitive to the optimal design of the input profile. On the diagonal, we illustrate the corresponding box-and-whisker plots. As it can be noticed, the GSA-based estimates are more precise and exhibit fewer outliers. Finally, in the upper-right triangle of Figure 3.13, the parameter correlations are shown.

Based on the illustrated median and spread, only a few parameters might have a Gaussian probability density function, as in Figure 3.12(a) for E_{a,k_n}. In most cases, the probability density functions are non-Gaussian or non-symmetric, which is common for non-linear identification problems. For instance, the probability density function of τ_s is bimodal and has two peaks, because of the two local minima of the parameter identification problem (see Figure 3.12(b)). The probability density function of τ_n, in turn, shows a significant skewness in its estimates (see Figure 3.12(c)).

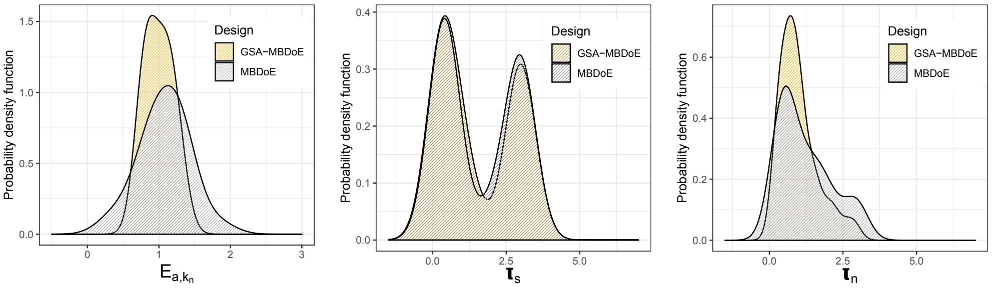

(a) Gaussian (b) Bimodal (c) Non-symmetric

FIGURE 3.12: Resulting probability density functions of the estimated parameters show: (a) Gaussian, (b) bimodal, and (c) non-symmetric distributions.

3.3 Conclusions About Optimal Design of Experiments

In this chapter the optimal design of experiments for parameter identification in the lithium-ion battery context has been addressed. In particular, two different methodologies have been discussed. The first one, which is based on the so-called Fisher information matrix described in Section 3.1, exploits local sensitivities of the outputs with respect to parameters variations. The second one presented in Section 3.2 relies instead on the concept of global sensitivity analysis in order to find an optimal input profile which provides higher accuracy during the estimation procedure. Further works in this field may include on one hand the experimental validation of the proposed methodologies and, on the other hand, the development of novel ideas which enhance fast OED in order to improve the identifiability of a larger set of model parameters, which translates in a more computational demanding optimization problem.

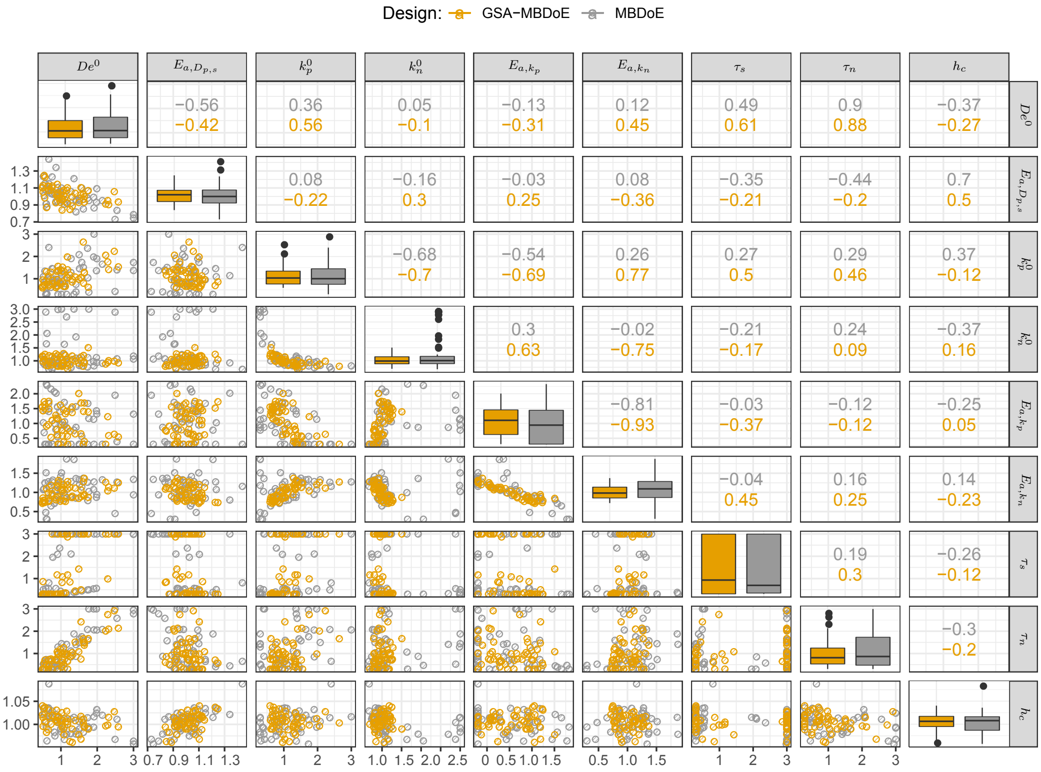

FIGURE 3.13: Statistics of the estimated parameters: scatter plots of all parameter combinations (lower-left triangle), corresponding box-and-whisker plots (diagonal), and parameter correlations (upper-right triangle).

Chapter 4

Optimal Control of Li-ion Batteries

As discussed in the previous chapters, the proper functioning of lithium-ion batteries requires a Battery Management System. One of the main tasks of a BMS is to safely charge the battery. This objective is usually addressed through standard protocols, such as constant-current constant-voltage. This latter protocol first applies the current I_{cc} in a galvanostatic charge, until the voltage threshold V_{cv} is achieved. Then a potentiostatic charge is applied, while the current through the cell decreases exponentially, until a current cutting threshold is reached (see Figure 4.1). Although the CC-CV protocol provides reasonable performance, it is based on conservative voltage limits, thus leading to a suboptimal exploitation of the battery. Moreover, when a battery pack composed of several cells is considered, the use of standard charging protocols such as CC-CV may lead to a situation in which some cells are undercharged and some are overcharged. As a consequence, some cells may experience fast degradation, thermal runaway, and, in certain cases, even explosions. For

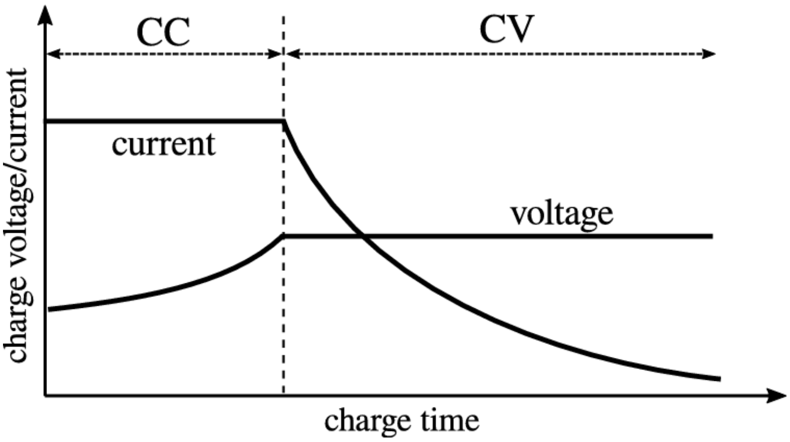

FIGURE 4.1: Typical CC-CV profiles, taken from (Marańda, 2015), where the applied current is depicted in terms of its absolute value.

this reason, the research challenge is to improve battery performances by developing advanced BMSs which, relying on mathematical models, are able to overcome the aforementioned issues. Within this context, the use of model-predictive control appears to be particularly suitable due to its ability of dealing with multi-variable nonlinear systems subject to input and state constraints.

In the following, the main historical milestones and theoretical concepts of MPC are summarized in Section 4.1, while its application to the control of a single lithium-ion cell is shown in Section 4.2, with the aim of mitigating energy dissipations and ageing effects. Finally, Section 4.3 considers the management of a whole battery pack in terms of SOC balancing and fast charging.

4.1 Model-Predictive Control

Nowadays, Model-Predictive Control (MPC) is one of the most exploited advanced management techniques for multi-variable industrial processes, due to its conceptual simplicity and its ability to deal with complex systems in presence of input and state constraints (Mayne, 2014). In MPC the current control action is obtained by solving, at each sampling instant, a finite horizon open-loop optimal control problem, using the current state of the plant as the initial states. According to the *receding-horizon* principle, only the first element of the resulting optimal control sequence is applied to the plant, thus allowing the controller to deal with uncertainties (Mayne et al., 2000). Moreover, MPC has been widely used in the control of processes in which the operating point is close to the boundary of the set of admissible states and controls, such as for instance petrochemical plants. It is important to notice that the essence of MPC is to optimize the predicted behaviour of the controlled process and, since the forecasting is obtained through a mathematical process model, this latter represents an essential element of the controller (Rawlings, 2000).

In this section, some of the main MPC results achieved during the last decades are firstly presented in 4.1.1. Then, a general MPC formulation is proposed in 4.1.2 that can be easily adapted to the problems addressed in the rest of the chapter.

4.1.1 Historical Overview of MPC

According to the interesting reconstruction given by (Lee, 2011), the historical development of MPC can be described by considering three different periods. In the first era, MPC can be seen as a raw algorithm which obtained an enormous success in the industry due to its ability of dealing with complex multi-variable systems and constraints. During the second phase, the main theoretical concepts of MPC, such as state-space formulations and stability proofs, have been formally stated by the control research community and a second generation of software, enhanced in generality and soundness, became available. Finally, the third epoch, that continues up to the present day, has mainly focused on the development of fast algorithms capable of mitigating the problem of high computation cost of the open-loop optimization, which limits the use of MPC in contexts that require a short sampling time, especially in the case of nonlinear systems.

4.1.1.1 First Period: Success in the Industry

Although essential features of MPC can be seen in some computer-based supervisory control schemes developed in the 1950s for petrochemical industries and the idea of *receding horizon* has already emerged in the 1960s (Lee and Markus, 1967), the official birth of MPC dates back to the early 1980s, when the appearance of cheaper, more reliable and more powerful microprocessors allowed to include constrained optimizations as part of the control algorithm. In particular, two papers marked the beginning of the rise of MPC as an advanced control methodology: the work in (Richalet et al., 1978) which introduced the concept of Model-Heuristic Predictive Control (MHPC) and the one in (Cutler and Ramaker, 1980) which proposes the so-called Dynamic Matrix Control (DMC). Note that both the algorithms obtain the control law as a solution of a constrained optimal control problem. Although this feature results to be extremely useful in applying MPC to the management of real industrial processes, it also constituted an obstacle to the control research community in placing MPC within an appropriate theoretical context, mainly due to the fact that the resulting control law appears to be implicit and nonlinear.

The two publications mentioned above have been a landmark for the practical implementation of these algorithms, which were quickly adopted by every petrochemical plant in the western world. Nevertheless, such primitive forms of MPC showed a heuristic nature and were based on the assumption that the exploitation of time-domain response models, such as step and finite-impulse responses, was fundamental in order to guarantee robustness. The latter claim was proved wrong in the 1990s by the control researchers, which showed that stability and robustness can be achieved also with a state-space formulation, as we discuss in 4.1.1.2.

4.1.1.2 Second Period: Theoretical Concepts

At the beginning of the second era of MPC the researchers showed that control robustness was not a prerogative of finite-impulse responses, but on the contrary the use of state-space models could bring numerous advantages. Therefore, in the case of linear systems, the following MPC formulation has been adopted as the standard one in the literature. Consider a linear system dynamics in the state-space form as

$$\dot{x}(t) = Ax(t) + Bu(t) \tag{4.1}$$

where $t \in \mathbb{R}$ is the time, $x(t) \in \mathbb{R}^{N_x}$ is the state vector, $u(t) \in \mathbb{R}^{N_u}$ is the control input, with $A \in \mathbb{R}^{N_x \times N_x}$ and $B \in \mathbb{R}^{N_x \times N_u}$. Moreover, assume that a digital controller applies a piecewise-constant input at the discrete times t_k, $k \in \mathbb{N}$ with sample time t_s. Within this context, define the generic input sequence applied in the time interval $[t_k, t_{k+H}]$, with $H \in \mathbb{N}$, as

$$\mathbf{u}_{[t_k,t_{k+H}]} = \left[u^\top(t_k),\, u^\top(t_{k+1}),\, \cdots, u^\top(t_{k+H-1})\right]^\top \tag{4.2}$$

while the corresponding temporal evolution of states is obtained by integrating the equations in (4.1) over $[t_k, t_{k+H}]$, with initial condition $x(t_k) = x_k$, to give

$$\mathbf{x}_{[t_k,t_{k+H}]} = \left[x^\top(t_{k+1}),\, x^\top(t_{k+2}),\, \cdots, x^\top(t_{k+H})\right]^\top \tag{4.3}$$

At each time step t_{k_0}, the MPC algorithm requires the solution of a finite-horizon optimization in order to compute the optimal control sequence $\mathbf{u}^\star{}_{[t_{k_0},t_{k_0+H}]}$ over a prediction horizon of H steps. According to the *receding-horizon* paradigm, only the first element of the obtained optimal control sequence is applied to the system, $u(t_{k_0}) = u^\star(t_{k_0})$ and the remaining future optimal moves are discarded. The optimization is then repeated at the next time step over a shifted prediction window, with the newly available measurements (Bemporad and Morari, 1999). The optimization to be solved at each time t_{k_0} is described below.

Finite-Horizon Optimal Control Problem 1 *Find the optimal input sequence* $\mathbf{u}^\star{}_{[t_{k_0}, t_{k_0+H}]}$ *that solves*

$$\mathbf{u}^\star{}_{[t_{k_0}, t_{k_0+H}]} = \arg\min_{\mathbf{u}_{[t_{k_0}, t_{k_0+H}]}} J(x(t_{k_0})) \tag{4.4}$$

for the cost function

$$J(x(t_{k_0})) = \sum_{k=k_0}^{k_0+H-1} \left[\|x(t_k) - x^{ref}\|_Q^2 + \|u(t_k) - u^{ref}\|_R^2 \right] + \|x(t_{k_0+H}) - x^{ref}\|_{Q_t}^2 \tag{4.5}$$

in which $x^{ref} \in \mathbb{R}^{N_x}$ *and* $u^{ref} \in \mathbb{R}^{N_u}$ *are the reference vectors for the state and the input, respectively, and the matrices* $Q \in \mathbb{R}^{N_x \times N_x}$, $Q_t \in \mathbb{R}^{N_x \times N_x}$ *and* $R \in \mathbb{R}^{N_u \times N_u}$ *are suitably designed weights, with* $Q, Q_t \geq 0$ *and* $R > 0$. *In particular,* Q_t *indicates the terminal penalty. The optimization is subject to the system dynamic in* (4.1) *and the constraints*

$$u(t_k) \in \mathcal{U}, \quad k = k_0, k_0 + 1, \cdots, k_0 + H - 1 \tag{4.6a}$$

$$x(t_k) \in \mathcal{X}, \quad k = k_0 + 1, k_0 + 1, \cdots, k_0 + H - 1 \tag{4.6b}$$

$$x(t_{k_0+H}) \in \mathcal{X}_t \tag{4.6c}$$

where $\mathcal{U}$, $\mathcal{X}$ *are the feasible sets for inputs and states, while* $\mathcal{X}_t \subset \mathcal{X}$ *is the feasible region for the terminal state. Such sets are in general convex and compact, and it holds that* $x^{ref} \in \mathcal{X}$ *and* $u^{ref} \in \mathcal{U}$.

The presented MPC formulation recalls to the memory the classical optimal control problems, such as Linear-Quadratic Regulator (LQR), for which an optimal state-feedback control law was explicitly derived off-line by solving the Hamilton-Jacobi-Bellman (HJB) equation. However, such explicit solution is not available in the presence of constraints. For this reason, the enormous success of MPC in the industry is motivated by its ability to bypass the need for solving the HJB equation, thanks to the fact that it relies on an open-loop optimal control problem to be solved on-line over a finite horizon according to the state feedback. Note that the practical implementation of MPC requires state measurements which in most of the cases are not directly available. For this reason, state observers are usually employed in order to reconstruct the system state from the available output measurements, thus allowing the extension of MPC to the output feedback case.

In the following, we briefly discuss stability and robustness of MPC, as well as its extension to the case of stochastic and nonlinear models.

Stability of MPC Considering an initial state which belongs to the stabilizable set, it is easy to prove that an MPC framework with an infinite horizon ($H = \infty$) is closed-loop stable. Nevertheless, such infinite-horizon approach can not be implemented in a realistic scenario, due to the fact that it would require the solution of an infinite dimensional optimization at each sampling time. Therefore, a lot of effort has been made by the researchers in order to prove that stability can be reached even in the case of a finite-horizon MPC formulation. In particular, it emerged that a suitable choice for the terminal penalty Q_t and for the terminal feasibility set $\mathcal{X}_t$ is crucial in order to guarantee stability. Moreover, it is interesting to notice that Lyapunov theory is the most common theoretical instrument which has been employed in the literature in order to prove the MPC stability, due to the fact that even if the system being controlled is linear, the presence of constraints makes the controller nonlinear. An exhaustive review about stability and optimality of constrained MPC is given by (Mayne et al., 2000).

Robust and Stochastic MPC The aforementioned MPC formulation is deterministic since it assumes the absence of model mismatches with respect to the real plant. Although deterministic MPC exhibits an inherent robustness typical of feedback control, it has been shown that including a quantitative description of the model uncertainty in the optimization if available may be beneficial. During the 1990s a lot of research effort has been oriented to both the concept of robust and stochastic MPC. In particular, the former approach corresponds to guaranteed stability and high performance in the worst-case scenario, while the latter aims at satisfying the constraints in expectation or with a guaranteed probability (i.e. in most of the cases). Exhaustive reviews on robust and stochastic MPC methods are respectively given by (Bemporad and Morari, 1999) and (Mesbah, 2016).

Nonlinear MPC Another important topic discussed during the second era of MPC was the employment of nonlinear models in the control framework, due to the fact that several problems in a realistic scenario present a nonlinear dynamics. If on one hand most of the stability results can be easily extended to constrained nonlinear MPC, on the other the research community had to cope with the high computational complexity that nonlinear optimizations exhibit in finding a global optimum. For this reason the research community focused in developing MPC formulations which rely on a suboptimal solution (see e.g (Mayne and Michalska, 1988)). Due to the fact that the control problems addressed in this chapter are based on nonlinear models, an example of nonlinear MPC algorithm is described in 4.1.2.

4.1.1.3 Third Period: Hybrid, Explicit and Fast MPC

The third era of MPC has seen its application in fields such as mechanical and electronic systems, which are substantially different from the petrochemical plants for which such control methodology has been developed in the early 1980s. This progress was possible due to the development of new algorithms able to cope with the need for a short sampling time. In particular, attention has been firstly devoted to hybrid systems, i.e. systems which can be modelled using both continuous dynamics and logical rules. For such models, mixed-integer programming (Floudas, 1995) appears to be a natural optimization approach. However, its exploitation within an on-line framework is limited by the prohibitive computational cost. For this reason, the research community focused on the development of faster algorithms. On one hand, the concept of explicit MPC has been proposed, which replaces the on-line optimization with a lookup table. This latter is obtained by storing the optimal control input resulting from the off-line solution of the constrained open-loop problem in different initial states (Bemporad et al., 2002). However, such approach is limited by the fact that the off-line computational complexity explodes with the increase of the prediction horizon, the states size and the constraints number, according to a phenomenon that Richard Bellman has defined *curse of dimensionality*. On the other hand, effort has been made in developing customized optimization algorithms in order to provide a speed up during the on-line solution of the open-loop problem. Such algorithms result to be order of magnitude faster than standard optimization methods (Rao, Wright, and Rawlings, 1998). The advantage of this approach compared to explicit MPC is the fact that both the weight parameters and the horizon length can be changed easily without the need of constructing a new lookup table every time.

4.1.1.4 Future of MPC

Among the several aspects of MPC discussed above, the ones related to robustness and stochasticity still lack of practical and efficient implementations, due to the difficulty of taking into account future feedback of uncertain models in the open-loop optimization. Dynamic programming (Bertsekas et al., 1995) has been considered in the past as a possible solution. However, DP is strongly limited by the aforementioned *curse of dimensionality* with respect to state and input size. The use of approximate dynamic programming (Powell, 2007) (see also Chapter 5 for further details), which belongs to the artificial intelligence field, can be used to properly address the aforementioned issues. In particular, the exploitation of ADP and data-driven methods within an MPC framework has received a lot of attention in recent years and appears to be one of the most appealing topics (Aswani et al., 2013; Lenz, Knepper, and Saxena, 2015; Limon, Calliess, and Maciejowski, 2017; Rosolia and Borrelli, 2017).

4.1.2 Adopted MPC Formulation

In the following, we describe the MPC formulation which has been adopted for solving the control problems addressed in this chapter. In particular, a very general framework is presented, in which a system of nonlinear Differential Algebraic Equations (DAEs) is considered as model for the control.

4.1.2.1 Nonlinear DAE System

Consider the continuous-time system of semi-explicit nonlinear DAEs described by

$$\dot{x}(t) = f(x(t), u(t), z(t)) \tag{4.7a}$$

$$0 = h(x(t), u(t), z(t)) \tag{4.7b}$$

$$y(t) = g(x(t), u(t), z(t)) \tag{4.7c}$$

where $t \in \mathbb{R}$ is the time, $x(t) \in \mathbb{R}^{N_x}$ is the state vector, $u(t) \in \mathbb{R}^{N_u}$ is the control input, $z(t) \in \mathbb{R}^{N_z}$ is the vector of the algebraic variables and $y(t) \in \mathbb{R}^{N_y}$ is the output. Moreover, $f : \mathbb{R}^{N_x} \times \mathbb{R}^{N_u} \times \mathbb{R}^{N_z} \to \mathbb{R}^{N_x}$ and $g : \mathbb{R}^{N_x} \times \mathbb{R}^{N_u} \times \mathbb{R}^{N_z} \to \mathbb{R}^{N_y}$ are the state and output functions, respectively, while $h : \mathbb{R}^{N_x} \times \mathbb{R}^{N_u} \times \mathbb{R}^{N_z} \to \mathbb{R}^{N_z}$ specifies the set of algebraic constraints. The system of DAEs in (4.7) is assumed to be index-1 (Campbell and Gear, 1995). Again, a digital controller is considered to apply a piecewise-constant input at the discrete times t_k, $k \in \mathbb{N}$ with sample time t_s. As in 4.1.1.2, the generic input sequence applied in the time interval $[t_k, t_{k+H}]$ is given by

$$\mathbf{u}_{[t_k, t_{k+H}]} = \left[u^\top(t_k),\, u^\top(t_{k+1}),\, \cdots, u^\top(t_{k+H-1})\right]^\top \tag{4.8}$$

while the corresponding temporal evolutions of states, algebraic variables, and outputs are obtained by integrating the equations in (4.7) over $[t_k, t_{k+H}]$, with initial condition $x(t_k) = x_k$, to give

$$\mathbf{x}_{[t_k, t_{k+H}]} = \left[x^\top(t_{k+1}),\, \cdots, x^\top(t_{k+H})\right]^\top \tag{4.9a}$$

$$\mathbf{z}_{[t_k, t_{k+H}]} = \left[z^\top(t_{k+1}),\, \cdots, z^\top(t_{k+H})\right]^\top \tag{4.9b}$$

$$\mathbf{y}_{[t_k, t_{k+H}]} = \left[y^\top(t_{k+1}),\, \cdots, y^\top(t_{k+H})\right]^\top \tag{4.9c}$$

Note that the particular case in which the model consists only of ordinary differential equations can be represented by removing the algebraic constraint (4.7b) and neglecting the variable $z(t)$.

4.1.2.2 Nonlinear MPC

This section summarizes the main features of nonlinear MPC, which is a control technique suitable for multivariable nonlinear systems, such as (4.7), in the presence of constraints. As for the linear MPC described in 4.1.1.2, at each time step t_{k_0} the nonlinear approach computes the optimal control sequence $\mathbf{u}^{\star}{}_{[t_{k_0},t_{k_0+H}]}$ as the solution of an optimization over a finite prediction horizon of H steps within a *receding-horizon* framework.

The resulting optimization to be solved at each time t_{k_0} is described below.

Finite-Horizon Optimal Control Problem 2 *Find the optimal input sequence* $\mathbf{u}^{\star}{}_{[t_{k_0},t_{k_0+H}]}$ *that solves*

$$\mathbf{u}^{\star}{}_{[t_{k_0},t_{k_0+H}]} = \arg\min_{\mathbf{u}_{[t_{k_0},t_{k_0+H}]}} J(x(t_{k_0})) \tag{4.10}$$

for the cost function

$$J(x(t_{k_0})) = j_t(x(t_{k+H})) + \sum_{k=k_0}^{k_0+H-1} j(x(t_k), u(t_k), z(t_k)) \tag{4.11}$$

in which $j : \mathbb{R}^{N_x} \times \mathbb{R}^{N_u} \times \mathbb{R}^{N_z} \to \mathbb{R}$ *and* $j_t : \mathbb{R}^{N_x} \to \mathbb{R}$*, where the latter represents the terminal penalty. Note that* $y(t_k) \in \mathbb{R}^{N_y}$ *is obtained by evaluating* (4.7c) *at discrete time instants* t_k*.*

The optimization is subject to the system dynamic in (4.7) *and the constraints*

$$\begin{aligned}
&u(t_k) \in \mathcal{U}, && k = k_0, k_0+1, \cdots, k_0+H-1 && \text{(4.12a)}\\
&x(t_k) \in \mathcal{X}, && k = k_0+1, k_0+1, \cdots, k_0+H-1 && \text{(4.12b)}\\
&z(t_k) \in \mathcal{Z}, && k = k_0+1, k_0+1, \cdots, k_0+H && \text{(4.12c)}\\
&y(t_k) \in \mathcal{Y}, && k = k_0+1, k_0+1, \cdots, k_0+H && \text{(4.12d)}\\
&x(t_{k_0+H}) \in \mathcal{X}_t && && \text{(4.12e)}\\
&g_{c,i}(x(t_k), u(t_k), z(t_k)) \leq 0, && i = 1, 2, \cdots, N_c && \text{(4.12f)}
\end{aligned}$$

where the sets $\mathcal{X}, \mathcal{U}, \mathcal{Z}, \mathcal{X}_t$ *are considered as box sets, such as for instance* $\mathcal{X} = \{x \in \mathbb{R}^{N_x} : x^{lb} \leq x \leq x^{ub}\}$*, with* $x^{lb}, x^{ub} \in \mathbb{R}^{N_x}$ *lower and upper bounds, respectively, and* $g_{c,i}$:

$\mathbb{R}^{N_x} \times \mathbb{R}^{N_u} \times \mathbb{R}^{N_z} \rightarrow \mathbb{R}$ *represents a generic nonlinear constraint, for* $i = 1, 2, \cdots, N_c$, *with* N_c *the total number of such constraints.*

4.2 Single-Cell Control

The model-based charging of a single lithium-ion cell has been addressed by many authors over the years. Within this context, different control approaches have been considered, such as fuzzy logic (Hsieh, Chen, and Huang, 2001; Wang and Liu, 2014), empirical rules (Purushothaman and Landau, 2006; Chen, Hsu, and Liu, 2008), and optimization-based strategies (Klein et al., 2011; Moura, Chaturvedi, and Krstić, 2013; Xavier and Trimboli, 2015; Torchio et al., 2015; Romagnoli et al., 2017). Model-predictive control appears to be the most used optimization-based methodology (Klein et al., 2011; Xavier and Trimboli, 2015; Torchio et al., 2015; Yan et al., 2011b; Torchio et al., 2016c; Torchio et al., 2017; Zou et al., 2017), in order to minimize the charging time while satisfying temperature and voltage constraints.

In this section, focus is devoted to the exploitation of MPC strategies for single-cell control oriented to energy saving (see 4.2.1) and ageing reduction (see 4.2.2), that have been little investigated in the literature. In particular, the validity of model-based control in order to achieve the aforementioned goals is assessed in comparison with standard methodologies.

4.2.1 Energy-Aware Charging Strategy

In the following, we focus on model-based minimization of energy losses during the charging of a lithium-ion cell (Pozzi, Torchio, and Raimondo, 2018a). Such losses are sources of heat generation inside the cell which, together with the consequent high temperature, leads to a faster cell degradation. For this reason, energy losses minimization is fundamental in order to improve battery performance. In particular, the objective of this section is to assess if existing models are appropriate for this goal. We first consider time-domain MPC, which has been adopted in the context of advanced BMS in many works, but without tackling the energy losses reduction. We employ, for control purposes, a nonlinear equivalent-circuit model, similar to the one described in 2.4.1.1, in combination with an Extended Kalman Filter (EKF)

(Welch, Bishop, et al., 1995). Results evaluated on the P2D model, which is considered as the real battery, suggest that only negligible improvements can be achieved. While time-domain optimization does not seem to be suitable for our purpose, previous experimental works, such as the ones in (Chen, Wu, and Chen, 2010; Chen et al., 2012a), show that a sinusoidal current input can lead to a less dissipative charging strategy. A theoretical justification to such results is provided in (Hussein, Fardoun, and Stephen, 2017), where a linear inductive ECM is considered. In particular, the authors propose a method to track the frequency that minimizes the battery impedance and claim that by charging the battery at such frequency it is possible to obtain optimal energy losses reduction. Inspired by the work in (Hussein, Fardoun, and Stephen, 2017), we provide a detailed theoretical analysis on the same linear inductive ECM. Specifically, we show that, when the objective is to attain a desired SOC at the end of charge, no reasonable sinusoidal charging strategy can result in energy saving improvements on such a linear model. Our analysis highlights the need for further research on battery modelling in order to better capture phenomena which have been exhibited in practice. This is a necessary step in order to make advanced BMSs more reliable and effective.

4.2.1.1 Time-Domain MPC

The aim of this section is to assess whether an MPC approach could reduce power losses during cell charging when compared to a Constant-Current (CC) profile which is considered as a benchmark. In order to make the comparison fair, we aim to fix the charging time of the optimization-based strategy to the one of a reference standard protocol. In order to achieve this goal, we develop an MPC formulation which is based on the concept a *shrinking horizon* rather than the *receding* one that is the horizon window is fixed and not shifted at each time step of the controller synthesis problem. In particular, we start with an initial prediction horizon which corresponds to the charging time t_{cc} of the CC benchmark, thus ensuring the existence of a current profile able to attain the target state of charge at the end of the horizon. Then, the optimal control sequence for the horizon is computed and the first step is applied. After observing the system evolution, the process is repeated, by decreasing the prediction horizon by 1 at each time step, until until charging is complete (Farahani et al., 2017).

Cell Model and Parameters In the following, the real plant is considered to be a numerical implementation of P2D model, obtained from the equations presented in 2.4.2.1 with the exception that the thermal and ageing dynamics are neglected. On the other hand, a nonlinear ECM similar to the one in 2.4.1.1 is used as the control model within an MPC framework due to its lower computational burden. Such ECM in particular, exhibits only one RC block (i.e. $V_{rc2}(t) = 0$) and neglects thermal and ageing dynamics, while its OCP is modelled through a high-order polynomial.

The P2D parameters as well as the open-circuit potential and electrolyte conductivity functions are taken as in (Torchio et al., 2016b), while the ones of the ECM are instead identified from the voltage measurements collected by performing virtual experiments with the P2D simulator. The parameter identification for the ECM is conducted through the System Identification Toolbox of MATLAB with a training dataset similar to the one adopted in (Thanagasundram et al., 2012). In particular, a train of impulses, each of them followed by a resting period, is applied as input in order to completely charge and discharge the cell, thus allowing to collect measurements over a wide range of SOC values. The identification data as well as the validation process are shown in Figure 4.2.

Optimization Problem The energy-saving optimal charging problem can be recasted into the MPC framework described in 4.1.2, by substituting the *receding-horizon* concept with the *shrinking* one and representing the proposed ECM as set of ODEs (expressed through (4.7) without considering (4.7b)). In particular, defining the model input as the applied current $u(t) = I_{app}(t)$, the states vector as

$$x(t) = [SOC(t),\, V_{rc1}(t)]^\top \tag{4.13}$$

and the dissipated power as

$$P_{diss}(t) = I_{app}(t)(V_{rc1}(t) + R_{sei} I_{app}(t)) \tag{4.14}$$

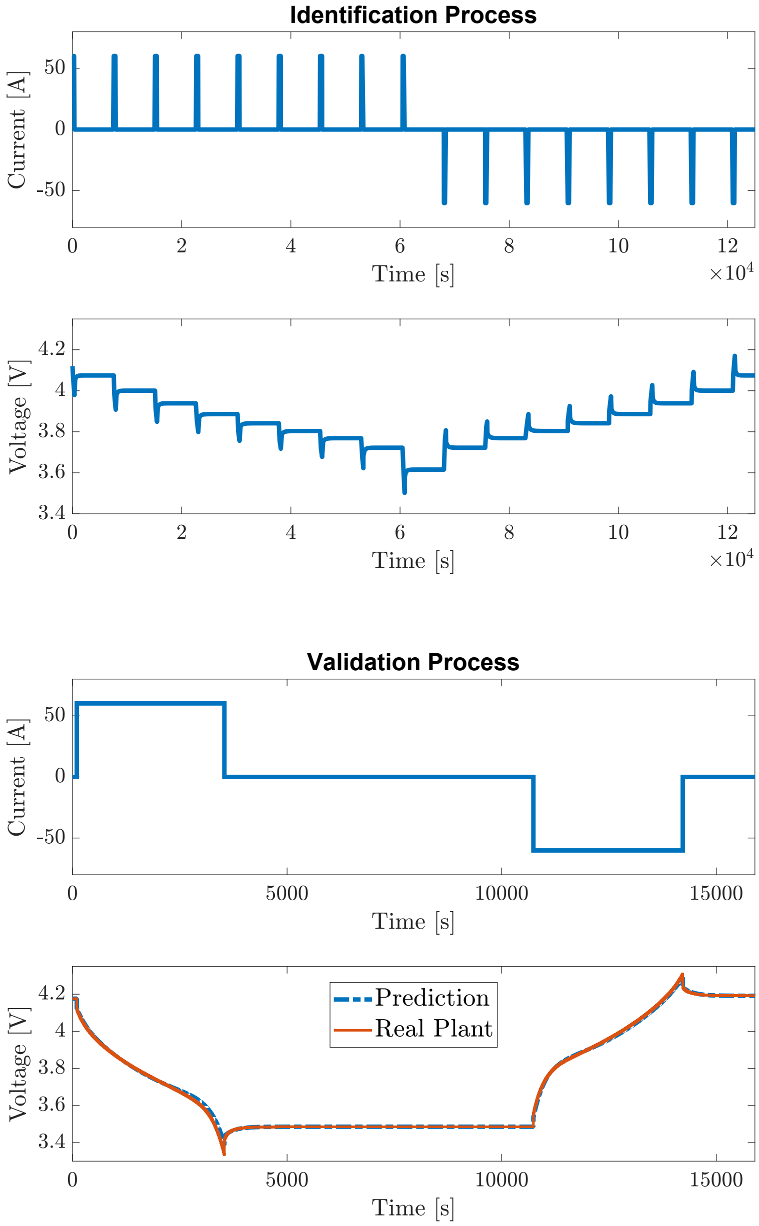

FIGURE 4.2: Identification and validation data set. The fitting performance (97.74%) is evaluated according to the normalized root-mean-square error in percentage. In the validation plot, the collected voltage measurements are depicted in red while the predicted ones are in blue.

one can express the cost function in (4.11) as

$$J(x(t_{k_0})) = \sum_{k=k_0+1}^{k_0+H} t_s P_{diss}(t_k) \tag{4.15}$$

while the constraints in (4.12) are represented by

$$I_{min} \leq I_{app}(t_k) \leq I_{max}, \qquad k = k_0, k_0+1, \cdots, k_0+H-1 \tag{4.16a}$$

$$SOC_{min} \leq SOC(t_k) \leq SOC_{max}, \quad k = k_0, k_0+1, \cdots, k_0+H \tag{4.16b}$$

$$SOC(t_{k_0+H}) = SOC_{ref} \tag{4.16c}$$

$$x(t_{k_0}) = x_0 \tag{4.16d}$$

where the horizon H at the first step has been chosen in order to satisfy $t_{cc} = Ht_s$, where t_{cc} is the time that a standard approach with constant current I_{cc} employs to reach a reference state of charge SOC_{ref} from the considered initial condition x_0. Note that the horizon H is decreased by 1 at each sample time according to the *shrinking-horizon* principle. The optimization above is a nonlinear program and can be solved using, e.g. *CasADi*, an open-source tool, fully compatible with MATLAB, which provides a symbolic framework for automatic differentiation and nonlinear numerical optimization algorithms.

Note that here we assume that the only available measurements are terminal voltage and SOC. This latter can be considered measurable if an initial condition is provided (e.g. with a lookup table OCP-SOC) and assuming that coulomb counting is accurate (i.e. in absence of *faradaic losses*). Therefore, the state $V_{rc1}(t)$ is not directly available. However, due to the fact that MPC relies on the state-feedback concept, an estimation of $V_{rc1}(t)$ is needed in order to provide a proper implementation. Considering the nonlinearity of the open-circuit potential expression, an extended Kalman filter is here adopted. Assuming that measurements/inputs are obtained/applied via digital processors at discrete time instants, a continuous-time EKF with discrete-time measurements appears to be the most suitable for the considered problem. Note that the development of such observer has been conducted with the aim of giving the reader an insight about the possibility of estimating the non-measurable states. The development of a more involved observer and its coupling with the presented control system goes beyond the scope of this section.

Simulation Results In the following, the optimal charging protocol, designed in the time domain, and the standard CC one are compared in terms of energy dissipation during the charging process. Both algorithms start with the cell at rest and with a state of charge of $SOC(t_0) = 0.05$. The state-of-charge reference is set as $SOC_{ref} = 0.735$, and the time needed by the CC approach with $I_{cc} = -60A$ to achieve the target SOC from the considered initial condition is $t_{cc} = 3000s$. The limits on current and state of charge are given as $I_{min} = -80A$, $I_{max} = 0$, $SOC_{min} = 0.1$ and $SOC_{max} = 0.9$. The sampling time is chosen as $t_s = 50s$.

Figure 4.3 reports the comparison between the CC protocol and the MPC-based when the P2D model is considered as the real battery. The latter approach shows a peak of current at the start and at the end of the charging, in a way that most of the current flows through the capacity in the RC block, thus reducing ohmic dissipation.

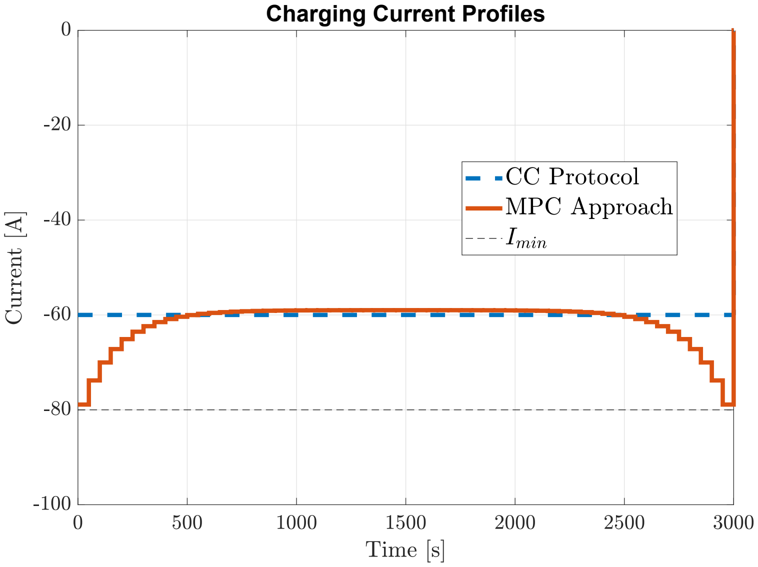

FIGURE 4.3: Constant-current and optimization-based charging current profiles.

Although the current profiles are very different, the reduction of the total energy given to the cell during a single charge by the optimization-based protocol is limited

(0.008%). Actually the reduction of energy dissipation is larger (0.5%), if one considers only energy losses, because most of the energy given to the battery during a charge is straightly accumulated while only power losses are sources of heat generation. Such a negligible improvement does not justify the practical implementation of this strategy. For this reason, also motivated by successful experiments reported in literature, in the following a frequency-domain approach is considered.

4.2.1.2 Frequency-Domain Optimization

Previous experimental works ((Chen, Wu, and Chen, 2010), (Chen et al., 2012b)) indicate that energy loss reduction can be achieved by using a sinusoidal charging strategy. Such a strategy, rather than exploiting a constant input profile I_{cc} (which corresponds to the constant current of the CC protocol), applies a negative DC-shifted sinusoidal current profile in order to reach a desired state of charge

$$I_{app}(t) = -I_{cc}(1 + \sin(\omega t)) \tag{4.17}$$

where $\omega = 2\pi f$, with f the frequency of the sinusoidal component. While the approach used in practice has been successful, it is based on impedance magnitude minimization only. A more theoretical analysis is conducted in (Hussein, Fardoun, and Stephen, 2017) on such linear inductive ECM in Figure 4.4, where the authors assume that the minimum impedance frequency is also the optimal charging frequency in terms of energy efficiency. In the following, we provide a detailed theoretical analysis on the linear inductive ECM in order to assess in which cases the assumption in (Hussein, Fardoun, and Stephen, 2017) is valid. This is investigated by formulating a frequency-domain optimization problem.

Analysis of the Linear Inductive ECM In order to improve energy efficiency, the real power dissipated on the series impedance must be minimized. Considering $V_z(t)$ the voltage drop over such impedance, the goal can be achieved by posing the

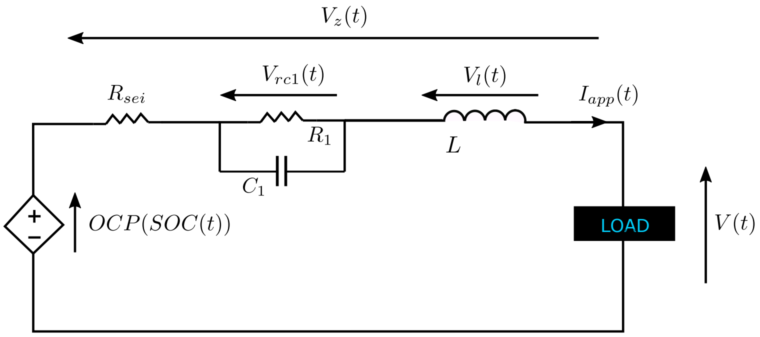

FIGURE 4.4: Equivalent circuit model with inductance.

following optimization problem

$$\min_{\omega} \int_{t_0}^{t_0+t_{cc}} V_z(t) I_{app}(t)\, dt \tag{4.18a}$$

$$\text{s. t.} \quad \text{model dynamics (4.19)} \tag{4.18b}$$

$$SOC(t_0 + t_{cc}) = SOC_{ref} \tag{4.18c}$$

$$\omega_{min} \leq \omega \leq \omega_{max} \tag{4.18d}$$

where t_0 is the starting time, t_{cc} the time required by a standard CC protocol to reach the target state of charge SOC_{ref}. Note that (4.18c) requires that the charging time of the sinusoidal profile coincides with the one of the CC scheme. The bounds ω_{min} and ω_{max} limit the search space for the optimal frequency. Note that (4.19) represents the transfer function between the voltage drop $V_z(t)$ on the series of eddy elements and the applied input current, i.e. the electrochemical impedance, as follows

$$Z(s) = sL + \frac{R_1}{1 + sR_1C_1} + R_{sei} \tag{4.19}$$

where s is the Laplace variable.

In the following, we aim to compute the real power on the series impedance as a function of the frequency of the DC-shifted sinusoidal input. The frequency at which the imaginary part of the impedance is equal to zero (i.e. the resonant frequency) is

$$\omega_{res} = \sqrt{\frac{C_1R_1^2 - L}{LC_1^2R_1^2}} \tag{4.20}$$

while the minimum impedance frequency is given by solving $\frac{dZ(\omega)}{d\omega} = 0$, as described in details in (Chen et al., 2012b). The Laplace transform of the input signal (4.17) is

$$I_{app}(s) = -I_{cc}\left(\frac{1}{s} + \frac{\omega}{s^2+\omega^2}\right) \tag{4.21}$$

while the Laplace transform of the voltage drop $V_z(t)$ is given by

$$V_z(s) = Z(s)I_{app}(s) \tag{4.22}$$

where $Z(s)$ is the system transfer function in (4.19).

Using the Heaviside method for the inverse Laplace transform, one can obtain the voltage drop in the time domain

$$V_z(t) = \overline{V}_z(t) + \tilde{V}_z(t,\omega) \tag{4.23}$$

where $\overline{V}_z(t)$ and $\tilde{V}_z(t,\omega)$ represent, respectively, the DC and the sinusoidal components of the output. The DC term is given by

$$\overline{V}_z(t) = -(R_{sei} + R_1)I_{cc} + \overline{V}_{z,trans}(t) \tag{4.24}$$

with

$$\overline{V}_{z,trans}(t) = -I_{cc}\left(L\delta_{t_0}(t) - R_1 e^{-\frac{t}{\tau}}\right) \tag{4.25}$$

where $\delta_{t_0}(t)$ is the *Dirac delta function* (i.e. $\delta_{t_0}(t_0) = 1$ and $\delta_{t_0}(t) = 0,\ \forall t \neq t_0$) and $\tau = R_1C_1$. The sinusoidal component is defined as

$$\tilde{V}_z(t,\omega) = -|Z(\omega)|I_{cc}\sin(\omega t + \underline{/Z}(\omega)) + \tilde{V}_{z,trans}(t,\omega) \tag{4.26}$$

with

$$\tilde{V}_{z,trans}(t,\omega) = -\omega\frac{C_1R_1^2I_{cc}}{1+(C_1R_1\omega)^2}e^{-\frac{t}{\tau}} \tag{4.27}$$

By substituting (4.17) and (4.23) into (4.18a), the optimization problem can be rewritten as follows

$$\min_{\omega} \left(E_{cc} + P(\omega)t_{cc} + \tilde{E}_{trans}(\omega) + \overline{E}_{trans}(\omega) \right) \tag{4.28}$$

where $E_{cc} = -\int_{t_0}^{t_0+t_{cc}} \overline{V}_z(t) I_{cc}\, dt$ is the energy dissipation of the CC protocol, $P(\omega) = 0.5|Z(\omega)|I_{cc}^2 \cos(\underline{/Z}(\omega))$ is the real power loss due to the sinusoidal current effect, and

$$\tilde{E}_{trans}(\omega) = \int_{t_0}^{t_0+t_{cc}} \tilde{V}_{z,trans}(t) I_{app}(t)\, dt \tag{4.29a}$$

$$\overline{E}_{trans}(\omega) = -\int_{t_0}^{t_0+t_{cc}} \overline{V}_{z,trans}(t) I_{cc} \sin(\omega t)\, dt \tag{4.29b}$$

are the energy losses during the transient. The optimization problem in (4.28) was obtained taking into account that, if $t_{cc} = mT$, with $m \in \mathbb{N}$, and $T = \frac{2\pi}{\omega}$ period of the sinusoidal signal, one has

$$\int_{t_0}^{t_0+t_{cc}} (R_0 + R_1) I_{cc}^2 \sin(\omega t)\, dt = 0 \tag{4.30a}$$

$$\int_{t_0}^{t_0+t_{cc}} |Z(\omega)| I_{cc}^2 \sin(\omega t + \underline{/Z}(\omega))\, dt = 0 \tag{4.30b}$$

In the following, we aim to determine for which values of the charging time t_{cc} the energy dissipated by an optimal DC-shifted sinusoidal charging protocol is actually higher than the one wasted by a CC protocol, i.e.

$$E_{cc} \le \min_{\omega} \left(E_{cc} + P(\omega)t_{cc} + \tilde{E}_{trans}(\omega) + \overline{E}_{trans}(\omega) \right) \tag{4.31}$$

Since $\tilde{V}_{z,trans}(t,\omega) \le 0$ for all $\omega, t \in \mathbb{R}$ and $I_{app}(t) \le 0, \forall t \in \mathbb{R}$ it holds that

$$\tilde{E}_{trans}(\omega) \ge 0, \qquad \forall \omega \in \mathbb{R}. \tag{4.32}$$

Moreover, by substituting (4.25) into (4.29b), and taking into account that

$$\int_{t_0}^{t_0+t_{cc}} L I_{cc}^2 \delta_{t_0}(t) \sin(\omega t)\, dt = L I_{cc}^2 sin(wt_0) \tag{4.33}$$

one has that

$$\overline{E}_{trans}(\omega) = LI_{cc}^2 sin(wt_0) - \int_{t_0}^{t_0+t_{cc}} R_1 I_{cc}^2 \sin(\omega t) e^{-\frac{t}{\tau}}\, dt \tag{4.34}$$

It can be noticed that $\overline{E}_{trans}(\omega)$ is the only term in (4.28) which might be negative. Therefore, in order to assess that the condition in (4.31) holds for a charging time t_{cc}, it is enough to show that,

$$P(\omega)t_{cc} + \overline{E}_{trans}(\omega) \geq 0, \forall \omega \in \mathbb{R} \tag{4.35}$$

that is

$$\min_{\omega} \left(P(\omega)t_{cc} + \overline{E}_{trans}(\omega) \right) \geq 0 \tag{4.36}$$

A lower bound on $\overline{E}_{trans}(\omega)$ is given by

$$\begin{aligned} \overline{E}_{trans}^{lb}(\omega) &= - LI_{cc}^2 - \textstyle\int_0^{+\infty} R_1 I_{cc}^2 \sin(\omega t) e^{-\frac{t}{\tau}}\, dt \\ &= - LI_{cc}^2 - R_1 I_{cc}^2 \frac{\omega\tau^2}{1+(\omega\tau)^2} \end{aligned} \tag{4.37}$$

in the case in which $\sin(\omega t_0) = -1$. The minimum of this latter with respect to ω is

$$\min_{\omega} \overline{E}_{trans}^{lb}(\omega) = -LI_{cc}^2 - \frac{1}{2} R_1 I_{cc}^2 \tau, \quad \omega = \frac{1}{\tau} \tag{4.38}$$

On the other side, since $P(\omega) = \frac{1}{2} I_{cc}^2 (R_{sei} + \frac{R_1}{1+(\omega R_1 C_1)^2})$, its minimum is

$$\min_{\omega} P(\omega) \quad = \quad \frac{1}{2} R_{sei} I_{cc}^2, \qquad \omega \to +\infty \tag{4.39}$$

By using the lower bounds (4.37) and (4.39) in equation (4.36), one concludes that a DC-shifted sinusoidal protocol is not better than a CC protocol in terms of energy reduction if

$$t_{cc} \geq \frac{1}{R_{sei}} (2L + R_1 \tau) \tag{4.40}$$

Considering the parameters in (Hussein, Fardoun, and Stephen, 2017), with $\tau =$

$0.8ms$, the condition in (4.40) is verified for each charging time $t_{cc} \geq 0.49ms$. If the parameters of the RC block are instead taken from (Xavier and Trimboli, 2015), where the value $\tau = 166.9s$ is more realistic, the condition (4.40) is verified for any $t_{cc} \geq 213.7s$. Due to the fact that the usual charging time for a lithium-ion cell is around one hour (i.e. $3600s$), we conclude that, for the considered linear inductive ECM, the use of a DC-shifted sinusoidal input does not lead to any energy savings with respect to a benchmark CC protocol.

Discussion of the Results In order to understand why our theoretical results differ from what discussed in (Hussein, Fardoun, and Stephen, 2017), one has to consider that in that work the authors assumed the charge completed when the cell voltage $V(t)$ reached a given threshold V_{th}. However, in this way, the DC-shifted sinusoidal approach and the CC protocol lead to different final SOC values. Therefore, the dissipation reduction highlighted in (Hussein, Fardoun, and Stephen, 2017) is attributable to the attainment of a lower SOC value, which strongly depends on the choice of V_{th}.

4.2.1.3 Conclusion to Energy-Aware Charging

The aim of an advanced BMS is to optimize battery performance, using a suitable model for the control. In this section we focused on the energy loss reduction when using model-based optimization in the time- and in the frequency-domain. The conducted analysis has highlighted that a time-domain optimization can lead only to negligible improvements when evaluated on the P2D model. Therefore, motivated by successful experiments, the possibility of a frequency-domain optimization has also been discussed. Still, our analysis on a simplified model fails to show any advantage in terms of energy loss reduction when using a sinusoidal charging current profile. The conclusion of our work is that more-detailed models are required in order to optimize energy losses through a model-based advanced BMS.

4.2.2 Ageing-Aware Charging Strategy

Today's charging strategies are designed to guarantee safe operation in a conservative way, but are far from being optimal in terms of ageing reduction and time charging minimization. The CC-CV protocol for instance provides reasonable performance, but, being based on conservative voltage limits, it is not able to account for battery changes with the ageing degradation. Despite over the years considerable predictive control strategies have been proposed as advanced battery management systems (Yan et al., 2011a; Torchio et al., 2015; Xavier and Trimboli, 2015), only few of them have focused on ageing reduction (Klein et al., 2011; Moura et al., 2010a; Torchio et al., 2016a; Lucia et al., 2017). Such approaches, however, obtain an ageing reduction to the detriment of the charging duration. Indeed, with a less aggressive charging strategy, it is straightforward to extend the battery lifetime. In general, comparing standard charging strategies with health-aware ones is difficult since they usually provide different charging times: are we willing to charge the battery in more time if this comes with an ageing reduction? When a customer is faced with such a question, the answer is not so trivial.

For all these reasons, in the following we discuss the use of an optimization-based battery management strategy which constrains the charging time to be the same as the CC-CV protocol, which is taken as benchmark. This peculiarity allows a fair comparison in terms of ageing reduction over a whole charging procedure. Furthermore, in order to guarantee safe operation, we consider the possibility of imposing a constraint on the plating-side-reaction overpotential in order to substitute the more conservative voltage limits. The results emphasize the significant ageing effects reduction for the same charging time, especially in terms of SEI layer thickness growing, for both the case of a constraint on the voltage and on the lithium plating (Pozzi, Torchio, and Raimondo, 2018b).

4.2.2.1 Cell Model and Parameters

In this section the real plant is represented by the P2D model described in 2.4.2.1, which is numerically implemented in the LIONSIMBA simulator. The same model is also exploited within the MPC framework as model for the control. The electrochemical parameters are taken as in (Torchio et al., 2016b), while the ones related to ageing are chosen as in (Torchio et al., 2016a). Note that the use of a detailed nonlinear model consisting of DAEs within an optimal control framework is not common in the battery field due to its high computational burden. The exploitation of an

MPC algorithm which relies on the P2D in order to achieve better performance is made possible thanks to a suitable space and temporal discretization, where finite volume method and direct collocation approach (Magnusson and Åkesson, 2012) are adopted, respectively.

4.2.2.2 MPC for Ageing-Aware Battery Charging

The proposed optimization framework is similar to the one discussed in 4.2.1.1, in the sense that also in this case the concept of *shrinking horizon* is adopted in order to allow a fair comparison with a standard protocol, but instead of energy minimization the focus is oriented to ageing reduction. In particular, a benchmark CC-CV algorithm (with constant current I_{cc} and voltage threshold V_{cv}) is firstly simulated on LIONSIMBA and the resulting charging time t_{cccv} is determined. This latter information is then used within the MPC framework.

Ageing-Aware MPC As previously discussed, in this section we rely on an MPC approach in order to find a current profile able to charge the battery in a fixed time while minimizing ageing phenomena and satisfying safety constraints. The optimal control problem to be solved at each time instant is here formulated as described in 4.1.2, with the exception that the *shrinking-horizon* paradigm is considered. In particular, the P2D equations are represented through (4.7), where $x(t)$ and $z(t)$ are the vectors of differential and algebraic states, respectively, while $u(t) = I_{app}(t)$ is the control input. The cost function can be expressed as in (4.11)

$$J(x(t_{k_0})) = \bar{R}_{sei}(t_{k_0+H}) + \sum_{k=k_0+1}^{k_0+H} \gamma \left[(SOC(t_k) - SOC_{ref})^2 + u(t_k)^2 \right] \tag{4.41}$$

where the first term represent the ageing factor that we aim to minimize, while the second one consists of a regularization term in order to improve the solver efficiency (a small weight is therefore chosen, $\gamma = 10^{-4}$). Note that $\bar{R}_{sei}(t_k)$ is the mean of the SEI resistance along the spatial dimension. The constraints in (4.12) are represented by

$$I_{min} \leq I_{app}(t_k) \leq I_{max}, \quad k = k_0, k_0+1, \cdots, k_0+H-1 \tag{4.42a}$$

$$T_M(t_k) \leq T_{max}, \quad k = k_0, k_0+1, \cdots, k_0+H \tag{4.42b}$$

$$V(t_k) \leq V_{max}, \quad k = k_0, k_0+1, \cdots, k_0+H \tag{4.42c}$$

$$SOC_{min} \leq SOC(t_k) \leq SOC_{max}, \quad k = k_0, k_0+1, \cdots, k_0+H \tag{4.42d}$$

$$SOC(t_{k_0+H}) = SOC_{ref} \tag{4.42e}$$

where the horizon H at the first step has been chosen in order to satisfy $t_{cccv} = Ht_s$, where t_{cccv} is the time that the benchmark CC-CV protocol needs to achieve a reference state-of-charge SOC_{ref}, and it is decreased by 1 at each sample time. The variable $T_M(t_k)$ corresponds to the maximum value that the temperature exhibits along the spatial dimension. Note that, the limits on the input current (4.42a), as well as the thermal (4.42b), voltage (4.42c) and state-of-charge constraints (4.42d), guarantee safe operation. The reaching of the reference SOC in the desired charging time is imposed by (4.42e).

The above formulation leads to a large-scale sparse nonlinear program which is solved by IPOPT (Wächter and Biegler, 2006), using the solver *ma27*. Due to the nonlinearities in the problem formulation, only a local minimum can be achieved. The exact derivatives are computed using CasADi (Andersson et al., 2019), whose automatic differentiation capability is essential for the efficient solution of the problem. In order to further improve the solver efficiency, a scaling procedure for all the model variables is performed. After the computation of the optimal control inputs, the battery charging procedure is simulated with LIONSIMBA, so to evaluate the effectiveness of the proposed strategy on a realistic simulator and comparing it with a standard CC-CV protocol.

Before presenting the obtained results, in the following paragraph we consider also the possibility of replacing the voltage constraints (4.42c) with a less conservative one in order to further improve the performance of the proposed methodology.

Constraint to Avoid Lithium-Ion Plating Deposition Terminal voltage limits avoid regimes in which undesirable side reactions become significant (Chaturvedi et al., 2010). Among them, one of the most important is the lithium-plating deposition, which takes place in the anode when the corresponding overpotential becomes negative (Arora, Doyle, and White, 1999) (see 2.2.1). Despite the voltage bounds are chosen to be conservative, standard charging operations with aged batteries might be dangerous anyway, due to the change over time of physical parameters. For this reason, it is of interest to directly constrain the plating-side-reaction overpotential to be positive as follows

$$\min_{x} \eta_{n,pl}^{side}(x, t_k) > 0 \tag{4.43}$$

where, with slight abuse of notation, x in this case represents the spatial dimension and not the state vector. Such constraint corresponds to the one defined in (2.39), which is also needed for guaranteeing that the adopted model for the SEI resistance growth is meaningful.

4.2.2.3 Simulation Results

The two optimal protocols discussed above, based on voltage and plating constraints respectively, are here compared with a benchmark CC-CV approach. For all the simulations, the battery cell is in a rest initial condition, with state of charge of 0.10, and the target SOC is chosen as $\mathrm{SOC}_{\mathrm{ref}} = 0.74$. The CC-CV approach is characterized by $I_{\mathrm{cc}} = -1.20 I_{1\mathrm{C}}$ and $V_{\mathrm{cv}} = 4.07\,V$, and exhibits a charging time $t_{cccv} = 3000s$, where the 1C-rate current is $I_{1\mathrm{C}} = 60A$. The sampling time is chosen as $t_s = 100s$. For all the optimization-based strategies the applied current density has been bounded within $I_{\min} = -2I_{1\mathrm{C}}$ and $I_{\max} = 0$, while the maximum temperature allowed inside the cell is $T_{max} = 320K$. The main features of the different simulations are summarized in Table 4.1 while the variables profiles are depicted in Figure 4.5.

Results with Voltage Constraint In the following, the potentiostatic threshold in the CC-CV algorithm is considered as the voltage bound in the MPC framework, i.e. $V_{\max} = V_{\mathrm{cv}}$. It can be noticed that the more significant variations introduced by the optimization-based strategy lie in the charging regimes in which the voltage

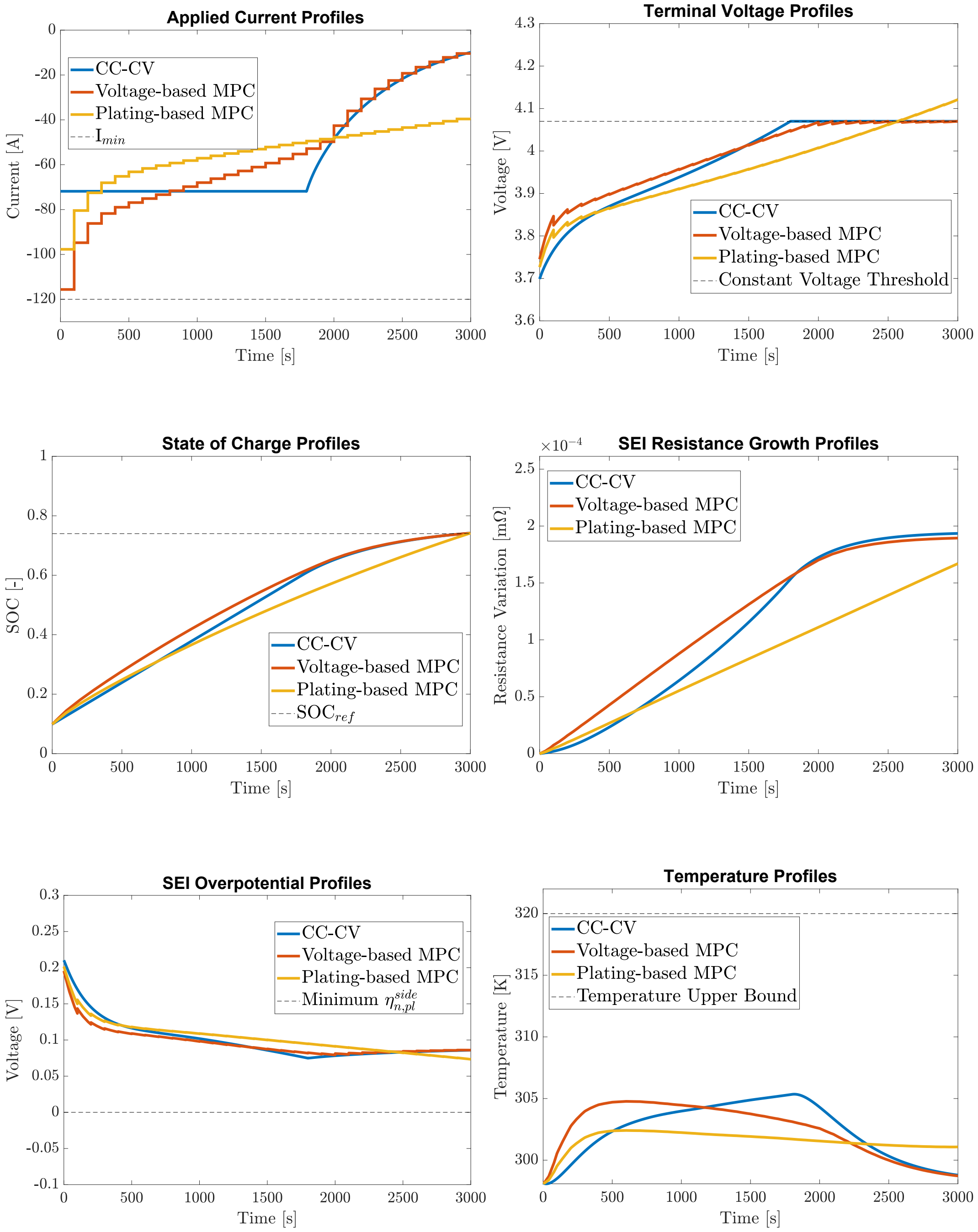

FIGURE 4.5: Input and states evolution of the cell battery due to CC-CV protocol and optimization-based strategies.

	CC-CV	Voltage-based MPC	Plating-based MPC
Max. voltage $[V]$	4.07	4.07	4.12
Max. temperature $[K]$	305.35	304.77	302.41
Min. plating potential $[V]$	0.0749	0.0793	0.0734
Max. current module $[A]$	72	115.2	97.2
$\Delta\bar{R}_{sei}(t_k)$ $[\%]$	-	-2.11%	-13.71%

TABLE 4.1: Main features of different charging protocols. In particular, the $\Delta\bar{R}_{sei}(t_k)$ indicates the reduction of SEI resistance that the MPC-based algorithms achive at the end of the charge with respect to the CC-CV.

constraint is not active (i.e. $t_k < 2000s$). For $t_k \geq 2000s$ the state evolution follows the CC-CV one. However, despite the higher absolute value of the applied current, the optimization-based strategy leads to a 2.11% reduction of the spatial mean of film thickness at the end of the charging procedure, with a reduction of the achieved maximum temperature of $0.58K$. Furthermore the maximum voltage and the minimum plating-side-reaction overpotential reached are the same of the CC-CV protocol, because of the voltage constraint.

Results with Plating Constraint The solution of the optimization problem by substituting (4.42c) with (4.43) in its formulation, leads to a completely different state evolution than the CC-CV standard charging protocol, with benefits from every point of view in terms of aging:

1. the spatial mean of the SEI resistance at the end of the charging procedure is reduced by about 13.71%;
2. the maximum temperature is reduced by about $3K$;

Furthermore the raising of the voltage over the maximum value reached by the CC-CV protocol does not degrade battery performance since the plating-side-reaction overpotential is far away enough from critical value for lithium-plating deposition, being positive during the whole charging procedure. One of the most important aspects emerging from the optimal solution with plating constraint is the linear growth of SEI resistance, that seems to be the key point in its reduction. At the same time this can be noticed in the side reaction flux profile (see Figure 4.6), that the plating-based strategy tries to keep as constant as possible, carrying out a sort of hysteresis control around a fixed value.

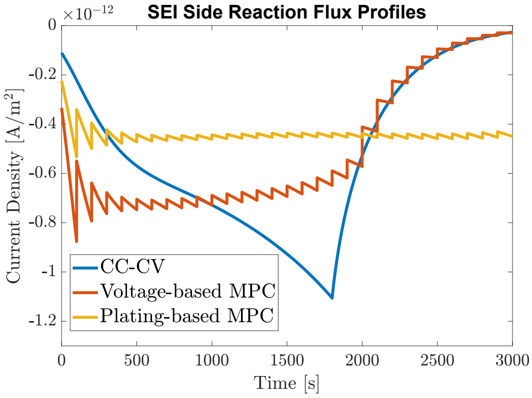

FIGURE 4.6: Side reaction flux profiles.

Finally, we can state that better results can be obtained increasing the number of control variables, due to the fact that this leads to a control law which smaller sampling time. However this would increase the computational cost and the average time to get a feasible solution. Using $t_s = 100s$ the time needed to solve the problem with plating overpotential constraint is $5s$ in average. However with $t_s = 50s$ the time needed to solve the problem raises to $50s$ in average, that might be challenging for an online closed-loop solution of the problem. The simulations have been performed on an Ubuntu 17.04 machine with 4Gbytes of RAM and i5vPro processor 2.5 GHz.

4.2.2.4 Conclusion to Ageing-Aware Charging

To the best of our knowledge, all the existing health-aware model-based charging strategies follow a trivial approach to reduce ageing, that is by increasing the charging time. In order to ease the user in the choice of an optimal charging procedure and make a fair comparison with standard charging protocols, the charging time has been kept equal to the CC-CV one, while a significant ageing-effects minimization is shown. For this reason the prediction horizon has to cover the whole charging procedure, increasing computational burden. Although automatic differentiation increases the efficiency of the problem solution, the implementation of an optimal state-feedback control law, using such a complex electrochemical model, still remains a critical aspect. Future work includes the design of a suitable observer for the considered electrochemical model, in order to relax the assumptions of measurable states, and experimental validation of the proposed optimization-based charging strategy.

4.3 Multiple-Cell Control

Batteries composed of several cells are necessary in many applications, such as hybrid electric vehicles. However, most of the available literature which tackles optimal charging of battery packs relies on very simple lumped ECMs (see e.g. (Liu and Peng, 2008; Moura et al., 2010a)). Few works tackle the optimal control of lithium-ion batteries by directly modelling each cell individually. This level of detail is necessary in important tasks such as the model-based state-of-charge balancing of series-connected cells (Einhorn, Roessler, and Fleig, 2011; Danielson et al., 2012), where most of the published works rely on linear ECMs for each cell. Although these latter allow for a real-time implementation even in the case of a high number of cells, the resulting control law may exhibit suboptimal performance due to the lack of accuracy of the employed model. The use of electrochemical models within a control framework would be a possibility, but it comes at the price of a prohibitive computational cost. As a compromise, the use of linearized electrochemical models seems promising in order to achieve high performance with a reasonable computational load.

In the following, we firstly describe a generic battery pack model in 4.3.1, while the issue of state-of-charge unbalance for series-connected cells is tackled in 4.3.2, where a simplified electrochemical model is employed within a nonlinear MPC framework with the aim of achieving both fast charging and SOC balancing, while mitigating degradation phenomena. Note that, while the SOC balancing would have been performed by relying only on an equivalent-circuit model, the use of an electrochemical one is here required to include ageing reduction in the balancing framework. Then, the case of a whole battery pack with both series and parallel arrangements is considered in 4.3.3, where a suitable model linearization around a nominal trajectory is proposed in order to reduce the computational cost.

4.3.1 Battery Pack Model

In this subsection we consider a battery pack with N series-connected modules, each of which is constituted of M parallel-connected cells, as in Figure 4.7, for a total cells number of $N_{cells} = NM$. We introduce the notation of referring to the j-th cell of the i-th module through the indexes $i = 1, 2, \dots, N$ and $j = 1, 2, \dots, M$. Moreover, the voltage, state of charge and temperature of the cells are indicated respectively by $V_{i,j}(t)$, $SOC_{i,j}(t)$ and $T_{i,j}(t)$, while we simplify the notation for the applied currents $I_{app,i,j}(t)$ by writing $I_{i,j}(t) = I_{app,i,j}(t)$. Finally, the voltage of the i-th module is defined as $V_i(t)$. The scheme in Figure 4.7 also includes a supply circuitry for the battery charging and a balancing system for the energy stored in the different cells (represented in the scheme by the current generators). In particular, the battery charger supplies the current $I_{ch}(t) \leq 0$, which, depending on the specific task, can be

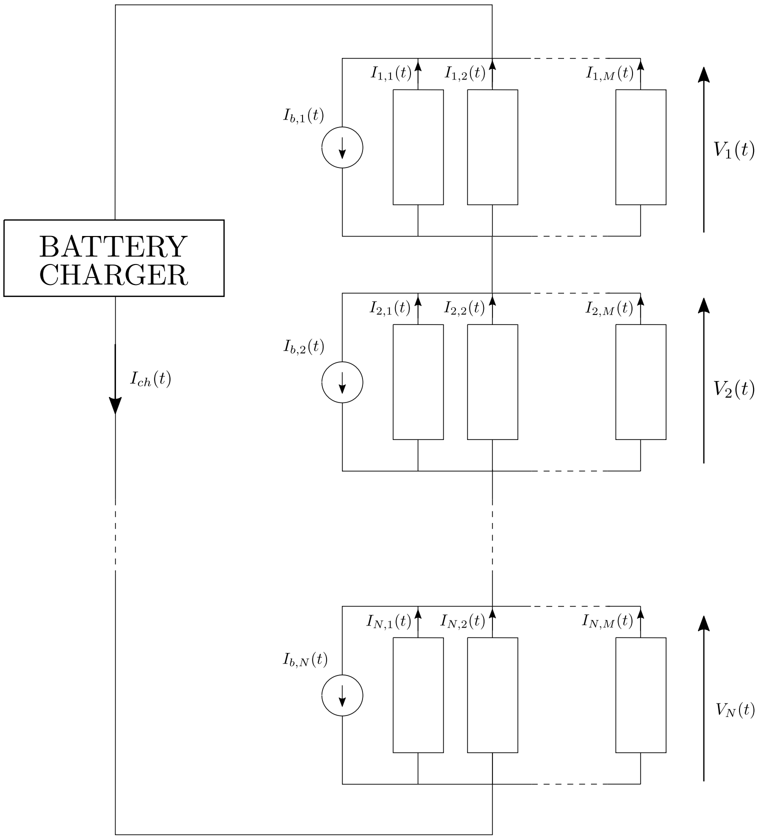

FIGURE 4.7: Simplified circuital scheme.

assumed constant ($I_{ch}(t) = I_{ch}$) or considered as a control variable, while the N generators $0 \leq I_{b,i}(t) \leq -I_{ch}(t)$, $i = 1, 2, \cdots, N$ enables the regulation of the current which flows through the different modules. In the case of constant charger current, the system inputs are represented only by the current generators $I_{b,i}(t)$ which result fundamental in order to provide an optimal charging management of the different cells. For several practical implementations of supply and balancing circuitry schemes the interested reader can refer to (Gallardo-Lozano et al., 2014). For instance simple proportional-integral-derivative (PID) controllers can be used to regulate the value of a variable resistor in parallel to each module. As an alternative, a Pulse-Width-Modulation (PWM) approach or a method based on the cell bypass through active elements can be adopted, as described in detail in 4.3.2.

Electric Coupling The model of the battery pack is given by a set of DAEs as in (4.7) with N_{cells} algebraic variables ($I_{i,j}(t)$, $i = 1, \cdots, N$, $j = 1, \cdots, M$) and corresponding N_{cells} algebraic equations. Each module i, with $i = 1, \cdots, N$, is described by M algebraic equations:

$$V_{i,1}(t) = V_{i,2}(t) \tag{4.44a}$$

$$V_{i,2}(t) = V_{i,3}(t) \tag{4.44b}$$

$$\vdots \tag{4.44c}$$

$$V_{i,M-1}(t) = V_{i,M}(t) \tag{4.44d}$$

$$I_{ch}(t) = \sum_{j=1}^{M} I_{i,j}(t) - I_{b,i}(t) \tag{4.44e}$$

The equations (4.44a)-(4.44d) describe the Kirchhoff's voltage laws between each pair of adjacent cells (in the sense of the electrical scheme) inside a module, while (4.44e) corresponds to the Kirchhoff's current law at each module. Note that we rely on the convention that the supply charger provides a negative current in order to charge the battery pack, thus inducing negative currents in the different cells, while the bypassing system mitigates the charging process by draining positive currents. Also we assume that the current generated by the battery charger is completely bypassed through the generators $I_{b,i}(t)$ when the i-th module completes its charging procedure, i.e.

$$I_{b,i}(t) = -I_{ch}(t), \quad t \geq \bar{t}_i \tag{4.45}$$

where $\bar{t}_i$ is the time at which the i-th module is completely charged.

Thermal Coupling If one considers a lumped thermal model as in 2.4.1.1 or in 2.4.2.2, the heat exchanged between the different cells can be accounted by updating the thermal dynamics of the j-th cell of the i-th module as follows

$$C_{th,i,j}\frac{dT_{i,j}(t)}{dt} = Q_{g,i,j}(t) - \frac{T_{i,j}(t) - T_{sink}}{R_{th,i,j}} - \sum_{l=1}^{N_{adj}} \frac{T_{i,j}(t) - T^{[l]}_{adj,i,j}(t)}{R^{[l]}_{adj,i,j}} \tag{4.46}$$

where $T^{[l]}_{adj,i,j}(t)$, with $l = 1, 2, \ldots, N_{adj}$, is the temperature of the cells which are adjacent to the considered one, given the spatial displacement between the cells inside the battery pack. Similarly, $R^{[l]}_{adj,i,j}$ indicates the thermal resistance between the considered cell and the l-th adjacent one. Finally, it is important to notice that the thermal coupling between two different cells is independent from the electric one, due to the fact that two electrically coupled cells could be thermally insulated from each other.

4.3.1.1 Series-Connected Cells

In the case in which only series-connected cells are considered, i.e. $M = 1$, the resulting system can be described through ODEs due to the fact that no Kirchhoff's voltage laws are considered and the Kirchhoff's current law at each module simply states that the current which flows in the single cell of the i-th module is a trivial function of the one supplied by the corresponding generator and the charger as follows

$$I_{i,1}(t) = I_{ch}(t) + I_{b,i}(t) \tag{4.47}$$

where the notation can be simplified as $I_i(t) = I_{i,1}(t)$. Note that (4.47) can be also expressed as follows

$$I_i(t) = \delta_i(t) I_{ch}(t) \tag{4.48}$$

where $\delta_i(t) = 1 + \frac{I_{b,i}(t)}{I_{ch}(t)}$, with $\delta_i(t) \in [0,1]$, is the fraction of the charging current $I_{ch}(t)$ which is not drained and actually flows into the i-th cell (as it is described in detail in 4.3.2).

It is important to notice that, in the case in which the bypassing generators are not implemented (i.e. $I_{b,i}(t) = 0$, $\forall t \in \mathbb{R}$ for $i = 1, \cdots, N$), the current flowing through each cell would coincide with the one of the battery charger (i.e. $I_i(t) = I_{ch}(t)$) and no SOC balancing strategies could be applied.

4.3.2 Balancing-Aware Charging Strategy for Series-Connected Cells

Charge unbalancing in series-connected cells can lead to lower storage capacity and shorter battery life. Specifically, an early interruption of the charging procedure due to the reaching of the voltage threshold by a subset of the cells produces an undercharging condition. Premature and non-uniform degradation, instead, can be caused by exposure to over-voltages and high temperature spikes, which also affect the self-discharge rates. Significant temperature gradients between different cells or even inside a single cell of a pack arising during standard operation can further increase the differences among the cells, which eventually leads to an accentuation of the imbalance.

In order to overcome the issues mentioned above, a remarkable research effort has been made to develop algorithms pursuing the idea of SOC equalization. These algorithms essentially implement two types of methods: passive methods and active methods (Moore and Schneider, 2001b; Daowd et al., 2011). The former are based on energy dissipation, while the latter mainly rely on charge redistribution, so as to limit energy losses. Active strategies have received increased attention in recent years due to their higher energy efficiency. Within this context, at an earlier research stage, equalization was carried out using only model-independent low-level control strategies, while subsequently it has been proven that model-based optimization techniques can be much more effective in addressing this problem.

Even if remarkable contributions have already been provided by the research on SOC balancing for lithium-ion batteries, some issues are still evident and need to be urgently addressed. As a matter of fact, not only the design but also the assessment of almost all the proposed solutions rely on relatively simple cell models, which are unable to capture some of the key features of the real devices. For instance, temperature as well as ageing dynamics are often neglected. This is clearly unrealistic in many application fields. Think for example of high-power applications like electric and hybrid vehicles in which cooling systems are used to dissipate the excessive heat. In such cases, the thermal couplings among cells and between the cells and the coolant significantly affects the outcomes of the equalization procedure. It follows that the assessment of SOC equalization algorithms performed on simple models is poorly informative.

Another drawback is that most of the equalization algorithms are designed to operate off-line, which is hardly applicable in a real scenario, since it requires a sort of idle time during which only the charge balancing is performed. Furthermore, the concept of SOC balancing is effective in maximizing the battery utilization if one supposes that the total capacity and the SEI resistance are always equal among the cells throughout the battery lifetime. In a real context, however, due to all the previously mentioned phenomena, this is never the case. Therefore, not only is an off-line algorithm unable to maximize the battery exploitation, but it can also lead to overcharge in the successive cycle as long as a standard method, such as the CC-CV protocol, is adopted. In fact, if one balances the SOC at a value lower than the maximum, right before a charge, then the individual SOCs of the cells will diverge because of the differences in the capacities, since a unique current is applied. The only reasonable solution in such cases appears to be the so-called *top balancing*, which consists in balancing the cells SOC to their maximum value at the end of the charge phase (Pozzi et al., 2020a).

In this section, we propose a general nonlinear MPC scheme for optimally charging a lithium-ion battery while achieving an on-line *top balancing* of the SOC. In view of the possibility of a practical implementation, the concepts are subsequently specialized for an easily implementable power supply scheme. Finally, the nonlinear MPC approach, which relies on a simplified electrochemical model, is validated on commercial cells using a detailed battery simulator, with sound evidence of its effectiveness both under the assumption of full state availability and in the presence of an observer scheme.

4.3.2.1 Balancing-Aware Optimal Control Problem

A nonlinear MPC scheme suitable for guaranteeing a balancing-aware charging for lithium-ion cells is here presented. In particular, we consider series-connected cells. As previously discussed in 4.3.1.1, it is known that, in the absence of a suitable supply scheme and controller, this configuration could not guarantee any balancing between cells exhibiting different initial SOC and physical parameters, due to the fact that the same branch current $I_{ch}(t)$ would flow through all the series-connected cells. For the sake of simplicity, we assume here that there exists a general supply scheme which allows to optimize the fraction of current flowing through each cell and the branch current itself. The practical implementation of the proposed algorithm with a specific circuitry will be discussed later in 4.3.2.2.

Considering the MPC framework discussed in 4.1.2.2, the set $u(t_k) \in \mathbb{R}^{N+1}$ of controllable inputs for the series-connected cells at each time step t_k is defined as

$$u(t_k) = [\delta_1(t_k) \cdots \delta_N(t_k)\ I_{ch}(t_k)]^\top \tag{4.49}$$

where $\delta_i(t_k) \in [0,1]$ is the fraction of the branch current $I_{ch}(t_k)$ flowing through the i-th cell during the time interval $[t_k, t_{k+1})$, i.e. $I_i(t_k) = \delta_i(t_k) I_{ch}(t_k)$. Note that also $I_{ch}(t_k)$ is considered as an optimization variable. In fact, if an adjustable current generator is available, the control of the branch current magnitude over time enables for better performance. The state vector $x(t_k)$ consists of all the differential variables in the simplified electrochemical model described in 2.4.2.2, that we assume to be used within the control framework.

Cost Function In order to consider the control objectives as a scalar index, the cost function (4.11) is represented through the following weighted sum

$$
\begin{aligned}
J(x(t_{k_0})) = \sum_{k=k_0}^{k_0+H} \sum_{i=1}^{N} \big(& J_{1,i}(t_k) + J_{2,i}(t_k) + J_{3,i}(t_k) + J_4(t_k) \\
& + J_{5,i}(t_k) + J_6(t_k) + J_{7,i}(t_{k_0}) \big)
\end{aligned}
\tag{4.50}
$$

with

$$J_{1,i}(t_k) = \alpha_1 \left(SOC_i(t_k) - SOC_{ref} \right)^2 \tag{4.51a}$$

$$J_{2,i}(t_k) = \alpha_2 \left(\frac{j_{n,i}^{side}(t_k)}{J_{norm}} \right)^2 \tag{4.51b}$$

$$J_{3,i}(t_k) = \alpha_3 \delta_i(t_k)^2 \tag{4.51c}$$

$$J_4(t_k) = \alpha_4 \left(\frac{I_{ch}(t_k)}{I_{max}} \right)^2 \tag{4.51d}$$

$$J_{5,i}(t_k) = \alpha_5(\delta_i(t_k) - \delta_i(t_{k-1}))^2 \tag{4.51e}$$

$$J_6(t_k) = \alpha_6 \left(\frac{I_{ch}(t_k) - I_{ch}(t_{k-1})}{I_{max}} \right)^2 \tag{4.51f}$$

$$J_{7,i}(t_{k_0}) = \alpha_7 \left(SOC_i(t_{k_0+H}) - \frac{1}{N} \sum_{h=1}^{N} SOC_h(t_{k_0+H}) \right)^2 \tag{4.51g}$$

where t_{k_0} is the time instant at which the optimization is performed, H is the prediction horizon, J_{norm} is a normalization factor, I_{max} the maximum applicable branch current in a module and SOC_{ref} the target SOC (usually, $SOC_{ref} = 1$) which the control algorithm aims to reach at the end of the charge. The coefficients $\alpha_1, \cdots, \alpha_7$ need to be chosen in order to guarantee an optimal trade-off between the different objectives. In particular, the first term (4.51a) accounts for the objective of charging the cells, i.e. reaching the target state of charge SOC_{ref}. The term (4.51b) aims to limit degradation effects due to ageing phenomena, with $j_{n,i}^{side}(t_k)$ being the side-reaction flux for the i-th cell. Finally, the control action can be penalized through costs (4.51c) and (4.51d), which account for the branch current and its fractions flowing through each of the cells respectively. By limiting the current magnitude, energy losses and heat generation are minimized thus improving overall battery health and efficiency. Costs (4.51e) and (4.51f) account for possible penalization of the input ramping rate. The final cost (4.51g), which is related to the distance between each cell SOC and the average SOC of the battery, is introduced with the aim of speeding up the charging process. In fact, it has been noticed in simulation that without such penalty the algorithm often tends to devote most of the charging capability to a subset of the cells in the initial phase, while letting the others at a lower SOC level, so that at the end the total charging time results increased. This could be explained by the fact that the prediction horizon is limited and therefore it is not possible to forecast the long-term future behaviour of the entire system. To this end, the terminal penalty is introduced to consider the fact that additional charging time will be required if differences in the SOCs increase at the end of a certain prediction horizon.

Remark 2 *Notice that, since the proposed balancing algorithm is designed with charging capabilities only (i.e. no redistribution is allowed),* SOC_{ref} *must be greater than all the cells* *initial SOC*

$$SOC_{ref} \geq SOC_i(t_0) \quad \forall i = 1, \cdots, N \tag{4.52}$$

with t_0 being the initial time.

Remark 3 *As it can be noticed, since the objective function (4.50) is the sum of several contributions, the quality of the obtained control clearly depends on the tuning of the coefficients $\alpha_1, \cdots, \alpha_7$. This is not a novelty in the MPC context where, even for a standard simple LQ problem, the tuning of the Q and R matrices requires major attention in order to obtain the best result.*

Constraints The proper functioning of a charging system requires the consideration of some crucial physical and safety constraints, which are accounted in the MPC formulation through (4.12) In particular, condition

$$\eta^{side}_{n,pl,i}(t_k) > 0 \tag{4.53a}$$

must be guaranteed in order to avoid lithium plating deposition, where $\eta^{side}_{n,pl,i}(t_k)$ is the plating overpotential for the i-th cell, in fact a module since $M = 1$. Notice that such a constraint is more preferable than limiting the voltage as done in the majority of the charging methods proposed in the literature. In fact, voltage limits might be too conservative for new batteries and not sufficient for aged ones (Chaturvedi et al., 2010; Klein et al., 2011). Analogously, the allowed temperature should not exceed a maximum limit T_{max}, i.e.

$$T_i(t_k) \leq T_{max} \tag{4.53b}$$

while the SOC must be ensured to remain in the interval $[0, 1]$

$$0 \leq SOC_i(t_k) \leq 1 \tag{4.53c}$$

The branch current fractions $\delta_i(t_k)$ satisfy

$$0 \leq \delta_i(t_k) \leq 1 \tag{4.53d}$$

by definition. Since the subject of the present work is not a redistributive charging algorithm, also a constraint on the sign of the branch current $I_{ch}(t_k)$ must be imposed, such that (considering the charging currents as negative, according to the adopted convention)

$$-I_{max} \leq I_{ch}(t_k) \leq 0 \tag{4.53e}$$

The total power supplied by the generator is bounded by the value $P_{max}(t_k)$ as follows

$$-P_{max}(t_k) \leq \sum_{i=1}^{N} V_i(t_k)\delta_i(t_k)I_{ch}(t_k) \tag{4.53f}$$

so that a realistic scenario is considered, where the input power cannot physically be infinite.

Optimization Problem At each time t_{k_0} we compute the sequence $u^\star_{[t_{k_0}, t_{k_0+H}]}$ which minimizes the cost function (4.50) over the horizon H, while satisfying the constraints in (4.53).

According to the *receding-horizon* principle, only the first element $u^\star(t_{k_0})$ of the obtained sequence is applied to the system. Then, at the successive time step, the values of the relevant model states are updated with the obtained measurements and, according to the *receding-horizon* principle, a new optimization is performed.

4.3.2.2 Power Supply Circuitry and Practical Implementation

The formulation of the problem in 4.3.2.1 is general in the sense that it is designed independently of the underlying power supply circuitry. With the aim of proposing a possible practical implementation, the following supply scheme is considered. Note that this is just one possible implementation which could be replaced by any other feasible one.

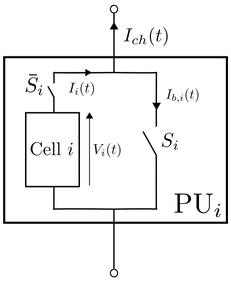

FIGURE 4.8: Schematic of the i-th power unit (PU$_i$), which is in accordance with the discussion in 4.3.1.1.

Power Supply System The elementary unit of the proposed supply system is a PU consisting of the i-th cell together with two power switches S_i and $\bar{S}_i$, as shown in Figure 4.8 and according to the formulation in 4.3.1.1 in which $I_{b,i}(t_k)$ is the drained current. The two switches work in a complementary way, i.e. when S_i is closed $\bar{S}_i$ is open and vice versa. Such design allows the cell bypass when necessary. Note that, since the conduction resistance of the switches is assumed to be negligible, the terminal voltage of the i-th PU happens to coincide with that of the corresponding cell $V_i(t_k)$. The scheme described above exhibits low cost of implementation, high efficiency and the ability to be easily modularized (Gallardo-Lozano et al., 2014). On the other hand, a possible drawback is the decay in efficiency when high currents or a large number of cells are considered. In these cases, alternative schemes can be adopted (Gallardo-Lozano et al., 2014), which still remain applicable in combination with the presented balancing-aware charging procedure. According to Figure 4.9 the variable input generator provides the branch current $I_{ch}(t_k)$ to the whole PUs series connection. Due to the fact that the considered supply scheme implements a

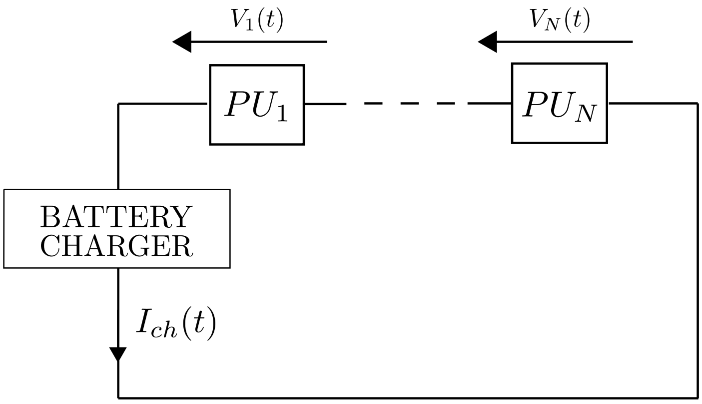

FIGURE 4.9: Schematic of the power supply circuit.

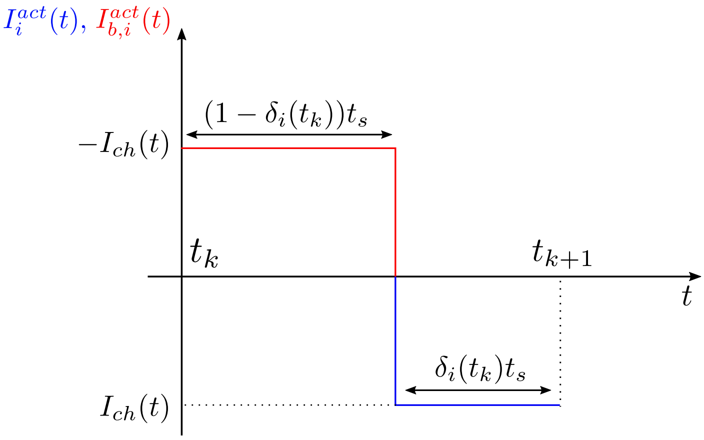

FIGURE 4.10: Representation of the currents inside the i-th power unit during a generic time interval.

switching regulator, in which $I_{b,i}(t_k)$ can only assume values from the discrete set $\{0, -I_{ch}(t)\}$, it appears convenient to consider the control variables $\delta_i(t_k)$ as duty cycles, i.e. fractions of the k-th time step in which the branch current $I_{ch}(t_k)$ flows through the i-th cell. The interval $[t_k,\ t_{k+1})$ is ideally divided into two parts $[t_k,\ t_k + (1-\delta_i(t_k))t_s)$ and $[t_k + (1-\delta_i(t_k))t_s,\ t_{k+1})$ as described in Figure 4.10, where $I_i^{act}(t)$ and $I_{b,i}^{act}(t)$ are the currents actually applied and drained with respect to the i-th cell over time. In the first part of the interval, the cell is completely bypassed (i.e. $\bar{S}_i$ is open and S_i closed in Figure 4.8), while in the second part the vice versa occurs so that the cell is charged with a current corresponding to $I_{ch}(t_k)$.

Remark 4 *Note that to avoid short circuit conditions for the charger, one must in practice make the branch current $I_{ch}(t)$ vanish when all the shunting switches are closed, i.e. for each $k \in \mathbb{N}$*

$$I_{ch}(t) = 0, \quad \text{if } t \geq t_k \text{ and } t < t_k + (1 - \max_i \delta_i(t_k))t_s \tag{4.54}$$

Practical Considerations The optimization problem discussed in 4.3.2.1 is designed considering the inputs as constant during the sampling interval. However, the profile of the applied current (Figure 4.10) is different from that of a constant current, which in this case can only correspond to the average one $I_{avg,i}(t_k) = \delta_i(t_k)I_{ch}(t_k)$. This leads to wrong predictions of the future states by the MPC algorithm, thus

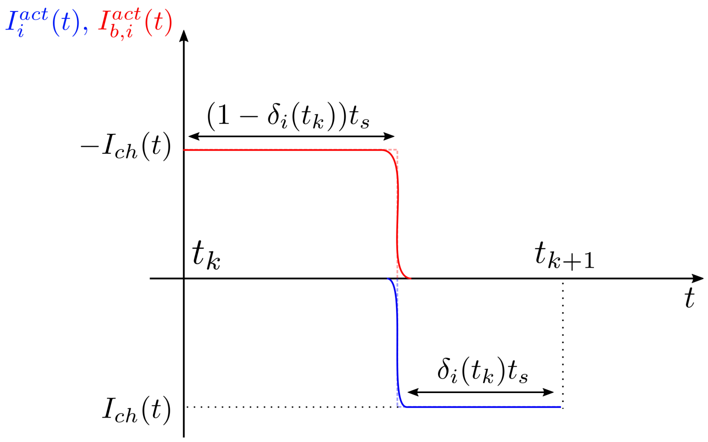

FIGURE 4.11: Approximation of the currents in Figure 4.10 with sigmoid functions.

harming optimality and constraints satisfaction if the average value is considered, especially for long prediction horizons. Due to the switching structure of the supply scheme, the problem could be naturally formulated as a mixed-integer program (Floudas, 1995). Nevertheless, the online solution of this latter is impracticable as it becomes computationally prohibitive even if only few cells are considered. In order to preserve the possibility of an online implementation, we address the adaptation of the proposed optimization problem to the considered supply circuitry. Since the applied input current $I_i^{act}(t)$ is a discontinuous function of the optimization variables $\delta_i(t_k)$, the solution of the optimization problem may experience convergence issues (related to the computation of the gradient) and consequently be slow or inaccurate. Therefore, a viable strategy is here proposed in order to approximate with sufficient and arbitrary accuracy the step current profiles in Figure 4.10. In particular, a continuous sigmoid function (see Figure 4.11) is considered for any time step t_k of the prediction horizon, such that

$$I_i^{act}(t) = \frac{I_{ch}(t_k)}{1+e^{-a(t-t_k-(1-\delta_i(t_k)))}}, \quad t_k \leq t \leq t_{k+1} \tag{4.55}$$

where the parameter a in (4.55) determines the slope of the sigmoid function in $t_k + 1 - \delta_i(t_k)$ and therefore the accuracy of the approximation, at the expense of a possibly increased stiffness of the resulting ODEs. A similar function is used also to approximate the step profile of the actual drained current $I_{b,i}^{act}(t)$. Simulation results, carried out for an horizon of 200s with the input in Figure 4.12 are shown

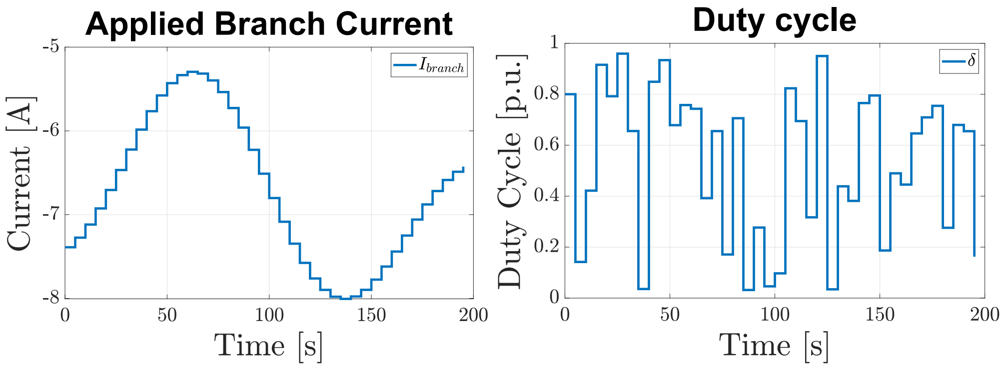

(a) Branch Current Input (b) Duty Cycle Input

FIGURE 4.12: Time-varying inputs applied in order to evaluate the accuracy of the approximations.

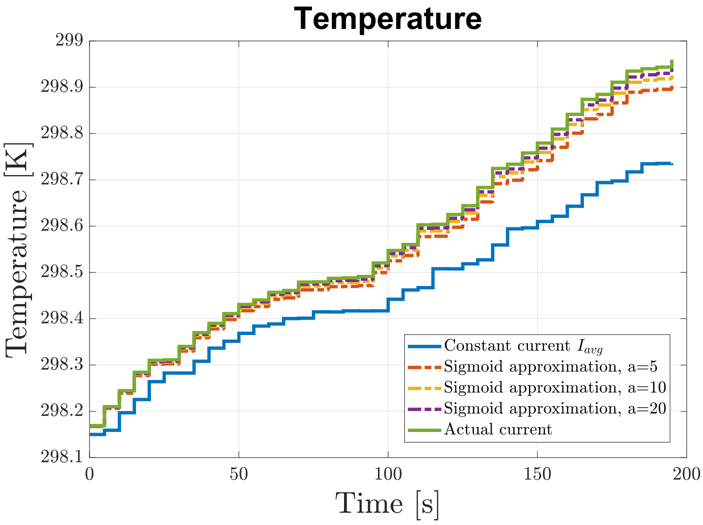

FIGURE 4.13: Cell temperature approximations.

in Figure 4.13, 4.14 and 4.15, where it appears evident that using the average value $I_{avg,i}(t_k)$ produces non-negligible errors, while increasing the parameter a in the sigmoid step approximation (4.55) enhances considerably the accuracy. Only the evolution of temperature, capacity loss and SEI resistance growth are reported, since they are the unique quantities which exhibit a nonlinear behaviour with respect to the applied current. On the other hand, no benefits in the SOC description can be achieved through the proposed approximation, since its dynamics is linear and sufficiently slow. Notice that the results refer to a simulation time much longer than that expected for an MPC prediction in which the real values of the considered quantities are updated every t_s with the measured ones.

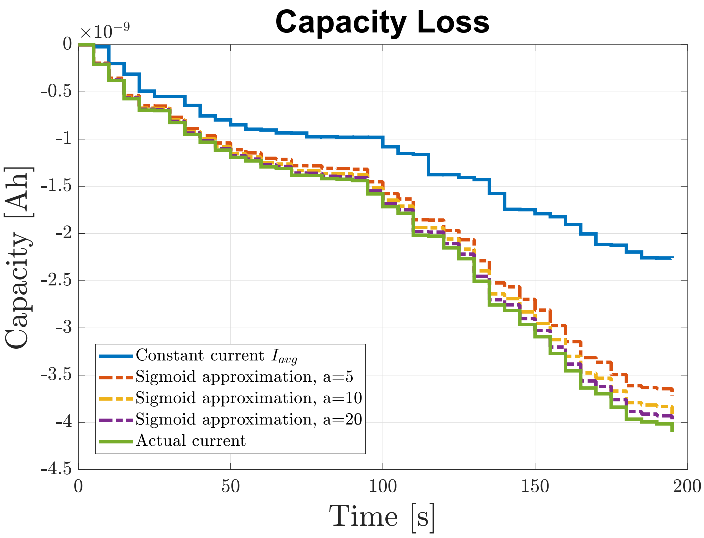

FIGURE 4.14: Capacity loss approximations.

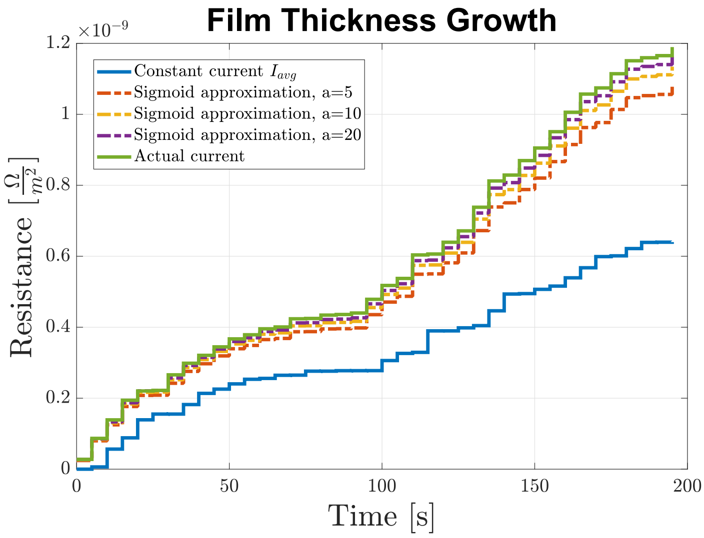

FIGURE 4.15: Film-growth resistance approximations.

Remark 5 *The possibility to control the branch current* $I_{ch}(t_k)$ *through a variable current generator leads to better results. In fact, in view of the highly nonlinear relationship between temperature and input current, both the magnitude and the duration of the current applied in the second part of the control step influence the resulting behaviour.*

In the following, a soft constraints formulation is considered in order to enhance the practical applicability of the presented equalization strategy.

Constraints Softening As for the MPC formulation, a real-world application could require the softening of the constraints in (4.53). Considering that the condition

(4.53a) must hold for the adopted model to be valid, (4.53c) and (4.53d) cannot be relaxed outside the ranges of definition, and (4.53e) only regards the input, all the other constraints can be relaxed by inserting slack variables s_1, s_2 as follows

$$T_i(t_k) \leq T_{max} + s_1(t_k) \tag{4.56a}$$

$$-P_{max}(t_k) \leq \sum_{i=1}^{N} V_i(t_k) I_{avg,i}(t_k) + s_2(t_k) \tag{4.56b}$$

$$s_1(t_k) \geq 0, \quad s_2(t_k) \geq 0 \tag{4.56c}$$

The total cost function $\bar{J}(x(t_{k_0}))$, at each time instant t_{k_0}, must then be reformulated accordingly as

$$\bar{J}(x(t_{k_0})) = J(x(t_{k_0})) + \sum_{k=k_0}^{k_0+H} \sum_{i=1}^{N} (J_{s_1}(t_k) + J_{s_2}(t_k)) \tag{4.57}$$

with $J(x(t_{k_0}))$ as in (4.50) and

$$J_{s_1}(t_k) = \alpha_{s_1} s_1(t_k) \tag{4.58a}$$

$$J_{s_2}(t_k) = \alpha_{s_2} s_2(t_k) \tag{4.58b}$$

where $\alpha_{s_1}, \alpha_{s_2} > 0$.

Remark 6 *Note that softening the maximum power constraint in* (4.56b) *is feasible in practice since generators can deliver a power slightly higher than the nominal one, at least for short periods of time.*

4.3.2.3 Battery Model, Parameters and Available Measurements

In this section a battery pack consisting of six series-connected cells is considered (i.e. $N = 6$ and $M = 1$). The mathematical equations of each cell used within the control framework are according to the simplified electrochemical model with temperature and ageing dynamics presented in 2.4.2.2. The numerical implementation of the P2D model provided by an extended version of LIONSIMBA is considered as the real plant for the validation of the proposed control strategy. The simulation environment includes a full-order model for the solid diffusion law and a lumped model for the thermal dynamics. All the parameters, except for the ones related to the ageing dynamics, which are taken from (Santhanagopalan et al., 2006), are those experimentally identified in (Ecker et al., 2015a; Ecker et al., 2015b), where a complete parametrization of the Kokam SLPB 75106100 cell is provided. Notice that this constitutes an appreciable feature, since in this way real commercial cells are accurately modelled. The open-circuit potentials and the electrolyte conductivity functions are taken as in (3.35) and (3.37). As for the the SEI and plating-reaction reference potentials, the values $U_{sei} = 0.4V$ and $U_{pl} = 0$ are chosen in accordance with (Ramadass et al., 2004; Klein et al., 2011).

It is important to notice that the battery is assumed to be wrapped by a coolant fluid, which constitutes the external environment with temperature $T_{env}(t)$. In particular, we assume that the thermal dynamics of the coolant is given by

$$C_{th,env}\frac{dT_{env}(t)}{dt} = \sum_i \frac{T_i(t) - T_{env}(t)}{R_{th,i}} - \xi(t) \tag{4.59}$$

where $\xi(t)$ is the thermal power in W released by the cooling, which is considered constant in the operating range, for the sake of simplicity

$$\xi(t) = \begin{cases} 5 & \text{if} \quad T_{env}(t) > T_{ref} \\ 0 & \text{otherwise} \end{cases} \tag{4.60}$$

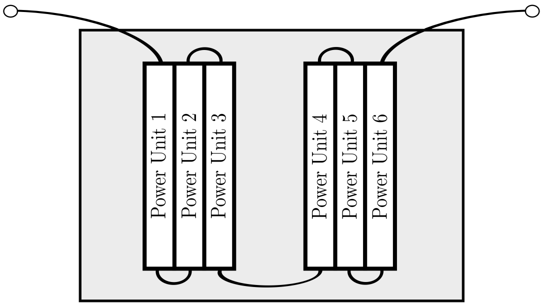

FIGURE 4.16: Battery configuration. The 6 series-connected cells are grouped into two packs which are wrapped by the coolant, here indicated in light gray.

The topology of the cells series connection is that depicted in Figure 4.16, with two packs of three adjacent cells divided by a space in which the coolant is able to flow (light gray area). The coolant also wraps the rest of the two packs, so that

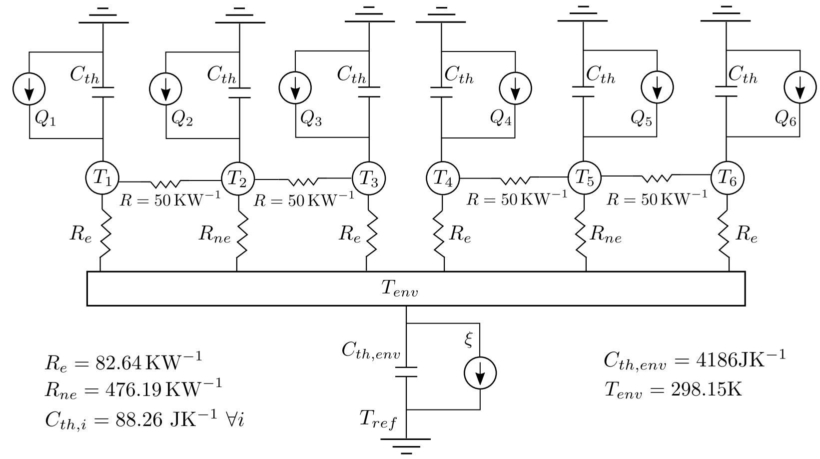

FIGURE 4.17: Schematic representation of the thermal couplings using an equivalent electric circuit. The resistances between cells are expressed in KW^{-1}.

the most external cells have a far higher heat exchange surface compared to the inner ones. A representation of the thermal couplings, described by means of an equivalent electric circuit, is reported in Figure 4.17 along with the adopted related values.

Measurements Availability and State Observer In 4.3.2.4 we assess the strategy intrinsic performance by assuming the availability of all the relevant states as output measurements. Then, with the aim of giving the readers an insight about the possibility of using an easy-to-design observer which provides reasonable performance, results obtained including an extended Kalman filter are reported in 4.3.2.5.

In the following, the assumption of availability of all the relevant states is made for the algorithm development. At first the strategy is assessed assuming the availability of the state measurements, in order to show the strategy intrinsic performance (i.e. the performance not altered by estimation errors referable to the observation scheme). Then, with the aim of giving the readers an insight about the possibility of using an easy-to-design observer which provides reasonable performance, results obtained including an Extended Kalman Filter (EKF) in the scheme are also reported. The development of a more involved observer and its coupling with the presented control system goes beyond the scope of this paper. The additional assumption that the measurable surface temperature coincides with the bulk one is made for the sake of simplicity. To address this aspect in practical scenarios, one of the effective models

Initial States	**Cell 1**	**Cell 2**	**Cell 3**	**Cell 4**	**Cell 5**	**Cell 6**
C^0 $[Ah]$	6.47	7.62	8.83	8.68	8.46	7.22
R^0_{sei} $[m\Omega]$	10.52	11.83	11.11	11.82	10.66	8.87
SOC^0 [-]	0.39	0.19	0.21	0.20	0.34	0.37

TABLE 4.2: Initial capacity (C^0), film resistance (R^0_{sei}) and normalized state-of-charge (SOC^0) values for the different cells of the pack.

available in the literature (e.g. the two-states thermal model (Lin et al., 2014)) can be used.

4.3.2.4 SOC Balancing Results With Measurable States

In the following, the effectiveness of the proposed approach is tested in simulation. In order to obtain a realistic scenario, the simplified electrochemical model described in 2.4.2.2 is used for the control, while the more accurate LIONSIMBA simulator, which implements the P2D model, is considered as the real battery.

The physical and thermal parameters of the cells are supposed to be equal to the nominal ones given in (Ecker et al., 2015a; Ecker et al., 2015b), with the exception of the initial capacity and SEI resistance. In fact, it is known in the literature that these latter exhibit significant variations due to both the manufacturing process and the different ageing exposure. In order to take into account such possible mismatches, the two mentioned parameters are randomly extracted as reported in Table 4.2, where also the initial normalized SOC is listed for each cell.

First, with the aim of considering benchmark strategies, a standard charging protocol (namely, the CC-CV) is applied and the results are commented. Subsequently, a simple method for equalization at the end of the charge is tested. At last, the same battery is charged with the proposed nonlinear MPC strategy described in Section 4.3.2.1 both under the assumption of ideally available states and noisy voltage and temperature measurements only. In the latter case (i.e. when non-measurable states are considered), an EKF is adopted so to estimate the SOC and filter the temperature. In the following, the improvements obtained with nonlinear MPC with respect to the previous ones are highlighted and a thorough discussion of the results is carried out. In particular, it is shown that the extractable capacity during the successive

Strategy	**SOC**			**max. T**	**max. V**
	avg.	**std.**	**max.**		
CC-CV	0.997	0.166	1.245	$324.08K$	$4.41V$
Voltage-Based	0.932	$9.5 \cdot 10^{-3}$	0.940	$326.15K$	$4.20V$
Nonlinear MPC	1	$2 \cdot 10^{-5}$	1	$323.15K$	$4.225V$
Nonlinear MPC with EKF	0.995	$7.9 \cdot 10^{-3}$	1.006	$323.21K$	$4.25V$

TABLE 4.3: Main simulation results obtained with the discussed methods: SOC, Temperature and Voltage metrics over the 6 considered cells. The values which exceed the limits are marked in red.

discharge cycle is maximized and the safety is guaranteed by constraints satisfaction throughout the charge. It is also evidenced that the ageing effects are reduced.

Benchmark Methods In the following, two charging methods based only on voltage measurements are tested in simulation. Their weaknesses are highlighted both in terms of constraints satisfaction and balancing features. The results are summarized in Table 4.3 and compared with those obtained using the proposed strategy.

CC-CV One of the most used charging protocols in industry is the well-known CC-CV protocol (Cope and Podrazhansky, 1999), which here has been applied to the virtual testbed described in 4.3.2.3. When this protocol is applied to a set of series-connected cells, these latter are charged while keeping the total branch voltage within a specified threshold. Such limit is computed as the voltage corresponding to SOC_{ref} for a nominal cell (in this case, taken as $4.15V$) multiplied by the number of cells in the series. In particular, at a first stage a constant current is applied until the limit voltage is reached and, then, such voltage is kept constant reducing the current until a specified threshold is attained. Due to the fact that only the branch voltage is considered, some of the cells usually result in being undercharged and others overcharged. For these latter safety is at risk, while the capacity of the former is obviously not fully exploited. In order to avoid overvoltage exposure, using a voltage sensor for each of the cells, it is possible to interrupt the charging procedure as soon as one of the cells reaches its upper voltage threshold (Barsukov and Qian, 2013). This, however, reduces even more the overall used battery capacity.

Voltage-Based Method In order to obtain better performance than the CC-CV protocol, we consider also as a benchmark a simple model-less charging method which exploits the supply circuit described in Section 4.3.2.2. Such a strategy only relies on voltage measurements and applies a constant branch current to all the cells until one of them hits its voltage threshold. Then, this latter is fully bypassed, while the charging continues for those with a voltage below the respective limit. Notice that in this case, since the constant-current phase is not followed by a constant-voltage one (a different voltage source for each cell would be required for performing the CV phase on each element of the series connection independently), we chose as voltage threshold the maximum allowed voltage rather than the one corresponding to SOC_{ref}. In the carried out simulation, a constant current of 1C-rate, with $I_{1C} = 7.5A$, has been applied, giving rise to the results reported in Table 4.3. The charging of each cell is interrupted as soon as the voltage threshold is hit (the maximum voltage $4.2V$, given in (Ecker et al., 2015a), is considered). Therefore, the voltage limits are always satisfied by design. With respect to the CC-CV, it can be noticed that the SOCs are more balanced (i.e. they exhibit a smaller variance at the end of the charge). In fact, the considered algorithm is designed so as to perform a crude voltage-based balancing. However, the SOCs maximum value does not reach the target value and even the cell with the lowest capacity is not fully exploited.

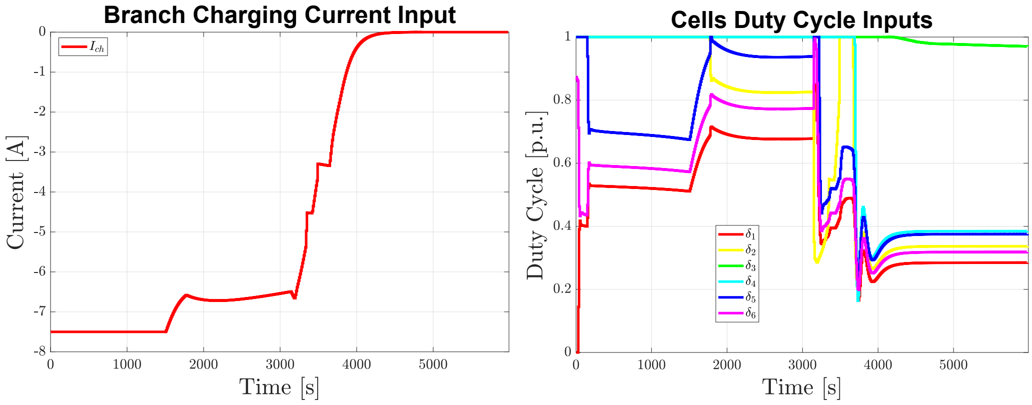

(a) Branch Current Input

(b) Duty Cycle Input

FIGURE 4.18: *Nonlinear MPC charging:* Optimal branch current and duty cycle inputs, where in spite of the problem highlighted in Remark 4, for clarity the time intervals when the branch current is null are omitted in the plot.

N	H	T_s	a	SOC_{ref}	I_{max}
6	3	10 s	5	1	7.5 A
T_{max}	T_{env}	P_{max}	α_1	α_2	α_3
323.15 K	298.15K	$0.75V_{max}I_{max}$	10^4	0.2	0
α_4	α_5	α_6	α_7	α_{s_i}, $\forall i$	J_{norm}
1	10^{-1}	10^{-3}	10^5	10^{15}	10^{-13}

TABLE 4.4: Parameters of the nonlinear MPC optimization.

Balancing-Aware Nonlinear MPC Method The algorithm proposed in this Section 4.3.2.1 is now applied to the same battery pack considered above, which is modelled by the P2D, while the SPMeT is used as model for the control in the nonlinear MPC optimization. The values of the parameters adopted in the optimization are listed in Table 4.4.

Notice that, due to the operating features of the considered supply scheme, the penalty on the variations of the duty cycles $\delta_i(t_k)$ and the branch current $I_{ch}(k)$ ((4.51e) and (4.51f)) does not lead to any physical benefits. Nevertheless, small values for the coefficients α_5 and α_6 can help to obtain smother input curves, which in turn improve the readability of the plots. The slack variables weights for the soft constraints are taken so high that practically no relaxation takes place, i.e. $\alpha_{s_1} = \alpha_{s_2} = 10^{15}$.

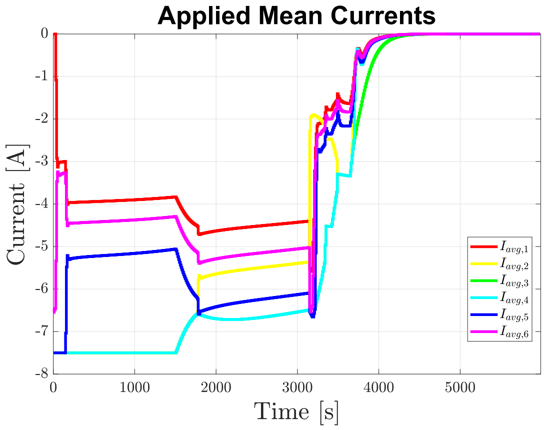

FIGURE 4.19: *Nonlinear MPC charging:* Applied mean current to the single cells.

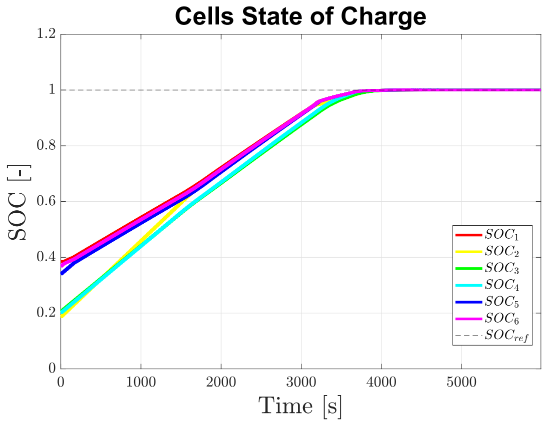

FIGURE 4.20: *Nonlinear MPC charging:* State of charge (SOC).

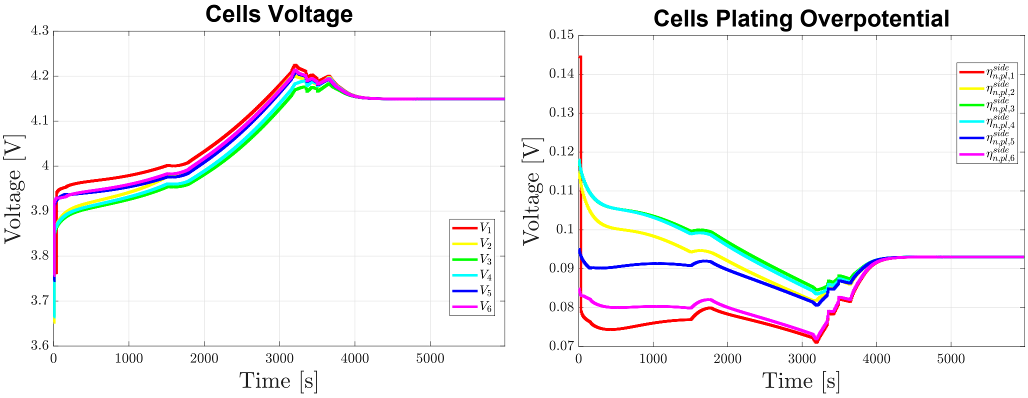

(a) Cell Voltage

(b) Side-Reaction Overpotential

FIGURE 4.21: *Nonlinear MPC charging:* Terminal voltages and side-reaction overpotentials for the different cells. As it can be noticed, the constraints on the latter are never violated (the side-reaction overpotentials are always positive).

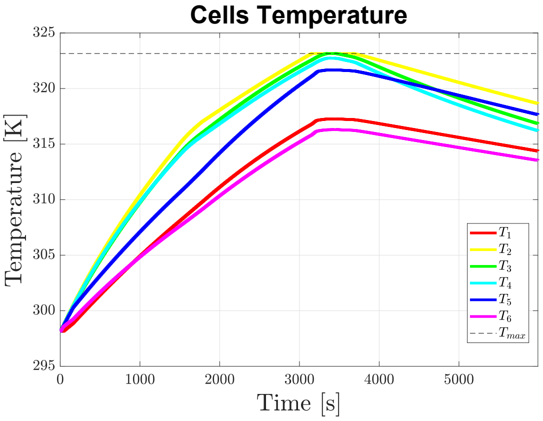

FIGURE 4.22: *Nonlinear MPC charging:* Temperature of the single cells.

Ideally Available States In the following the results obtained assuming ideal availability of the relevant states of the P2D model are briefly discussed. Notice that the conversion between the states of the P2D model employed in LIONSIMBA and the ones of the SPMeT is made by means of simple algebraic relationships well known in the literature. Figure 4.18 reports branch current $I_{ch}(t_k)$ and duty cycles $\delta_i(t_k)$, which produce the average currents plotted in Figure 4.19. During the whole process, the cells are charged with different mean currents, with the objective of reaching for each cell the reference SOC while reducing the unbalance. These goals are achieved by a suitable tuning of α_1 and α_7, respectively. The inputs are obtained taking also into account the power curve of the generator. This translates into a full power supply exploitation, thus allowing the employment of smaller and cheaper generators. As can be evidenced from Figure 4.20, the SOC unbalance is reduced over time and the procedure is stopped when all the cells are fully charged. Figure 4.21 and 4.22 highlight the fact that both the side-reaction overpotentials and the temperatures remain safely within the imposed limits (only the cells 2 and 3 hit and keep the temperature threshold near the end of the charge). This helps reducing wear and ageing, as well as improving safety.

A key feature of the nonlinear MPC algorithm is that, with respect to the other two tested strategies, it provides a full exploitation of the cells at the end of the charge, i.e. the SOC of all the cells is the maximum possible according to the limits. As the main benefit of this fact, the charge extractable during the successive discharge cycle is maximum. In fact, assuming to discharge the whole battery pack with a constant current of 1C-rate until a cut-off voltage threshold ($2.7V$) is reached by one of the cells, the charge obtainable after the application of the voltage-based method is $5.94Ah$, while after the nonlinear MPC it is as high as $6.50Ah$ (9.6% more). The same arguments do not hold when taking into account the CC-CV, since it appears evident that the extractable charge could be higher than that of the nonlinear MPC. However, the comparison is not fair since this comes at the cost of an overcharge of some of the cells (which reach a normalized SOC as high as 1.24) with sure harm to safety. The durations of the charging phase of the three presented algorithms are respectively $4200s$ for the nonlinear MPC, $3110s$ for the voltage-based method and $3650s$ for the CC-CV method.

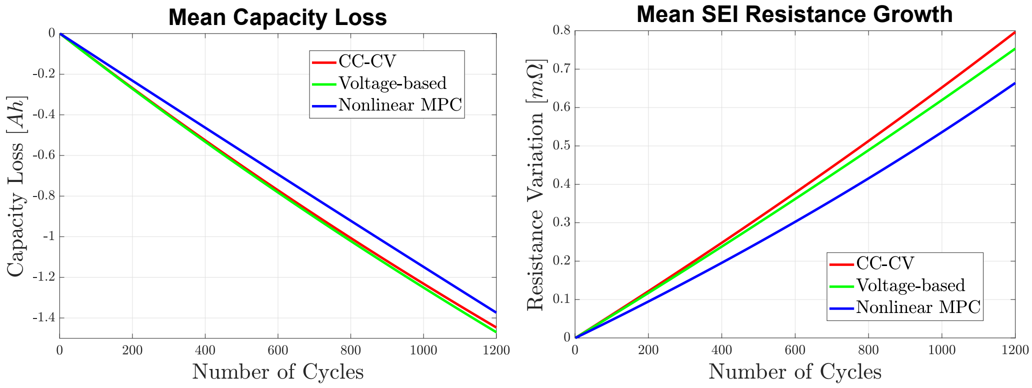

(a) Cell Capacity Loss

(b) Cell Resistance Growth

FIGURE 4.23: Average capacity loss and SEI resistance growth over 1200 cycles with the three discussed methods.

With the aim of evaluating the effect of both the benchmarks and the proposed method on the ageing evolution, the three different algorithms have been applied over 1200 cycles. At the beginning of each cycle the cells are considered at rest and starting from the same SOC as reported in Table 4.2. As it can be noticed, the proposed algorithm outperforms the CC-CV and the voltage-based algorithm, both from the point of view of capacity loss (Figure 4.23(a)) and resistance growth (Figure4.23(b)).

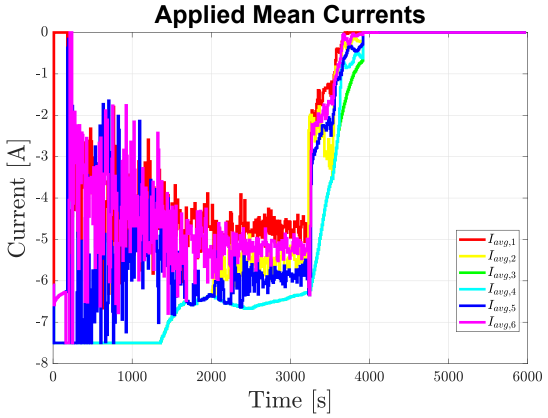

FIGURE 4.24: *Nonlinear MPC with EKF charging:* Applied mean current to the single cells.

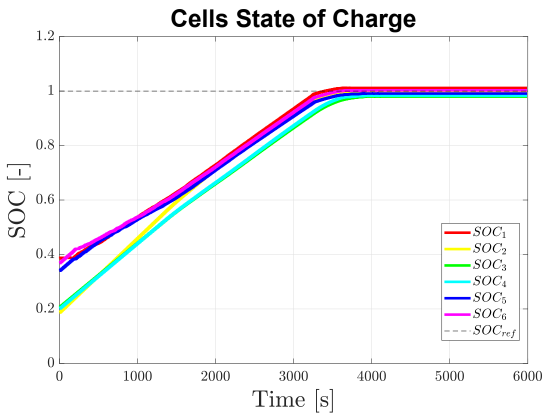

FIGURE 4.25: *Nonlinear MPC with EKF charging:* State of charge (SOC).

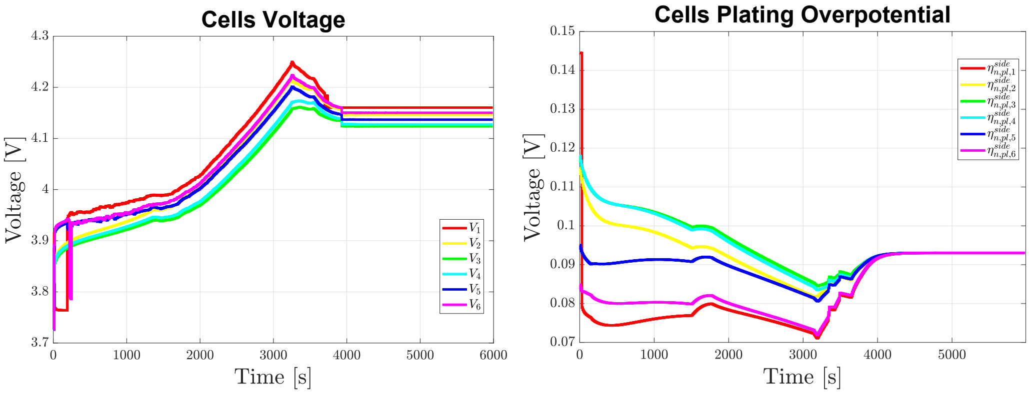

(a) Cell Voltage (b) Side-Reaction Overpotential

FIGURE 4.26: *Nonlinear MPC with EKF charging:* Voltage and side-reaction overpotentials over the different cells.

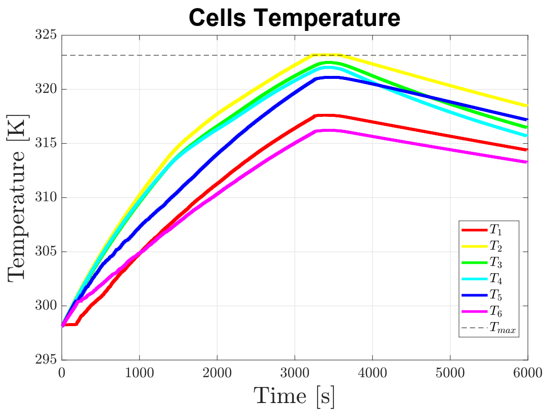

FIGURE 4.27: *Nonlinear MPC with EKF charging:* Temperature of the single cells.

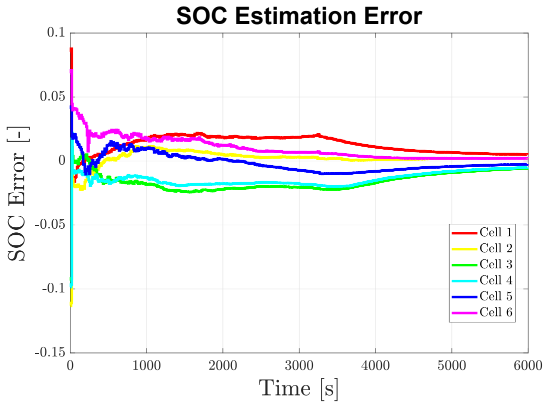

FIGURE 4.28: *Nonlinear MPC with EKF charging:* SOC estimation error for the single cells.

4.3.2.5 SOC Balancing Results With States Observer

In order to assess the practical implementability of the nonlinear MPC scheme, the same simulation has been carried out dropping the assumption of full states availability. The introduction of an observer is therefore necessary in order to reconstruct the required relevant states on the basis of the available voltage and temperature measurements. Notice that in this case a Gaussian zero-mean measurement noise has been applied, with standard deviations of, respectively, $5mV$ and $0.5K$.

The aim of developing a precise state observer for lithium-ion cells is outside of the scope of the present work. Therefore, only an insight on the possibility of employing a simple observer in a practical implementation of the proposed strategy is given here. Among the different solutions previously proposed in the literature (Waag, Fleischer, and Sauer, 2014), we consider an EKF for continuous-time models with discrete-time measurements (Brown, Hwang, et al., 1992; Jazwinski, 2007). In particular, the interest is devoted to observe the SOC and the temperature, while all the other states are left to evolve in open-loop since the average concentration flux as well as the electrolyte concentration exhibit an asymptotically stable behaviour (Moura et al., 2016), and the states related to the ageing phenomena present a very slow dynamics. The initial values of the former can be set equal to their equilibrium condition (zero for the average concentration flux and $1000\,\frac{mol}{m^3}$ for the electrolyte concentration) while the latter can be considered as model parameters and, therefore, identified off-line by means of a suitable estimation procedure (the initial capacity $\hat{C}^0$ and the SEI resistance $\hat{R}^0_{sei}$ in the observer are taken as in Table 4.2). The initial value for the normalized SOC considered in the EKF ($\hat{SOC}^0$) is taken as 0.3 for all the cells.

With the aim of taking into account the uncertainty on the model dynamics, the voltage equation in the observer model $\hat{V}_i(t)$ has been modified, for every cell i, as

$$\hat{V}_i(t) = V_i(t) + f_i(t) \tag{4.61}$$

In (4.61), $f_i(t)$ is an additional term which represents the modelling error with respect to the real plant. This latter is considered as an additional state with zero time derivative (i.e. $\frac{df_i(t)}{dt} = 0$) and it is estimated by the EKF as well. The results obtained with the nonlinear MPC strategy coupled with the EKF are reported in Figure 4.24, 4.25, 4.26, 4.27 and 4.28, and in Table 4.3. As can be noticed, the evolution of the relevant quantities is similar to that of the previous simulation although a small estimation error is present (see Figure 4.28). The presence of an estimation error is inherent to the aim of the proposed simulation, which is that of reproducing a real application scenario with limited knowledge of the necessary quantities. In particular, even though more accurate estimation schemes could be employed, it can be argued that a standard EKF constitutes a sufficiently effective way of practically implementing the proposed charging strategy. Within this context it is important to notice that in the case of inaccurate ageing model or initial conditions the performance of the nonlinear MPC strategy in terms of ageing reduction may be significantly affected.

Machine Characteristics and Computational Time All the simulations are carried out on an Intel Core i7 - 8750H, ranging from 2.20 to 4.10 GHz. The time per iteration spent for computing the optimal input in the simulation involving the Kalman filter is, on average, compatible with the sample time. Although there exist some exceptional cases in which the computational time is higher than the sample time, suitable countermeasures can be adopted. Nevertheless, such performance-oriented considerations, as well as the performance analysis with respect to other possible computational units on which the algorithm can be implemented, are not part of the scope of the presented work.

4.3.2.6 Conclusions to Balancing-Aware Charging Strategy

A nonlinear MPC strategy has been presented for optimally charging series-connected lithium-ion cells, while avoiding the necessity of periodic off-line balancing. A sufficiently detailed electrochemical model, suitable for control, has been considered, which takes into account also ageing and thermal effects (comprising the coolant dynamics). This latter has then been used to establish a general nonlinear MPC framework (4.3.2.1). Finally, a possible practical implementation has been considered in 4.3.2.2, in which the formulation is adapted to the case of a specific implementable power supply scheme. The effectiveness of the proposed methodology has been validated on a virtual testbed based on the P2D electrochemical model, in which real cell parameters have been considered in order to obtain a realistic scenario. Simulations have shown the ability of the presented algorithm to rapidly achieve state-of-charge balancing while guaranteeing safety and battery health-related constraints. The comparison with a standard charging protocol (CC-CV) and a simple voltage-based procedure has highlighted that the proposed approach outperforms the other considered methods from all points of view, even in the presence of unmeasurable states.

4.3.3 Sensitivity-based MPC for Optimal Charging Battery Packs

A battery pack is usually composed by series-connected modules, each of which is constituted of parallel-connected cells, as depicted in the scheme in Figure 4.7. As previously discussed, many works in the literature address the optimal management of a battery pack by exploiting MPC strategies, due to their ability in dealing with constraints and nonlinear multi-variable systems. However, most of these works model the battery pack as a single lumped equivalent circuit, which does not take into account the individual behaviour of the different cells. In the few cases in which the cells are modelled individually, see for instance the works which cope with the SOC balancing, simple linear models, such as integrators and internal resistance ECMs, are used. On the one hand, the usage of such models in the battery optimal control context has the advantage of a low computational cost, which allows for real-time implementation even in the case of a high number of cells. On the other hand, simple linear models often fail to grasp the real behaviour of the battery pack. As a consequence, the resulting charging may be suboptimal and may not even satisfy the safety constraints on all the different cells. The possibility of exploiting electrochemical models within a control algorithm could be considered, but comes at the price of a prohibitive computational cost when the number of parallel and series-connections increases. As a compromise, the use of linearized electrochemical models seems promising in order to achieve high performance with a reasonable computational load.

In the following, a battery pack with series- and parallel-connected cells is considered, where each cell is described according to the reduced electrochemical model presented in 2.4.2.2. The resulting model consists of a set of nonlinear differential algebraic equations, for which suitable linearization methods are applied. In the following, in order to provide a model for the control accurate and simple at the same time, we rely on a sensitivity-based linearization method, which is well-known in the literature and has been described in detail in (De Oliveira and Biegler, 1995; Šantin et al., 2016) for a system of ordinary differential equations and here applied to the case of a system of DAEs (Pozzi et al., 2020c). Such an approach differs from standard LTV techniques (Campbell, 1995), since the sensitivities of the states and outputs to input variations are continuously integrated together with the model equations rather than evaluated only at discrete time steps. Moreover, a survey on different methods which exploit the sensitivity informations in MPC context can be found in (Biegler, 2013).

The main contribution of this section is the application of the well-known sensitivity-based linear MPC to the management of large battery packs, taking into account safety constraints (such as temperature and voltage limits) on all the different cells. To the best of our knowledge, this is the first time that such an approach is used in the context of the control of battery packs. As shown in the results section, a detailed analysis is conducted by comparing, over an increasing number of series- and parallel-connected cells, the proposed sensitivity-based MPC with both a standard nonlinear MPC and the CC-CV algorithm, which are taken as benchmark. The sensitivity-based MPC has much lower computational cost than the nonlinear one while achieving comparable performance. Since the choice of the nominal trajectory is fundamental in order to obtain an accurate linearization, we also provide an adaptive method in order to update the nominal trajectory during the charging process. In addition, the need for an optimal management of the different cells is made evident by highlighting the disadvantages of standard charging protocols, such as the CC-CV protocol. Finally, the proposed methodology is applied in simulation to the optimal management of an electric motorbike battery pack composed by 156 cells, each of them modelled as the SPMeT. In this application, the sensitivity-based MPC provides optimal performance with a computational cost compatible with the sampling time.

4.3.3.1 Sensitivity-Based Linear Model Predictive Control

A sensitivity-based linear MPC (sMPC) is here proposed for the control of a general nonlinear continuous-time system described by semi-explicit DAEs as in (4.7). The main advantage of this approach is the significant computational time reduction with respect to a standard nonlinear MPC (nMPC, see 4.1.2.2), while having comparable performance.

The sMPC strategy, which is presented in the following, relies on the model linearization around a nominal input trajectory, and it is based on the computation of the sensitivities of states, outputs, and algebraic variables with respect to input perturbations. Such sensitivities are obtained by integrating additional continuous-time differential equations together with the model in (4.7). Using this approach, the resulting linearized model provides higher accuracy than standard LTV approaches, in which the sensitivities are evaluated only at discrete time steps.

Sensitivity-Based Linearization Along a Nominal Trajectory The main drawback of the optimal control formulation in Section 4.1.2.2 is its high computational cost, which comes from the use of a nonlinear model to predict the future system behaviour, involving the solution of a nonlinear optimization at each time step whose complexity can be prohibitive for certain online control applications. As an alternative, we propose a sensitivity-based linearization of the system (4.7), which can be exploited to provide a fast MPC solution. As in the previous sections, the discussion is carried out by considering a digital controller which applies a piecewise-constant input at the discrete times t_k, with sample time t_s.

Consider a nominal input signal $\overline{u}(t)$ and the nominal input sequence $\overline{\mathbf{u}}_{[t_k,t_{k+H}]} = [\overline{u}^\top(t_k), \overline{u}^\top(t_{k+1}), \cdots, \overline{u}^\top(t_{k+H-1})]^\top$ over the time window $[t_k, t_{k+H}]$. The corresponding nominal trajectories for states, algebraic variables, and outputs are $\overline{\mathbf{x}}_{[t_{k+1},t_{k+H}]}$, $\overline{\mathbf{z}}_{[t_{k+1},t_{k+H}]}$, and $\overline{\mathbf{y}}_{[t_{k+1},t_{k+H}]}$. Define $S_x(t,t_k) = \frac{\partial x(t)}{\partial u(t_k)}$, $S_z(t,t_k) = \frac{\partial z(t)}{\partial u(t_k)}$, and $S_y(t,t_k) = \frac{\partial y(t)}{\partial u(t_k)}$ which are the sensitivities of the states, algebraic variables, and outputs to a variation in the input $u(t_k)$ with respect to its nominal value $\overline{u}(t_k)$ at the discrete time t_k. In particular, the matrices $S_x(t,t_k) \in \mathbb{R}^{N_x \times N_u}$, $S_z(t,t_k) \in \mathbb{R}^{N_z \times N_u}$, and $S_y(t,t_k) \in \mathbb{R}^{N_y \times N_u}$ are obtained by solving, together with (4.7), the system of equations

$$\dot{S}_x(t,t_k) = \overline{F}_x(t)S_x(t,t_k) + \overline{F}_z(t)S_z(t,t_k) + \overline{F}_u(t)\Delta_{t_k}(t) \tag{4.62a}$$

$$0 = \overline{H}_x(t)S_x(t,t_k) + \overline{H}_z(t)S_z(t,t_k) + \overline{H}_u(t)\Delta_{t_k}(t) \tag{4.62b}$$

$$S_y(t,t_k) = \overline{G}_x(t)S_x(t,t_k) + \overline{G}_z(t)S_z(t,t_k) + \overline{G}_u(t)\Delta_{t_k}(t) \tag{4.62c}$$

with initial condition $S_x(t_k,t_k) = \mathbf{0}_{\mathbf{N_x \times N_u}}$ – since we assume that (4.7) is a causal system – and

$$\overline{F}_\nu(t) = \nabla_\nu f(\overline{x}(t), \overline{z}(t), \overline{u}(t)), \quad \nu = \{x, z, u\} \tag{4.63a}$$

$$\overline{H}_\nu(t) = \nabla_\nu h(\overline{x}(t), \overline{z}(t), \overline{u}(t)), \quad \nu = \{x, z, u\} \tag{4.63b}$$

$$\overline{G}_\nu(t) = \nabla_\nu g(\overline{x}(t), \overline{z}(t), \overline{u}(t)), \quad \nu = \{x, z, u\} \tag{4.63c}$$

where ∇_ν is the Jacobian operator with respect to ν and $\Delta_{t_k}(t) = H(t - t_k) - H(t - t_k - t_s)$, with $H(t - t_k)$ being the unitary Heaviside step function (see Figure 4.29).

$$H(t - t_k) = \begin{cases} 0, & t < t_k \\ 1, & t \geq t_k \end{cases} \tag{4.64}$$

Note that the initial conditions for the equations in (4.62) are given by $S_x(t_k,t_k) = \mathbf{0}_{\mathbf{N_x \times N_u}}$ but in general it may be necessary to obtain the initial conditions by directly applying the definition of sensitivity. Now consider a modified input sequence

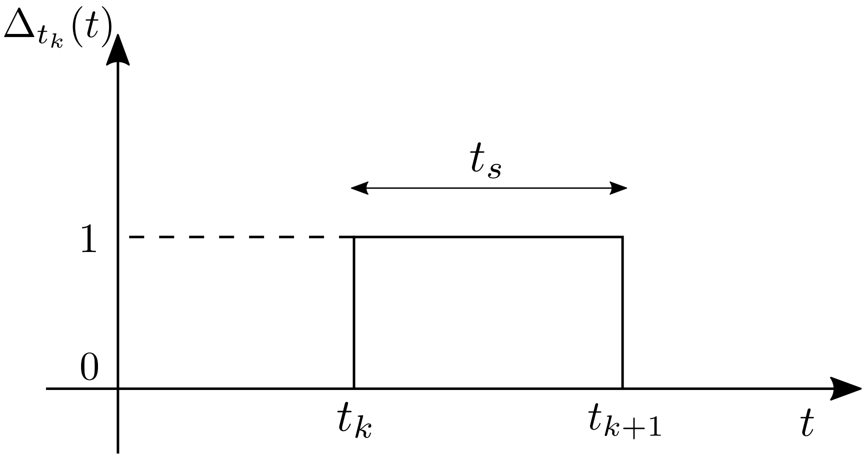

FIGURE 4.29: Representation of the signal $\Delta_{t_k}(t)$ as sum of unitary Heaviside functions.

$\tilde{\mathbf{u}}_{[t_k,t_{k+H}]} = [\tilde{u}(t_k), \tilde{u}(t_{k+1}), \cdots, \tilde{u}(t_{k+H-1})]$ which can be obtained from the nominal input sequence by

$$\tilde{\mathbf{u}}_{[t_k,t_{k+H}]} = \overline{\mathbf{u}}_{[t_k,t_{k+H}]} + \delta\mathbf{u}_{[t_k,t_{k+H}]} \tag{4.65}$$

where $\delta\mathbf{u}_{[t_k,t_{k+H}]} = [\delta u^\top(t_k), \delta u^\top(t_{k+1}), \cdots, \delta u^\top(t_{k+H-1})]^\top$ is the sequence of the input variations over the time window $[t_k, t_{k+H}]$. The sensitivity-based approximation of the states, algebraic variables, and output trajectories which correspond to the sequence $\tilde{\mathbf{u}}_{[t_k,t_{k+H}]}$ is given by (Li and Biegler, 1989; De Oliveira and Biegler, 1995; Šantin et al., 2016)

$$\tilde{\mathbf{x}}_{[t_k,t_{k+H}]} \sim \hat{\mathbf{x}}_{[t_k,t_{k+H}]} = \overline{\mathbf{x}}_{[t_k,t_{k+H}]} + \Pi^x_{[t_k,t_{k+H}]}\delta\mathbf{u}_{[t_k,t_{k+H}]} \tag{4.66a}$$

$$\tilde{\mathbf{z}}_{[t_k,t_{k+H}]} \sim \hat{\mathbf{z}}_{[t_k,t_{k+H}]} = \overline{\mathbf{z}}_{[t_k,t_{k+H}]} + \Pi^z_{[t_k,t_{k+H}]}\delta\mathbf{u}_{[t_k,t_{k+H}]} \tag{4.66b}$$

$$\tilde{\mathbf{y}}_{[t_k,t_{k+H}]} \sim \hat{\mathbf{y}}_{[t_k,t_{k+H}]} = \overline{\mathbf{y}}_{[t_k,t_{k+H}]} + \Pi^y_{[t_k,t_{k+H}]}\delta\mathbf{u}_{[t_k,t_{k+H}]} \tag{4.66c}$$

where the matrices $\Pi^{\nu}_{[t_k,t_{k+H}]}$, with $\nu = \{x, z, y\}$, are defined by

$$\Pi^{\nu}_{[t_k,t_{k+H}]} = \begin{bmatrix} S_\nu(t_k, t_k) & 0 & \cdots & 0 \\ S_\nu(t_{k+1}, t_k) & S_\nu(t_{k+1}, t_{k+1}) & \cdots & 0 \\ S_\nu(t_{k+2}, t_k) & S_\nu(t_{k+2}, t_{k+1}) & \cdots & 0 \\ \vdots & \vdots & \ddots & \vdots \\ S_\nu(t_{k+(H-1)}, t_k) & S_\nu(t_{k+(H-1)}, t_{k+1}) & \cdots & S_\nu(t_{k+(H-1)}, t_{k+(H-1)}) \end{bmatrix} \tag{4.67}$$

in which the sensitivities matrices are obtained by integrating the continuous-time system in (4.62) together with (4.7). This step constitutes the main difference with respect to a standard LTV approach, for which the model sensitivities are computed only at discrete time instants, resulting in a loss of accuracy.

Sensitivity-Based MPC This section presents a model-predictive control approach for the system (4.7) based on the linearized model (4.66). Using the latter together with a proper cost function, which aims to track a reference output point, the optimization can be formulated as a Quadratic Program (QP). In this way, it is possible to significantly reduce the computational cost compared to nonlinear MPC, thus enabling the use of the proposed strategy in on-line control applications. The objective function to be minimized at each time step t_{k_0} is

$$\begin{aligned} J(x(t_{k_0})) = & \|\hat{x}(t_{k_0+H}) - x^{ref}\|^2_{Q_t} + \sum_{k=k_0}^{k_0+H-1} \|\hat{x}(t_k) - x^{ref}\|^2_{Q_x} + \sum_{k=k_0}^{k_0+H} \|\hat{z}(t_k) - z^{ref}\|^2_{Q_z} \\ & + \sum_{k=k_0}^{k_0+H} \|\hat{y}(t_k) - y^{ref}\|^2_{Q_y} + \sum_{k=k_0}^{k_0+H-1} \|\bar{u}(t_k) + \delta u(t_k) - u^{ref}\|^2_{R} + J_{reg}(t_{k_0}) \end{aligned} \tag{4.68}$$

where the vectors $x^{ref} \in \mathbb{R}^{N_x}$, $z^{ref} \in \mathbb{R}^{N_z}$, $y^{ref} \in \mathbb{R}^{N_y}$ and $u^{ref} \in \mathbb{R}^{N_u}$ correspond to the reference point that the MPC aims to track and the matrices $Q_x \in \mathbb{R}^{N_x \times N_x}$, $Q_z \in \mathbb{R}^{N_z \times N_z}$, $Q_y \in \mathbb{R}^{N_y \times N_y}$ and $R \in \mathbb{R}^{N_u \times N_u}$ are design parameters which are weights in the MPC cost function, with $Q_x, Q_z, Q_y \geq 0$ and $R > 0$. The matrix $Q_t \geq 0$ is used as terminal penalty and the additional term $J_{reg}(t_{k_0})$ acts as a small regularization factor in order to avoid abrupt variations and spikes in the input control law and it is given by

$$J_{reg}(t_{k_0}) = \sum_{k=k_0}^{k_0+H-1} \|u(t_k) - u(t_{k-1})\|^2_{R_{reg}} \tag{4.69}$$

where $R_{reg} \in \mathbb{R}^{N_u \times N_u}$. The resulting optimization to be solved at each time step t_{k_0}, within a *receding-horizon* fashion, consists in finding the sequence $\delta\mathbf{u}^{\star}{}_{[t_{k_0}, t_{k_0+H}]}$ which minimizes the cost function (4.68), subject to the system dynamics in (4.66) and the following constraints

$$\begin{aligned}
&\bar{u}(t_k) + \delta u(t_k) \in \mathcal{U}, \quad k = k_0, k_0+1, \cdots, k_0+H-1 && \text{(4.70a)}\\
&\hat{x}(t_k) \in \mathcal{X}, \quad k = k_0+1, k_0+1, \cdots, k_0+H-1 && \text{(4.70b)}\\
&\hat{z}(t_k) \in \mathcal{Z}, \quad k = k_0+1, k_0+1, \cdots, k_0+H && \text{(4.70c)}\\
&\hat{y}(t_k) \in \mathcal{Y}, \quad k = k_0+1, k_0+1, \cdots, k_0+H && \text{(4.70d)}\\
&\hat{x}(t_{k_0+H}) \in \mathcal{X}_t && \text{(4.70e)}\\
&A_x^{\top}\hat{x}(t_k) + A_z^{\top}\hat{z}(t_k) + A_y^{\top}\hat{y}(t_k) \leq b, \quad k = k_0, \cdots, k_0+H && \text{(4.70f)}
\end{aligned}$$

where the sets $\mathcal{U}$, $\mathcal{X}$, $\mathcal{Z}$, $\mathcal{X}_t$ are considered as box sets, such as for instance $\mathcal{U} = \{u \in \mathbb{R}^{N_u} : u^{lb} \leq u \leq u^{ub}\}$, with u^{lb}, $u^{ub} \in \mathbb{R}^{N_u}$ lower and upper bounds, respectively, and (4.70f) represents a generic linear constraint, with $A_x \in \mathbb{R}^{N_x}$, $A_z \in \mathbb{R}^{N_z}$ and $A_y \in \mathbb{R}^{N_y}$ and $b \in \mathbb{R}$. The optimal control sequence is finally obtained as

$$\tilde{\mathbf{u}}^{\star}_{[t_{k_0}, t_{k_0+H}]} = \bar{\mathbf{u}}_{[t_{k_0}, t_{k_0+H}]} + \delta\mathbf{u}^{\star}{}_{[t_{k_0}, t_{k_0+H}]} \tag{4.71}$$

and the first element $\tilde{u}^{\star}(t_{k_0})$ is applied to the system. The process is then repeated at the successive time step.

Note that the corresponding nonlinear MPC formulation (nMPC) can be obtained by substituting the approximated sequences $\hat{\mathbf{x}}_{[t_{k_0}, t_{k_0+H}]}$, $\hat{\mathbf{z}}_{[t_{k_0}, t_{k_0+H}]}$ and $\hat{\mathbf{y}}_{[t_{k_0}, t_{k_0+H}]}$ in the cost function and the constraints above with $\tilde{\mathbf{x}}_{[t_{k_0}, t_{k_0+H}]}$, $\tilde{\mathbf{z}}_{[t_{k_0}, t_{k_0+H}]}$ and $\tilde{\mathbf{y}}_{[t_{k_0}, t_{k_0+H}]}$, which are the ones computed by simulating the nonlinear system (4.7) when the input $\tilde{\mathbf{u}}_{[t_{k_0}, t_{k_0+H}]}$ is applied.

Remark 7 *The performance of the sensitivity-based linearization and the corresponding MPC algorithm is significantly affected by the choice of the nominal input sequence* $\bar{\mathbf{u}}_{[t_{k_0}, t_{k_0+H}]}$

and this constitutes in the authors opinion the main limitation of the proposed approach. Here we adopt the following choice. Suppose that, at the beginning, the nominal input sequence is not known. Then the most likely input sequence should be used as the initial guess, since no further information is available. Then, after each iteration of the MPC algorithm, the nominal input sequence is updated as

$$\bar{\mathbf{u}}_{[t_{k_0+1},t_{k_0+H+1}]} = \begin{bmatrix} \tilde{\mathbf{u}}^{\star}_{[t_{k_0+1},t_{k_0+H}]} \\ \tilde{\mathbf{u}}^{\star}_{[t_{k_0+H-1},t_{k_0+H}]} \end{bmatrix} \tag{4.72}$$

where $\tilde{\mathbf{u}}^{\star}_{[t_{k_0},t_{k_0+H}]}$ *is the optimal solution of the sMPC at the time* t_{k_0}. *In case of highly nonlinear systems, the initialization of the nominal input sequence has to be done carefully to achieve a sufficiently accurate linearized model in the first iteration.*

4.3.3.2 Simulation Results

The proposed methodology is here evaluated to the control of a lithium-ion battery pack. In particular, simulation results are described with focus on the comparison between the sensitivity-based approach and the one based on a nonlinear MPC. Moreover, the results obtained in the same simulation settings with a standard CC-CV algorithm are also presented. Finally, an analysis on how the computational times of sMPC and nMPC grow with the increase in the number of cells is considered and the methodologies are tested on a challenging scenario of the battery pack of an electric motorbike.

Control of a Lithium-Ion Battery The optimal control method proposed in 4.3.3.1 is here adapted to the management of a lithium-ion battery, whose cells are arranged as in Figure 4.7, with N series modules of M parallel-connected cells. The total number of cells is given by $N_{cells} = NM$. The objective of the control algorithm is to bring the state of charge of each cell as close as possible to SOC_{ref} while satisfying all the safety constraints. Each cell is modelled according to the equations described in 2.4.2.2, while the model of the whole battery pack is given in Section 4.3.1. The variables are defined by

$$u(t_k) = [I_{b,1}(t_k),\, I_{b,2}(t_k),\, \cdots,\, I_{b,N}(t_k)]^\top \tag{4.73a}$$

$$x(t_k) = [x_{1,1}^\top(t_k),\, x_{1,2}^\top(t_k),\, \cdots,\, x_{N,M}^\top(t_k)]^\top \tag{4.73b}$$

$$z(t_k) = [I_{1,1}(t_k),\, I_{1,2}(t_k),\, \cdots,\, I_{N,M}(t_k)]^\top \tag{4.73c}$$

$$y(t_k) = [y_{1,1}^\top(t_k),\, y_{1,2}^\top(t_k),\, \cdots,\, y_{N,M}^\top(t_k)]^\top \tag{4.73d}$$

where $x_{i,j}(t_k) \in \mathbb{R}^{N_x^{cell}}$ and $y_{i,j}(t_k) \in \mathbb{R}^{N_y^{cell}}$ represent respectively the states and outputs of the j-th cell of the i-th module. While the former consist of all the differential variables defined in 2.4.2.2 (i.e. positive stoichiometry, average concentration fluxes, electrolyte concentrations in the different volumes, temperature, SEI resistance and capacity loss), the latter are defined as follows,

$$y_{i,j}(k) = \left[V_{i,j}(k),\, SOC_{i,j}(k)\right]^\top \tag{4.74}$$

Note that, since we consider in the following a constant battery charger current $I_{ch}(t) = I_{ch}$, the system inputs are given by the N generators $I_{b,i}(t) \geq 0$, $i = 1, \ldots, N$ which allow to drain the current flowing through the different modules. The resulting model is a semi-explicit continuous-time system of DAEs (see (4.7)) where $N_x = N_{cells} N_x^{cell}$, $N_u = N$, $N_z = N_{cells}$, and $N_y = N_{cells} N_y^{cell}$, in which $N_x^{cell} = 6 + 3P$ (for a P number of finite volumes) and $N_y^{cell} = 2$ are the number of states and outputs of each single cell, respectively.

A suitable choice of the weights allows to adapt the cost function (4.68) in order to the track the reference state of charge SOC_{ref} with limited input utilization

$$J(x(t_{k_0})) = J_{reg}(t_{k_0}) + \sum_{j=1}^{M} \sum_{i=1}^{N} \sum_{k=k_0}^{k_0+H} \|SOC_{i,j}(t_k) - SOC_{ref}\|^2_{q_{SOC}} + \sum_{i=1}^{N} \sum_{k=k_0}^{k_0+H-1} \|I_{b,i}(t_k)\|^2_r \tag{4.75}$$

with Q_x, Q_z and Q_t considered as null matrices and $q_{SOC}, r \in \mathbb{R}_{>0}$. In addition, the constraints in (4.70) are used in order to impose limits for every cell on temperature, voltage, and applied and drained currents as follows

$$0 \geq I_{b,i}(t_k) \leq |I_{ch}|, \quad k = k_0, k_0+1, \cdots, k_0+H-1 \tag{4.76a}$$

$$T_{i,j}(t_k) \leq T_{max}, \quad k = k_0, k_0+1, \cdots, k_0+H \tag{4.76b}$$

$$I_{min} \leq I_{i,j}(t_k) \leq I_{max}, \quad k = k_0, k_0+1, \cdots, k_0+H \tag{4.76c}$$

$$V_{min} \leq V_{i,j}(t_k) \leq V_{max}, \quad k = k_0, k_0+1, \cdots, k_0+H \tag{4.76d}$$

$$SOC_{min} \leq SOC_{i,j}(t_k) \leq SOC_{max}, \quad k = k_0, k_0+1, \cdots, k_0+H \tag{4.76e}$$

where we assume that the maximum current that the generators can drain corresponds to the absolute value of the battery charger one.

Model Parameters and Simulations Settings We consider a battery pack as described in 4.3.1, with both series and parallel connections. Each cell is modelled according to the control-oriented electrochemical model in 2.4.2.2, where the open-circuit potentials and electrolyte conductivity functions are given as in (3.35) and (3.37). Even in this case, the parameters, except for the ones related to the ageing dynamics, which are taken from (Santhanagopalan et al., 2006), are those experimentally identified in (Ecker et al., 2015a; Ecker et al., 2015b). The thermal capacity, thermal resistance, and environmental temperature are assumed equal to $C_{th} = 4186\,\mathrm{J/K}$, $R_{th} = 169.5\,\mathrm{K/W}$, and $T_{env} = 298.15\,\mathrm{K}$, and the initial value for the temperature is set to $T^0 = 298.15\,\mathrm{K}$ for all cells. The initial electrolyte concentration and average concentration flux are assumed to start at equilibrium values $1000\,\mathrm{mol/m^3}$ and zero respectively. The initial state of charge of the different cells, as well as the capacity and the SEI resistance, are extracted from a Gaussian distribution as

$$SOC^0_{i,j} \in \mathcal{N}(SOC^0, \sigma^2_{SOC}) \tag{4.77a}$$

$$C^0_{i,j} \in \mathcal{N}(C^0, \sigma^2_C) \tag{4.77b}$$

$$R^0_{sei,i,j} \in \mathcal{N}(R^0_{sei}, \sigma^2_{R_{sei}}) \tag{4.77c}$$

with $SOC^0 = 0.50$, $R^0_{sei} = 15\,\mathrm{m\Omega}$, and $C^0 = 7.5\,\mathrm{Ah}$ (i.e., $I_{1C} = 7.5\,\mathrm{A}$), while the standard deviations are $\sigma_{SOC} = 0.1$, $\sigma_{R_{sei}} = 0.75\,\mathrm{m\Omega}$, and $\sigma_C = 0.375\,\mathrm{Ah}$ (see Table

	Cell 1	Cell 2	Cell 3	Cell 4
Nominal Capacity $[Ah]$	7.2415	7.5301	7.8321	7.7944
Series Resistance $[m\Omega]$	15.2	15.7	15.4	15.7

TABLE 4.5: Cell parameters employed in the simulation.

P	H	t_s	SOC_{ref}	I_{ch}	q^{SOC}	r
2	3	40 s	1	$1.5MI_{1C}$	10^{-2}	1.78×10^{-5}
V_{min}	V_{max}	T_{max}	I_{min}	I_{max}	SOC_{min}	SOC_{max}
2.7 V	4.2 V	318.15 K	$-1.5I_{1C}$	0 A	0	1

TABLE 4.6: Parameters of the optimal control algorithms.

4.5 for the resistance and capacity of the cells).

Note that, differently from what has been done in 4.3.2, the nMPC framework relies on the same model considered as the real plant, while the sMPC exploits a sensitivity-based linearization of this latter. Moreover, although the internal states of each cell are not measurable in practice, we draw here the assumption of measurability of all the relevant states. The use of observers goes beyond our scope, which is to highlight the suitability of the sensitivity-based approach to real-time optimal control. For the design of observers for battery states, the interested reader can refer to e.g. (Waag, Fleischer, and Sauer, 2014). The optimization settings are reported in Table 4.6.

All the simulations were performed on a Windows 10 personal computer with 16 Gbytes of RAM and a 2.5 GHz i7vPro processor. The control problems were solved using *CasADi* (Andersson et al., 2019), a symbolic framework for automatic differentiation. This software offers a Matlab interface for the Interior Point Optimization Method (IPOPT) (Wächter and Biegler, 2006) used for solving the optimizations, and for the SUNDIALS suite used for integrating the process dynamics. Moreover, *CasADi* was used for the computation of the sensitivity matrices along the nominal trajectory. In order to provide a fair comparison between sMPC and nMPC, both of the underlying optimizations were solved using IPOPT.

Comparison Between sMPC and nMPC This section considers a battery pack composed by $N = 2$ modules with $M = 2$ parallel-connected cells for each module and

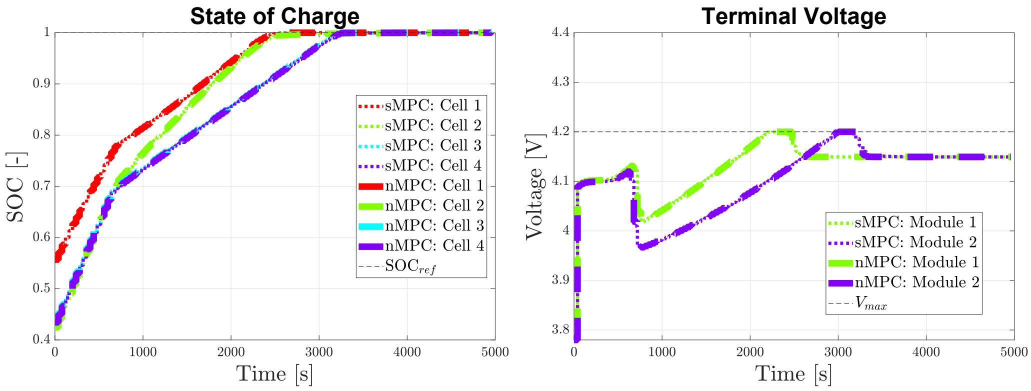

(a) State of charge (b) Voltage

FIGURE 4.30: Temporal evolution of the state of charge and voltage for sMPC and nMPC. Only the voltage of the two modules is shown in (b) since all the cells of a particular module present the same voltage due to the parallel connection.

provides a comparison between the performance of the proposed sensitivity-based MPC and the one of a nonlinear MPC taken as benchmark. The temporal evolution of the states and outputs obtained by sMPC (dotted line) and nMPC (dashed line) are very similar (see Figures 4.30–4.32), with nearly complete overlap. For both the formulations, the state of charge for all of the cells reaches the desired target within 3500 s (Figure 4.30(a)), while the constraints on the voltage and temperature for all of the battery cells are satisfied for all time (Figures 4.30(b) and 4.31(a)). The current flowing in the different cells as well as the input actions (i.e. the drained currents $I_{b,1}$ and $I_{b,2}$) are nearly identical for the two MPC formulations, as it is shown in Figure 4.31(b) and 4.32(a). Figure 4.32(b) reports the mean computational times needed by the two methods to compute the optimal control sequence at each time step. As it can be noticed, while having very similar closed-loop performance, the on-line computational cost of the sensitivity-based MPC is significantly lower than for the nMPC, motivating the use of sMPC algorithms in the context of real-time control of battery packs. Also, the on-line computational time of nMPC is highly variable while being nearly deterministic for the sMPC, due to the fact that the time required for obtaining a solution in a quadratic program is weakly dependent on the values of its parameters. Note that having low variability in the computational burden is another desirable feature of the sMPC.

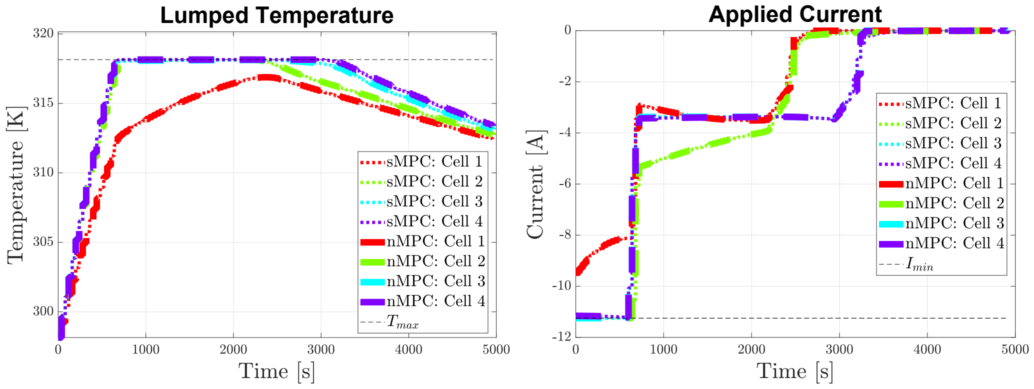

(a) Temperature

(b) Current

FIGURE 4.31: Temporal evolution of the temperature and current for sMPC and nMPC.

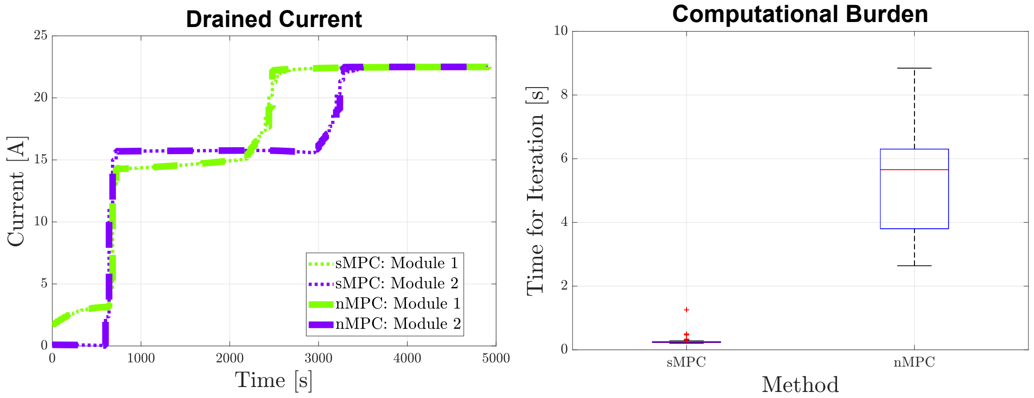

(a) Drained current

(b) Computational time

FIGURE 4.32: Temporal evolution of the drained current for the two modules and the computational times for sMPC and nMPC.

Standard CC-CV Method To demonstrate the need for an optimal management of a lithium-ion battery pack that is able to take into account input and output constraints, a standard CC-CV algorithm is applied to the same configuration considered in the previous paragraph. In order to implement the CC-CV, the battery pack needs to be equipped with a system of switches which allows to commute from the galvanostatic constant current phase to the potentiostatic constant voltage one. The temporal evolution of the state of charge, voltage, temperature, and currents of the different cells when a CC-CV is applied are shown in Figures 4.33(a), 4.33(b), 4.34(a), and 4.34(b). Two scenarios were considered which differ in the value of the current

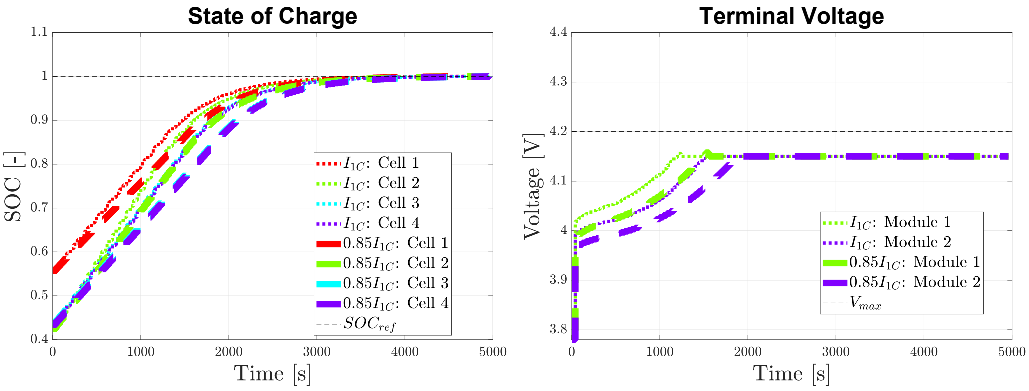

(a) State of charge (b) Voltage

FIGURE 4.33: Temporal evolution of the state of charge and voltage for CC-CV charging for two values for the value of the constant current

applied during the galvanostatic phase. A constant current of $I_{cc} = MI_{1\mathrm{C}}$ (dotted line) results in high temperature constraint violation in most of the cells, with a charging time of 3960 s. On the other hand, for a lower constant current (dashed line) of $I_{cc} = 0.85MI_{1\mathrm{C}}$, the temperature constraint is satisfied for each cell, but the charging time increases significantly (4360 s). Moreover, the value of the constant current I_{cc} which guarantees the satisfaction of the temperature constraint must be found experimentally and can change according to the external environment conditions as well as with the battery ageing and degradation.

Table 4.7 compares the charging time, computational time, and maximum temperature and voltage for the sMPC, the nMPC, and the two CC-CV charging protocols. The MPC algorithms exhibit the same charging times as well as the same maximum temperatures and voltages, while the sMPC required only about 6% of the on-line computational time.

Scaling of the Computational Time for Increasing Number of Cells The above simulations showed that the sMPC method has much lower on-line computational cost than nMPC for a battery pack of 4 cells. Figure 4.35 displays the mean computational time for sMPC and nMPC for an increasing the number of series and parallel connections. sMPC is about one order of magnitude faster than nMPC, which is a significant saving in on-line computational cost when dealing with large battery packs.

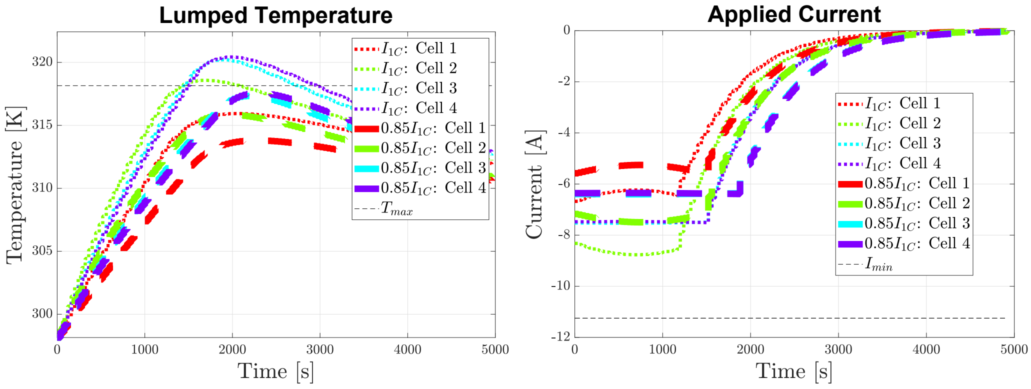

(a) Temperature

(b) Current

FIGURE 4.34: Temporal evolution of the temperature and applied current (the sum of the current for the cells of each module produces the CC-CV profile) for CC-CV charging for two values for the constant current.

	sMPC	nMPC	CC-CV (I_{1C})	CC-CV ($0.85I_{1C}$)
Charging Time	3280 s	3280 s	3960 s	4360 s
Computational Time	0.24 s	3.91 s	–	–
Maximum Temperature	318.15 K	318.15 K	320.42 K	317.55 K
Maximum Voltage	4.2 V	4.2 V	4.15 V	4.15 V

TABLE 4.7: Comparison of charging time, computational time and maximum temperature and voltage reached for sMPC, nMPC, and CC-CV charging.

Remark 8 *In this section we have taken into account a battery which consists of N series-connected modules, each of which is constituted of M parallel-connected cells (see Figure 4.7). It has to be noticed that the only coupling element among cells of different series modules is the heat exchange between adjacent ones in (4.46). Therefore, each series module can be simulated independently if we consider the temperature of adjacent cells which belong to other modules to be constant over the sampling time and we assume the possibility of efficient transfer data among parallel threads. This may further increase the computational performance of the sensitivity-based MPC. Also, a distributed MPC can be employed in which the optimal control input for each series module is computed in parallel with the others, by relying on local measurements and local dynamics (Camponogara et al., 2002). Notice that, in the event in which such distributed solutions were adopted, we could rely on parallelization over the various processors of the on-board computer in the battery management system.*

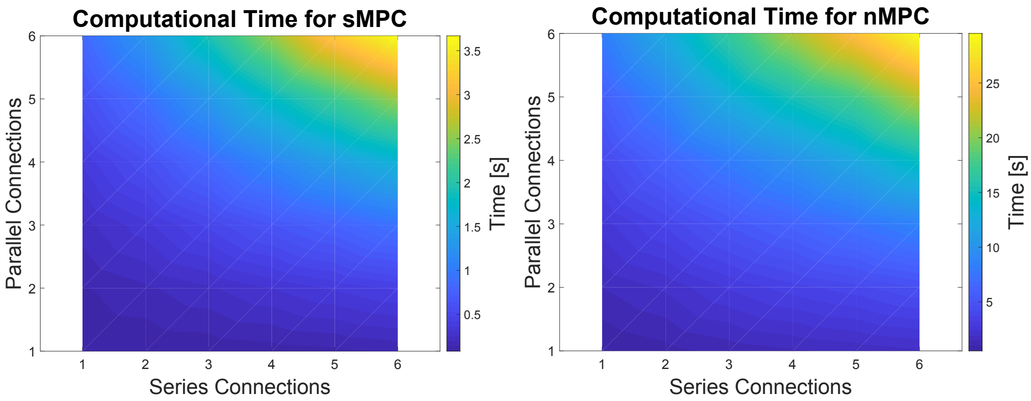

(a) sMPC

(b) nMPC

FIGURE 4.35: Mean computational time for the two MPC formulations for up to 6 series and 6 parallel connections. The mean value was computed for hundreds of iterations to ensure statistical significance.

Optimal Control of an Electric Motorbike Battery Pack This section shows, by means of simulative results, the applicability of the proposed sensitivity-based MPC to the control of large battery packs modelled as in 4.3.1, for which nMPC has high on-line computational cost. In this case study, the task is to control the battery of a fully electric motorbike, namely, the electric Vespa Piaggio with a stored energy of $86Ah$ and a nominal voltage of $48V$ (i.e., a configuration with 156 cells, arranged in 13 series-connected modules, each with 12 parallel-connected cells, for the Kokam SLPB 75106100). All the cells composing the battery are modelled as SPMeT with ageing dynamics (see 2.4.2.2). The mean computational time required for each iteration of nMPC is $250s$, which is incompatible with the desired sampling time ($t_s = 40s$). On the other hand, the mean computational time of sMPC is $30s$, which is less than the sampling time.

FIGURE 4.36: Electirc Vespa Piaggio. Credit by *Redazione EcoDesign*.

4.3.3.3 Conclusions about Sensitivity-based MPC

While in 4.3.2 a nonlinear MPC formulation has been demonstrated to achieve high performance and ensuring constraints satisfaction for series-connected cells, an alternative sensitivity-based MPC formulation is here proposed for the optimal charging of a battery pack composed of several cells arranged in series and parallel connections. Each cell is described through an electrochemical model that includes kinetics, mass transport, and thermal effects in order to capture the internal physico-chemical phenomena. Results show that the sMPC approach has closed-loop performance similar to the nMPC one but greatly reduces the on-line computational cost, thus making optimal model-based control suitable for a real-time implementation on a battery pack composed of dozens of cells. The effectiveness of the strategy is tested in simulation, where it is shown that the sensitivity-based MPC is successful in providing real-time optimal charging for a fully electric motorbike composed of 156 cells, each of them modelled as single-particle model with electrolyte and thermal dynamics. Future works may imply the experimental validation of the sensitivity-based MPC on a real battery pack.

4.4 Conclusions

In this chapter different formulations of model-predictive control have been applied for the management of lithium-ion batteries. Specifically, we firstly consider the problem of single-cell optimal charging, with focus on energy dissipation and ageing reduction when the charging time is fixed to be the same of a benchmark approach. Subsequently, a balancing-aware charging procedure for series-connected cells is proposed, together with a specific circuitry scheme which allows for the cell bypass. Finally, the optimal management of a whole battery pack with series and parallel arrangements of the cells is considered and, in particular, a control methodology is exploited such that, by relying on the so-called sensitivity-based linearization, allows for a real-time implementation. The results shown in this chapter aim at highlighting that the use of optimization-based methodologies can enhance significantly the performance of lithium-ion battery management when compared with standard rule-based protocols.

Chapter 5

Reinforcement Learning for Batteries and HEVs Management

In the previous chapter the exploitation of MPC concepts has been largely proposed for the solution of typical battery problems. Although MPC has been successfully employed in several practical applications during the last decades, it is known that the controller performance is significantly affected by model inaccuracies. Also, the *receding-horizon* approach requires the repeated solution of a possibly large-scale optimization problem, which can be computationally prohibitive for real-time application in the case of nonlinear systems. In addition, due to the fact that the MPC formulation lacks the proper accounting of future feedbacks, it appears inherently limited to handle uncertain systems in an optimal manner (Lee, 2011). Within this context, the use of dynamic programming appears more suited, due to the fact that DP directly accounts for an uncertain setting by relying on the concept of Markov Decision Process (MDP) and provides an explicit feedback control law which is computed off-line according to the Bellman's principle (Bertsekas et al., 1995). Nevertheless, dynamic programming still requires an accurate model of the probability distributions which are involved in the process to be controlled and its practical use is limited to simple tasks due to the so-called "curse of dimensionality" issue (Rust, 1997).

In recent years, reinforcement-learning techniques have been employed in the literature with the aim of overcoming some of the aforementioned issues. In particular, reinforcement learning is based on the MDP framework exactly like dynamic programming, but it differs from the latter in that it is able to compute an optimal feedback control law by exploiting a model-free configuration (i.e. it learns directly interacting with the plant), and, even most importantly, solves the "curse of dimensionality" with the use of function approximators (Powell, 2007).

In the following, the main features of RL are presented in Section 5.1, while its applicability to the context of lithium-ion battery fast charging is considered in Section 5.2. Finally, the RL performance in the field of optimal eco-driving for autonomous hybrid electric vehicles is assessed in Section 5.3.

5.1 Reinforcement-Learning Methodology

In a reinforcement-learning framework we usually refer to the controller as the agent, whose control actions are taken according to the state configuration of the environments. This latter, according to the MDP formulation, includes everything but the agent, i.e. in particular the process to be managed together with disturbances and uncertainties. In the model-free formulation, the agent learns the feedback control policy through a direct interaction with the environment in terms of reward and the state observation, which are received by the agent at each time step (Sutton, Barto, et al., 1998). Note that it is the responsibility of the control system designer to construct a proper reward function in order to make the agent learn how to accomplish the desired task.

Among all the RL algorithms two main groups can be identified: tabular methods (e.g. Q-learning and SARSA) and approximate solution methods which are also known as approaches based on Approximate Dynamic Programming (ADP). Although the convergence of the former to an optimal solution has been proven under mild assumptions, their exploitation is limited to tasks with small and discrete set of actions and states, due to the curse of dimensionality, while the latter can be used even with continuous state and action spaces. However, no proof of convergence exists for ADP methods in the general case. Note that, when deep neural networks (Liu et al., 2017) are considered as function approximators, we usually speak of deep RL (Arulkumaran et al., 2017).

The interest of the scientific community in deep RL has greatly increased due to its recent successes in several applications (Mnih et al., 2015; Schulman et al., 2015; Lillicrap et al., 2015). While all these works provide a description of RL from the computer science point of view, a control engineering perspective can be found in (Lewis, Vrabie, and Vamvoudakis, 2012), where a link between RL and optimal adaptive control is depicted.

In the following, the MDP framework and the dynamic programming approach are firstly recalled in 5.1.1. Then, the concept of state-action value function is defined in 5.1.2, while an overview of the main reinforcement-learning features together with its differences and advantages with respect to dynamic programming is given in 5.1.3. Finally, the policy-gradient algorithms are described in 5.1.4, with particular attention to the deep-deterministic policy gradient (Lillicrap et al., 2015) which is implemented for the solution of the problems discussed in the rest of the chapter.

5.1.1 Markov Decision Process and Dynamic Programming

Most of the optimal control problems can be formulated as an MDP. Consider a discrete-time formulation in which the variables of interest are evaluated at the discrete instants $t_k \in \mathbb{R}$, with $k \in \mathbb{N}$ such that $t_{k+1} = t_k + t_s$, where t_s is the adopted sampling time. Then, every feasible action $u(t_k) \in \mathcal{U}$ that the agent takes in a particular state configuration $x(t_k) \in \mathcal{X}$ of the environment, leads to both a transition to the next state $x(t_{k+1}) \in \mathcal{X}$ and a reward $r(t_k) \in \mathbb{R}$. These variables may be stochastic according to the probability distributions $p_x(x(t_{k+1})|x(t_k), u(t_k))$ and $p_r(r(t_k))|x(t_{k+1}), x(t_k), u(t_k))$. Given a policy π such that $u(t_k) = \pi(x(t_k))$, we define the state value function $V^\pi(x(t_k))$ as the expected discounted return

$$V^\pi(x(t_k)) = \mathbb{E}\left[\sum_{\bar{k}=k}^{\infty} \gamma^{\bar{k}} r(t_{\bar{k}}) \mid x(t_k)\right] \tag{5.1}$$

where γ is the discount factor.

The agent's goal is to solve the MDP by retrieving the optimal policy $\pi^\star$ which maximizes the following optimization problem

$$V^\star(x(t_k)) = \max_\pi \; V^\pi(x(t_k)) \tag{5.2}$$

where $V^\star(x(t_k))$ is the optimal state value function. Note that such MDP formulation will be considered through the rest of the chapter.

The use of dynamic programming is quite common in solving MDPs, and has been extensively employed. The optimal policy $\pi^\star$ is computed iteratively (see value and policy iteration methods (Howard, 1960)) through the exploitation of the Bellman's optimality principle. However, the DP concept solves (5.2) by assuming a perfect knowledge of the environment probability distributions p_x and p_r. This constitutes a huge limitation for realistic scenarios in which the model accuracy is questionable. Moreover, DP is subject to the so-called curse of dimensionality, which implies an exponential growth of computational burden and memory as the state and action dimensions grow (Rust, 1997).

5.1.2 State-Action Value Function

As previously discussed, the computation of the optimal state value function $V^\star(x(t_k))$ and the optimal policy $\pi^\star$ through DP requires an explicit knowledge of the environment's dynamics. To alleviate this requirement, we consider the state-action value function $Q^\pi(x(t_k), u(t_k))$, related to the policy π, which is the key mathematical object in many model-free reinforcement learning methodologies

$$Q^\pi(x(t_k), u(t_k)) = \mathbb{E}\left[\sum_{\bar{k}=k}^{\infty} \gamma^{\bar{k}} r(t_{\bar{k}}) \mid x(t_k), u(t_k)\right] \tag{5.3}$$

Note that the state-action value function (also known as *Q-function*) at the time instant t_k depends on the action $u(t_k)$ chosen at that time. In this way, the Q-function associated with the policy π describes the expected return by taking an action $u(t_k)$ in the state $x(t_k)$, and then following the policy π henceforth. If one considers the state-action value function $Q^\star(x(t_k), u(t_k))$ obtained as follows

$$Q^\star(x(t_k), u(t_k)) = \max_{\pi} Q^\pi(x(t_k), u(t_k)) \tag{5.4}$$

then it holds that

$$V^\star(x(t_k)) = \max_{u(t_k)\in\mathcal{U}} Q^\star(x(t_k), u(t_k)) \tag{5.5}$$

and the optimal policy $u^\star(t_k) = \pi^\star(x(t_k))$ can be retrieved as

$$u^\star(t_k) = \underset{u(t_k)\in\mathcal{U}}{\arg\max}\ Q^\star(x(t_k), u(t_k)) \tag{5.6}$$

It is important to notice that if the function $Q^\star(x(t_k), u(t_k))$ is known, then the optimal policy can be directly computed through (5.6) without knowing the environment dynamics.

5.1.3 Reinforcement Learning: Tabular Methods and Approximated Solutions

Several model-free reinforcement-learning strategies are based on computing the Q-function, which is learned from interactions with the surrounding environment by means of a reward collected over time. In particular, tabular methods have been widely exploited at an early stage of research. These latter are based on the concept of storing the values of the function $Q^\star(x(t_k), u(t_k))$ in a table whose entries represent the different states and actions (Watkins and Dayan, 1992). However, such approaches still suffer the "curse of dimensionality". As a consequence, tabular methods are limited to small and discrete action and state spaces, similar to dynamic programming. A possible solution can be provided by the use of approximate dynamic programming techniques (Powell, 2007). The main feature of ADP is the parametrization of the Q-function using value function approximators, as in the following

$$Q^\pi(x(t_k), u(t_k)) \approx Q(x(t_k), u(t_k)|\,\theta^{Q^\pi}) \tag{5.7}$$

with the learning process that seeks for the optimal parameter vector $\theta^{Q^\star}$, instead of directly computing the function $Q^\star(x(t_k), u(t_k))$. This significantly reduces the size of the optimization problem. The main drawback is that convergence is no longer guaranteed (in general) when a value function approximator is used. In contrast, the convergence of tabular methods has been proven under general assumptions (Sutton, Barto, et al., 1998).

Several function approximators have been employed in the literature, e.g. linear approximators, neural networks, kernel-based functions. In (Mnih et al., 2015), the deep Q-learning (DQN) algorithm is presented, which constitutes one of the most famous examples of ADP using deep neural networks as approximators. However, the DQN approach results to be limited to discrete sets of actions. Since we consider here the possibility of varying the control input in a continuous domain, our focus will be devoted to an actor-critic paradigm belonging to the class of policy-gradient methods which allows the use of continuous actions.

5.1.4 Reinforcement Learning: Policy-Gradient Methods

Here we consider the class policy-gradient methods (Sutton et al., 2000), which constitute a subset of ADP approaches able handle a continuous set of actions. In particular, with such algorithms the optimal policy is not obtained through (5.6), but is parametrized and optimized directly, i.e.

$$\pi(x(t_k)) \approx \pi(x(t_k)|\,\theta^{\pi}) \tag{5.8}$$

The simplest advantage that policy-gradient algorithms may have over action-value ones is that in certain cases the policy may be a simpler function to learn (Sutton, Barto, et al., 1998). However, pure policy-gradient methods can suffer from high variance in the optimal policy estimation. To overcome this issue, we focus on the actor-critic concept. In particular, the actor-critic method relies on two components: the actor which learns the parametrized policy, and the critic which learns the parametrized Q-function. The information provided by the critic is used as a reinforcing signal for the actor, thus being more informative than rewards obtained from the environment.

In the following the deep-deterministic policy gradient is presented (Lillicrap et al., 2015), which consists of an actor-critic algorithm that extends to continuous actions the concept of deep reinforcement learning proposed by the DQN algorithm, while maintaining some of its more important features. These latter include the use of (i) random sampling from a replay buffer, and (ii) target networks for stable learning. We model both the actor and the critic with deep neural networks following the same learning algorithm presented in (Lillicrap et al., 2015).

5.1.4.1 DDPG Algorithm

The DDPG algorithm relies on the parametrization of the critic, $Q(x(t_k),\, u(t_k)|\, \theta^Q)$, and the actor, $\pi(x(t_k)|\, \theta^\pi)$, as deep neural network. In addition, the correspondent target networks are defined as $Q'(x(t_k),\, u(t_k)|\, \theta^{Q'})$ and $\pi'(x(t_k)|\, \theta^{\pi'})$, where the parameters $\theta^{Q'}$ and $\theta^{\pi'}$ are slowly updated in order to track and filter the ones of the actual network (θ^Q and θ^π) thus reducing the chattering due to the learning process and enhancing its convergence. In the next paragraphs the concepts of critic and actor are explained in detail. Both the actual and target parameters are initialized to θ_0^π and θ_0^Q.

Critic The role of the critic is to evaluate the current policy prescribed by the actor. During the learning process (also known as training), at each time t_k, the action is obtained by adding the output of the actor network with a noise signal $\mathcal{N}(t_k)$ which allows for the exploration of the actions space, namely

$$u(t_k) = \pi(x(t_k)|\, \theta^\pi) + \mathcal{N}(t_k) \tag{5.9}$$

where the exploration noise is a random variable (e.g. Ornstein-Uhlenbeck process or Guassian process). After applying the action, the reward $r(t_k)$ and the next state $x(t_{k+1})$ are observed. At each time step, the tuple $(x(t_k),\, u(t_k),\, r(t_{k+1}),\, x(t_{k+1}))$ is stored in a replay buffer memory. Consider t_n the time instant at which the number of tuples collected in the replay memory exceeds a certain threshold $n \in \mathcal{N}$, whose value should be properly tuned by the designer. Then, at each time step t_k, with $k > n$, a random mini-batch of n tuples is sampled from the replay memory, and the index $i \in \{1, \cdots, n\}$ is used to specify that the i-th tuple corresponds to the instant t_{k_i}. Hence, we set

$$y(t_{k_i}) = r(t_{k_i+1}) + \gamma Q'(x(t_{k_i+1}),\, \pi'(x(t_{k_i+1})|\theta^{\pi'})|\theta^{Q'}) \tag{5.10}$$

According to the gradient descent method, the critic network is updated, at each time step t_k with $k > n$, as

$$\theta^Q_{k+1} = \theta^Q_k - \eta_Q \nabla_{\theta^Q} \mathcal{L}(\theta^Q_k) \tag{5.11}$$

where η_Q represents the learning rate of the critic network, and $\mathcal{L}(\theta^Q)$ is the loss function to be minimized

$$\mathcal{L}(\theta^Q) = \frac{1}{N} \sum_{i=1}^{n} \Big(y(t_{k_i}) - Q(x(t_{k_i}, x(t_{k_i} | \theta^Q) \Big)^2 \tag{5.12}$$

It is important to notice that $\theta^Q_n = \theta^Q_0$.

Actor The parameters of the actor network are updated in order to maximize the cumulative expected reward $V^\pi(x(t_k))$. In this paragraph we refer to the cumulative reward with the variable $\mathcal{J}(\theta^\pi)$, in order to highlight its dependency on the actor parametrization. The update of the actor parameters at each time t_k, with $k > n$ as in the previous paragraph, is done according to the gradient ascent method as follows

$$\theta^\pi_{k+1} = \theta^\pi_k + \eta_\pi \nabla_{\boldsymbol{\theta}^\pi} \mathcal{J}(\theta^\pi_k) \tag{5.13}$$

where η_π denotes the learning rate of the actor network. Notice that, according to the proof in (Silver et al., 2014), the policy gradient in (5.13) for the generic parameters vector θ^π and θ^Q can be expressed as

$$\nabla_{\theta^\pi} \mathcal{J}(\theta^\pi) \approx \mathbb{E} \Big[\nabla_u Q(x(t_k), \, \pi(x(t_k)) | \theta^Q) \nabla_{\theta^\pi} \pi(x(t_k) | \theta^\pi) \Big] \tag{5.14}$$

which is then approximated by samples as follows

$$\nabla_{\theta^\pi} \mathcal{J}(\theta^\pi) \approx \frac{1}{N} \sum_{i=1}^{n} \nabla_u Q(x(t_{k_i}), \, \pi(x(t_{k_i})) | \theta^Q) \nabla_{\theta^\pi} \pi(x(t_{k_i} | \theta^\pi) \tag{5.15}$$

Soft Update of Target Networks Once the parameters of critic and actor network are updated based on the randomly extracted mini-batch, then the parameters of the target networks are also updated as follows:

$$\begin{aligned} \theta^{Q'} &\leftarrow \tau\theta^{Q} + (1-\tau)\theta^{Q'} \\ \theta^{\pi'} &\leftarrow \tau\theta^{\pi} + (1-\tau)\theta^{\pi'} \end{aligned} \tag{5.16}$$

where $\tau > 0$ allows to adjust the aggressiveness of the update. Note that (5.16) improves the stability of the learning procedure, although convergence is no longer guaranteed, in general, when function approximators are used. Therefore, the choice of τ becomes a crucial point in the DDPG tuning. It is known from the literature that a small value of τ should be chosen, in order to guarantee a soft-update and reduce the possibility of divergence in the network parameters.

5.2 RL for Li-Ion Battery Fast-Charging

We have previously discussed that the most common charging algorithm in the industry is the well known CC-CV protocol, which is based on excessively conservative constraints which reduce the probability of safety hazards at the expense of higher charging times. Therefore, it is evident that the CC-CV algorithm does not constitute an optimal policy for the fast-charging problem under safety constraints. In the previous chapters we have largely considered as a possible solution the exploitation of model-based advanced battery management strategies which seek to find an optimal input trajectory based on a specified battery model (the reader is referred to 2.4 for a detailed description of the different lithium-ion cell models with their advantages and limitations). However, the exploitation of a model-based charging procedure has to face some crucial challenges:

- every model is subject to uncertainties and modeling mismatches, which affect its accuracy. Since the controller’s performance depends on the model accuracy, a proper parameter identification procedure has to be conducted based on experimentally collected data. Note that, the effectiveness of such estimation procedure is limited when electrochemical models are considered, due to the fact that in this case dozens of parameters need to be identified simultaneously;

- electrochemical models usually consist of a large number of states, thus leading to a large-scale optimization problem. Moreover, most of the states are not measurable in a realistic scenario and, therefore, the presence of an observer is required to reconstruct the full state information from the available measurements;
- the model parameters drift as the battery ages. It is important to notice that none of the model-based strategies proposed in the literature considers the adaptability of the control strategy to variations in the parameters.

In order to overcome these limitations, there has been substantial effort in the literature to design fast-charging strategies that do not rely on a mathematical model. Among them, some rule-based adaptations of the CC-CV protocol are considered, such as the one proposed in (Patnaik, Praneeth, and Williamson, 2018), where the authors have proposed a closed-loop charging technique called Constant Current - Constant Temperature - Constant Voltage (CC-CT-CV). Such approach, based on a proportional-integral-derivative (PID) controller, constitutes an output-feedback control law which enables the CC-CV protocol to consider a temperature constraint. It is important to notice that the difficulty in the state observation and in the parameter identification is no longer an issue as this strategy relies only on the output measurements. Nevertheless, some problems remain unsolved, that is (i) the optimality of the resulting charging policy is no longer guaranteed, (ii) the controller gain should be obtained by trial and error, and finally (iii) the controller does not adapt to parameters changes.

All these challenges can be addressed by using a charging procedure based on reinforcement learning. This latter consists of an agent (the battery management system) which interacts with the environment (the battery) by taking specific actions (the applied current) according to the environment configuration (the battery states or the available measurements) (Park et al., 2020). For the first time to the knowledge of the authors, a model-free reinforcement-learning framework is here proposed for the fast charging of lithium-ion batteries subject to safety constraints. The use of such a methodology enables adaptation to uncertain and drifting parameters. Moreover, the exploitation of ADP-based approaches allows one to mitigate the curse of dimensionality for large-scale nonlinear optimal control problems by adopting parametrized actor/critic networks. We rely on the DDPG algorithm described in 5.1.4.1 which allows for continuous action space and includes deep neural networks as function approximators. The control technique is tested by considering a reduced electrochemical model as the battery environment and the safety constraints are taken into account in the strategy by including a penalty in the reward function in case of violation. Note that in the following two different scenarios are presented: in the first one all the states are assumed measurable from the agent (full-states configuration), while in the second one this assumption is dropped in view of a more realistic setting and only voltage, temperature and state of charge are considered available (simplified-states configuration), with the SOC assumed to be retrieved through the Coulomb-Counting approach. The results show that the RL-agent is able to achieve high performance in both the scenarios.

In the following, the fast-charging control problem is presented in 5.2.1, while in 5.2.2 the modelling of the lithium-ion cell is discussed together with its parametrization. Finally, in 5.2.3 the simulation settings and the results are discussed.

5.2.1 Fast-Charging Control Problem

One of the crucial goals in a battery management system is to find the fastest charging algorithm which is able to satisfy safety constraints, namely finding the highest input current $I(t)$ (in the sense of absolute value) that can be applied without excessively aging and damaging the cell. The input current is limited by the hardware configuration of the battery charger, namely,

$$-I_{max} \leq I(t) \leq 0, \tag{5.17a}$$

with the convention that a negative current is charging the battery. In order to avoid safety hazards, we also consider constraints on temperature and voltage that have to be satisfied during the whole charging process. On one hand, the cell temperature is not allowed to exceed a maximum threshold T_{max},

$$T(t) \leq T_{max}. \tag{5.17b}$$

with such bound not only preventing thermal runaway but also limiting the ageing mechanism, due to the fact that the temperature is closely related to the SEI resistance growth (Tomaszewska et al., 2019). On the other hand, overcharging should be also avoided, and this can be done by constraining the voltage below a predefined threshold V_{max}, as follows

$$V(t) \leq V_{max}. \tag{5.17c}$$

It is interesting to notice that a limit on the voltage allows for a conservative charging strategy in order to avoid lithium plating deposition, which is a particularly harmful phenomenon which happens when ions in the electrolyte appear as a lithium metal on the surface of the negative electrode instead of intercalating (Tomaszewska et al., 2019). More precisely, the lithium plating phenomenon is directly related to the side-reaction overpotential $\eta_{sr}(t)$, which should remain positive in order to avoid plating formation. However, such variable can be computed only through a model-based framework and, even if it is assumed available in the full-states formulation, we prefer to rely on the voltage constraints in order to guarantee the reliability of the proposed model-free approach in a realistic setting (i.e. in the case of the simplified-states framework).

Therefore, we can formulate the fast-charging problem that both the full- and simplified-states policies aim to solve as follows:

$$\begin{aligned} \min_{\mathbf{I}_{[t_0,t_f]}} \quad & t_f \\ \text{subject to} \quad & \\ & \text{battery dynamics} \\ & \text{constraints in (5.17)} \\ & x(t_0) = x_0 \\ & SOC(t_f) = SOC_{ref} \end{aligned} \tag{5.18}$$

where $\mathbf{I}_{[t_0,t_f]} = [I(t_0),\, I(t_0+t_s),\, \ldots,\, I(t_f)]^\top$ is the sequence of control variables, with t_0 and t_f being the initial and final times of the charging procedure. Moreover, x_0

is the initial state vector and SOC_{ref} is the reference SOC at which the charging is considered to be complete.

5.2.2 Virtual Testbed Based on SPMeT

In this section we consider a reduced-order electrochemical model, namely the SPMeT, as the battery simulator. Such simulator is able to achieve high accuracy and represent physical details of the battery dynamics. In particular, we recall that the SPMeT is derived from the DFN model in 2.4.2.1. This latter is a full-order electrochemical model which employs a continuum of particles in both the anode and cathode of the cell. The SPMeT uses instead a simplified representation of solid-phase diffusion that employs a single spherical particle in each electrode. Specifically, the SPMeT here considered can be described through the same equations used for the control-oriented electrochemical model in 2.4.2.2, with the exception that full-order Fick's law is considered in this section for the diffusion of the ions along the particles radius, as follows

$$\frac{\partial \bar{c}_{s,i}(r,t)}{\partial t} = \frac{1}{r^2}\frac{\partial}{\partial r}\left[r^2 D_{s,i}(T(t))\frac{\partial \bar{c}_{s,i}(r,t)}{\partial r}\right] \tag{5.19}$$

instead of adopting the polynomial approximation proposed in (Subramanian, Diwakar, and Tapriyal, 2005). The boundary conditions for the Fick's laws are

$$\frac{\partial \bar{c}_{s,i}(0,t)}{\partial t} = 0 \tag{5.20a}$$

$$\frac{\partial \bar{c}_{s,p}(R_{p,p},t)}{\partial t} = \frac{I_{app}(t)}{D_{s,p}(T(t))Fa_p(t)L_p} \tag{5.20b}$$

$$\frac{\partial \bar{c}_{s,n}(R_{p,n},t)}{\partial t} = -\frac{I_{app}(t)}{D_{s,n}(T(t))Fa_n(t)L_n} \tag{5.20c}$$

The PDEs representing the Fick's law and the ions diffusion within the electrolyte are both spatially discretized through a finite-difference method (Forsythe and Wasow, 1960). The resulting state-space system consists of a relatively large-scale dynamics, which presents 61 different states in the considered case study. Therefore, it is evident that the use of ADP methods for optimal battery management becomes a sensible choice even in the case of a reduced electrochemical model. Note that the virtual testbed here considered consists of a single lithium-ion cell (with graphite-based anode and LiNiMnCoO2-based cathode) although the adopted methodology can easily be extended to the case of multiple cells arranged in series and parallel connections.

Finally, it is important to take into account that in the following we consider two scenarios in which different assumptions hold. Firstly, we assume that all the states of the SPMeT are directly measurable (full-states approach). Subsequently, we consider a more realistic scenario in which only output measurements are available (simplified-states approach), such as voltage, temperature and SOC, with the SOC obtained through Coulomb-Counting. Note that the full-states formulation can be realized in practice only if a suitable state observer is developed. Due to the fact that the latter implies the exploitation of a battery model it follows that the full-states framework allows only for a partial model-free control methodology.

5.2.3 Simulation Results

In this section we aim to assess the performance of RL for fast charging a lithium-ion cell, while satisfying safety constraints on voltage and temperature. We examine the performance of the actor-critic framework for the *minimum-time charging* problem using the SPMeT as battery simulator. We first assume that all the states are available to the agent. Then, we drop this assumption and consider the more realistic scenario in which only voltage, temperature and SOC can be retrieved.

5.2.3.1 DDPG Parameters

The actor-critic networks are based on neural-network architectures (Lillicrap et al., 2015) with different numbers of neurons. Specifically, the actor network uses two hidden layers with 20 - 20 neurons, while for the critic network two hidden layers with 100 - 75 neurons are employed. The other hyper parameters are detailed in Table 5.1.

Variable	Description	Value
γ	Discount factor	0.99
η_π, η_Q	Learning rate of actor, critic	$10^{-4}, 10^{-3}$
τ	Soft update of target networks	10^{-3}

TABLE 5.1: DDPG hyper parameters used for the battery fast charging.

5.2.3.2 Reward Function Design and Simulation Settings

The reward function is designed with the aim of both achieving fast charging and guaranteeing safety, according to the optimization problem in (5.18)

$$r(t_k) = r_{fc}(t_k) + r_s(t_k) \tag{5.21}$$

where $r_{fc} = -\alpha_{fc}\Delta t_k$, with $\Delta t_k = t_{k+1} - t_k$, is a negative penalty for each time step which passes before the reference SOC is achieved, thus accounting for fast charging. In addition, a negative penalty is also introduced at each time step t_k in which voltage and temperature constraints are violated

$$r_s(t_k) = r_V(t_k) + r_T(t_k) \tag{5.22}$$

This is done in particular by means of linear penalty functions (Smith and Coit, 1997):

$$r_V(t_k) = \begin{cases} -\alpha_V(V(t_k) - V_{max}), & \text{if } V(t_k) \geq V_{max} \\ 0, & \text{otherwise} \end{cases} \tag{5.23}$$

$$r_T(t_k) = \begin{cases} -\alpha_T(T(t_k) - T_{max}), & \text{if } T(t_k) \geq T_{max} \\ 0, & \text{otherwise} \end{cases} \tag{5.24}$$

where the bounds are set to $V_{max} = 4.2V$, $T_{max} = 320.15K$ (i.e. $47°C$) in this case study. The current is limited within the range $[-1.8I_{1C}, 0]$, where I_{1C} is the 1C-rate current related to the considered cell. In particular, the current constraint is imposed by considering the agent action inherently bounded in the interval $[-1, 1]$ (due to the choice of its last layer as a hyperbolic tangent operator, i.e., $-1 \leq \tanh(\cdot) \leq 1$), which is then scaled and translated according to the desired current limits.

The weights in the reward function are here chosen as $\alpha_{fc} = 0.1$, $\alpha_V = 100$ and $\alpha_T = 5$. Finally, the sample time for the simulations is set as $t_s = 50$.

5.2.3.3 Comparison Between Full-States and Simplified-States Approaches

In this section we aim to assess the DDPG performance in solving the fast-charging problem. In particular, a comparative analysis between the case in which the agent has access to the whole states vector (full-states) and the one in which only the output measurements are considered available (simplified-states) is conducted. In the following simulations, the full-states approach utilizes a vector of 61 states for feedback control, while the simplified method relies on voltage, temperature and SOC. Note that in the following we refer to the *training* performance as the one obtained during the learning process in which the actual applied actions are affected by exploration noise, while we refer to *testing* for the phase in which the trained agent performance is evaluated without the presence of exploration noise.

In Figure 5.1 the cumulative reward obtained during the training process for both the full-states and simplified-states approaches is shown. Note that, the shadow band in the graph denotes a confidence interval based on the standard deviation obtained by a statistical analysis over 4 different training experiments.

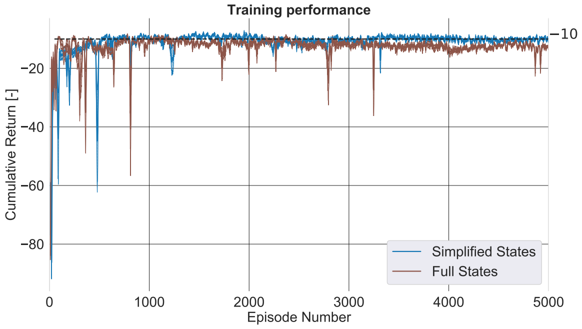

FIGURE 5.1: Cumulative reward obtained during 5000 training episodes.

The low value of the cumulative reward at the beginning of the training process is due to constraints violation and long charging time. The latter is represented, for different checkpoint episodes, in Figure 5.2. As it is shown, after 2000 episodes no further improvements are obtained, thus indicating that the agent achieves a locally optimal control policy. Note that, during the training process, different initial conditions for the battery states are considered for each episode, thus enhancing the exploration.

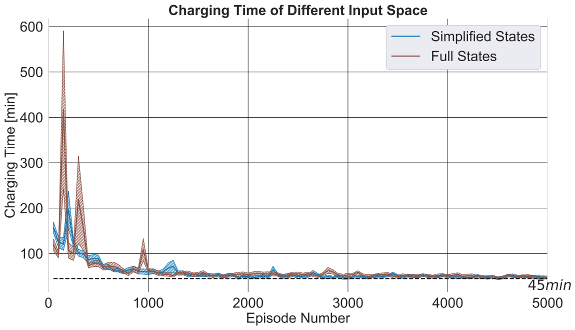

FIGURE 5.2: Charging time evaluated by testing the trained agent at different checkpoint episodes.

The validation of the optimal policy obtained at the end of the training for a specific scenario is presented in Figure 5.3, where the cell is charged from the initial condition of $SOC(t_0) = 0.3$ to the reference of $SOC_{ref} = 0.8$. The graphs show that both full-states and simplified-states methods achieve the goal of charging the cell in minimum time without violating the constraints. The cumulative rewards obtained by the two strategies for this specific scenario show that the full-states approach can achieve slightly better performance with a return of -4.69 while the one of the simplified-states configuration is -5.38, due to the fact that a full-states information allows for a deeper knowledge of the cell behaviour. Such result, however, can be read also from the point of view of a practical implementation: the simplified-states approach constitutes a reliable strategy which is able to achieve performance almost as high as the one of a full-states configuration which is not actually implementable. Finally, we can say that the derived feedback control policy exhibits a profile qualitatively similar to model-based control results in (Klein et al., 2011; Torchio et al., 2015; Perez et al., 2017; Kandel et al., 2020; Patnaik, Praneeth, and Williamson, 2018), i.e.

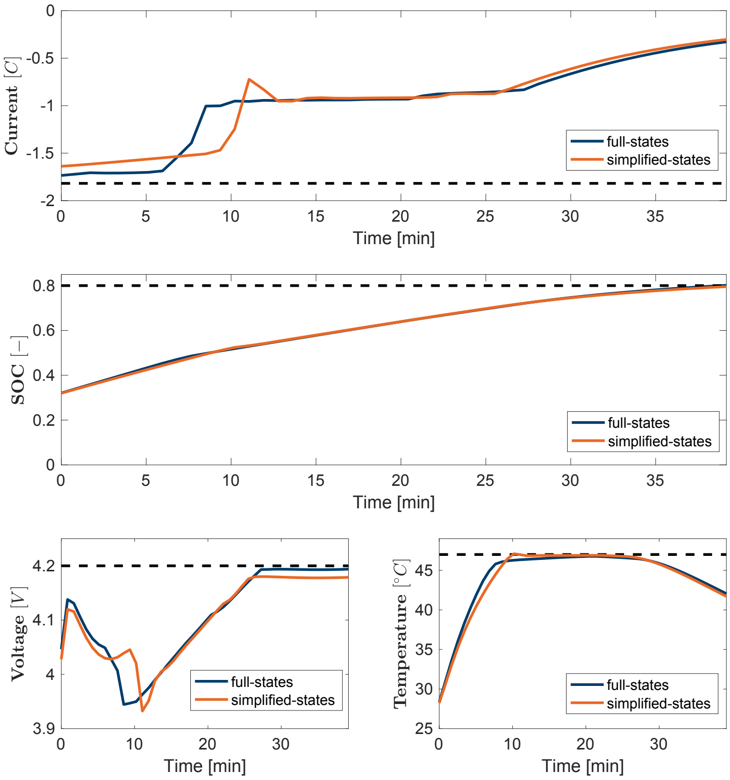

FIGURE 5.3: Validation of the performance over a specific scenario. Note that the charging current is expressed in terms of C-rate while the temperature is in degrees Celsius.

.

characterized by a constant current - constant temperature - constant voltage (CC-CT-CV) shape. The only difference is that the use of RL algorithms does not require any knowledge of the model dynamics.

5.2.4 Conclusions to RL-Based Battery Charging

In the previous sections, we have examined a reinforcement-learning approach for the battery fast-charging problem in the presence of safety constraints. In particular, we have shown how RL can overcome many of the limitations of the model-based methods. Among all the RL paradigms, the actor-critic one, and specifically the DDPG algorithm, has been adopted due to its ability to deal with continuous state and action spaces. To address the state constraints, the reward function has been designed such that the agent learns how to avoid constraint violation. The control strategy has been tested in simulation on an electrochemical battery model and the presented results are consistent with model-based approaches. In addition, the performance of the actor-critic strategy has been evaluated both in the case of full and partial state feedback. It is important to notice that, although the initial conditions are changed at each episode, the cell parameters are kept constant during the training. This fact implies that the obtained optimal policy can be exploited only with cells similar to the one considered during the training phase. Introducing some variability in the parameters during the training can allow the policy to achieve optimal results in a statistic sense for a class of parameter uncertainty.

5.3 RL in Optimal Eco-Driving for Autonomous HEVs

In this section, the focus is directed to the control of plug-in hybrid electric vehicles due to the fact that these represent one of the most important fields of application for lithium-ion batteries. While on one hand the power management of HEVs appears to be a largely explored topic in the literature (Liu and Peng, 2008), on the other hand the problem of eco-driving has been addressed only in the last few years (Sciarretta, De Nunzio, and Ojeda, 2015), as a consequence of an increasingly active research in the field of connected autonomous vehicles (Guanetti, Kim, and Borrelli, 2018). Indeed, the integration of vehicles infrastructure, based on wireless communication technologies, allows for the development of strategies able to enhance the driving safety in urban areas (e.g. adaptive cruise control, braking assistance, safe crossing at the intersections, etc), as well as to improve vehicle energy management. In particular, the main goal of optimal eco-driving is to find a proper vehicle velocity profile in order to address the trade-off between travel time and fuel consumption, especially in the presence of signalized intersections. Furthermore, in the case in which the considered autonomous vehicle is equipped with a hybrid powertrain, such energy-oriented control becomes even more complicated due to the presence of multiple power sources.

Most of the research in this field relies on model-based optimization as dynamic programming, where a finite horizon is considered in order to mitigate the curse of dimensionality and to enable on-line computation. However, the fact that the horizon is limited leads also to a short-sighted control, while the presence of vehicle-infrastructure communication should enable to gain notable energy savings by computing an optimal velocity trajectory with a long-sighted horizon given upcoming traffic-lights information. Furthermore, the use of DP in a realistic scenario is also limited by the assumption of perfect knowledge of the vehicle, powertrain and battery dynamics.

In the following, the use of deep RL (see Section 5.1) is considered as a possible solution to the aforementioned issues in the context of optimal eco-driving for an autonomous HEV through signalized intersections. It is important to notice that while the use of RL approaches has been already proposed for the power management of hybrid vehicles, its exploitation within the context of eco-driving constitutes a source of novelty. In particular, we combine the RL agent for velocity planning with a safety controller in a two-stage structure, to ensure successful crossing of the intersections while tracking the ecological velocity profile, thus enhancing the practicality of RL in autonomous driving. Note that, while the safety controller implements a robust MPC which relies on the realistic assumption of an approximative knowledge of the vehicle dynamics, the high-level velocity planner is completely model-free. Moreover, it is known from the literature that the use of approximate dynamic programming inherently allows for an infinite-horizon optimization while solving the curse-of-dimensionality issues. Finally, it is important to underline that, after a suitable training process that can be conducted off-line, the inference of the RL agent in order to compute the optimal action is real-time, since no DP or MPC needs to be solved on-line.

The rest of the section is organized as follows. In 5.3.1 the environment model is described, where particular attention is paid to vehicle dynamics, powertrain and traffic-lights behaviour. The hierarchical control scheme of an autonomous HEV is explained in Section 5.3.2, while the training process and the validation of the proposed methodology are discussed in 5.3.3 and 5.3.4, respectively. Finally, in 5.3.5 conclusions and future works are reported.

5.3.1 Environment Model

In this section we briefly detail the plug-in hybrid electric vehicle model, which is considered as a simulator for the real system. As previously done in this context, the equations are divided into two different groups which refer to the vehicle and the powertrain dynamics, respectively. The urban context which surrounds the vehicle is presented in terms of signalized intersections and a traffic-light model. Finally, we also carry out a description of the uncertainties exhibited by the environment.

5.3.1.1 Vehicle Dynamics

Several models for the vehicle dynamics exist in the literature, with different levels of accuracy and computational complexity. In the following, we consider the longitudinal vehicle dynamics model studied previously in (Bae et al., 2019a; Bae et al., 2019b).

In the following, a sampling time t_s is considered for the model discretization and a digital controller, which applies a piecewise-constant input at the discrete times $t_k = kt_s$, with $k \in \mathbb{N}$, is adopted. The longitudinal vehicle acceleration $a_v(t_k)$ is obtained via Newton's second law of motion, as follows

$$a_v(t_k) = \frac{1}{m}\left(\frac{\tau_w(t_k)}{R_w} - \frac{1}{2}\rho A_v C_d v^2(t_k) - f_r(t_k)\right) - a_g(t_k) \tag{5.25}$$

where m is the vehicle mass, $\tau_w(t_k)$ is the wheel torque, R_w is the wheel radius, ρ is the air density, C_d is the air drag coefficient, A_v is the frontal area of the vehicle, $a_g(t_k) = g \sin(\theta(t_k))$ is the component of gravitational acceleration g which is parallel to the road, with $\theta(t_k)$ being the road grade (with the convention that $\theta(t_k) \in (0, \frac{\pi}{2}]$ for an uphill road and $\theta(t_k) \in [-\frac{\pi}{2}, 0]$ otherwise) which in general depends on the position of the vehicle $s(t_k) \in \mathbb{R}$, $v(t_k)$ is the longitudinal velocity and $f_r(t_k)$ is the rolling resistance force. This latter depends on the velocity as follows

$$f_r(t_k) = \begin{cases} mgC_r \cos(\theta(t_k)) & \text{if } v(t_k) > 0 \\ 0 & \text{otherwise} \end{cases} \tag{5.26}$$

with C_r the rolling resistance coefficient. The acceleration enters the dynamics as follows

$$s(t_{k+1}) = s(t_k) + v(t_k)t_s \tag{5.27a}$$

$$v(t_{k+1}) = v(t_k) + a_v(t_k)t_s \tag{5.27b}$$

in which a forward Euler scheme is applied to the differential equations of motion. Note that we assume $\theta(t_k) = 0,\ \forall k \in \mathbb{N}$, i.e. the road is considered flat.

5.3.1.2 Powertrain Dynamics

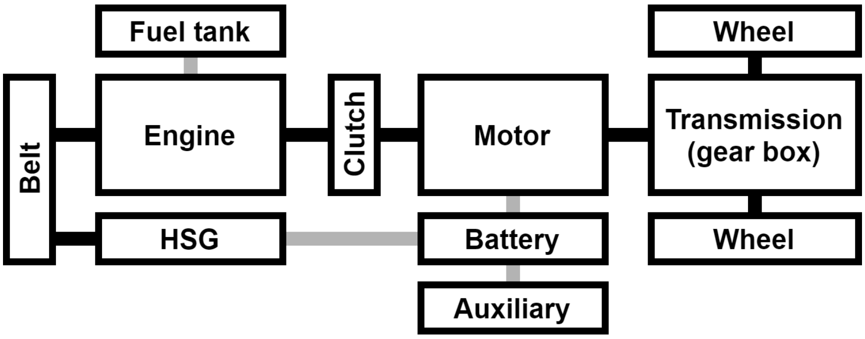

FIGURE 5.4: PHEV powertrain architecture.

The powertrain of a plug-in hybrid electric vehicle consists of the energy storage systems (battery and fuel tank), the power generators (internal combustion engine and electric motor), and the transmission to the wheels (gearbox). The pre-transmission parallel hybrid configuration is here used for the powertrain as depicted in Figure 5.4. Black connections between components represent mechanical connections and grey connections represent electrical and fuel connections. In particular, the wheel torque is defined as

$$\tau_w(t_k) = r_g(t_k)\tau_{sh}(t_k) - \tau_{br}(t_k) \tag{5.28}$$

where $\tau_{sh}(t_k)$ and $\tau_{br}(t_k)$ are the shaft and brake torque respectively, while $r_g(t_k)$ is the product between the gearbox and the final drive ratios. The shaft torque of a plug-in HEV with a parallel configuration is given by

$$\tau_{sh}(t_k) = \tau_m(t_k) + \eta_{cl} e_{on}(t_k)\tau_e(t_k) \tag{5.29}$$

in which $\tau_m(t_k)$ and $\tau_e(t_k)$ are the electric motor and internal combustion engine torques, respectively, η_{cl} is the clutch efficiency (here we assume $\eta_{cl} = 1$) and $e_{on} \in \{0, 1\}$ is a variable which indicates the status of the engine.

The battery dynamics depends on the electric battery power demand $P_b(t_k)$. In particular, the state-of-charge dynamics evolves as follows

$$SOC(t_{k+1}) = SOC(t_k) + \frac{I_b(t_k)}{3600C_b} t_s \tag{5.30}$$

where C_b is the battery capacity in Ah and $I_b(t_k)$ is the battery current. This latter is simulated as the solution of a second-order equation which comes from the fact that the battery is modelled as the internal-resistance equivalent circuit (He, Xiong, and Fan, 2011) with the power as input

$$I_b(t_k) = -\frac{OCP(t_k) - \sqrt{OCP^2(t_k) - 4R_b(t_k)P_b(t_k)}}{2R_b(t_k)} \tag{5.31}$$

where $R_b(t_k) = R_b(SOC(t_k))$ is the series resistance and $OCP(t_k) = OCP(SOC(t_k))$ is the open-circuit potential. Both are nonlinear expressions of the SOC. Note that, differently from Section 2.4, we assume the convention that a negative current $I_b(t_k)$, which corresponds to a positive power $P_b(t_k)$, is discharging the battery. The battery power is exchanged with the motor ($P_m(t_k)$), the hybrid starter generator ($P_{hsg}(t_k)$) which is responsible for starting the combustion engine and the auxiliary systems ($P_{aux}(t_k)$) which may include the necessary lights and heating as well as air conditioner, sound system, satellite navigation, etc. It holds that

$$P_b(t_k) = P_m(t_k) + P_{aux}(t_k) + P_{hsg}(t_k) \tag{5.32}$$

in which the motor power can be expressed as

$$P_m(t_k) = \frac{\omega_m(t_k)\tau_m(t_k)}{\eta_m(t_k)^{\text{sgn}(\tau_m(t_k))}} \tag{5.33}$$

where $\omega_m(t_k) = \frac{v(t_k)}{R_w} r_g(t_k)$ is the motor's angular velocity and $\eta_m(t_k) = \eta_m(\tau_m(t_k),\ \omega_m(t_k))$ is the motor efficiency, which is a nonlinear expression of the motor torque and angular velocity. We assume here that the auxiliary power is constant over time, i.e. $P_{aux}(t_k) = P_{aux},\ \forall t_k \in \mathbb{N}$. On the other hand, the power for the hybrid started generator is demanded only when the combustion engine is started, i.e.

$$P_{hsg}(t_k) = \begin{cases} P_{hsg} \in \mathbb{R} & \text{if } e_{on}(t_{k-1}) \neq e_{on}(t_k) = 1 \\ 0 & \text{otherwise} \end{cases} \tag{5.34}$$

Finally, from the energy consumption perspective, it is important to consider the power required by the engine

$$P_e(t_k) = \frac{\omega_e(t_k)\tau_e(t_k)}{\eta_e(t_k)} \tag{5.35}$$

where $\omega_e(t_k)$ is the engine's angular velocity and it is constrained to $\omega_e(t_k) = \omega_m(t_k)$ if $e_{on}(t_k) = 1$. The engine efficiency is also a nonlinear expression of engine torque and angular velocity, i.e. $\eta_e(t_k) = \eta_e(\tau_e(t_k), \omega_e(t_k))$. According to (Choi et al., 2020), the fuel consumption of the engine is regulated by the following equation

$$\Delta G_e(t_k) = N_{kg}^{gal} \frac{P_e(t_k)}{E_{lhv}} t_s \tag{5.36}$$

where E_{lhv} is the lower heating value for gasoline and N_{kg}^{gal} is the mass in kg of a gallon of gasoline, while the consumption of equivalent fuel from the battery is

$$\Delta G_m(t_k) = -k_m \frac{I_b(t_k)}{C_b} t_s \tag{5.37}$$

with $k_m = \frac{E_b}{N_{kWh}^{gal}}$, where E_b is the maximum energy in kWh that can be stored in the battery and N_{kWh}^{gal} is amount of energy in kWh which corresponds to a gallon of gasoline.

5.3.1.3 Traffic-Light Dynamics

In this section, we consider an autonomous plug-in HEV travelling through signalized intersections, while the surrounding traffic is neglected. We also take into account $n_{tf} \in \mathbb{N}_0$ traffic lights located at the positions $s_{tf}^i \in \mathbb{R},\ i = 1, \cdots, n_{tf}$. Each traffic light is characterized by the cycle length l_c^i, the time shift for the starting point of the cycle $l_{c,0}^i$, the green and yellow light duration l_g^i and l_y^i, respectively. For each time instant t_k we can compute the corresponding time value within the traffic-light cycle reference as follows

$$l_t^i(t_k) = (l_{c,0}^i + t_k) \mod l_c^i \tag{5.38}$$

These elements allow us to define the Signal-Phase-and-Timing (SPaT) information for the different signalized intersections, where $s_p^i(t_k) \in \{\text{green, yellow, red}\}$ is the current signal phase and $s_t^i(t_k)$ is the remaining time in the current status. We consider that the crossing of the i-th intersection will be successful if the following condition holds

$$s(t_k) = s_{tf}^i \quad \text{and} \quad s_p^i(t_k) = \text{green} \tag{5.39}$$

5.3.1.4 Available Measurements and Uncertainties

In the considered environment we assume that the known parameters and available measurements are only a subset of the variables described in the previous sections.

Vehicle All the vehicle parameters are assumed to be known, except for the rolling resistance and the air drag coefficients, the air density and the frontal area, which are considered uncertain. In particular, a generic uncertain parameter ψ is generated from a truncated Gaussian distribution centered around an estimated value μ_ψ with standard deviation σ_ψ, as follows

$$\psi \sim \mathcal{N}\left(\mu_\psi,\ \sigma_\psi^2;\ \mu_\psi - \frac{\delta_\psi}{2},\ \mu_\psi + \frac{\delta_\psi}{2}\right) \tag{5.40}$$

with $\psi \in [\mu_\psi - \frac{\delta_\psi}{2}, \mu_\psi + \frac{\delta_\psi}{2}]$, where δ_ψ is the symmetric interval in which the parameter can lie. Moreover, the position and the velocity of the vehicle are assumed to be measurable. Notice that all these assumptions are required for the development of a proper velocity controller which is able to guarantee a safe travel (see Figure 5.5).

Powertrain In the following we assume that the battery state of charge, the motor and engine powers, and their energy consumptions are measurable for state feedback control. The energy consumption measurement is necessary since this represents the reward signal for the RL agent. Note that our main goal is to plan the velocity profile in the case in which the powertrain controller is already implemented and designed *a priori*. Within this context, a velocity planner based on model-free RL does not require the knowledge of the powertrain parameters, differently from a model-based one (e.g. dynamic programming). Nevertheless, an accurate powertrain model is necessary in order to provide a satifactory powertrain controller.

Intersections and Traffic Lights The literature on eco-driving through signalized intersections vigorously examines uncertainties in the traffic-light models, see e.g. (Sun et al., 2020). In the following, we assume for the i-th intersection that the green light duration (l_g^i), the cycle length (l_c^i) and the time shift for the initial point of the cycle ($l_{c,0}^i$) are random variables with Gaussian distributions as in (5.40), where the mean values can be estimated from historical data. The measurable outputs depend on the distance between the vehicle and the considered traffic light. More specifically, accurate measurements of signal phase ($s_p^i(t_k)$) and signal timing ($s_t^i(t_k)$) for the i^{th} intersection are available when the vehicle is in the communication range, i.e.

if $|s^i_{tf} - s(t_k)| \leq d_{th}$. Otherwise, if $|s^i_{tf} - s(t_k)| > d_{th}$, then only historical data can be used in computing nominal values for the SPaT information.

5.3.2 Control Scheme

The control of an autonomous plug-in hybrid electric vehicle in urban environments is a complex task which involves optimization of multiple and competitive objectives, as well as enforcing multiple nonlinear constraints. For this reason a hierarchical control structure is usually employed, as depicted in Figure 5.5. This structure can be organized into four different levels: (i) the routing optimizer, (ii) the velocity profile planner along the selected path, (iii) the velocity controller for tracking the reference profile and guaranteeing safety, and finally (iv) the powertrain control, which manages the motor and engine powers, the battery, the gear selection, and the mechanical brake.

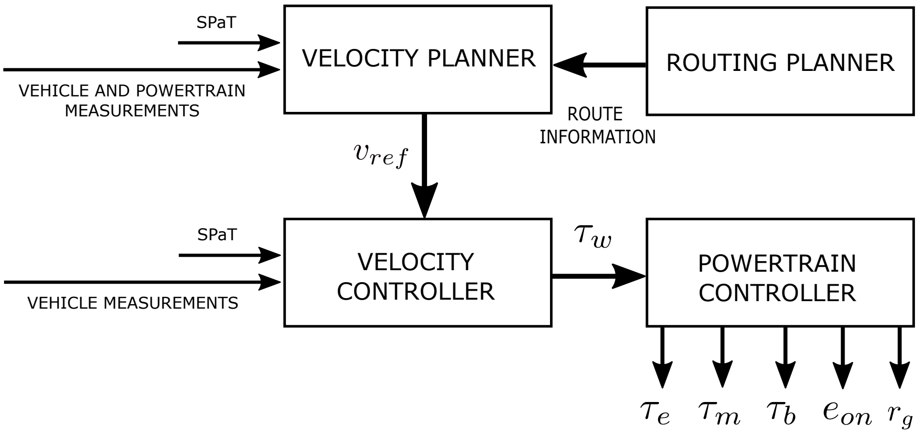

FIGURE 5.5: Hierarchical control scheme.

The focus of this section is the development of an RL-based velocity profile planner, whose knowledge about the road comes from the routing optimizer level. We also design a velocity controller, which is based on MPC in order to guarantee safety, i.e. successfully crossing at the different signalized intersections, as previously done in this context by (Bae et al., 2019a). Note that we assume here the absence of surrounding traffic (see 5.3.2.1 for further details). The powertrain controller is also assumed to be developed *a priori* with the aim of satisfying the reference power and torque coming from the velocity controller, while minimizing an energy-related cost function. Moreover, the design of the powertrain control is oriented to guarantee a charge-sustaining operation mode if the battery SOC drops below a certain threshold ($z_{th} = 0.16$ is used here).

5.3.2.1 Adaptive Cruise Control

As previously mentioned, the velocity controller here adopted comes from (Bae et al., 2019a) and is based on a model-predictive control framework. In short, the velocity controller has two main goals: (i) tracking the reference velocity profile v_{ref} and (ii) ensuring a safe crossing at the intersections, that is achieved by preventing the vehicle from stranding in the middle of the intersection, especially during transitions of phase (e.g., green light turns to yellow while crossing). The two goals are achieved by leveraging the wheel torque $\tau_w(t_k)$, which is determined by a standard nonlinear programming method (due to the presence of nonlinear vehicle dynamics). Note that, in the case in which surrounding traffic were considered, the velocity controller would act as an Adaptive Cruise Control (ACC). The model used in the MPC consists only of the equations relating to the vehicle dynamics, i.e. (5.25)-(5.27) and the interested reader is referred to II-B in (Bae et al., 2019a) for more details.

5.3.2.2 Velocity Planner

Velocity planning along a specific route constitutes a fundamental step in the management of an autonomous vehicle, since it allows one to achieve high performance in terms of travel time and energy efficiency. Moreover, this task acquires even more importance when a plug-in HEV is considered, since an optimal reference velocity can lead to a proper exploitation of the powertrain.

Within this section, safety is defined in terms of successfully crossing the signalized intersections. This is guaranteed by the velocity control module. Therefore, the velocity planner is devoted only to the optimization of an energy- and time-related cost function. In the following, we briefly recall some standard velocity planning approaches that will be used as benchmarks in order to evaluate the performance of the reinforcement-learning-based method. This latter has been discussed in detail in Section 5.1 and is here applied, for the first time to the knowledge of the authors, to the context of eco-driving.

5.3.2.3 Benchmarks

We consider two simple benchmark algorithms for the velocity planner. The first one, that we refer to as *ACC-only*, is based on a constant reference velocity, regardless of the measurements including the SPaT information. This approach has been used as a benchmark in (Sun et al., 2020; Bae et al., 2019b), and it is apparent that it does not account for the trade-off between fuel consumption and travel time. The second benchmark strategy, that we refer to as *modified ACC*, adjusts the velocity profile according to the SPaT information for the upcoming intersection. The SPaT information is assumed deterministic within the sensing range d_{th}, while outside the sensing range it is based on historical data. In particular, in the *modified ACC* method, the velocity between two intersections is kept constant and computed as the minimum value that allows the vehicle to successfully cross in the same time as the *ACC-only* approach, taking into account a possible safety margin. In this way, we aim at minimizing the time wasted at a red light and, as a consequence, reducing the energy consumption without affecting the travel time.

5.3.3 Training Process

In this section, the optimal velocity planning problem is formulated via ADP. In particular, a proper reward function is defined and the training testbed along with the training results are presented in 5.3.3.2.

5.3.3.1 ADP-Based Optimal Velocity Planning

The focus of this section is addressing the trade-off between energy consumption and travel time, which corresponds to solving the following optimization problem

$$\min_{v_{ref}(\cdot), t_{k_f}} \quad \sum_{\bar{k}=k}^{k_f-1} \alpha_1 \left(\Delta G_e(t_{\bar{k}}) + \Delta G_m(t_{\bar{k}}) \right) + \alpha_2 \Delta t_{\bar{k}} \tag{5.41a}$$

subject to

$$\text{dynamics (5.25)-(5.39)} \tag{5.41b}$$

$$\text{uncertainties in 5.3.1.4} \tag{5.41c}$$

$$\text{velocity and powertrain control modules in 5.3.2} \tag{5.41d}$$

where $\Delta t_{\bar{k}} = t_{\bar{k}+1} - t_{\bar{k}}$ and t_{k_f} is the time instant in which the vehicle crosses the last intersection along the predefined road, while α_1 and α_2 are suitably chosen weights. This problem can be formulated as ADP by considering the following reward function

$$r(t_k) = -\,\alpha_1 \left(\Delta G_e(t_k) + \Delta G_m(t_k)\right) - \alpha_2 \Delta t_k \tag{5.42}$$

The constraints in (5.41c) and (5.41d) are learned by the agent when interacting with the environment.

To interpret the problem formulation in terms of the RL definitions given in Section 5.1, it is important to notice that the RL agent's action corresponds to the reference velocity profile, i.e. $u(t_k) = v_{ref}(t_k)$. The state vector $x(t_k)$ is more complex. It is composed of features based on the measurements which are available and relevant to the agent at different time instants. These features include the vehicle velocity, the gear, the battery SOC, and the distances to the first and second upcoming intersections. Moreover, we include some features which exclusively belong to the first and second upcoming intersections in order to generalize the policy over different road and intersections scenarios. In particular, we consider their SPaT as well as green light duration and cycle length. Some of these SPaT features can be measured directly within the detection distance, or obtained from historical data in accordance with 5.3.1.3. It is evident that the definition of the *first* and *second* intersection is related to the position of the vehicle. Therefore, the features corresponding to intersection parameters should be updated accordingly.

5.3.3.2 Training Testbed and Results

The vehicle parameters are randomly chosen according to the uncertainties defined in 5.3.1.4 at the beginning of the training process and kept constant through different episodes. The same vehicle and powertrain parameters will be used in the validation phase in 5.3.4. Note that the nominal values of the parameters are omitted for confidentiality reasons.

In every training episode we consider a route consisting of 3 signalized intersections, and we end the episode when the vehicle crosses the second one. This choice is related to the fact that the agent observations include the parameters of the 2 upcoming intersections. For each episode the distances between the intersections as well as the traffic-light parameters are extracted from their range of definition with uniform probability, in order to explore as many scenarios as possible. In this way, the agent is trained across a variety of road configurations. The same is done for some vehicle initial states such as the battery SOC and car velocity. Finally, for every episode the historical data of the traffic light are extracted randomly according to 5.3.1.4.

The results are depicted in Figure 5.6, where the return over 5000 training episodes is shown as well as the moving average over 200 episodes. The DDPG structure and its parameters are taken exactly as in (Lillicrap et al., 2015).

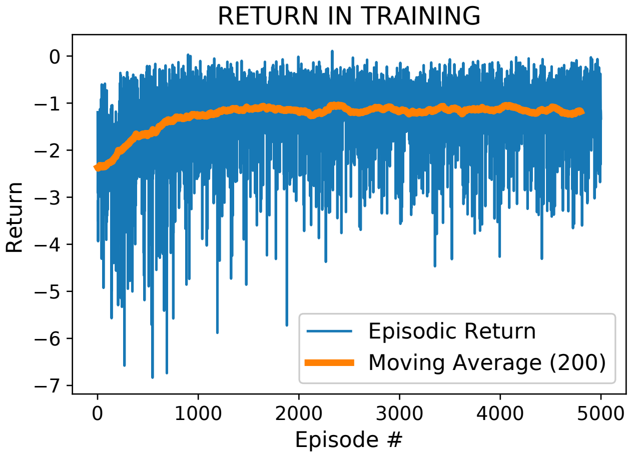

FIGURE 5.6: Return during the training procedure.

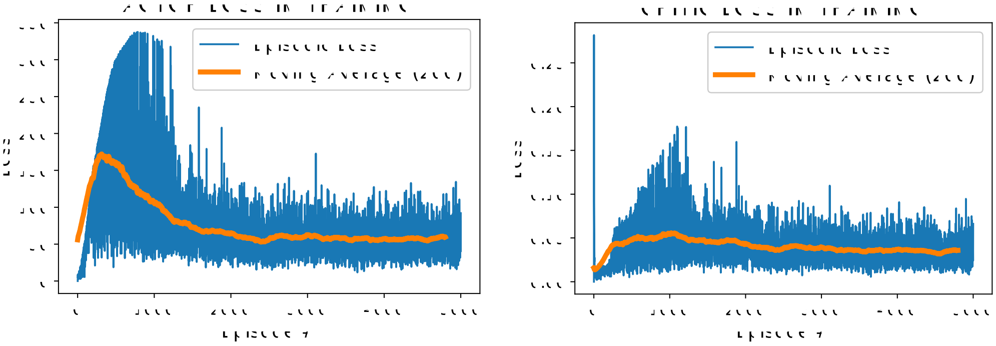

FIGURE 5.7: Loss of actor and critic.

5.3.4 Performance Validation

In this section the proposed RL-based algorithm is compared in simulation with the two benchmarks discussed in 5.3.2.2 (*ACC-only* and *modified ACC*). First, we evaluate the different strategies over several scenarios and statistical analysis of the performance is provided for both the cases of charge-sustaining and charge-depleting mode. Second, a specific scenario is considered and the trajectories for the vehicle velocity, the battery SOC, the motor and engine torques are shown. Note that we assume the vehicle used for validation has the same parameters as the vehicle considered during the training process.

5.3.4.1 Statistical Analysis Over Multiple Scenarios

We test here the control methodologies over 500 different scenarios. In each of them we consider a configuration of 8 intersections, while the initial vehicle states and the traffic-light parameters are randomly generated. The samples are then grouped in two different sets according to the initial battery SOC, thus separating the case of charge-depleting ($SOC(t_0) \in (0.18, 0.95]$) and charge-sustaining ($SOC(t_0) \in [0.15, 0.18]$), where t_0 is the initial time instant for each simulation scenario.

The performance of each approach is compared in terms of the mean value and standard deviation of the following metrics: travel time, miles travelled per equivalent gallon of fuel (MPGe), and cumulative return obtained at the end of each episode. As defined in the previous sections, we consider the optimal control strategy that minimizes the cumulative return, while the optimality in the sense of travel time and fuel consumption depends on the tuning of the weighting factors in (5.42). The statistical analysis of the cumulative return, shown in Table 5.2, highlights that the RL-based algorithm outperforms the benchmarks in both the charge-depleting and the charge-sustaining modes. In particular, RL produces a larger mean and smaller standard deviation, yielding higher and more consistent performance.

Charge-Depleting Operation The distribution of travel time and fuel consumption (expressed in MPGe) is depicted in Figure 5.8 for all the methodologies. The inset text indicates the mean and standard deviation values. Both travel time and MPGe follow a Gaussian-like distribution for all the algorithms, due to randomly

RETURN	Charge Depleting		Charge Sustaining	
	Mean	Std	Mean	Std
RL-agent	-3.199	0.396	-5.521	0.877
ACC-only	-3.653	0.546	-6.559	1.002
modified ACC	-3.492	0.457	-6.125	0.904

TABLE 5.2: Statistical analysis of the return over 250 experiments for each operating mode.

generated initial states and road configurations for each scenario. The weights in (5.42) have been tuned such that the travel time of the RL-agent is similar to the other benchmarks, while producing a large reduction in energy consumption. We can say that, in this simulation, the RL-agent is tuned to be eco-driving-oriented.

Charge-Sustaining Operation A similar analysis is conducted under charge-sustaining mode. The results are shown in Figure 5.9, which highlights that, with the current tuning of the weights in the reward function, the MPGe of the RL-agent increases (48.22% and 32.47% compared to *ACC-only* and *modified ACC*, respectively) at the expense of higher travel time (23.05% and 19.32%). Nevertheless, the RL-based strategy is still considered superior, since it achieves on average the maximum cumulative return over the different episodes. Note that the weights can be adjusted in order to provide similar results to the charge-depleting case.

5.3.4.2 Validation in a Specific Scenario

Next we consider a specific scenario to illustrate the evolution of vehicle and battery states for charge-sustaining mode, for each control strategy. In particular, we still consider 8 signalized intersections with the same properties as before. The vehicle trajectory and traffic light SPaT are depicted in Figure 5.10. The red lines indicate the red-phase duration for the different intersections. It is evident that the RL-agent achieves the smoothest trajectory, thus reducing the vehicle acceleration and the energy consumption. In Figure 5.11 the velocity and the state-of-charge profiles are shown. The RL velocity trajectory exhibits the smallest variance, while all controllers successfully sustain SOC above 0.15. Finally, the engine and motor torques are depicted in Figure 5.12. It is important to notice that the RL-agent exhibits the lowest

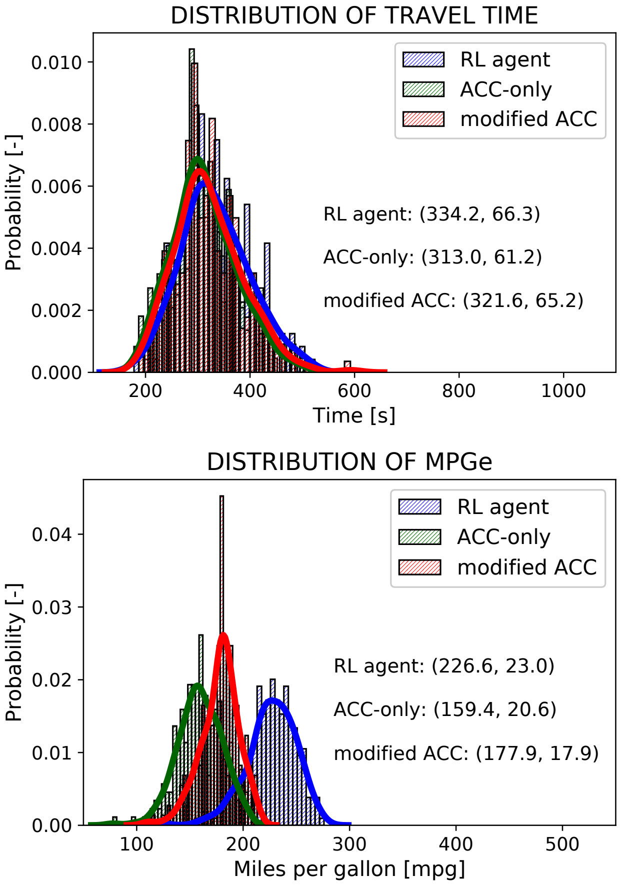

FIGURE 5.8: Charge depleting: travel time and miles per gallon equivalent (MPGe) for each velocity planning controller. When tuned to produce equal travel times, RL increases MPGe by 42% and 27% on average relative to *ACC-only* and *modified ACC*, respectively.

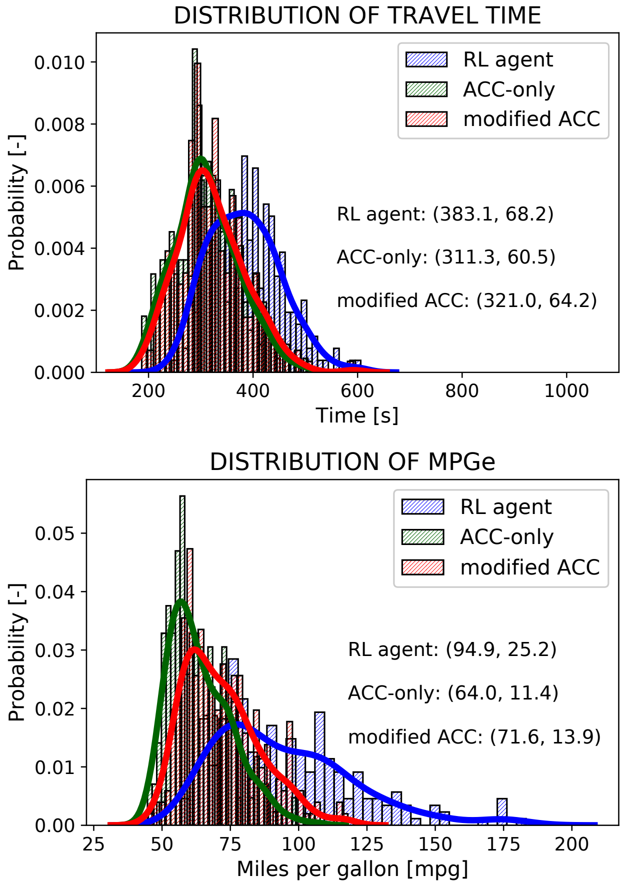

FIGURE 5.9: Charge sustaining: travel time and miles per gallon equivalent (MPGe) for each velocity planning controller. RL increases MPGe by 48% and 32% on average relative to *ACC-only* and *modified ACC*, respectively. However, the travel time is 23% and 19% longer.

usage of the engine in average (the fraction of time in which the engine is ON corresponds to 0.25, 0.37 and 0.38 for RL-agent, *ACC-only* and *modified ACC* respectively) and a variance of electric motor torque ($47.54Nm$) which is comparable to the one of *modified ACC* ($49.72Nm$) and far lower than *ACC-only* ($61.94Nm$). In particular, the latter information provides an insight on which controller shows the most energy-wasteful behaviour.

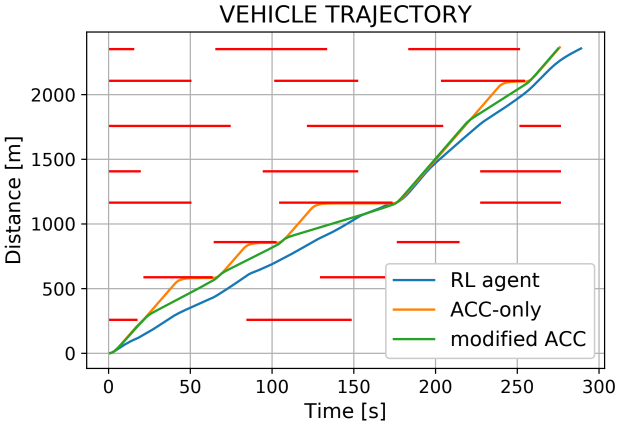

FIGURE 5.10: Vehicle trajectory with SPaT information. All approaches pass intersections safely, but RL minimizes idle time at red lights.

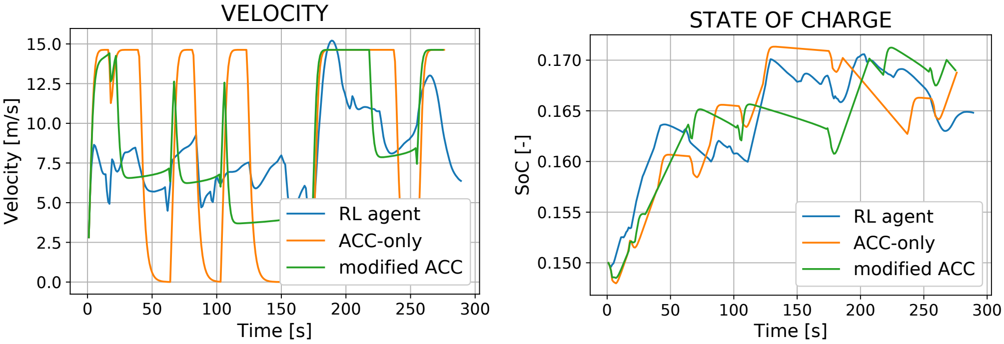

FIGURE 5.11: Velocity and state-of-charge evolutions. RL produces the lowest variance velocity profile.

5.3.5 Conclusions to RL-Based Velocity Planning for Autonomous HEVs

In this section we utilize deep reinforcement learning for optimal velocity planning of plug-in HEVs in an urban context. In particular, a multi-objective optimization problem is formulated to minimize both travel time and energy consumption, while

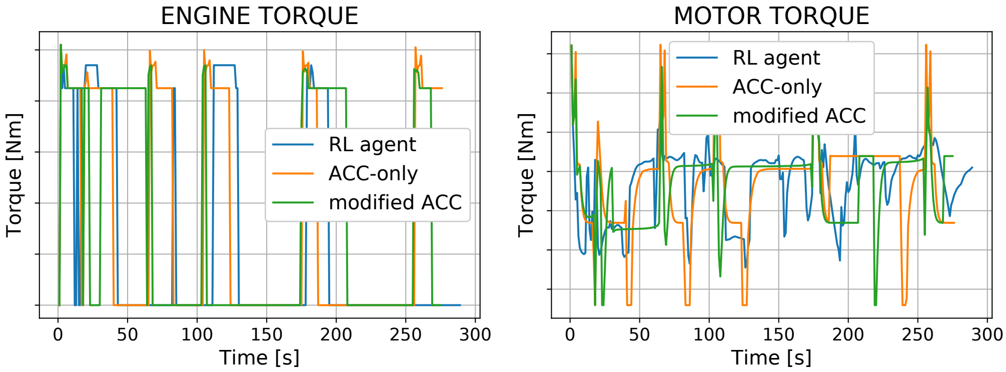

FIGURE 5.12: Engine and motor torque profiles. The vertical scales of both plots have been omitted for confidentiality reasons.

traveling through signalized intersections that broadcast their SPaT over a limited range. This problem is solved via the DDPG algorithm, which is an approximate dynamic programming method that enables for continuous actions. Finally, the proposed methodology is validated in simulation by conducting a comparative statistical analysis between the RL-agent and two benchmark approaches. The results highlight the effectiveness of the presented approach. In particular, we find that utilizing either real-time or historic SPaT information can significantly improve the trade-off between travel time and energy consumption. Somewhat surprisingly, the RL algorithm also generalizes well across a diversity of signalized intersection configurations. Future work may examine how many upcoming intersections should be accounted for in the state vector of the RL-agent in order to achieve sufficient performance, while maintaining a reasonable computational time and stable training process.

5.4 Conclusions

In this chapter we have discussed the main features of reinforcement learning together with its applicability to the context of batteries fast charging and HEVs control. The obtained results are promising due to the fact that they allow to solve complex optimization problems without the need for an accurate modelling procedure. However, specific methodologies for addressing competing objectives are still missing as well as the possibility of explicitly implementing safety constraints during the training phase. Future discoveries in these contexts may avoid the need for including penalty terms and weighting factors in the reward function, thus enabling an easier reward-shaping process which would enhance the reliability of reinforcement learning in solving practical problems.

Chapter 6

Conclusions and Future Work

The present Thesis focuses mainly on lithium-ion batteries for electric vehicle applications. In particular, attention has been devoted to both the mathematical modelling, the parameter identification and the control of such complex electrochemical accumulators. The state of the art of these latter is described in details in Chapter 2, where a thorough discussion related to the historical development of such technology, with particular attention to the innovations in the employed materials, together with a review of the key issues for lithium-ion battery management is presented. Moreover, the equations of most common mathematical models in the literature are recalled, with the aim of underlying the differences between equivalent-circuit models and the electrochemical ones, considering also the concept of reduced-order models. Note that the use of a mathematical model in a control context is possible only in the case in which such a model corresponds to an accurate representation of the plant to be controlled. For this reason, in Chapter 3 the identification of the battery parameters is addressed, with focus oriented to the design of suitable experiments in order to enhance the identifiability of the parameters. Firstly, the model-based experimental design is carried out by exploiting the concept of Fisher-information matrix, whose inverse provides an approximation to the parameter covariance matrix. Subsequently, due to the fact that the Fisher-information matrix exhibits only a local nature according to the guess parameter vector in which it is evaluated, a global design of experiments based on the Sobol index is considered. Results show the effectiveness of the proposed methodologies in increasing the accuracy of the parameter estimation process.

The development of a control algorithm for lithium-ion batteries is addressed in

Chapter 4, where different formulations of the well known model-predictive control approach are exploited. The ability of dealing with complex nonlinear and multivariable systems, subject to state and input constraints, makes MPC particularly suitable for lithium-ion battery management. The charging current profile for these latter needs to be computed to achieve multiple objectives (e.g. fast charging, SOC balancing, ageing and energy dissipation reduction, etc.) while satisfying constraints on the applied current, voltage, temperature and side-reaction overpotential to limit the risk for safety hazards, such as thermal runaway, fires and even explosions. At first, the focus is devoted to the optimal charging of a single cell, to minimize the wasted energy and the degradation mechanism. Specifically, this goal is achieved through the exploitation of the *shrinking-horizon* principle within the MPC framework, thus guaranteeing a fixed charging time which allows for a fair comparison with benchmark charging protocols (e.g. constant-current constant-voltage). Then, the problem of SOC balancing for series-connected cells is addressed, and a solution based on nonlinear MPC is tailored for the specifically considered supply circuitry. Moreover, it is important to notice that model-predictive control relies on the state-feedback concept and therefore a measurement of all the states is required. Due to the fact that, in the case of batteries, only terminal voltage and surface temperature measurements are available, in a realistic scenario the internal quantities need to be reconstructed through the exploitation of a state observer and, therefore, the development of an easy-to-tune extended Kalman filter is also presented. Note that several observers have been proposed in the literature during the recent years and the design of a more sophisticated one goes beyond the scope of this Dissertation. Finally, the optimal management of a whole battery pack with both series and parallel arrangements is taken into account and a sensitivity-based MPC is proposed in order to provide high performance while maintaining the computational cost within a reasonable level which allows for real-time implementation.

Lastly, Chapter 5 is dedicated to the exploitation of reinforcement-learning strategies both to the context of lithium-ion battery charging and autonomous HEVs velocity planning. The use of RL-based control has the aim of dealing with uncertain systems, for which an accurate model is not available, in presence of a huge number of states. Such capabilities come from the fact that the RL-agent learns the optimal control policy by interacting directly with the unknown environment and, thanks to the exploitation of function approximation, it has proven to be a suitable technique for solving the so-called curse of dimensionality. Among the different algorithms, particular attention is paid to the deep-deterministic policy-gradient method, which enables for continuous control actions. Firstly, DDPG is employed for the fast charging of a single lithium-ion cell in presence of safety constraints and simulation results show that an optimal policy can be achieved without any knowledge related to the battery model and parameters. Then, the same algorithm is applied to the optimal velocity planning for an autonomous HEV in an urban context, which has become a particularly relevant task in recent years due to both the increasing attention to sustainable mobility and the development of suitable communication infrastructures. Specifically, the velocity profile along a given path is computed by the RL-agent in order to manage the trade-off between travel time and energy consumption, while guaranteeing a safe crossing at the intersections. The results show that the proposed model-free methodology is able to outperform benchmark techniques over a statistically significant number of scenarios.

In conclusion, the topics addressed in this Dissertation cover only a small part of the lithium-ion batteries and electric vehicles management field, which is still attracting a lot of research effort and for which several open issues remain. While from the chemistry point of view the research is oriented to the employment of new materials able to increase energy and power density of the batteries, control engineers are now facing the fact that an accurate state and parameter estimation is necessary to achieve high performance. Therefore, future work from the control perspective may involve the use of stochastic MPC for dealing with uncertainty in model parameters as well as algorithms for the joint estimation of states and parameters from output measurements only. Furthermore, a lack of software packages, able to simulate the behaviour of large battery packs in a timely manner, is still present. We believe that a step forward in such direction would significantly enhance the development of the control methodologies suitable for electric-vehicle battery packs as well as a more efficient design of the latter.

Chapter 7

Peer-Reviewed Scientific Publications

Scientific Journals

- (Pozzi et al., 2018b) - Pozzi, A., Ciaramella, G., Volkwein, S., Raimondo, D. M. (2018). Optimal design of experiments for a lithium-ion cell: parameters identification of an isothermal single particle model with electrolyte dynamics. Industrial Engineering Chemistry Research, 58(3), 1286-1299.

- (Pozzi et al., 2020a) - Pozzi, A., Zambelli, M., Ferrara, A., Raimondo, D. M. (2020). Balancing-aware charging strategy for series-connected lithium-ion cells: A nonlinear model predictive control approach. IEEE Transactions on Control Systems Technology, 28(5), 1862-1877.

- (Pozzi et al., 2020c) - Pozzi, A., Torchio, M., Braatz, R. D., Raimondo, D. M. (2020). Optimal charging of an electric vehicle battery pack: A real-time sensitivity-based model predictive control approach. Journal of Power Sources, 461, 228133.

Conference Proceedings

- (Pozzi, Torchio, and Raimondo, 2018b) - Pozzi, A., Torchio, M., Raimondo, D. M. (2018, June). Film growth minimization in a Li-ion cell: a Pseudo Two Dimensional model-based optimal charging approach. In 2018 European Control

Conference (ECC) (pp. 1753-1758). IEEE.

- (Pozzi, Torchio, and Raimondo, 2018a) - Pozzi, A., Torchio, M., Raimondo, D. M. (2018, August). Assessing the performance of model-based energy saving charging strategies in Li-ion cells. In 2018 IEEE Conference on Control Technology and Applications (CCTA) (pp. 806-811). IEEE.

- (Mosca, Pozzi, and Raimondo, 2018) - Mosca, A., Pozzi, A., Raimondo, D. M. (2018, October). Battery ageing-aware stochastic management of power networks in islanded mode. In 2018 22nd International Conference on System Theory, Control and Computing (ICSTCC) (pp. 571-578). IEEE.

- (Pozzi et al., 2018a) - Pozzi, A., Ciaramella, G., Gopalakrishnan, K., Volkwein, S., Raimondo, D. M. (2018, December). Optimal Design of Experiment for Parameter Estimation of a Single Particle Model for Lithiumion Batteries. In 2018 IEEE Conference on Decision and Control (CDC) (pp. 6482-6487). IEEE.

- (Pozzi et al., 2020b) - Pozzi, A., Xie, X., Raimondo, D.M. , Schenkendorf, R. (2020). Global Sensitivity Methods for Design of Experiments in Lithium-ion Battery Context. In IFAC World Congress 2020, Germany.

- (Park et al., 2020) - Park, S., Pozzi, A., Whitmeyer, M., Perez, H., Joe, W. T., Raimondo, D. M., Moura, S. (2020, August). Reinforcement learning-based fast charging control strategy for li-ion batteries. In 2020 IEEE Conference on Control Technology and Applications (CCTA) (pp. 100-107). IEEE.

- Pozzi, A., Bae, S., Choi, Y., Borrelli, F., Raimondo, D. M., Moura, S. (2020, December). Ecological Velocity Planning through Signalized Intersections: A Deep Reinforcement Learning Approach. In 2020 59th IEEE Conference on Decision and Control (CDC) (pp. 245-252). IEEE.

Bibliography

Agubra, Victor and Jeffrey Fergus (2013). "Lithium ion battery anode aging mechanisms". In: *Materials* 6.4, pp. 1310–1325.

Akaike, Hirotogu (1998). "Information theory and an extension of the maximum likelihood principle". In: *Selected papers of hirotugu akaike*. Springer, pp. 199–213.

Albertus, Paul and John Newman (2007). "Introduction to dualfoil 5.0". In: *University of California Berkeley, Berkeley, CA, Tech. Rep.*

Altaf, Faisal, Bo Egardt, and Lars Johannesson Mårdh (2016). "Load management of modular battery using model predictive control: Thermal and state-of-charge balancing". In: *IEEE Transactions on Control Systems Technology* 25.1, pp. 47–62.

Andersson, Joel AE et al. (2019). "CasADi: a software framework for nonlinear optimization and optimal control". In: *Mathematical Programming Computation* 11.1, pp. 1–36.

Arora, Pankaj, Marc Doyle, and Ralph E White (1999). "Mathematical modeling of the lithium deposition overcharge reaction in lithium-ion batteries using carbon-based negative electrodes". In: *Journal of The Electrochemical Society* 146.10, p. 3543.

Arora, Pankaj, Ralph E White, and Marc Doyle (1998). "Capacity fade mechanisms and side reactions in lithium-ion batteries". In: *Journal of the Electrochemical Society* 145.10, p. 3647.

Arulkumaran, Kai et al. (2017). "Deep reinforcement learning: A brief survey". In: *IEEE Signal Processing Magazine* 34.6, pp. 26–38.

Aswani, Anil et al. (2013). "Provably safe and robust learning-based model predictive control". In: *Automatica* 49.5, pp. 1216–1226.

Attia, Peter M et al. (2020). "Closed-loop optimization of fast-charging protocols for batteries with machine learning". In: *Nature* 578.7795, pp. 397–402.

Bae, Sangjae et al. (2019a). "Design and implementation of ecological adaptive cruise control for autonomous driving with communication to traffic lights". In: *2019 American Control Conference (ACC)*. IEEE, pp. 4628–4634.

Bae, Sangjae et al. (2019b). "Real-time ecological velocity planning for plug-in hybrid vehicles with partial communication to traffic lights". In: *2019 IEEE 58th Conference on Decision and Control (CDC)*. IEEE, pp. 1279–1285.

Balbuena, Perla B and Yixuan Wang (2004). *Lithium-ion batteries: solid-electrolyte interphase*. Imperial college press.

Bandhauer, Todd M, Srinivas Garimella, and Thomas F Fuller (2011). "A critical review of thermal issues in lithium-ion batteries". In: *Journal of the Electrochemical Society* 158.3, R1.

Barsukov, Yevgen and Jinrong Qian (2013). *Battery power management for portable devices*. Artech house.

Bemporad, Alberto and Manfred Morari (1999). "Robust model predictive control: A survey". In: *Robustness in identification and control*. Springer, pp. 207–226.

Bemporad, Alberto et al. (2002). "The explicit linear quadratic regulator for constrained systems". In: *Automatica* 38.1, pp. 3–20.

Bentley, WF (1997). "Cell balancing considerations for lithium-ion battery systems". In: *The Twelfth Annual Battery Conference on Applications and Advances*. IEEE, pp. 223–226.

Berckmans, Gert et al. (2017). "Cost projection of state of the art lithium-ion batteries for electric vehicles up to 2030". In: *Energies* 10.9, p. 1314.

Bergveld, Henk Jan, Wanda S Kruijt, and Peter HL Notten (2002). "Battery management systems". In: *Battery Management Systems*. Springer, pp. 9–30.

Bertsekas, Dimitri P et al. (1995). *Dynamic programming and optimal control*. Vol. 1. 2. Athena scientific Belmont, MA.

Biegler, Lorenz T (2013). "A survey on sensitivity-based nonlinear model predictive control". In: *IFAC Proceedings Volumes* 46.32, pp. 499–510.

Bizeray, Adrien M et al. (2015). "Lithium-ion battery thermal-electrochemical model-based state estimation using orthogonal collocation and a modified extended Kalman filter". In: *Journal of Power Sources* 296, pp. 400–412.

Bizeray, Adrien M et al. (2018). “Identifiability and parameter estimation of the single particle lithium-ion battery model”. In: *IEEE Transactions on Control Systems Technology* 27.5, pp. 1862–1877.

Brown, Robert Grover, Patrick YC Hwang, et al. (1992). *Introduction to random signals and applied Kalman filtering*. Vol. 3. Wiley New York.

Camacho, Eduardo F and Carlos Bordons Alba (2013). *Model predictive control*. Springer Science & Business Media.

Campbell, Ian D et al. (2019). “Optimising lithium-ion cell design for plug-in hybrid and battery electric vehicles”. In: *Journal of Energy Storage* 22, pp. 228–238.

Campbell, Stephen L (1995). “Linearization of DAEs along trajectories”. In: *Zeitschrift für angewandte Mathematik und Physik ZAMP* 46.1, pp. 70–84.

Campbell, Stephen L and C William Gear (1995). “The index of general nonlinear DAEs”. In: *Numerische Mathematik* 72.2, pp. 173–196.

Camponogara, Eduardo et al. (2002). “Distributed model predictive control”. In: *IEEE control systems magazine* 22.1, pp. 44–52.

Cao, Jian, Nigel Schofield, and Ali Emadi (2008). “Battery balancing methods: A comprehensive review”. In: *2008 IEEE Vehicle Power and Propulsion Conference*. IEEE, pp. 1–6.

Caspar, Maurice and Sören Hohmann (2014). “Optimal cell balancing with model-based cascade control by duty cycle adaption”. In: *IFAC Proceedings Volumes* 47.3, pp. 10311–10318.

Chaturvedi, Nalin A et al. (2010). “Algorithms for advanced battery-management systems”. In: *IEEE Control systems magazine* 30.3, pp. 49–68.

Chemali, Ephrem et al. (2018). “State-of-charge estimation of Li-ion batteries using deep neural networks: A machine learning approach”. In: *Journal of Power Sources* 400, pp. 242–255.

Chen, Liang-Rui, Roy Chaoming Hsu, and Chuan-Sheng Liu (2008). “A design of a grey-predicted Li-ion battery charge system”. In: *IEEE Transactions on Industrial Electronics* 55.10, pp. 3692–3701.

Chen, Liang-Rui, Shing-Lih Wu, and Tsair-Rong Chen (2010). “Improving battery charging performance by using sinusoidal current charging with the minimum

AC impedance frequency”. In: *2010 IEEE International Conference on Sustainable Energy Technologies (ICSET)*. IEEE, pp. 1–4.

Chen, Liang-Rui et al. (2012a). “Sinusoidal-ripple-current charging strategy and optimal charging frequency study for Li-ion batteries”. In: *IEEE Transactions on Industrial Electronics* 60.1, pp. 88–97.

Chen, Wei, Ruichen Jin, and Agus Sudjianto (2005). “Analytical variance-based global sensitivity analysis in simulation-based design under uncertainty”. In:

Chen, Xiaopeng et al. (2012b). “An overview of lithium-ion batteries for electric vehicles”. In: *2012 10th International Power & Energy Conference (IPEC)*. IEEE, pp. 230–235.

Choi, Yongkeun et al. (2020). “Data-driven Energy Management Strategy for Plug-in Hybrid Electric Vehicles with Real-World Trip Information”. In: *arXiv preprint arXiv:2006.03704*.

Cope, Richard C and Yury Podrazhansky (1999). “The art of battery charging”. In: *Fourteenth Annual Battery Conference on Applications and Advances. Proceedings of the Conference (Cat. No. 99TH8371)*. IEEE, pp. 233–235.

Crestaux, Thierry, Olivier Le Maıtre, and Jean-Marc Martinez (2009). “Polynomial chaos expansion for sensitivity analysis”. In: *Reliability Engineering & System Safety* 94.7, pp. 1161–1172.

Cutler, Charles R and Brian L Ramaker (1980). “Dynamic matrix control?? A computer control algorithm”. In: *joint automatic control conference*. 17, p. 72.

Danielson, Claus et al. (2012). “Balancing of battery networks via constrained optimal control”. In: *2012 American Control Conference (ACC)*. IEEE, pp. 4293–4298.

Daowd, Mohamed et al. (2011). “Passive and active battery balancing comparison based on MATLAB simulation”. In: *2011 IEEE Vehicle Power and Propulsion Conference*. IEEE, pp. 1–7.

De Oliveira, Nuno MC and Lorenz T Biegler (1995). “An extension of Newton-type algorithms for nonlinear process control”. In: *Automatica* 31.2, pp. 281–286.

Di Domenico, Domenico, Anna Stefanopoulou, and Giovanni Fiengo (2010). “Lithium-ion battery state of charge and critical surface charge estimation using an electrochemical model-based extended Kalman filter”. In: *Journal of dynamic systems, measurement, and control* 132.6.

Dib, Wissam et al. (2014). “Optimal energy management for an electric vehicle in eco-driving applications”. In: *Control Engineering Practice* 29, pp. 299–307.

Doyle, Marc, Thomas F Fuller, and John Newman (1993). “Modeling of galvanostatic charge and discharge of the lithium/polymer/insertion cell”. In: *Journal of the Electrochemical society* 140.6, p. 1526.

Dubarry, Matthieu, Nicolas Vuillaume, and Bor Yann Liaw (2010). “Origins and accommodation of cell variations in Li-ion battery pack modeling”. In: *International Journal of Energy Research* 34.2, pp. 216–231.

Dunn, Bruce, Haresh Kamath, and Jean-Marie Tarascon (2011). “Electrical energy storage for the grid: a battery of choices”. In: *Science* 334.6058, pp. 928–935.

Ecker, Madeleine et al. (2015a). “Parameterisation of a Physico-Chemical Model of a Lithium-Ion Battery Part I: Determination of Parameters”. In: *J. Electrochem. Soc* 162.9, A1836–A1848.

Ecker, Madeleine et al. (2015b). “Parameterization of a physico-chemical model of a lithium-ion battery: II. Model validation”. In: *Journal of The Electrochemical Society* 162.9, A1849.

Eichi, Habiballah Rahimi and Mo-Yuen Chow (2012). “Modeling and analysis of battery hysteresis effects”. In: *2012 IEEE Energy Conversion Congress and Exposition (ECCE)*. IEEE, pp. 4479–4486.

Einhorn, Markus, Werner Roessler, and Juergen Fleig (2011). “Improved performance of serially connected Li-ion batteries with active cell balancing in electric vehicles”. In: *IEEE Transactions on Vehicular Technology* 60.6, pp. 2448–2457.

Eymard, Robert, Thierry Gallouët, and Raphaèle Herbin (2000). “Finite volume methods”. In: *Handbook of numerical analysis* 7, pp. 713–1018.

Farahani, Samira S et al. (2017). “Shrinking horizon model predictive control with chance-constrained signal temporal logic specifications”. In: *2017 American Control Conference (ACC)*. IEEE, pp. 1740–1746.

Floudas, Christodoulos A (1995). *Nonlinear and mixed-integer optimization: fundamentals and applications*. Oxford University Press.

Forman, Joel C et al. (2012). “Genetic identification and fisher identifiability analysis of the Doyle–Fuller–Newman model from experimental cycling of a LiFePO4 cell”. In: *Journal of Power Sources* 210, pp. 263–275.

Forsythe, George E and Wolfgang R Wasow (1960). “Finite Difference Methods”. In: *Partial Differential*.

Gallardo-Lozano, Javier et al. (2014). “Battery equalization active methods”. In: *Journal of Power Sources* 246, pp. 934–949.

Gao, Yang et al. (2017). “Lithium-ion battery aging mechanisms and life model under different charging stresses”. In: *Journal of Power Sources* 356, pp. 103–114.

Garcıa, Javier and Fernando Fernández (2015). “A comprehensive survey on safe reinforcement learning”. In: *Journal of Machine Learning Research* 16.1, pp. 1437–1480.

Gomadam, Parthasarathy M et al. (2002). “Mathematical modeling of lithium-ion and nickel battery systems”. In: *Journal of power sources* 110.2, pp. 267–284.

Guanetti, Jacopo, Yeojun Kim, and Francesco Borrelli (2018). “Control of connected and automated vehicles: State of the art and future challenges”. In: *Annual Reviews in Control* 45, pp. 18–40.

Hametner, Christoph and Stefan Jakubek (2013). “State of charge estimation for Lithium Ion cells: Design of experiments, nonlinear identification and fuzzy observer design”. In: *Journal of Power Sources* 238, pp. 413–421.

Han, Jihun et al. (2018). “Safe-and eco-driving control for connected and automated electric vehicles using analytical state-constrained optimal solution”. In: *IEEE Transactions on Intelligent Vehicles* 3.2, pp. 163–172.

Hanusa, Timothy P (2015). *The lightest metals: Science and technology from Lithium to Calcium*. John Wiley & Sons.

He, Hongwen, Rui Xiong, and Jinxin Fan (2011). “Evaluation of lithium-ion battery equivalent circuit models for state of charge estimation by an experimental approach”. In: *energies* 4.4, pp. 582–598.

Howard, Ronald A (1960). “Dynamic programming and markov processes.” In:

Hsieh, Guan-Chyun, Liang-Rui Chen, and Kuo-Shun Huang (2001). “Fuzzy-controlled Li-ion battery charge system with active state-of-charge controller”. In: *IEEE Transactions on industrial electronics* 48.3, pp. 585–593.

Hu, Xiaosong, Shengbo Eben Li, and Yalian Yang (2015). “Advanced machine learning approach for lithium-ion battery state estimation in electric vehicles”. In: *IEEE Transactions on Transportation electrification* 2.2, pp. 140–149.

Huang, Yanjun et al. (2017). "Model predictive control power management strategies for HEVs: A review". In: *Journal of Power Sources* 341, pp. 91–106.

Hussein, Ala A, Abbas A Fardoun, and Samantha S Stephen (2017). "An ultrafast maximum power point tracking technique for optimal battery charging". In: *IEEE Transactions on Sustainable Energy* 8.3, pp. 1321–1329.

Jain, Anubhav et al. (2015). "Relating voltage and thermal safety in Li-ion battery cathodes: a high-throughput computational study". In: *Physical Chemistry Chemical Physics* 17.8, pp. 5942–5953.

Jazwinski, Andrew H (2007). *Stochastic processes and filtering theory*. Courier Corporation.

Kandel, Aaron et al. (2020). "Distributionally robust surrogate optimal control for large-scale dynamical systems". In: *2020 American Control Conference (ACC)*. IEEE, pp. 2225–2231.

Keil, Peter and Andreas Jossen (2016). "Charging protocols for lithium-ion batteries and their impact on cycle life—An experimental study with different 18650 high-power cells". In: *Journal of Energy Storage* 6, pp. 125–141.

Kesler, Stephen E et al. (2012). "Global lithium resources: Relative importance of pegmatite, brine and other deposits". In: *Ore geology reviews* 48, pp. 55–69.

Kiefer, Jack (1959). "Optimum experimental designs". In: *Journal of the Royal Statistical Society: Series B (Methodological)* 21.2, pp. 272–304.

Kiehne, Heinz Albert (2003). *Battery technology handbook*. Vol. 118. CRC Press.

Klein, Reinhardt et al. (2011). "Optimal charging strategies in lithium-ion battery". In: *Proceedings of the 2011 american Control Conference*. IEEE, pp. 382–387.

Körkel, Stefan and Ekaterina Kostina (2005). "Numerical methods for nonlinear experimental design". In: *Modeling, simulation and optimization of complex processes*. Springer, pp. 255–272.

Körkel, Stefan et al. (2004). "Numerical methods for optimal control problems in design of robust optimal experiments for nonlinear dynamic processes". In: *Optimization Methods and Software* 19.3-4, pp. 327–338.

Larminie, James and John Lowry (2012). *Electric vehicle technology explained*. John Wiley & Sons.

Laue, Vincent et al. (2020). “Model-Based Uncertainty Quantification for the Product Properties of Lithium-Ion Batteries”. In: *Energy Technology* 8.2, p. 1900201.

Lee, Ernest Bruce and Lawrence Markus (1967). *Foundations of optimal control theory*. Tech. rep. Minnesota Univ Minneapolis Center For Control Sciences.

Lee, Jay H (2011). “Model predictive control: Review of the three decades of development”. In: *International Journal of Control, Automation and Systems* 9.3, p. 415.

Lenz, Ian, Ross A Knepper, and Ashutosh Saxena (2015). “DeepMPC: Learning deep latent features for model predictive control.” In: *Robotics: Science and Systems*. Rome, Italy.

Lerner, Uri N (2002). “Hybrid Bayesian networks for reasoning about complex systems”. PhD thesis. Citeseer.

Lewis, Frank L, Draguna Vrabie, and Kyriakos G Vamvoudakis (2012). “Reinforcement learning and feedback control: Using natural decision methods to design optimal adaptive controllers”. In: *IEEE Control Systems Magazine* 32.6, pp. 76–105.

Li, Wei C and Lorenz T Biegler (1989). “A multistep, Newton-type control strategy for constrained, nonlinear processes”. In: *1989 American Control Conference*. IEEE, pp. 1526–1527.

Lillicrap, Timothy P et al. (2015). “Continuous control with deep reinforcement learning”. In: *arXiv preprint arXiv:1509.02971*.

Limon, Daniel, J Calliess, and Jan Marian Maciejowski (2017). “Learning-based nonlinear model predictive control”. In: *IFAC-PapersOnLine* 50.1, pp. 7769–7776.

Lin, Xinfan et al. (2014). “A lumped-parameter electro-thermal model for cylindrical batteries”. In: *Journal of Power Sources* 257, pp. 1–11.

Lisbona, Diego and Timothy Snee (2011). “A review of hazards associated with primary lithium and lithium-ion batteries”. In: *Process safety and environmental protection* 89.6, pp. 434–442.

Liu, Chang and Yi Lu Murphey (2019). “Optimal power management based on Q-learning and neuro-dynamic programming for plug-in hybrid electric vehicles”. In: *IEEE Transactions on Neural Networks and Learning Systems*.

Liu, Ji et al. (2016). “Can an identifiability-optimizing test protocol improve the robustness of subsequent health-conscious lithium-ion battery control? an illustrative case study”. In: *2016 American Control Conference (ACC)*. IEEE, pp. 6320–6325.

Liu, Jinming and Huei Peng (2008). "Modeling and control of a power-split hybrid vehicle". In: *IEEE transactions on control systems technology* 16.6, pp. 1242–1251.

Liu, Kailong et al. (2020). "An evaluation study of different modelling techniques for calendar ageing prediction of lithium-ion batteries". In: *Renewable and Sustainable Energy Reviews* 131, p. 110017.

Liu, Weibo et al. (2017). "A survey of deep neural network architectures and their applications". In: *Neurocomputing* 234, pp. 11–26.

Lopez, Diana C et al. (2016). "A computational framework for identifiability and ill-conditioning analysis of lithium-ion battery models". In: *Industrial & Engineering Chemistry Research* 55.11, pp. 3026–3042.

Lu, Languang et al. (2013). "A review on the key issues for lithium-ion battery management in electric vehicles". In: *Journal of power sources* 226, pp. 272–288. URL: `https://www.sciencedirect.com/science/article/pii/S0378775312016163`.

Lucia, Sergio et al. (2017). "Towards adaptive health-aware charging of li-ion batteries: A real-time predictive control approach using first-principles models". In: *2017 American Control Conference (ACC)*. IEEE, pp. 4717–4722.

Magnusson, Fredrik and Johan Åkesson (2012). "Collocation methods for optimization in a Modelica environment". In: *Proceedings of the 9th International MODELICA Conference; September 3-5; 2012; Munich; Germany*. 076. Linköping University Electronic Press, pp. 649–658.

Maiser, Eric (2014). "Battery packaging-Technology review". In: *AIP Conference Proceedings*. Vol. 1597. 1. American Institute of Physics, pp. 204–218.

Manesso, Erica, Srinath Sridharan, and Rudiyanto Gunawan (2017). "Multi-objective optimization of experiments using curvature and fisher information matrix". In: *Processes* 5.4, p. 63.

Marańda, Witold (2015). "Capacity degradation of lead-acid batteries under variable-depth cycling operation in photovoltaic system". In: *2015 22nd International Conference Mixed Design of Integrated Circuits & Systems (MIXDES)*. IEEE, pp. 552–555.

Mathieu, Romain et al. (2017). "D-optimal design of experiments applied to lithium battery for ageing model calibration". In: *Energy* 141, pp. 2108–2119.

Mayne, David Q (2014). “Model predictive control: Recent developments and future promise”. In: *Automatica* 50.12, pp. 2967–2986.

Mayne, David Q and Hannah Michalska (1988). “Receding horizon control of nonlinear systems”. In: *Proceedings of the 27th IEEE Conference on Decision and Control*. IEEE, pp. 464–465.

Mayne, David Q et al. (2000). “Constrained model predictive control: Stability and optimality”. In: *Automatica* 36.6, pp. 789–814.

McCurlie, Lucas, Matthias Preindl, and Ali Emadi (2016). “Fast model predictive control for redistributive lithium-ion battery balancing”. In: *IEEE Transactions on Industrial Electronics* 64.2, pp. 1350–1357.

Mekonnen, Yemeserach, Aditya Sundararajan, and Arif I Sarwat (2016). “A review of cathode and anode materials for lithium-ion batteries”. In: *SoutheastCon 2016*. IEEE, pp. 1–6.

Mendoza, Sergio et al. (2017). “Maximizing parameter identifiability of a combined thermal and electrochemical battery model via periodic current input optimization”. In: *IFAC-PapersOnLine* 50.1, pp. 7314–7320.

Mesbah, Ali (2016). “Stochastic model predictive control: An overview and perspectives for future research”. In: *IEEE Control Systems Magazine* 36.6, pp. 30–44.

Miyatake, Masafumi, Motoi Kuriyama, and Yuzuru Takeda (2011). “Theoretical study on eco-driving technique for an electric vehicle considering traffic signals”. In: *2011 IEEE Ninth International Conference on Power Electronics and Drive Systems*. IEEE, pp. 733–738.

Mnih, Volodymyr et al. (2015). “Human-level control through deep reinforcement learning”. In: *nature* 518.7540, pp. 529–533.

Moore, Stephen W and Peter J Schneider (2001a). *A review of cell equalization methods for lithium ion and lithium polymer battery systems*. Tech. rep. SAE Technical Paper.

— (2001b). *A review of cell equalization methods for lithium ion and lithium polymer battery systems*. Tech. rep. SAE Technical Paper.

Mosca, Alessio, Andrea Pozzi, and Davide M Raimondo (2018). “Battery ageing-aware stochastic management of power networks in islanded mode”. In: *2018 22nd International Conference on System Theory, Control and Computing (ICSTCC)*. IEEE, pp. 571–578.

Moura, Scott J (2015). "Estimation and control of battery electrochemistry models: A tutorial." In: *CDC*. Citeseer, pp. 3906–3912.

Moura, Scott J, Nalin A Chaturvedi, and M Krstić (2013). "Constraint management in Li-ion batteries: A modified reference governor approach". In: *2013 American Control Conference*. IEEE, pp. 5332–5337.

Moura, Scott J et al. (2010a). "Optimal control of film growth in lithium-ion battery packs via relay switches". In: *IEEE Transactions on Industrial Electronics* 58.8, pp. 3555–3566.

Moura, Scott J et al. (2016). "Battery state estimation for a single particle model with electrolyte dynamics". In: *IEEE Transactions on Control Systems Technology* 25.2, pp. 453–468.

Moura, Scott Jason et al. (2010b). "A stochastic optimal control approach for power management in plug-in hybrid electric vehicles". In: *IEEE Transactions on control systems technology* 19.3, pp. 545–555.

Nafsun, AI and N Yusoff (2011). "Effect of model-plant mismatch on MPC controller performance". In: *Journal of Applied Sciences* 11.21, pp. 3579–3585.

Nejad, S, DT Gladwin, and DA Stone (2016). "A systematic review of lumped-parameter equivalent circuit models for real-time estimation of lithium-ion battery states". In: *Journal of Power Sources* 316, pp. 183–196.

Nocedal, Jorge and Stephen Wright (2006). *Numerical optimization*. Springer Science & Business Media.

Notten, Peter HL, JHG Op het Veld, and JRG Van Beek (2005). "Boostcharging Li-ion batteries: A challenging new charging concept". In: *Journal of Power Sources* 145.1, pp. 89–94.

Nuhic, Adnan et al. (2013). "Health diagnosis and remaining useful life prognostics of lithium-ion batteries using data-driven methods". In: *Journal of power sources* 239, pp. 680–688.

Omar, Noshin et al. (2014). "Lithium iron phosphate based battery–Assessment of the aging parameters and development of cycle life model". In: *Applied Energy* 113, pp. 1575–1585.

Park, Saehong et al. (2018). “Optimal experimental design for parameterization of an electrochemical lithium-ion battery model”. In: *Journal of The Electrochemical Society* 165.7, A1309.

Park, Saehong et al. (2020). “Reinforcement learning-based fast charging control strategy for li-ion batteries”. In: *2020 IEEE Conference on Control Technology and Applications (CCTA)*. IEEE, pp. 100–107.

Patnaik, Lalit, AVJS Praneeth, and Sheldon S Williamson (2018). “A closed-loop constant-temperature constant-voltage charging technique to reduce charge time of lithium-ion batteries”. In: *IEEE Transactions on Industrial Electronics* 66.2, pp. 1059–1067.

Perez, HE et al. (2017). “Optimal charging of Li-ion batteries via a single particle model with electrolyte and thermal dynamics”. In: *Journal of The Electrochemical Society* 164.7, A1679.

Perrin, Marion et al. (2005). “Lead–acid batteries in stationary applications: competitors and new markets for large penetration of renewable energies”. In: *Journal of Power Sources* 144.2, pp. 402–410.

Petzold, Linda (1982). “Differential/algebraic equations are not ODE’s”. In: *SIAM Journal on Scientific and Statistical Computing* 3.3, pp. 367–384.

Pollet, Bruno G, Iain Staffell, and Jin Lei Shang (2012). “Current status of hybrid, battery and fuel cell electric vehicles: From electrochemistry to market prospects”. In: *Electrochimica Acta* 84, pp. 235–249.

Pop, Valer et al. (2008). *Battery management systems: Accurate state-of-charge indication for battery-powered applications*. Vol. 9. Springer Science & Business Media.

Powell, Warren B (2007). *Approximate Dynamic Programming: Solving the curses of dimensionality*. Vol. 703. John Wiley & Sons.

Pozzi, Andrea, Marcello Torchio, and Davide M Raimondo (2018a). “Assessing the performance of model-based energy saving charging strategies in Li-ion cells”. In: *2018 IEEE Conference on Control Technology and Applications (CCTA)*. IEEE, pp. 806–811.

— (2018b). “Film growth minimization in a Li-ion cell: a Pseudo Two Dimensional model-based optimal charging approach”. In: *2018 European Control Conference (ECC)*. IEEE, pp. 1753–1758.

Pozzi, Andrea et al. (2018a). “Optimal Design of Experiment for Parameter Estimation of a Single Particle Model for Lithiumion Batteries”. In: *2018 IEEE Conference on Decision and Control (CDC)*. IEEE, pp. 6482–6487.

Pozzi, Andrea et al. (2018b). “Optimal design of experiments for a lithium-ion cell: parameters identification of an isothermal single particle model with electrolyte dynamics”. In: *Industrial & Engineering Chemistry Research* 58.3, pp. 1286–1299.

Pozzi, Andrea et al. (2020a). “Balancing-aware charging strategy for series-connected lithium-ion cells: A nonlinear model predictive control approach”. In: *IEEE Transactions on Control Systems Technology* 28.5, pp. 1862–1877.

Pozzi, Andrea et al. (2020b). “Global Sensitivity Methods for Design of Experiments in Lithium-ion Battery Context”. In: *arXiv preprint arXiv:2004.09668*.

Pozzi, Andrea et al. (2020c). “Optimal charging of an electric vehicle battery pack: A real-time sensitivity-based model predictive control approach”. In: *Journal of Power Sources* 461, p. 228133.

Pronzato, Luc (2008). “Optimal experimental design and some related control problems”. In: *Automatica* 44.2, pp. 303–325.

Purushothaman, BK and U Landau (2006). “Rapid charging of lithium-ion batteries using pulsed currents: A theoretical analysis”. In: *Journal of The Electrochemical Society* 153.3, A533.

Rahimi-Eichi, Habiballah et al. (2013). “Battery management system: An overview of its application in the smart grid and electric vehicles”. In: *IEEE Industrial Electronics Magazine* 7.2, pp. 4–16.

Ramadass, P et al. (2004). “Development of first principles capacity fade model for Li-ion cells”. In: *Journal of the Electrochemical Society* 151.2, A196.

Ramadesigan, Venkatasailanathan et al. (2012). “Modeling and simulation of lithium-ion batteries from a systems engineering perspective”. In: *Journal of the electrochemical society* 159.3, R31.

Rao, Christopher V, Stephen J Wright, and James B Rawlings (1998). “Application of interior-point methods to model predictive control”. In: *Journal of optimization theory and applications* 99.3, pp. 723–757.

Rawlings, James B (2000). “Tutorial overview of model predictive control”. In: *IEEE control systems magazine* 20.3, pp. 38–52.

Richalet, Jacques et al. (1978). "Model predictive heuristic control". In: *Automatica (Journal of IFAC)* 14.5, pp. 413–428.

Rolison, Debra R and Linda F Nazar (2011). "Electrochemical energy storage to power the 21st century". In: *Mrs Bulletin* 36.7, pp. 486–493.

Romagnoli, Raffaele et al. (2017). "Control of the state-of-charge of a li-ion battery cell via reference governor". In: *IFAC-PapersOnLine* 50.1, pp. 13747–13753.

Rosolia, Ugo and Francesco Borrelli (2017). "Learning model predictive control for iterative tasks. a data-driven control framework". In: *IEEE Transactions on Automatic Control* 63.7, pp. 1883–1896.

Rust, John (1997). "Using randomization to break the curse of dimensionality". In: *Econometrica: Journal of the Econometric Society*, pp. 487–516.

Santhanagopalan, Shriram et al. (2006). "Review of models for predicting the cycling performance of lithium ion batteries". In: *Journal of power sources* 156.2, pp. 620–628.

Šantin, Ondřej et al. (2016). "Towards ECU-ready nonlinear model predictive control: Tip-in maneuver case study". In: *2016 IEEE 55th Conference on Decision and Control (CDC)*. IEEE, pp. 1602–1607.

Scharf, Louis L and L Todd McWhorter (1993). "Geometry of the Cramer-Rao bound". In: *Signal Processing* 31.3, pp. 301–311.

Schenkendorf, René (2014). "Optimal experimental design for parameter identification and model selection". In:

Schenkendorf, René et al. (2018). "The impact of global sensitivities and design measures in model-based optimal experimental design". In: *Processes* 6.4, p. 27.

Schulman, John et al. (2015). "Trust region policy optimization". In: *International conference on machine learning*, pp. 1889–1897.

Sciarretta, Antonio, Giovanni De Nunzio, and Luis Leon Ojeda (2015). "Optimal eco-driving control: Energy-efficient driving of road vehicles as an optimal control problem". In: *IEEE Control Systems Magazine* 35.5, pp. 71–90.

Sciarretta, Antonio and Lino Guzzella (2007). "Control of hybrid electric vehicles". In: *IEEE Control Systems Magazine* 27.2, pp. 60–70.

Scrosati, Bruno (2011). "History of lithium batteries". In: *Journal of solid state electrochemistry* 15.7-8, pp. 1623–1630.

Scrosati, Bruno and Jürgen Garche (2010). "Lithium batteries: Status, prospects and future". In: *Journal of power sources* 195.9, pp. 2419–2430.

Sharma, Aabhas and Hosam K Fathy (2014). "Fisher identifiability analysis for a periodically-excited equivalent-circuit lithium-ion battery model". In: *2014 American Control Conference*. IEEE, pp. 274–280.

Shen, Weixiang, Thanh Tu Vo, and Ajay Kapoor (2012). "Charging algorithms of lithium-ion batteries: An overview". In: *2012 7th IEEE conference on industrial electronics and applications (ICIEA)*. IEEE, pp. 1567–1572.

Silver, David et al. (2014). "Deterministic policy gradient algorithms". In:

Smith, Alice E and David W Coit (1997). "Penalty functions". In: *Handbook of evolutionary computation* 97.1, p. C5.

Smith, Raymond B and Martin Z Bazant (2017). "Multiphase porous electrode theory". In: *Journal of The Electrochemical Society* 164.11, E3291.

Sobol, Ilya M (2001). "Global sensitivity indices for nonlinear mathematical models and their Monte Carlo estimates". In: *Mathematics and computers in simulation* 55.1-3, pp. 271–280.

Subramanian, Venkat R, Vinten D Diwakar, and Deepak Tapriyal (2005). "Efficient macro-micro scale coupled modeling of batteries". In: *Journal of The Electrochemical Society* 152.10, A2002.

Sulzer, Valentin et al. (2020). "Python Battery Mathematical Modelling (PyBaMM)". In:

Sun, Chao et al. (2014a). "Dynamic traffic feedback data enabled energy management in plug-in hybrid electric vehicles". In: *IEEE Transactions on Control Systems Technology* 23.3, pp. 1075–1086.

Sun, Chao et al. (2014b). "Velocity predictors for predictive energy management in hybrid electric vehicles". In: *IEEE Transactions on Control Systems Technology* 23.3, pp. 1197–1204.

Sun, Chao et al. (2020). "Optimal eco-driving control of connected and autonomous vehicles through signalized intersections". In: *IEEE Internet of Things Journal* 7.5, pp. 3759–3773.

Sutton, Richard S, Andrew G Barto, et al. (1998). *Introduction to reinforcement learning*. Vol. 135. MIT press Cambridge.

Sutton, Richard S et al. (2000). "Policy gradient methods for reinforcement learning with function approximation". In: *Advances in neural information processing systems*, pp. 1057–1063.

Tarascon, J-M and Michel Armand (2011). "Issues and challenges facing rechargeable lithium batteries". In: *Materials for sustainable energy: a collection of peer-reviewed research and review articles from Nature Publishing Group*. World Scientific, pp. 171–179.

Thanagasundram, Suguna et al. (2012). "A cell level model for battery simulation". In: *European Electric Vehicle Congress*, pp. 1–13.

Tomaszewska, Anna et al. (2019). "Lithium-ion battery fast charging: a review". In: *ETransportation* 1, p. 100011.

Torchio, M et al. (2016a). "Optimal health-aware charging protocol for Lithium-ion batteries: A fast model predictive control approach". In: *IFAC-PapersOnLine* 49.7, pp. 827–832.

Torchio, Marcello et al. (2015). "Real-time model predictive control for the optimal charging of a lithium-ion battery". In: *2015 American Control Conference (ACC)*. IEEE, pp. 4536–4541.

Torchio, Marcello et al. (2016b). "Lionsimba: a matlab framework based on a finite volume model suitable for li-ion battery design, simulation, and control". In: *Journal of The Electrochemical Society* 163.7, A1192.

Torchio, Marcello et al. (2016c). "Optimal charging of a Li-ion cell: A hybrid model predictive control approach". In: *2016 IEEE 55th Conference on Decision and Control (CDC)*. IEEE, pp. 4053–4058.

Torchio, Marcello et al. (2017). "Design of piecewise affine and linear time-varying model predictive control strategies for advanced battery management systems". In: *Journal of The Electrochemical Society* 164.4, A949.

Tran, Manh-Kien and Michael Fowler (2020). "A Review of Lithium-Ion Battery Fault Diagnostic Algorithms: Current Progress and Future Challenges". In: *Algorithms* 13.3, p. 62.

Vetter, Jens et al. (2005). "Ageing mechanisms in lithium-ion batteries". In: *Journal of power sources* 147.1-2, pp. 269–281.

Waag, Wladislaw, Christian Fleischer, and Dirk Uwe Sauer (2014). “Critical review of the methods for monitoring of lithium-ion batteries in electric and hybrid vehicles”. In: *Journal of Power Sources* 258, pp. 321–339.

Wächter, Andreas and Lorenz T Biegler (2006). “On the implementation of an interior-point filter line-search algorithm for large-scale nonlinear programming”. In: *Mathematical programming* 106.1, pp. 25–57.

Walter, Eric and Luc Pronzato (1997). “Identification of parametric models”. In: *Communications and control engineering* 8.

Wang, Shun-Chung and Yi-Hua Liu (2014). “A PSO-based fuzzy-controlled searching for the optimal charge pattern of Li-ion batteries”. In: *IEEE Transactions on Industrial Electronics* 62.5, pp. 2983–2993.

Watkins, Christopher JCH and Peter Dayan (1992). “Q-learning”. In: *Machine learning* 8.3-4, pp. 279–292.

Welch, Greg, Gary Bishop, et al. (1995). *An introduction to the Kalman filter*.

Whittingham, M Stanley (2012). “History, evolution, and future status of energy storage”. In: *Proceedings of the IEEE* 100.Special Centennial Issue, pp. 1518–1534.

Whittle, Peter (1973). “Some general points in the theory of optimal experimental design”. In: *Journal of the Royal Statistical Society: Series B (Methodological)* 35.1, pp. 123–130.

Wu, Jingda et al. (2018). “Continuous reinforcement learning of energy management with deep Q network for a power split hybrid electric bus”. In: *Applied energy* 222, pp. 799–811.

Xavier, Marcelo A and M Scott Trimboli (2015). “Lithium-ion battery cell-level control using constrained model predictive control and equivalent circuit models”. In: *Journal of Power Sources* 285, pp. 374–384.

Xie, Xiangzhong, Ulrike Krewer, and René Schenkendorf (2018). “Robust optimization of dynamical systems with correlated random variables using the point estimate method”. In: *IFAC-PapersOnLine* 51.2, pp. 427–432.

Yan, Jingyu et al. (2011a). “Model predictive control-based fast charging for vehicular batteries”. In: *Energies* 4.8, pp. 1178–1196.

— (2011b). “Model predictive control-based fast charging for vehicular batteries”. In: *Energies* 4.8, pp. 1178–1196.

Yan, Xing-Gang and Christopher Edwards (2007). "Nonlinear robust fault reconstruction and estimation using a sliding mode observer". In: *Automatica* 43.9, pp. 1605–1614.

Yoshida, Toshihiro et al. (2006). "Degradation mechanism and life prediction of lithium-ion batteries". In: *Journal of The Electrochemical Society* 153.3, A576.

Zhao, Xiangmo et al. (2020). "Dynamic Eco-Driving on Signalized Arterial Corridors during the Green Phase for the Connected Vehicles". In: *Journal of Advanced Transportation* 2020.

Zou, Changfu, Chris Manzie, and Sohel Anwar (2014). "Control-oriented modeling of a lithium-ion battery for fast charging". In: *IFAC Proceedings Volumes* 47.3, pp. 3912–3917.

Zou, Changfu, Chris Manzie, and Dragan Nešić (2015). "A framework for simplification of PDE-based lithium-ion battery models". In: *IEEE Transactions on Control Systems Technology* 24.5, pp. 1594–1609.

— (2018). "Model predictive control for lithium-ion battery optimal charging". In: *IEEE/ASME Transactions on Mechatronics* 23.2, pp. 947–957.

Zou, Changfu et al. (2017). "Electrothermal dynamics-conscious lithium-ion battery cell-level charging management via state-monitored predictive control". In: *Energy* 141, pp. 250–259.